

TESLA Technical Design Report

PART VI **Appendices**

March 2001

Editors: R.Klanner

Chapter 1: V.Telnov

Chapter 2: U.Katz, M.Klein, A.Levy

Chapter 3: R.Kaiser, W.D.Nowak

Chapter 4: E.DeSanctis, J.-M.Laget, K.Rith

Introduction

These appendices to the TESLA Technical Design Report (TDR) describe four additional particle-physics projects, which can be carried out at the TESLA e^+e^- -collider. Two of them make use of HERA and thus require TESLA to be located at DESY.

The first program, the **Photon Collider at TESLA**, uses a high power laser to produce high-energy photon beams from one or both electron beams via Compton scattering. In this way the study of photon-photon and photon-electron interactions at energies similar to e^+e^- -collisions and at similar luminosity become feasible. These experiments would be conducted in a second interaction region by a second experiment. They complement and add to the e^+e^- -physics program of TESLA. A few examples of the exciting physics questions which can be studied with the “Photon Collider” are:

1. In photon-photon collisions, in contrast to e^+e^- -interactions, the scalar Higgs-bosons can be produced singly. This allows on the one hand to explore Higgs-bosons with higher masses, and on the other hand to measure precisely the two-photon decay width of the Higgs, which is particularly sensitive to new heavy charged particles with masses well beyond the reach of planned accelerators.
2. The production cross-sections of pairs of any charged particles (supersymmetric particles, Higgs, etc.) are about a factor ten larger in photon-photon than in e^+e^- -interactions and depend differently on physics parameters. This enhances the sensitivity for the study of such particles.
3. In photon-electron interactions certain types of charged supersymmetric particles can be produced with masses higher than in e^+e^- -interactions.
4. Photon-photon and photon-electron scattering allow the study of the hadronic and electromagnetic structure of the photon in a new kinematic domain.

This experimental program is proposed and supported by a strong high energy physics community with a large overlap with the e^+e^- -community. The detailed studies of the physics of photon-photon and photon-electron interactions at TESLA are only just starting and are far less advanced than for e^+e^- .

The remaining three projects are called THERA, TESLA-N and ELFE. They mainly concentrate on the physics of strong interactions and the structure of hadrons.

THERA: Electron Scattering at 1 TeV uses the polarised and/or unpolarised electrons from the linear collider and brings them into collision with the protons of

HERA in the W-hall of HERA on the DESY site. To achieve this, the direction of the protons in HERA has to be reversed and the TESLA tunnel, which is built tangential to the HERA-ring, has to be connected to the HERA tunnel. The electron energy can be either the full single beam TESLA energy (250 up to 400 GeV after the energy upgrade) or even twice the TESLA energy using both TESLA arms as accelerators in the same direction. In this way a wide range of electron-proton energies, up to 1.7 TeV, about five times the present HERA energy, becomes feasible.

Obtaining high luminosities for THERA is a big challenge. Initial studies show that $4 \cdot 10^{30} \text{cm}^{-2}\text{s}^{-1}$ may be feasible for 250 GeV electrons on 920 GeV protons. A further increase beyond $10^{31} \text{cm}^{-2}\text{s}^{-1}$ requires major studies to demonstrate its feasibility and technical realisation. For equal electron and proton energies (e.g. 500 GeV on 500 GeV when using both arms of TESLA for acceleration) a luminosity of $2.5 \cdot 10^{31} \text{cm}^{-2}\text{s}^{-1}$ has been estimated.

The proposed physics is an extension of the successful HERA-program:

1. Strong interaction studies at small parton momenta and at high parton densities, where THERA has a real possibility to reach the new strong interaction domain of saturation and thus contribute to the understanding of the question of confinement.
2. Investigation of the transition from small distance to large distance QCD in an extended kinematic range.
3. Precision measurement of the strong coupling constant.
4. Extension of the measurement of the proton and photon structure as well as heavy flavour physics to smaller parton momenta and highest momentum transfers corresponding distance scales of 10^{-19} m.
5. Measurement of electro-weak parameters and search for new, exotic particles, in particular for leptoquarks and excited fermions.

A possible extension of this programme to electron-nucleon and to $\vec{e}\vec{p}$ scattering is also presented.

This physics program and first ideas for a detector have been designed and are strongly supported by members of the present HERA-experiments H1 and ZEUS and an enthusiastic theoretical community interested in a deeper understanding of the strong interactions.

TESLA-N: Electron Scattering with Polarised Targets at TESLA uses the interactions of the 250 - 400 GeV longitudinally polarised electrons of TESLA with a solid state target, which can be either longitudinally or transversely polarised. The maximum centre-of-mass energy is 30 GeV and a luminosity up to $10^{35} \text{cm}^{-2}\text{s}^{-1}$ can be achieved; using several beam extraction points along the accelerator, centre-of-mass energies between 7 and 30 GeV are possible.

The main goal of TESLA-N is the precise measurement of the so far completely unknown transverse quark spin structure functions, which will provide complete information on the quark spin structure functions of the nucleon. In addition the polarised structure function of the gluon will be determined with high precision. The dependence of the structure functions on momentum transfer will provide unique precision tests of the predictive power of Quantum Chromodynamics (QCD) in the spin sector.

With the option of also using unpolarised targets and real photons, TESLA-N represents a versatile next-generation facility at the intersection of particle and nuclear physics. The program has been devised and is supported by members of the present lepton-hadron fixed-target experiments like HERMES at DESY and COMPASS at CERN.

ELFE: the Electron Laboratory for Europe uses 15 to 27.5 GeV electrons extracted from TESLA about 8 km from the electron source, reversed in direction, transported along TESLA and finally injected into the modified HERA electron ring. HERA is used in stretcher-mode with continuous extraction onto the target of the ELFE experiment. The repetition rate for injection into HERA is 10 Hz. The current stored in HERA is 150 mA for an extracted beam current of $30\mu\text{A}$. Longitudinal electron polarisation can be obtained at 27.5 GeV. The centre-of-mass energies range from 5 to 7 GeV and luminosities between 10^{35} and $10^{38}\text{cm}^{-2}\text{s}^{-1}$ are obtained with a large duty cycle. This enables coincidence experiments for small cross section exclusive reactions, which are impossible otherwise. The small energy spread of the beam of 0.1% together with a large acceptance spectrometer of superb momentum and angular resolution will enable the identification of exclusive reactions.

The detailed investigation of exclusive processes in electron-proton scattering allows the measurement of properties of the hadronic wave function which were hitherto not accessible. Examples are the determination of the orbital angular momentum of quarks in a hadron or the spin structure of unstable particles. The so called Skewed Parton Distributions (SPD) are the theoretical framework in which the data is discussed. The program is proposed and supported by a large fraction of the community of nuclear and particle physicists who now investigate the structure of hadrons at lower energy facilities like MAMI, GRAAL, ELSA and TJNAF, or high-energy facilities at CERN, DESY and FNAL.

The four projects outlined in the appendix have not been worked out in the same detail and depth as the remainder of the TESLA TDR. They represent high quality physics programs, which are supported by strong international communities and which can be performed at relatively modest additional cost if the TESLA linear accelerator is located at the DESY laboratory at Hamburg.

1 The Photon Collider at TESLA

B. Badelek⁴³, C. Blöchinger⁴⁴, J. Blümlein¹², E. Boos²⁸, R. Brinkmann¹²,
 H. Burkhardt¹¹, P. Bussey¹⁷, C. Carimalo³³, J. Chyla³⁴, A.K. Çiftçi⁴, W. Decking¹²,
 A. De Roeck¹¹, V. Fadin¹⁰, M. Ferrario¹⁵, A. Finch²⁴, H. Fraas⁴⁴, F. Franke⁴⁴,
 M. Galynskii²⁷, A. Gamp¹², I. Ginzburg³¹, R. Godbole⁶, D.S. Gorbunov²⁸,
 G. Gounaris³⁹, K. Hagiwara²², L. Han¹⁹, R.-D. Heuer¹⁸, C. Heusch³⁶, J. Illana¹²,
 V. Ilyin²⁸, P. Jankowski⁴³, Yi Jiang¹⁹, G. Jikia¹⁶, L. Jönsson²⁶, M. Kalachnikov⁸,
 F. Kapusta³³, R. Klanner^{12,18}, M. Klasen¹², K. Kobayashi⁴¹, T. Kon⁴⁰, G. Kotkin³⁰,
 M. Krämer¹⁴, M. Krawczyk⁴³, Y.P. Kuang⁷, E. Kuraev¹³, J. Kwiecinski²³,
 M. Leenen¹², M. Levchuk²⁷, W.F. Ma¹⁹, H. Martyn¹, T. Mayer⁴⁴, M. Melles³⁵,
 D.J. Miller²⁵, S. Mtingwa²⁹, M. Mühlleitner¹², B. Muryn²³, P.V. Nickles⁸, R. Orava²⁰,
 C. Pancheri¹⁵, A. Penin¹², A. Potylitsyn⁴², P. Poulou⁶, T. Quast⁸, P. Raimondi³⁷,
 H. Redlin⁸, F. Richard³², S.D. Rindani², T. Rizzo³⁷, E. Saldin¹², W. Sandner⁸,
 H. Schönrogge⁸, E. Schneidmiller¹², H.J. Schreiber¹², S. Schreiber¹², K.P. Schüller¹²,
 V. Serbo³⁰, A. Seryi³⁷, R. Shanidze³⁸, W. da Silva³³, S. Söldner-Rembold¹¹,
 M. Spira³⁵, A.M. Stasto²³, S. Sultansoy⁵, T. Takahashi²¹, V. Telnov^{10,12},
 A. Tkabladze¹², D. Trines¹², A. Undrus⁹, A. Wagner¹², N. Walker¹², I. Watanabe³,
 T. Wengler¹¹, I. Will^{8,12}, S. Wipf¹², Ö. Yavaş⁴, K. Yokoya²², M. Yurkov¹²,
 A.F. Zarnecki⁴³, P. Zerwas¹², F. Zomer³².

- | | |
|--|---|
| ¹ RWTH Aachen, Germany | ²⁴ University of Lancaster, UK |
| ² PRL, Ahmedabad, India | ²⁵ UCL, London, UK |
| ³ Akita KeizaiHoka University, Japan | ²⁶ University of Lund, Sweden |
| ⁴ Ankara University, Turkey | ²⁷ Inst. of Physics, Minsk, Belarus |
| ⁵ Gazi University, Ankara, Turkey | ²⁸ Moscow State University, Russia |
| ⁶ Indian Institute of Science, Bangalore, India | ²⁹ N.Carolina Univ., USA |
| ⁷ Tsinghua University, Beijing, P.R. China | ³⁰ Novosibirsk State University, Russia |
| ⁸ Max-Born-Institute, Berlin, Germany | ³¹ Inst. of Math., Novosibirsk, Russia |
| ⁹ BNL, Upton, USA | ³² LAL, Orsay, France |
| ¹⁰ Budker INP, Novosibirsk, Russia | ³³ Université de Paris VI-VII, France |
| ¹¹ CERN, Geneva, Switzerland | ³⁴ IP, Prague, Czech Republic |
| ¹² DESY, Hamburg and Zeuthen, Germany | ³⁵ PSI, Villingen, Switzerland |
| ¹³ JINR, Dubna, Russia | ³⁶ UCSC, Santa Cruz, USA |
| ¹⁴ University of Edinburgh, UK | ³⁷ SLAC, Stanford, USA |
| ¹⁵ INFN-LNF, Frascati, Italy | ³⁸ Tbilisi State University, Georgia |
| ¹⁶ Universität Freiburg, Germany | ³⁹ University of Thessaloniki, Greece |
| ¹⁷ University of Glasgow, UK | ⁴⁰ Seikei University, Tokyo, Japan |
| ¹⁸ Universität Hamburg, Germany | ⁴¹ Sumimoto Heavy Industries, Tokyo, Japan |
| ¹⁹ CUST, Hefei, P.R.China | ⁴² Polytechnic Institute, Tomsk, Russia |
| ²⁰ University of Helsinki, Finland | ⁴³ Warsaw University, Poland |
| ²¹ Hiroshima University, Japan | ⁴⁴ Universität Würzburg, Germany |
| ²² KEK, Tsukuba, Japan | |
| ²³ INP, Krakow, Poland | |

Contents

1	The Photon Collider at TESLA	1
1.1	Introduction	5
1.1.1	Principle of a photon collider	6
1.1.2	Particle production in high energy $\gamma\gamma$, γe Collisions	8
1.2	The Physics	12
1.2.1	Possible scenarios	12
1.2.2	Higgs boson physics	12
1.2.3	Supersymmetry	20
1.2.4	Extra dimensions	21
1.2.5	Gauge bosons	22
1.2.6	Top quark	24
1.2.7	QCD and hadron physics	26
1.2.8	Table of gold-plated processes	27
1.3	Electron to Photon Conversion	29
1.3.1	Processes in the conversion region	29
1.3.2	The choice of laser parameters	40
1.4	The Interaction Region	44
1.4.1	The collision scheme, crab-crossing	44
1.4.2	Collision effects in $\gamma\gamma$, γe collisions	45
1.4.3	The simulation code	50
1.4.4	Luminosity limitations due to beam collision effects	50
1.4.5	$\gamma\gamma$ and γe luminosities at TESLA	53
1.4.6	Monitoring and measurement of the $\gamma\gamma$ and γe luminosities	57
1.4.7	Backgrounds	62
1.4.8	The detector, experimentation issues	69
1.5	The Lasers and Optics	69
1.5.1	The laser optics at the interaction region	69
1.5.2	The lasers	79
1.6	Summary	85
	Bibliography	86

1.1 Introduction

In addition to the e^+e^- physics program, the TESLA linear collider will provide a unique opportunity to study $\gamma\gamma$ and γe interactions at energies and luminosities comparable to those in e^+e^- collisions [1, 2, 3]. High energy photons for $\gamma\gamma$, γe collisions can be obtained using Compton backscattering of laser light off the high energy electrons. Modern laser technology provides already the laser systems for the $\gamma\gamma$ and γe collider (“Photon Collider”).

The physics potential of the Photon Collider is very rich and complements in an essential way the physics program of the TESLA e^+e^- mode. The Photon Collider will considerably contribute to the detailed understanding of new phenomena (Higgs boson, supersymmetry, quantum gravity with extra dimensions etc.). In some scenarios the Photon Collider is the best instrument for the discovery of elements of New Physics. Although many particles can be produced both at e^+e^- and $\gamma\gamma$, γe collisions, the reactions are different and will give complementary information about new physics phenomena. A few examples:

- The study of charged parity $\mathcal{C} = -$ resonances in e^+e^- collisions led to many fundamental results. In $\gamma\gamma$ collisions, resonances with $\mathcal{C} = +$ are produced directly. One of the most important examples is the Higgs boson of the Standard Model. The precise knowledge of its two-photon width is of particular importance. It is sensitive to heavy virtual charged particles. Supersymmetry predicts three neutral Higgs bosons. Photon colliders can produce the heavy Higgs bosons with masses about 1.5 times higher than in e^+e^- collisions at the same collider and allow to measure their $\gamma\gamma$ widths. Moreover, the photon collider will allow us to study electroweak symmetry breaking (EWSB) in both the weak-coupling and the strong-coupling scenarios.
- A $\gamma\gamma$ collider can produce pairs of any charged particles (charged Higgs, supersymmetric particles etc.) with a cross section about one order of magnitude higher than those in e^+e^- collisions. Moreover, the cross sections depend in a different form on various physical parameters. The polarisation of the photon beams and the large cross sections allow to obtain valuable information on these particles and their interactions.
- At a γe collider charged particles can be produced with masses higher than in pair production of e^+e^- collisions (like a new W' boson and a neutrino or a supersymmetric scalar electron plus a neutralino).
- Photon colliders offer unique possibilities for measuring the $\gamma\gamma$ fusion of hadrons for probing the hadronic structure of the photon.

Polarised photon beams, large cross sections and sufficiently large luminosities allow to significantly enhance the discovery limits of many new particles in SUSY and other models and to substantially improve the accuracy of the precision measurements of

anomalous W boson and top quark couplings thereby complementing and improving the measurements at the e^+e^- mode of the TESLA.

In order to make this new field of particle physics accessible, the Linear Collider needs two interaction regions (IR): one for e^+e^- collisions and the other one for $\gamma\gamma$ and γe collisions.

In the following we describe the physics programme of photon colliders, the basic principles of a photon collider and its characteristics, the requirements for the lasers and possible laser and optical schemes, the expected $\gamma\gamma$ and γe luminosities, and accelerator, interaction region, background and detector issues specific for photon colliders.

The second interaction region for $\gamma\gamma$ and γe collisions is considered in the TESLA design and the special accelerator requirements are taken into account. The costs however are not included in the Technical Design Report.

1.1.1 Principle of a photon collider

The basic scheme of the Photon Collider is shown in Fig. 1.1.1. Two electron beams of energy E_0 after the final focus system travel towards the interaction point (IP) and at a distance b of about 1–5 mm from the IP collide with the focused laser beam. After scattering, the photons have an energy close to that of the initial electrons and follow their direction to the interaction point (IP) (with small additional angular spread of the order of $1/\gamma$, where $\gamma = E_0/mc^2$), where they collide with a similar opposite beam of high energy photons or electrons. Using a laser with a flash energy of several Joules one can “convert” almost all electrons to high energy photons. The photon spot size at the IP will be almost equal to that of the electrons at the IP and therefore the total luminosity of $\gamma\gamma$, γe collisions will be similar to the “geometric” luminosity of the basic e^+e^- beams (positrons are not necessary for photon colliders). To avoid background from the disrupted beams, a crab crossing scheme is used (Fig. 1.1.1).

The maximum energy of the scattered photons is [1, 2]

$$\omega_m = \frac{x}{x+1}E_0; \quad x \approx \frac{4E_0\omega_0}{m^2c^4} \simeq 15.3 \left[\frac{E_0}{\text{TeV}} \right] = 19 \left[\frac{E_0}{\text{TeV}} \right] \left[\frac{\mu\text{m}}{\lambda} \right], \quad (1.1.1)$$

where E_0 is the electron beam energy and ω_0 the energy of the laser photon. For example, for $E_0 = 250$ GeV, $\omega_0 = 1.17$ eV ($\lambda = 1.06$ μm) (Nd:Glass and other powerful lasers) we obtain $x = 4.5$ and $\omega_m = 0.82 E_0 = 205$ GeV (it will be somewhat lower due to nonlinear effects in Compton scattering (Section 1.3)).

For increasing values of x the high energy photon spectrum becomes more peaked towards maximum energies. The value $x \approx 4.8$ is a good choice for photon colliders, because for $x > 4.8$ the produced high energy photons create QED e^+e^- pairs in collision with the laser photons, and as result the $\gamma\gamma$ luminosity is reduced [2, 4, 5]. Hence, the maximum centre of mass system (c.m.s.) energy in $\gamma\gamma$ collisions is about 80%, and in γe collisions 90% of that in e^+e^- collisions. If for some study lower photon energies are needed, one can use the same laser and decrease the electron beam energy. The same laser with $\lambda \approx 1$ μm can be used for all TESLA energies. At $2E_0 = 800$ GeV

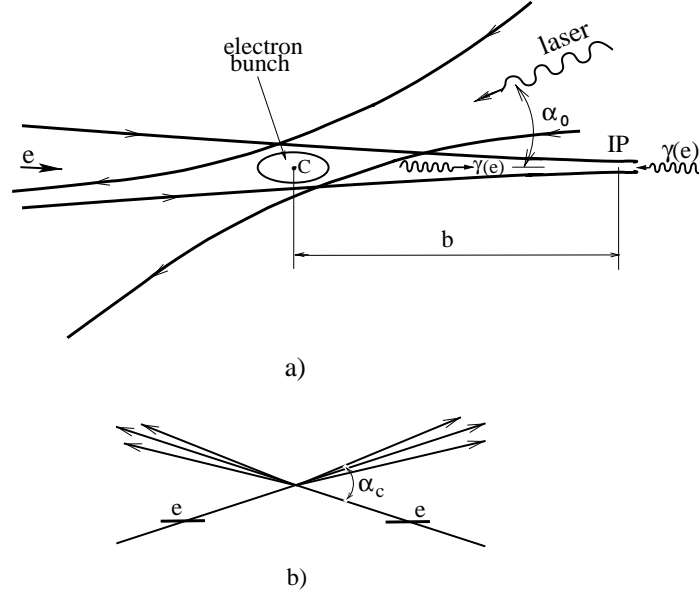


Figure 1.1.1: *Scheme of $\gamma\gamma$, γe collider.*

the parameter $x \approx 7$, which is larger than 4.8. But nonlinear effects at the conversion region effectively increase the threshold for e^+e^- production, so that e^+e^- production is significantly reduced.

The luminosity distribution in $\gamma\gamma$ collisions has a high energy peak and a low energy part (Section 1.4). The peak has a width at half maximum of about 15%. The photons in the peak can have a high degree of circular polarisation. This peak region is the most useful for experimentation. When comparing event rates in $\gamma\gamma$ and e^+e^- collisions we will use the value of the $\gamma\gamma$ luminosity in this peak region $z > 0.8z_m$ where $z = W_{\gamma\gamma}/2E_0$ ($W_{\gamma\gamma}$ is the $\gamma\gamma$ invariant mass) and $z_m = \omega_m/E_0$.

The energy spectrum of high energy photons becomes most peaked if the initial electrons are longitudinally polarised and the laser photons are circularly polarised (Section 1.3.1). This gives almost a factor of 3–4 increase of the luminosity in the high energy peak. The average degree of the circular polarisation of the photons within the high-energy peak amounts to 90–95%. The sign of the polarisation can easily be changed by changing the signs of electron and laser polarisations.

A linear polarisation l_γ of the high energy photons can be obtained by using linearly as well as circularly polarised laser light [3]. The degree of the linear polarisation at maximum energy depends on x , it is 0.334, 0.6, 0.8 for $x = 4.8, 2, 1$ respectively (Section 1.3). Polarisation asymmetries are proportional to l_γ^2 , therefore low x values are preferable. The study of Higgs bosons with linearly polarised photons constitutes a very important part of the physics program at photon colliders.

The luminosities expected at the TESLA Photon Collider are presented in Table 1.1.1, for comparison the e^+e^- luminosity is also included (a more detailed table is given in Section 1.4.5.2).

$2E_0$, GeV	200	500	800
L_{geom} , $10^{34} \text{ cm}^{-2}\text{s}^{-1}$	4.8	12.0	19.1
$W_{\gamma\gamma, max}$, GeV	122	390	670
$L_{\gamma\gamma}(z > 0.8z_{m,\gamma\gamma})$, $10^{34} \text{ cm}^{-2}\text{s}^{-1}$	0.43	1.1	1.7
$W_{\gamma e, max}$, GeV	156	440	732
$L_{e\gamma}(z > 0.8z_{m,\gamma e})$, $10^{34} \text{ cm}^{-2}\text{s}^{-1}$	0.36	0.94	1.3
$L_{e^+e^-}$, $10^{34} \text{ cm}^{-2}\text{s}^{-1}$	1.3	3.4	5.8

Table 1.1.1: *Parameters of the Photon Collider based on TESLA. $\gamma\gamma$, γe luminosities are given for $z > 0.8z_m$. The laser wave length $\lambda = 1.06 \mu\text{m}$ and nonlinear effects in Compton scattering are taken into account. The luminosity of the basic e^+e^- collider is given in the last line.*

One can see that *for the same beam parameters and energy*¹

$$L_{\gamma\gamma}(z > 0.8z_m) \approx \frac{1}{3}L_{e^+e^-}. \quad (1.1.2)$$

The $\gamma\gamma$ luminosity in the high energy luminosity peak for TESLA is just proportional to the geometric luminosity L_{geom} of the electron beams: $L_{\gamma\gamma}(z > 0.8z_m) \approx 0.09L_{geom}$. The latter can be made larger for $\gamma\gamma$ collisions than the e^+e^- luminosity because beamstrahlung and beam repulsion are absent for photon beams. It is achieved using beams with smallest possible emittances and stronger beam focusing in the horizontal plane (in e^+e^- collisions beams should be flat due to beamstrahlung). Thus, using electron beams with smaller emittances one can reach higher $\gamma\gamma$ luminosities than e^+e^- luminosities, which are restricted by beam collision effects.

The laser required must be in the micrometer wave length region, with few Joules of flash energy, about one picosecond duration and, very large, about 100 kW average power. The optical scheme with multiple use of the same laser pulse allows to reduce the necessary average laser power at least by one order of magnitude. Such a laser can be a solid state laser with diode pumping, chirped pulse amplification and elements of adaptive optics. All this technologies are already developed for laser fusion and other projects. It corresponds to a large-room size laser facility. A special tunable FEL is another option (Section 1.5.2).

1.1.2 Particle production in high energy $\gamma\gamma$, γe Collisions

In the collision of photons any charged particle can be produced due to direct coupling. Neutral particles are produced via loops built up by charged particles ($\gamma\gamma \rightarrow$ Higgs,

¹in e^+e^- collisions at $2E_0 = 800 \text{ GeV}$ beams are somewhat different

$\gamma\gamma, ZZ$). The comparison of cross-sections for some processes in e^+e^- and $\gamma\gamma, \gamma e$ collisions is presented in Fig. 1.1.2 [6].

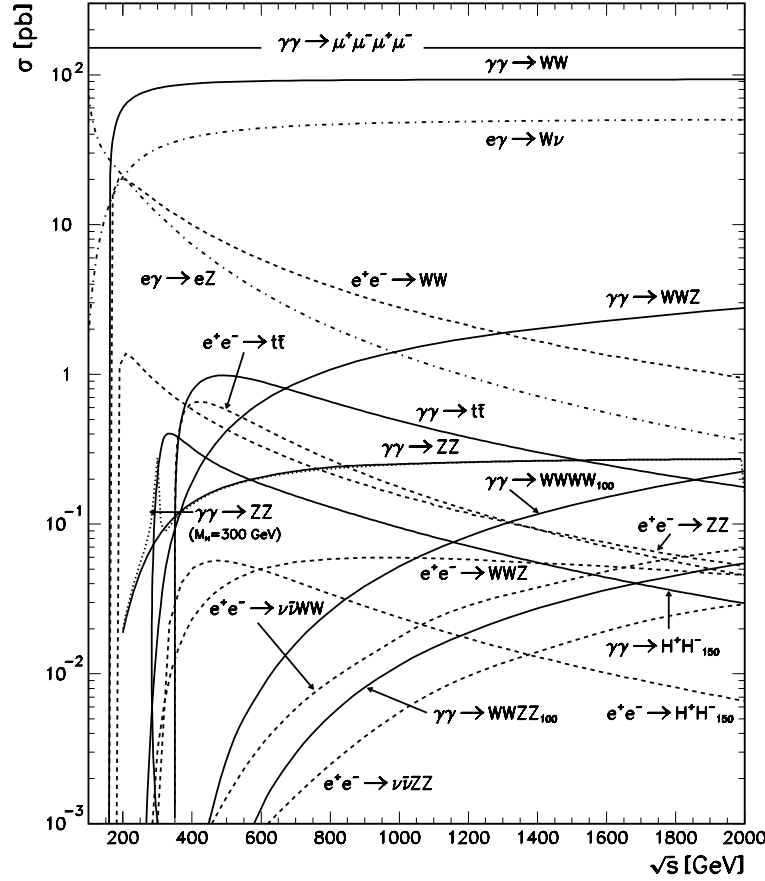


Figure 1.1.2: Typical cross sections in $\gamma\gamma, \gamma e$ and e^+e^- collisions. The polarisation is assumed to be zero. Solid, dash-dotted and dashed curves correspond to $\gamma\gamma, \gamma e$ and e^+e^- modes respectively. Unless indicated otherwise the neutral Higgs mass was taken to be 100 GeV. For charged Higgs pair production, $M_{H^\pm} = 150$ GeV was assumed.

The cross sections for pairs of scalars, fermions or vector particles are all significantly larger (about one order of magnitude) in $\gamma\gamma$ collisions compared with e^+e^- collisions, as shown in Fig. 1.1.3 [4, 5, 7, 8]. For example, the maximum cross section for H^+H^- production with unpolarised photons is about 7 times higher than that in e^+e^- collisions (see Fig. 1.1.2). With polarised photons and not far from threshold it is even larger by a factor of 20, Fig. 1.1.4 [9]. Using the luminosity given in the Table 1.1.1 the event rate is 8 times higher.

The two-photon production of pairs of charged particles is a pure QED process, while the cross section for pair production in e^+e^- collision is mediated by γ and Z exchange so that it depends also on the weak isospin of the produced particles. The

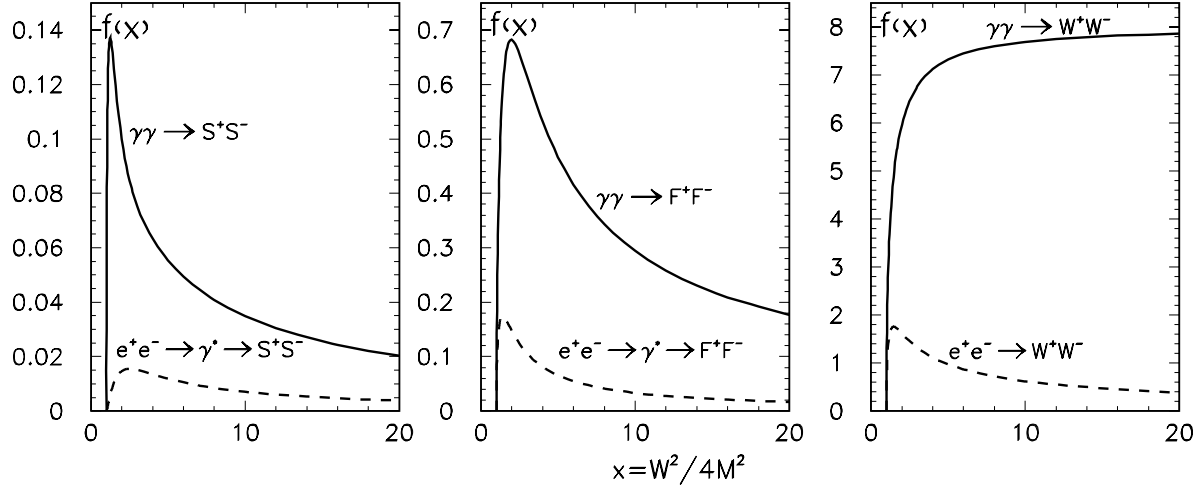


Figure 1.1.3: Comparison between cross sections for charged pair production in unpolarised e^+e^- and $\gamma\gamma$ collisions. S (scalars), F (fermions), W (W bosons); $\sigma = (\pi\alpha^2/M^2)f(x)$, M is the particle mass, W is the invariant mass (c.m.s. energy of colliding beams), $f(x)$ are shown. Contribution of Z boson for production of S and F in e^+e^- collisions was not taken into account, it is less than 10%

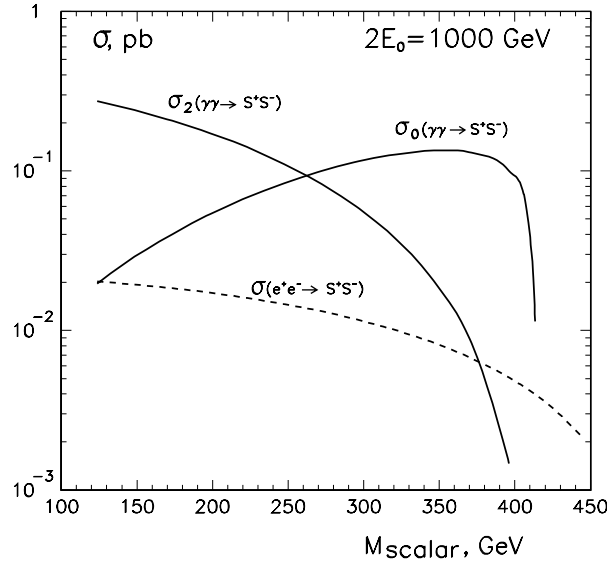


Figure 1.1.4: Pair production cross sections for charged scalars in e^+e^- and $\gamma\gamma$ collisions at $2E_0 = 1\text{ TeV}$ collider (in $\gamma\gamma$ collision $W_{\text{max}} \approx 0.82\text{ TeV}$ ($x = 4.6$)); σ_0 and σ_2 correspond to the total $\gamma\gamma$ helicity 0 and 2 respectively. Comparison is valid for other beam energies if masses are scaled proportionally.

e^+e^- process may also be affected by the exchange of new particles in the t-channel. Therefore, measurements of pair production both in e^+e^- and $\gamma\gamma$ collisions help to disentangle different couplings of the charged particles.

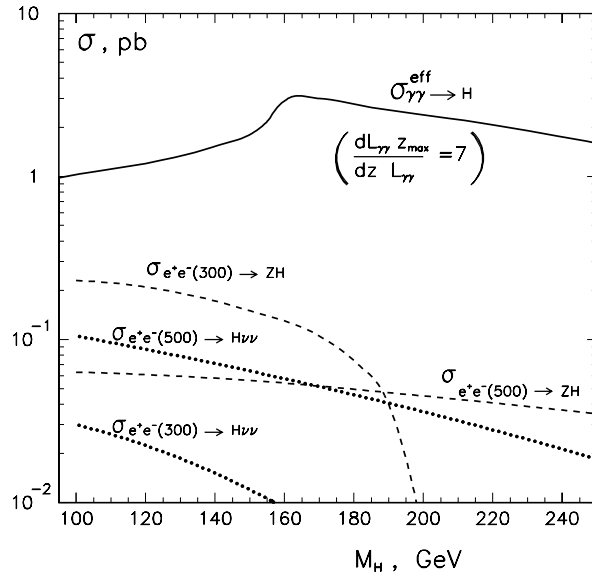


Figure 1.1.5: Total cross sections of the Higgs boson production in $\gamma\gamma$ and e^+e^- collisions. To obtain the Higgs boson production rate at the photon collider the cross section should be multiplied by the luminosity in the high energy peak $L_{\gamma\gamma}(z > 0.65)$ given in the Table 1.1.1.

Another example is the direct resonant production of the Higgs boson in $\gamma\gamma$ collisions. It is evident from Fig. 1.1.5 [10], that the cross section at the photon collider is several times larger than the Higgs production cross section in e^+e^- collisions. Although the $\gamma\gamma$ luminosity is smaller than the e^+e^- luminosity (Table 1.1.1), the production rate of the Standard Model (SM) Higgs boson with mass between 130 and 250 GeV in $\gamma\gamma$ collisions is nevertheless 1–10 times the rate in e^+e^- collisions at $2E_0 = 500$ GeV.

Photon colliders used in the γe mode can produce particles which are kinematically not accessible at the same collider in the e^+e^- mode. For example, in γe collisions one can produce a heavy charged particle in association with a light neutral one, such as supersymmetric selectron plus neutralino, $\gamma e \rightarrow \tilde{e}\tilde{\chi}^0$ or a new W' boson and neutrino, $\gamma e \rightarrow W'\nu$. In this way the discovery limits can be extended.

Based on these arguments alone, and without knowing *a priori* the particular scenario of new physics, there is a strong complementarity for e^+e^- and $\gamma\gamma$ or γe modes for new physics searches.

The idea of γe and $\gamma\gamma$ collisions at linear colliders via Compton backscattering has been proposed by the Novosibirsk group [1, 2, 3]. Reviews of further developments can be found in [4, 5, 6, 8, 9, 10, 11, 12, 13, 14, 15, 16, 17, 18, 19, 20, 21] and the conceptual(zero) design reports [22, 23, 24] and references therein.

A review of the physics potential and available technologies of $\gamma\gamma$, γe colliders, can be found in the proceedings of workshops on photon colliders held in 1995 at Berkeley [25] and in 2000 at DESY [26].

1.2 The Physics

1.2.1 Possible scenarios

The two goals of studies at the next generation of colliders are the proper understanding of electroweak symmetry breaking, associated with the problem of mass, and the discovery of new physics beyond the Standard Model (SM). Three scenarios are possible for future experiments [27]:

- New particles or interactions will be directly discovered at the TEVATRON and LHC. A Linear Collider (LC) in the e^+e^- and $\gamma\gamma$ modes will then play a crucial role in the detailed and thorough study of these new phenomena and in the reconstruction of the underlying fundamental theories.
- LHC and LC will discover and study in detail the Higgs boson but no spectacular signatures of new physics or new particles will be observed. In this case the precision studies of the deviations of the properties of the Higgs boson, electroweak gauge bosons and the top quark from their Standard Model (SM) predictions can provide clues to the physics beyond the Standard Model.
- Electroweak symmetry breaking (EWSB) is a dynamical phenomenon. The interactions of W bosons and t quarks must then be studied at high energies to explore new strong interactions at the TeV scale.

Electroweak symmetry breaking in the SM is based on the Higgs mechanism, which introduces one elementary Higgs boson. The model agrees with the present data, partly at the per-mille level, and the recent global analysis of precision electroweak data in the framework of the SM [28] suggests that the Higgs boson is lighter than 200 GeV. A Higgs boson in this mass range is expected to be discovered at the TEVATRON or the LHC. However, it will be the LC in all its modes that tests whether this particle is indeed the SM Higgs boson or whether it is eventually one of the Higgs states in extended models like the two Higgs doublets (2HDM) or the minimal supersymmetric generalisation of the SM, e.g. MSSM. At least five Higgs bosons are predicted in supersymmetric models, h^0 , H^0 , A^0 , H^+ , H^- . Unique opportunities are offered by the Photon Collider to search for the heavy Higgs bosons in areas of SUSY parameter space not accessible elsewhere.

1.2.2 Higgs boson physics

The Higgs boson plays an essential role in the EWSB mechanism and the origin of mass. The lower bound on M_h from direct searches at LEP is presently 113.5 GeV at 95% confidence level (CL) [29]. A surplus of events at LEP provides tantalising indications of a Higgs boson with $M_h = 115_{-0.7}^{+1.3}$ GeV (90% CL) at a level of 2.9σ [29, 30, 31]. Recent global analyses of precision electroweak data [28] suggest that the

Higgs boson is light, yielding at 95% CL that $M_h = 62_{-30}^{+53}$ GeV. There is remarkable agreement with the well known upper bound of ~ 130 GeV for the lightest Higgs boson mass in the minimal version of supersymmetric theories, the MSSM [32, 33]. Such a Higgs boson should definitely be discovered at the LHC if not already at the TEVATRON.

Once the Higgs boson is discovered, it will be crucial to determine the mass, the total width, spin, parity, \mathcal{CP} -nature and the tree-level and one-loop induced couplings in a model independent way. Here the e^+e^- and $\gamma\gamma$ modes of the LC should play a central role. The $\gamma\gamma$ collider option of a LC offers the unique possibility to produce the Higgs boson as an s-channel resonance [34, 35, 36, 37]:

$$\gamma\gamma \rightarrow h^0 \rightarrow b\bar{b}, WW^*, ZZ, \tau\tau, gg, \gamma\gamma \dots$$

The total width of the Higgs boson at masses below 400 GeV is much smaller than the characteristic width of the $\gamma\gamma$ luminosity spectra (FWHM ~ 10 –15%), so that the Higgs production rate is proportional to $dL_{\gamma\gamma}/dW_{\gamma\gamma}$:

$$\dot{N}_{\gamma\gamma \rightarrow h} = L_{\gamma\gamma} \times \frac{dL_{\gamma\gamma} M_h}{dW_{\gamma\gamma} L_{\gamma\gamma}} \frac{4\pi^2 \Gamma_{\gamma\gamma} (1 + \lambda_1 \lambda_2)}{M_h^3} \equiv L_{\gamma\gamma} \times \sigma^{eff}. \quad (1.2.1)$$

$\Gamma_{\gamma\gamma}$ is the two-photon width of the Higgs boson and λ_i are the photon helicities.

The search and study of the Higgs boson can be carried out best by exploiting the high energy peak of the $\gamma\gamma$ luminosity energy spectrum where $dL_{\gamma\gamma}/dW_{\gamma\gamma}$ has a maximum and the photons have a high degree of circular polarisation. The effective cross section for $(dL_{\gamma\gamma}/dW_{\gamma\gamma})(M_h/L_{\gamma\gamma}) = 7$ and $1 + \lambda_1 \lambda_2 = 2$ is presented in Fig. 1.1.5. The luminosity in the high energy luminosity peak ($z > 0.8z_m$) was defined in Section 1.1.1. For the luminosities given in Table 1.1.1 the ratio of the Higgs rates in $\gamma\gamma$ and e^+e^- collisions is about 1 to 10 for $M_h = 100$ –250 GeV.

The Higgs boson at photon colliders can be detected as a peak in the invariant mass distribution or (and) it can be searched for by scanning the energy using the sharp high-energy edge of the luminosity distribution [10, 38]. The scanning allows also to determine backgrounds. A cut on the acollinearity angle between two jets from the Higgs decay ($b\bar{b}$ for instance) allows to select events with a narrow (FWHM $\sim 8\%$) distribution of the invariant mass [9, 39].

The Higgs $\gamma\gamma$ partial width $\Gamma(h \rightarrow \gamma\gamma)$ is of special interest, since it is generated at the one-loop level including all heavy charged particles with masses generated by the Higgs mechanism. In this case the heavy particles do not in general decouple. As a result the Higgs cross section in $\gamma\gamma$ collisions is sensitive to contributions of new particles with masses beyond the energy covered directly by accelerators. Combined measurements of $\Gamma(h \rightarrow \gamma\gamma)$ and the branching ratio $\text{BR}(h \rightarrow \gamma\gamma)$ at the e^+e^- and $\gamma\gamma$ LC provide a model-independent measurement of the total Higgs width [40].

The required accuracy of the $\Gamma(h \rightarrow \gamma\gamma)$ measurements in the SUSY sector can be inferred from the results of the studies of the coupling of the lightest SUSY Higgs boson to two photons in the decoupling regime [41, 42]. It was shown that in the decoupling limit, where all other Higgs bosons and the supersymmetric particles are very heavy,

chargino and top squark loops can generate a sizable difference between the standard and the SUSY two-photon Higgs couplings. Typical deviations are at the few percent level. Top squarks heavier than 250 GeV can induce deviations larger than $\sim 10\%$ if their couplings to the Higgs boson are large.

The ability to control the polarisations of the back-scattered photons provides a powerful tool for exploring the \mathcal{CP} properties of any single neutral Higgs boson that can be produced with reasonable rate at the Photon Collider [43, 44, 45]. The \mathcal{CP} -even Higgs bosons h^0 , H^0 couple to the combination $\vec{\varepsilon}_1 \cdot \vec{\varepsilon}_2$, while the \mathcal{CP} -odd Higgs boson A^0 couples to $[\vec{\varepsilon}_1 \times \vec{\varepsilon}_2] \cdot \vec{k}_\gamma$, where the $\vec{\varepsilon}_i$ are the photon polarisation vectors. The \mathcal{CP} -even Higgs bosons couple to linearly polarised photons with a maximal strength for parallel polarisation vectors, the \mathcal{CP} -odd Higgs boson for perpendicular polarisation vectors:

$$\sigma \propto 1 \pm l_{\gamma 1} l_{\gamma 2} \cos 2\phi, \quad (1.2.2)$$

The degrees of linear polarisation are denoted by $l_{\gamma i}$ and ϕ is the angle between $l_{\gamma 1}$ and $l_{\gamma 2}$; the \pm signs correspond to $\mathcal{CP} = \pm 1$ scalar particles.

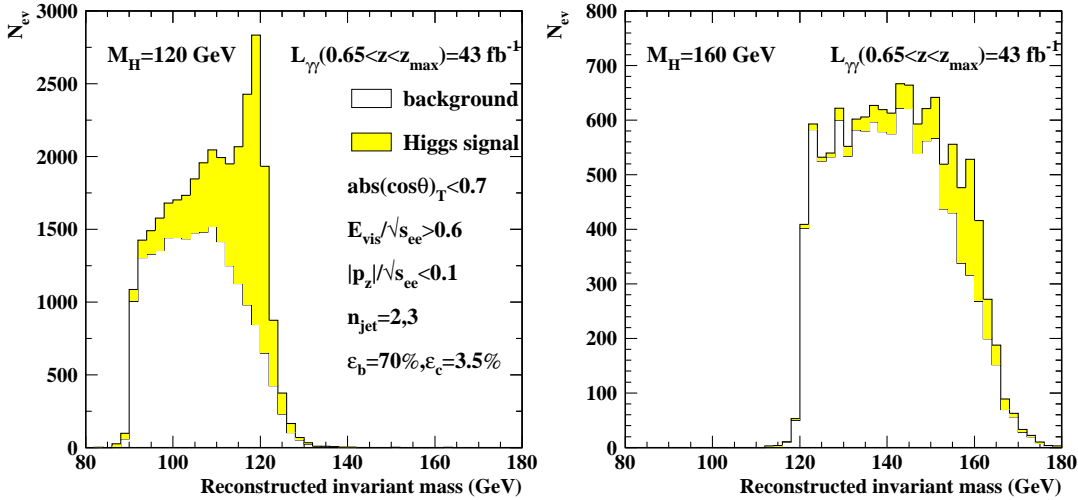


Figure 1.2.1: Mass distributions for the Higgs signal and heavy quark background for a) $M_h = 120$ GeV and b) 160 GeV. The Compton parameter $x = 4.8$ was assumed. The text in the figure shows cuts on the jets parameters [46, 47].

1.2.2.1 Light SM and MSSM Higgs boson

A light Higgs boson h with mass below the WW threshold can be detected in the $b\bar{b}$ decay mode. Simulations of this process have been performed in [18, 46, 47, 37, 48, 49, 50, 51]. The main background to the h boson production is the continuum production of $b\bar{b}$ and $c\bar{c}$ pairs. A high degree of circular polarisation of the photon beams is crucial in this case, since for equal photon helicities ($\pm\pm$), which produce

the spin-zero resonant states, the $\gamma\gamma \rightarrow q\bar{q}$ QED Born cross section is suppressed by a factor $M_q^2/W_{\gamma\gamma}^2$ [34, 52, 53].

A Monte Carlo simulation of $\gamma\gamma \rightarrow h \rightarrow b\bar{b}$ for $M_h = 120$ and 160 GeV has been performed for an integrated luminosity in the high energy peak of $L_{\gamma\gamma}(0.8z_m < z < z_m) = 43 \text{ fb}^{-1}$ in [46, 47, 54]. Real and virtual gluon corrections for the Higgs signal and the backgrounds [50, 51, 54, 55, 56, 57, 58, 59, 60, 61] have been taken into account.

The results for the invariant mass distributions for the combined $b\bar{b}(\gamma)$ and $c\bar{c}(\gamma)$ backgrounds, after cuts, and for the Higgs signal are shown in Fig. 1.2.1 [46, 47]. Due to the large charm production cross-section in $\gamma\gamma$ collisions, excellent b tagging is required [46, 47, 50, 51]. A b tagging efficiency of 70% for $b\bar{b}$ events and residual efficiency of 3.5% for $c\bar{c}$ events were used in these studies. A relative statistical error of

$$\frac{\Delta[\Gamma(h \rightarrow \gamma\gamma)\text{BR}(h \rightarrow b\bar{b})]}{[\Gamma(h \rightarrow \gamma\gamma)\text{BR}(h \rightarrow b\bar{b})]} \approx 2\% \quad (1.2.3)$$

can be achieved in the Higgs mass range between 120 and 140 GeV [46, 47].

It has been shown that the $h \rightarrow b\bar{b}$ branching ratio can be measured at the LC in e^+e^- (and $\gamma\gamma$) collisions with an accuracy of 1% [62], the partial two-photon Higgs width can then be calculated using the relation

$$\Gamma(h \rightarrow \gamma\gamma) = \frac{[\Gamma(h \rightarrow \gamma\gamma)\text{BR}(h \rightarrow b\bar{b})]}{[\text{BR}(h \rightarrow b\bar{b})]}$$

with almost the same accuracy as in eq. (1.2.3). Such a high precision for the $\Gamma(h \rightarrow \gamma\gamma)$ width can only be achieved at the $\gamma\gamma$ mode of the LC. On this basis it should be possible to discriminate between the SM Higgs particle and the lightest scalar Higgs boson of the MSSM or the 2HDM [41, 42], and contributions of new heavy particles should become apparent.

The SM Higgs boson with mass $135 < M_H < 190$ GeV is expected to decay predominantly into WW^* or WW pairs (W^* is a virtual W boson). This decay mode should permit the detection of the Higgs boson signal below and slightly above the threshold of WW pair production [63, 64, 65, 66]. In order to determine the two-photon Higgs width in this case one can use the same relation as above after replacing the b quark by the real/virtual W boson.

The branching ratio $\text{BR}(WW^*)$ is obtained from Higgs-strahlung. It was shown [65, 66] that for $M_h = 160$ GeV the product $\Gamma(h \rightarrow \gamma\gamma)\text{BR}(h \rightarrow WW^*)$ can be measured at the Photon Collider with the statistical accuracy better than 2% at the integrated $\gamma\gamma$ luminosity of 40 fb^{-1} in the high energy peak. The accuracy of $\Gamma(h \rightarrow \gamma\gamma)$ will be determined by the accuracy of the $\text{BR}(h \rightarrow WW^*)$ measurement in e^+e^- collisions which is expected to be about 2%.

Above the ZZ threshold the most promising channel to detect the Higgs signal is the reaction $\gamma\gamma \rightarrow ZZ$ [67, 68, 69, 70]. In order to suppress the significant background from the tree level W^+W^- pair production, leptonic (l^+l^- l^+l^- , $\text{BR} = 1\%$) or semileptonic (l^+l^- $q\bar{q}$, $\text{BR} = 14\%$) decay modes of the ZZ pairs must be selected. Although in the

SM there is only a one-loop induced continuum production of ZZ pairs, it represents a large irreducible background for the Higgs signal well above the WW threshold [67, 68, 69, 70]. Due to this background the intermediate mass Higgs boson signal can be observed at the $\gamma\gamma$ collider in the ZZ mode if the Higgs mass lies below 350–400 GeV.

Hence, the two-photon SM Higgs width can be measured at the photon collider, either in $b\bar{b}$, WW^* or ZZ decay modes, up to the Higgs mass of 350–400 GeV. Other decay modes, like $h \rightarrow \tau\tau, \gamma\gamma$, may also be exploited at photon colliders, but no studies have been done so far.

Assuming that in addition to the measurement of the $h \rightarrow b\bar{b}$ branching ratio also the $h \rightarrow \gamma\gamma$ branching ratio can be measured (with an accuracy of 10–15%) at TESLA [71, 72], the total width of the Higgs boson can be determined in a model-independent way to an accuracy as dominated by the error on $\text{BR}(h \rightarrow \gamma\gamma)$

$$\Gamma_h = \frac{[\Gamma(h \rightarrow \gamma\gamma)\text{BR}(h \rightarrow b\bar{b})]}{[\text{BR}(h \rightarrow \gamma\gamma)][\text{BR}(h \rightarrow b\bar{b})]}.$$

The measurement of this branching ratio at the Photon Collider (normalised to $\text{BR}(h \rightarrow b\bar{b})$ from the e^+e^- mode) will improve the accuracy of the total Higgs width.

1.2.2.2 Heavy MSSM and 2HDM Higgs bosons

The minimal supersymmetric extension of the Standard Model contains two charged (H^\pm) Higgs bosons and three neutral Higgs bosons: the light \mathcal{CP} -even Higgs particle (h), and heavy \mathcal{CP} -even (H) and the \mathcal{CP} -odd (A) Higgs states. If we assume a large value of the A mass, the properties of the light \mathcal{CP} -even Higgs boson h are similar to those of the light SM Higgs boson, and can be detected in the $b\bar{b}$ decay mode, just as the SM Higgs. Its mass is bound to $M_h \lesssim 130$ GeV. However, the masses of the heavy Higgs bosons H, A, H^\pm are expected to be of the order of the electroweak scale up to about 1 TeV. The heavy Higgs bosons are nearly degenerate. The WW and ZZ decay modes are suppressed for the heavy H case, and these decays are forbidden for the A boson. Instead of the WW, ZZ decay modes, the $t\bar{t}$ decay channel may be useful if the Higgs boson masses are heavier than M_t , and if $\tan\beta \ll 10$ ($\tan\beta$ is the Goldstone mixing-parameter of MSSM). An important property of the SUSY couplings is the enhancement of the bottom Yukawa couplings with increasing $\tan\beta$. For moderate and large values of $\tan\beta$, the decay mode to $b\bar{b}$ [73, 74] (and to $\tau^+\tau^-$ in some cases) is substantial.

Extensive studies have demonstrated that, while the light Higgs boson h of MSSM can be found at the LHC, the heavy bosons H and A may escape discovery for intermediate values of $\tan\beta$ [75, 76]. At an e^+e^- LC the heavy MSSM Higgs bosons can only be found in associated production $e^+e^- \rightarrow HA$ [77, 78, 79], with H and A having very similar masses. In the first phase of the LC with a total e^+e^- energy of 500 GeV the heavy Higgs bosons can thus be discovered for masses up to about 250 GeV. The mass reach can be extended by a factor of 1.6 in the $\gamma\gamma$ mode of TESLA, in which the Higgs bosons H, A can be singly produced.

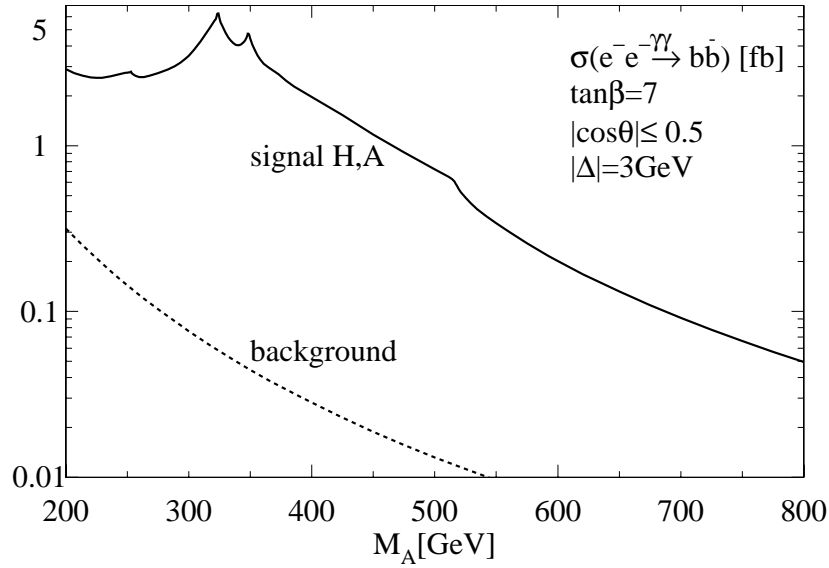


Figure 1.2.2: Cross section for resonant heavy Higgs H, A boson production as a function of the pseudoscalar Higgs mass M_A with decay into $b\bar{b}$ pairs, and the corresponding background cross section. The maximum of the photon luminosity in the $J_z = 0$ configuration has been tuned to coincide with M_A . The cross sections are defined in $b\bar{b}$ mass bins of $M_A \pm 3 \text{ GeV}$ around the A resonance. An angular cut on the bottom production angle θ has been imposed: $|\cos\theta| < 0.5$. The MSSM parameters have been chosen as $\tan\beta = 7, M_2 = -\mu = 200 \text{ GeV}$. See also comments in the text.

The results for the cross section of the H, A signal in the $b\bar{b}$ decay mode and the corresponding background for the value of $\tan\beta = 7$ are shown in Fig. 1.2.2 as a function of the pseudoscalar mass M_A [73, 74]. From the figure one can see that the background is strongly suppressed with respect to the signal. The significance of the heavy Higgs boson signals is sufficient for a discovery of the Higgs particles with masses up to about 70–80% of the LC c.m.s. energy. For $2E_0 = 500 \text{ GeV}$ the H, A bosons with masses up to about $0.8 \times 2E_0 \approx 400 \text{ GeV}$ can be discovered in the $b\bar{b}$ channel at the Photon Collider. For a LC with $2E_0 = 800 \text{ GeV}$ the range can be extended to about 660 GeV [74, 80]. Also the one-loop induced two-photon width of the H, A Higgs states will be measured. For heavier Higgs masses the signal becomes too small to be detected. Note that the cross section given in Fig. 1.2.2 takes into account the $e \rightarrow \gamma$ conversion $k^2 L_{geom} \sim 0.4 L_{geom}$ (k being the $e \rightarrow \gamma$ conversion coefficient) which results in a luminosity of $4.8 \times 10^{34} \text{ cm}^{-2}\text{s}^{-1} \sim 1.5 L_{e^+e^-}$ for $2E_0 = 500 \text{ GeV}$ and which grows proportional to the energy.

The separation of the almost degenerate H and A states may be achieved using the linear polarisation of the colliding photons (see eq. 1.2.2). The H and A states can be produced from collisions of parallel and perpendicularly polarised incoming photons, respectively [43, 44, 45, 81, 82, 83]. The possible \mathcal{CP} -violating mixing of H and A can be distinguished from the overlap of these resonances by analysing the polarisation

asymmetry in the two-photon production [84].

The interference between H and A states can be also studied in the reaction $\gamma\gamma \rightarrow t\bar{t}$ with circularly polarised photon beams by measuring the top quark helicity [85, 86]. The corresponding cross sections are shown in Fig. 1.2.3. The effect of the interference is clearly visible for the value of $\tan\beta = 3$. The RR cross section is bigger than the LL cross section ($R(L)$ is right(left) helicity) due to the continuum. Large interference effects are visible in both modes. Without the measurement of the top quark polarisation there still remains a strong interference effect between the continuum and the Higgs amplitudes, which can be measured.

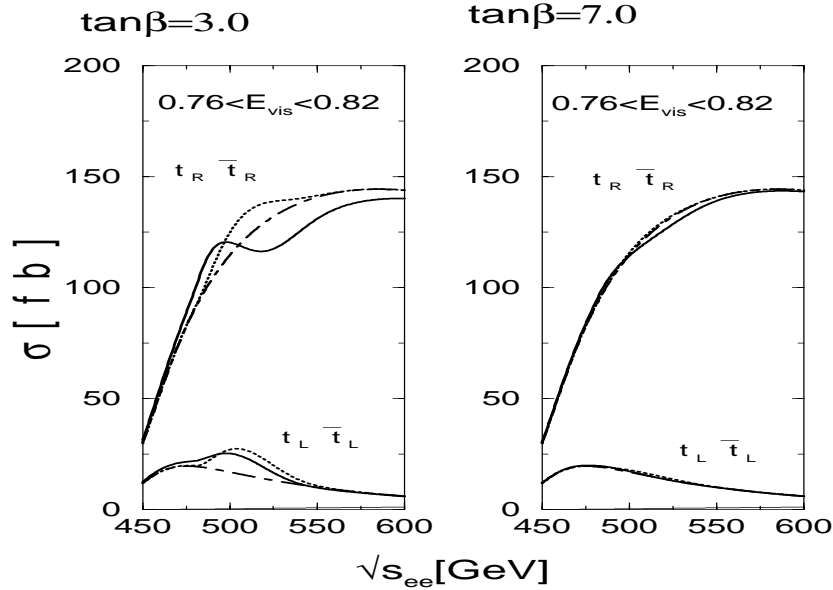


Figure 1.2.3: The effective top pair cross sections $\gamma\gamma \rightarrow t\bar{t}$ convoluted with the $e \rightarrow \gamma$ conversion efficiency within the visible energy range as indicated. The bold-solid curves correspond to the correct cross sections, the dotted curves are the ones neglecting the interference, and the dot-dashed are the continuum cross sections, respectively. The upper curves are for $t_R\bar{t}_R$, and the lower ones for $t_L\bar{t}_L$. The sum of the cross sections for $t_R\bar{t}_L$ and $t_L\bar{t}_R$, are also plotted as thin-continuous line very near to the bottom horizontal axis. The left figure is for $\tan\beta = 3$, and the right for $\tan\beta = 7$ [85, 86].

For energies corresponding to the maximum cross sections (not far from the threshold) with proper polarisation the pair production rate of charged Higgs $\gamma\gamma \rightarrow H^+H^-$ at the TESLA Photon Collider will be almost an order of magnitude larger than at the e^+e^- LC due to the much larger cross section.

Scenarios, in which all new particles are very heavy, may be realised not only in the MSSM but also in other extended models of the Higgs sector, for example in models with just two Higgs doublets. In this case the two-photon Higgs boson width, for h

or H , will differ from the SM value even if all direct couplings to the gauge bosons W/Z and the fermions are equal to the corresponding couplings in the SM, driven by the contributions of extra heavy charged particles. In the 2HDM these particles are the charged Higgs bosons. Different realizations of the 2HDM have been discussed in [87, 88]. Assuming that the partial widths of the observed Higgs boson to quarks, Z or W bosons are close to their SM values, three sets of possible values of the couplings to $\gamma\gamma$ can be obtained. Fig. 1.2.4 shows deviations of the two-photon Higgs width from the SM value for these three variants. The shaded regions are derived from the anticipated 1σ experimental bounds around the SM values for the Higgs couplings to fermions and gauge bosons. Comparing the numbers in these figures with the achievable accuracy of the two-photon Higgs width at a photon collider (1.2.3) the difference between SM and 2HDM should definitely be observable [87, 88].

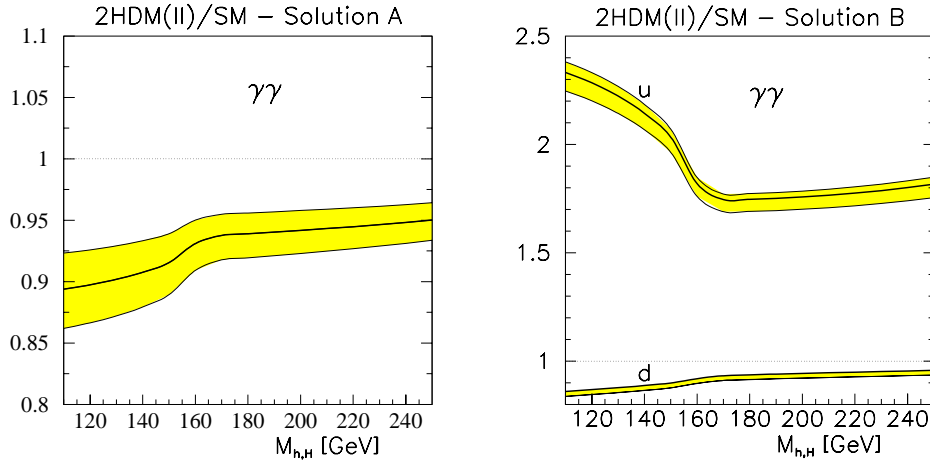


Figure 1.2.4: The ratio of the two-photon Higgs width in the 2HDM to its SM value, for two different solutions [87, 88].

The \mathcal{CP} parity of the neutral Higgs boson can be measured using linearly polarised photons. Moreover, if the Higgs boson is a mixture of \mathcal{CP} -even and \mathcal{CP} -odd states, for instance in a general 2HDM with a \mathcal{CP} -violating neutral sector, the interference of these two terms gives rise to a \mathcal{CP} -violating asymmetry [43, 44, 45, 84, 89]. Two \mathcal{CP} -violating ratios could be observed to linear order in the \mathcal{CP} -violating couplings:

$$\mathcal{A}_1 = \frac{|\mathcal{M}_{++}|^2 - |\mathcal{M}_{--}|^2}{|\mathcal{M}_{++}|^2 + |\mathcal{M}_{--}|^2}, \quad \mathcal{A}_2 = \frac{2\Im(\mathcal{M}_{--}^* \mathcal{M}_{++})}{|\mathcal{M}_{++}|^2 + |\mathcal{M}_{--}|^2}.$$

In terms of experimental values the first asymmetry can be found from

$$T_- = \frac{N_{++} - N_{--}}{N_{++} + N_{--}} = \frac{\langle \xi_2 \rangle + \langle \tilde{\xi}_2 \rangle}{1 + \langle \xi_2 \tilde{\xi}_2 \rangle} \mathcal{A}_1,$$

where $N_{\pm\pm}$ correspond to the event rates for positive (negative) initial photon helicities

and $\xi_i, \tilde{\xi}_i$ are the Stokes polarisation parameters. The measurement of the asymmetry is achieved by simultaneously flipping the helicities of the laser beams used for production of polarised electrons and $\gamma \rightarrow e$ conversion. The asymmetry to be measured with linearly polarised photons is given by

$$T_\psi = \frac{N(\phi = \frac{\pi}{4}) - N(\phi = -\frac{\pi}{4})}{N(\phi = \frac{\pi}{4}) + N(\phi = -\frac{\pi}{4})} = \frac{\langle \xi_3 \tilde{\xi}_1 \rangle + \langle \xi_1 \tilde{\xi}_3 \rangle}{1 + \langle \xi_2 \tilde{\xi}_2 \rangle} \mathcal{A}_2, \quad (1.2.4)$$

where ϕ is the angle between the linear polarisation vectors of the photons. The asymmetries are typically larger than 10% and they are observable for a large range of the 2HDM parameter space if \mathcal{CP} violation is present in the Higgs potential.

Hence, high degrees of both circular and linear polarisations for the high energy photon beams provide additional analysing power for the detailed study of the Higgs sector at the $\gamma\gamma$ collider.

1.2.3 Supersymmetry

In $\gamma\gamma$ collisions, any kind of charged particle can be produced in pairs, provided the mass is below the kinematical bound. Potential SUSY targets for a photon collider are the charged sfermions [18, 90], the charginos [18, 91] and the charged Higgs bosons.

For the $\gamma\gamma$ luminosity given in the Table 1.1.1, the production rates for these particles will be larger than that in e^+e^- collisions and detailed studies of the charged supersymmetric particles should be possible. In addition, the cross sections in $\gamma\gamma$ collisions are given just by QED to leading order, while in e^+e^- collisions also Z boson and (sometimes) t -channel exchanges contribute. So, studying these processes in both channels provides complementary information about the interactions of the charged supersymmetric particles.

The γe collider could be the ideal machine for the discovery of scalar electrons (\tilde{e}) and neutrinos ($\tilde{\nu}$) in the reactions $\gamma e \rightarrow \tilde{e}^- \tilde{\chi}_1^0, \tilde{W} \tilde{\nu}$ [18, 92, 93, 94, 95, 96]. Selectrons and neutralinos may be discovered in γe collisions up to the kinematical limit of

$$M_{\tilde{e}^-} < 0.9 \times 2E_0 - M_{\tilde{\chi}_i^0}, \quad (1.2.5)$$

where $2E_0$ is the energy of the original e^+e^- collider. This bound is larger than the bound obtained from $\tilde{e}^+\tilde{e}^-$ pair production in the e^+e^- mode, if $M_{\tilde{\chi}_i^0} < 0.4 \times 2E_0$.

In Fig. 1.2.5 the cross section of the process $\gamma e \rightarrow \tilde{\chi}_1^0 \tilde{e}_{L/R}^- \rightarrow \tilde{\chi}_1^0 \tilde{\chi}_1^0 e^-$ is compared to the cross section of the process $e^+e^- \rightarrow \tilde{e}_{L/R}^+ \tilde{e}_{L/R}^- \rightarrow \tilde{\chi}_1^0 \tilde{\chi}_1^0 e^+e^-$ for the MSSM parameters $M_2 = 152$ GeV, $\mu = 316$ GeV, $\tan\beta = 3$ and $M_{\tilde{e}_R} = 260$ GeV, $M_{\tilde{e}_L} = 290$ GeV (Fig. 1.2.5a) and $M_{\tilde{e}_R} = 230$ GeV, $M_{\tilde{e}_L} = 270$ GeV (Fig. 1.2.5b) [97, 98]. The $\tilde{\chi}_1^0$ mass in this case is about 70 GeV. For higher selectron masses pair production in e^+e^- annihilation at $2E_0 = 500$ GeV is kinematically forbidden, whereas in γe collisions the cross section at $2E_0 = 500$ GeV is 96 fb. According to (1.2.5) the highest accessible selectron mass for $2E_0 = 500$ GeV is $M_{\tilde{e}} < 380$ GeV in this scenario.

In some scenarios of supersymmetric extensions of the Standard Model the stoponium bound states $\tilde{t}\tilde{t}$ is formed. A photon collider would be the ideal machine for the

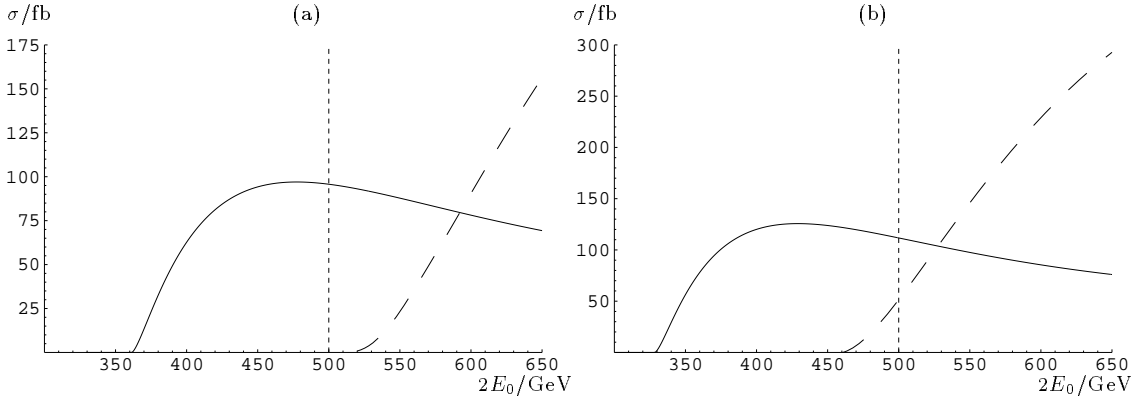


Figure 1.2.5: Total cross sections for $\gamma e \rightarrow \tilde{\chi}_1^0 \tilde{e}_{L/R}^- \rightarrow \tilde{\chi}_1^0 \tilde{\chi}_1^0 e^-$ (solid curves) for longitudinal polarisation $P_{e^-} = 0.8$ and longitudinal (circular) polarisation $P_{e^+} = 0.8$ ($\lambda_L = -1$) of the converted electrons (laser photons) compared to $e^+ e^- \rightarrow \tilde{e}_{L/R}^+ \tilde{e}_{L/R}^- \rightarrow \tilde{\chi}_1^0 \tilde{\chi}_1^0 e^+ e^-$ (dashed curves) with longitudinally polarised electrons, $P_{e^-} = 0.8$, and unpolarised positrons. MSSM parameters: $M_2 = 152 \text{ GeV}$, $\mu = 316 \text{ GeV}$, $\tan\beta = 3$. (a) $M_{\tilde{e}_R} = 260 \text{ GeV}$, $M_{\tilde{e}_L} = 290 \text{ GeV}$. (b) $M_{\tilde{e}_R} = 230 \text{ GeV}$, $M_{\tilde{e}_L} = 270 \text{ GeV}$.

discovery and study of these new narrow strong resonances [99]. About ten thousand stoponium resonances for $M_S = 200 \text{ GeV}$ will be produced for an integrated luminosity in the high energy peak of 100 fb^{-1} . Thus precise measurements of the stoponium effective couplings, mass and width should be possible. At e^+e^- colliders the counting rate will be much lower and in some scenarios the stoponium cannot be detected due to the large background [99].

1.2.4 Extra dimensions

New ideas have recently been proposed to explain the weakness of the gravitational force [100, 101, 102]. The Minkowski world is extended by extra space dimensions which are curled up at small dimensions R . While the gauge and matter fields are confined in the (3+1) dimensional world, gravity propagates through the extended 4+n dimensional world. While the effective gravity scale, the Planck scale, in four dimensions is very large, the fundamental Planck scale in 4+n dimensions may be as low as a few TeV so that gravity may become strong already at energies of the present or next generation of colliders.

Towers of Kaluza–Klein graviton excitations will be realised on the compactified 4+n dimensional space. Exchanging these KK excitations between SM particles in high-energy scattering experiments will generate effective contact interactions, carrying spin=2 and characterised by a scale M_s of order few TeV. They will give rise to substantial deviations from the predictions of the Standard Model for the cross sections and angular distributions for various beam polarisations [103, 104, 105, 106, 107, 108].

Of the many processes examined so far, $\gamma\gamma \rightarrow WW$ provides the largest reach for M_s for a given centre of mass energy of the LC [109, 108]. The main reasons are that

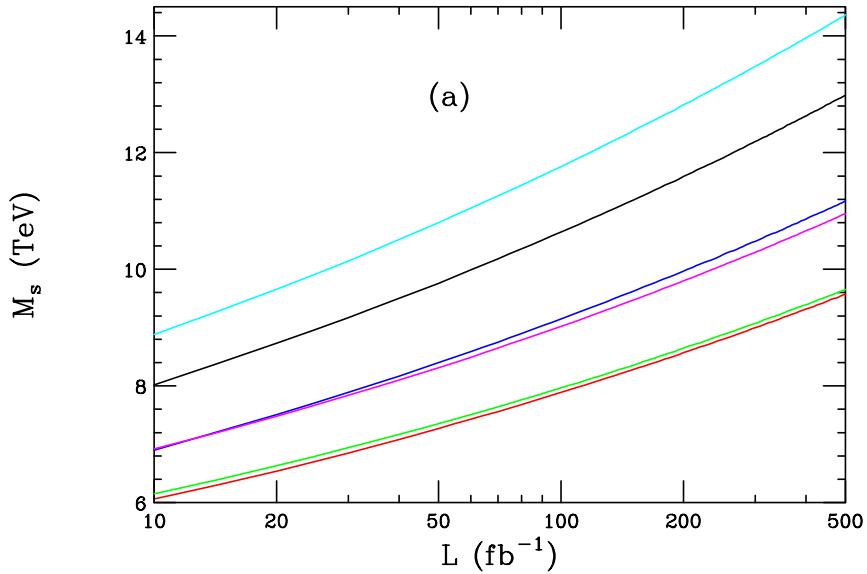


Figure 1.2.6: M_s discovery reach for the process $\gamma\gamma \rightarrow W^+W^-$ at a $2E_0 = 1 \text{ TeV}$ LC as a function of the integrated luminosity for the different initial state polarizations assuming $\lambda = 1$. From top to bottom on the right hand side of the figure the polarisations are $(- + + -)$, $(+ - - -)$, $(+ + - -)$, $(+ - + -)$, $(+ - - -)$, and $(+ + + +)$.

the WW final state offers many observables which are particularly sensitive to the initial electron and laser polarisations and the very high statistics due to the 80 pb cross section.

By performing a combined fit to the total cross sections and angular distributions for various initial state polarisation choices and the polarisation asymmetries, the discovery reach for M_s can be estimated as a function of the total $\gamma\gamma$ integrated luminosity. This is shown in Fig. 1.2.6 [108]. The reach is in the range of $M_s \sim (11-13) \cdot 2E_0$, which is larger than that obtained from all other processes examined so far. By comparison, a combined analysis of the processes $e^+e^- \rightarrow f\bar{f}$ with the same integrated luminosity leads to a reach of only $(6-7) \cdot 2E_0$.

Other $\gamma\gamma$ final states are also sensitive to graviton exchanges, two examples being the $\gamma\gamma$ [110, 111] and ZZ [109] final states, which however result in smaller search reaches.

1.2.5 Gauge bosons

New strong interactions that might be responsible for the electroweak symmetry breaking can affect the triple and quartic couplings of the weak vector bosons. Hence, the precision measurements of these couplings, as well as corresponding effects on the top quark couplings, can provide clues to the mechanism of the electroweak symmetry breaking.

Due to the large cross sections of the order of 10^2 pb well above the thresholds, the $\gamma\gamma \rightarrow W^+W^-$ and $\gamma e \rightarrow \nu W$ processes seem to be ideal reactions to study such

anomalous gauge interactions [112, 113].

1.2.5.1 Anomalous gauge boson couplings

The relevant process at the e^+e^- collider is $e^+e^- \rightarrow W^+W^-$. This reaction is dominated by the large t -channel neutrino exchange term which however can be suppressed using electron beam polarisation. The cross section of W^+W^- pair production in e^+e^- collisions with right-handed electron beams, for which the neutrino exchange is negligible, has a maximum of about 2 pb at LEP2 and decreases at higher energy.

The two main processes at the Photon Collider are $\gamma\gamma \rightarrow W^+W^-$ and $\gamma e \rightarrow W\nu$. Their total cross sections for centre-of-mass energies above 200 GeV are about 80 pb and 40 pb, respectively, and they do not decrease with energy. Hence the W production cross sections at the Photon Collider are at least 20–40 times larger than the cross section at the e^+e^- collider. This enhancement makes event rates at the Photon Collider one order of magnitude larger than at an e^+e^- collider, even when the lower $\gamma\gamma$, γe luminosities are taken into account. Specifically for the integrated $\gamma\gamma$ luminosity of 100 fb^{-1} , about 8×10^6 W^+W^- pairs are produced at the Photon Collider. Note that while $\gamma e \rightarrow W\nu$ and $\gamma\gamma \rightarrow WW$ isolate the anomalous photon couplings to the W , $e^+e^- \rightarrow WW$ involves potentially anomalous Z couplings so that the two LC modes are complementary with each other.

The analysis of $\gamma\gamma \rightarrow WW$ has been performed in [18, 114] with the detector simulation. The W boson by photon colliders is compared to that from e^+e^- colliders. The results have been obtained only from analyses of the total cross section. With the W decay properties taken into account further improvements can be expected. The resulting accuracy on λ_γ is comparable with e^+e^- analyses, while a similar accuracy on $\delta\kappa_\gamma$ can be achieved at 1/20-th of the e^+e^- luminosity. In addition, the process $\gamma e \rightarrow W\nu$, which has a large cross section, is very sensitive to the admixture of right-handed currents in the W couplings with fermions: $\sigma_{\gamma e \rightarrow W\nu} \propto (1-2\lambda_e)$.

Many processes of 3rd and 4th order have quite large cross sections [115, 116, 117, 118] at the Photon Collider:

$$\begin{array}{ll} \gamma e \rightarrow eWW & \gamma\gamma \rightarrow ZWW \\ \gamma e \rightarrow \nu WZ & \gamma\gamma \rightarrow WWWW \\ & \gamma\gamma \rightarrow WWZZ \end{array}$$

It should also be noted, that in $\gamma\gamma$ collisions the anomalous $\gamma\gamma W^+W^-$ quartic couplings can be probed. However, the higher event rate does not necessarily provide better bounds on anomalous couplings. In some models electroweak symmetry breaking leads to large deviations mainly in longitudinal $W_L W_L$ pair production [119]. On the other hand the large cross section of the reaction $\gamma\gamma \rightarrow W^+W^-$ is due to transverse $W_T W_T$ pair production. In such a case transverse $W_T W_T$ pair production would represent a background for the longitudinal $W_L W_L$ production. The relative yield of $W_L W_L$ can be considerably improved after a cut on the W scattering angle. Asymptotically for $s_{\gamma\gamma} \gg M_W^2$ the production of $W_L W_L$ is as much as 5 times larger than at a e^+e^- LC.

However, if anomalous couplings manifest themselves in transverse $W_T W_T$ pair production, e.g. in theories with large extra dimensions, then the interference with the large SM transverse contribution is of big advantage in the Photon Collider.

1.2.5.2 Strong $WW \rightarrow WW, WW \rightarrow ZZ$ scattering

If the strong electroweak symmetry breaking scenario is realised in Nature, W and Z bosons will interact strongly at high energies. If no Higgs boson exists with a mass below 1 TeV, the longitudinal components of the electroweak gauge bosons must become strongly interacting at energies above 1 TeV. In such scenarios novel resonances can be formed in $W_L W_L$ collisions at energies $\lesssim 3$ TeV. If the energy of the $\gamma\gamma$ collisions is sufficiently high, the effective W luminosities in $\gamma\gamma$ collisions allow the study of $W^+ W^- \rightarrow W^+ W^-$, ZZ scattering in the reactions

$$\gamma\gamma \rightarrow WWWW, WWZZ$$

for energies in the threshold region of the new strong interactions. Each incoming photon turns into a virtual WW pair, followed by the scattering of one W from each such pair to form WW or ZZ [120, 121, 122, 123, 124, 125, 126]. The same reactions can be used to study quartic anomalous $WWWW, WWZZ$ couplings.

1.2.6 Top quark

The top quark is heavy and up to now point-like at the same time. The top Yukawa coupling $\lambda_t = 2^{3/4} G_F^{1/2} M_t$ is numerically very close to unity, and it is not clear whether or not this is related to a deep physics reason. Hence one might expect deviations from SM predictions to be most pronounced in the top sector [127, 128]. Besides, top quarks decay before forming a bound state with any other quark. Top quark physics will be a very important part of research programs for all future hadron and lepton colliders. The $\gamma\gamma$ collider is of special interest because of the clean production mechanism and the high rate (review [129]). Moreover, the S and P partial waves of the final state top quark–antiquark pair produced in $\gamma\gamma$ collisions can be separated by choosing the same or opposite helicities of the colliding photons.

1.2.6.1 Probe for anomalous couplings in $t\bar{t}$ pair production

There is a difference for the case of $\gamma\gamma$ and e^+e^- collisions with respect to the couplings: the $\gamma t\bar{t}$ coupling is separated from $Z t\bar{t}$ coupling in $\gamma\gamma$ collisions while in e^+e^- collisions both couplings contribute.

The effective Lagrangian contains four parameters f_i^α for the electric and magnetic type couplings [130], where $i = 1-4$ and $\alpha = \gamma, Z$ but only couplings with $\alpha = \gamma$ occur in $\gamma\gamma$ collisions. It was demonstrated [131] that if the cross section can be measured with 2% accuracy, scale parameter for new physics Λ up to 10 TeV for $2E_0 = 500$ GeV can be probed for form factors taken in the form $f_i^\alpha = (f_i^\alpha)^{SM} (1 + s/\Lambda^2)$. The sensitivity to the anomalous magnetic moment f_2^γ is of similar size in $\gamma\gamma$ and e^+e^- collisions. The f_4^α

term describes the \mathcal{CP} violation. The best limit on the imaginary part of the electric dipole moment $\Im(f_4^\gamma) \sim 2.3 \times 10^{-17} e \text{ cm}$ [132] by measuring the forward–backward asymmetry A_{fb} with initial–beam helicities of electron and laser beams $\lambda_e^1 = \lambda_e^2$ and $\lambda_l^1 = -\lambda_l^2$. The achievable limit for the real part of the dipole moment is also of the order of $10^{-17} e \text{ cm}$ and is obtained from the linear polarisation asymmetries [133, 134].

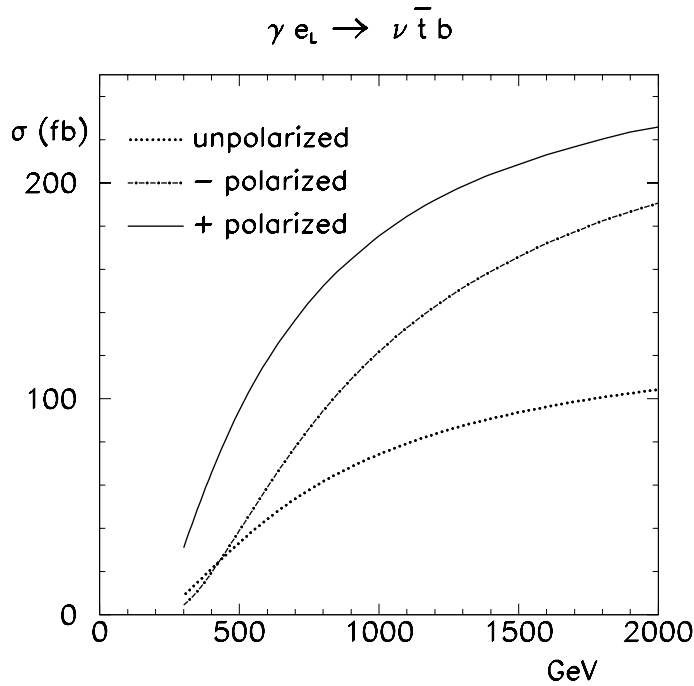


Figure 1.2.7: Single top quark production cross section in γe collisions as a function of $2E_0$.

1.2.6.2 Single top production in $\gamma\gamma$ and γe Collisions

Single top production in $\gamma\gamma$ collisions results in the same final state as top quark pair production [135] and invariant mass cuts are required to suppress direct $t\bar{t}$ contributions. Single top production is preferentially realised in γe collisions [136, 137, 138, 139, 140]. In contrast to the top pair production rate, the single top rate is directly proportional to the Wtb coupling and the process is very sensitive to its structure. The anomalous part of the effective Lagrangian [130] contains terms $f_{2L(R)} \propto 1/\Lambda$, where Λ is the scale of a new physics.

In Table 1.2.1 [141, 142] limits on anomalous couplings from measurements at different accelerators are collected. The best limits can be reached at very high energy γe colliders, even in the case of unpolarised collisions. In the case of polarised collisions, the production rate increases significantly as shown in Fig. 1.2.7 [135] and more stringent bounds on anomalous couplings may be achieved.

	f_{2L}	f_{2R}
TEVATRON ($\Delta_{sys.} \approx 10\%$)	$-0.18 \div +0.55$	$-0.24 \div +0.25$
LHC ($\Delta_{sys.} \approx 5\%$)	$-0.052 \div +0.097$	$-0.12 \div +0.13$
e^+e^- ($2E_0 = 0.5$ TeV)	$-0.025 \div +0.025$	$-0.2 \div +0.2$
γe ($2E_0 = 0.5$ TeV)	$-0.045 \div +0.045$	$-0.045 \div +0.045$
γe ($2E_0 = 2.0$ TeV)	$-0.008 \div +0.035$	$-0.016 \div +0.016$

Table 1.2.1: *Expected sensitivity for the Wtb anomalous couplings. The total integrated luminosity was assumed to be $500fb^{-1}$ for e^+e^- collisions and $250fb^{-1}$ and $500fb^{-1}$ for γe collisions at 500 GeV and 2 TeV, respectively.*

1.2.7 QCD and hadron physics

Photon colliders offer a unique possibility to probe QCD in a new unexplored regime. The very high luminosity, the (relatively) sharp spectrum of the backscattered laser photons and their polarisation are of great advantage. At the Photon Collider the following measurements can be performed, for example:

1. The total cross section for $\gamma\gamma$ fusion to hadrons [143].
2. Deep inelastic γe \mathcal{NC} and \mathcal{CC} scattering, and measurement of the quark distributions in the photon at large Q^2 .
3. Measurement of the gluon distribution in the photon.
4. Measurement of the spin dependent structure function $g_1^\gamma(x, Q^2)$ of the photon.
5. J/Ψ production in $\gamma\gamma$ collisions as a probe of the hard QCD pomeron [144, 145, 146].

$\gamma\gamma$ fusion to hadrons

The total cross section for hadron production in $\gamma\gamma$ collisions is a fundamental observable. It provides us with a picture of hadronic fluctuations in photons of high energy which reflect the strong-interaction dynamics as described by quarks and gluons in QCD. Since these dynamical processes involve large distances, predictions, due to the theoretical complexity, cannot be based yet on first principles. Instead, phenomenological models have been developed which involve elements of ideas which have successfully been applied to the analysis of hadron-hadron scattering, but also elements transferred from perturbative QCD in eikonalised mini-jet models. Differences between hadron-type models and mini-jet models are dramatic in the TESLA energy range. $\gamma\gamma$ scattering experiments are therefore extremely valuable in clarifying the dynamics in complex hadronic quantum fluctuations of the simplest gauge particle in Nature.

Deep inelastic γe scattering (DIS)

The large c.m. energy in the γe system and the possibility of precise measurement of the kinematical variables x, Q^2 in DIS provide exciting opportunities at a photon collider. In particular it allows precise measurements of the photon structure function(s) with much better accuracy than in the single tagged e^+e^- collisions. The γe collider offers a unique opportunity to probe the photon at low values of x ($x \sim 10^{-4}$) for reasonably large values of $Q^2 \sim 10 \text{ GeV}^2$ [147]. At very large values of Q^2 the virtual γ exchange in deep inelastic γe scattering is supplemented by significant contributions from Z exchange. Moreover, at very large values of Q^2 charged-current exchange becomes effective in deep inelastic scattering, $\gamma e \rightarrow \nu X$, which is mediated by virtual W exchange. The study of this process can in particular give information on the flavour decomposition of the quark distributions in the photon [148].

Gluon distribution in the photon

The gluon distribution in the photon can be studied in dedicated measurements of the hadronic final state in $\gamma\gamma$ collisions. The following two processes are of particular interest:

1. Dijet production [149, 150], generated by the subprocess $\gamma g \rightarrow q\bar{q}$.
2. Charm production [151], which is sensitive to the mechanism $\gamma g \rightarrow c\bar{c}$

Both these processes, which are at least in certain kinematical regions dominated by the photon-gluon fusion mechanisms, are sensitive to the gluon distribution in the photon. The detailed discussion of these processes have been presented in [152, 153].

Measurement of the spin dependent structure function $g_1^\gamma(x, Q^2)$ of the Photon

Using polarised beams, photon colliders offer the possibility to measure the spin dependent structure function $g_1^\gamma(x, Q^2)$ of the photon [154, 155, 156]. This quantity is completely unknown and its measurement in polarised γe DIS would be extremely interesting for testing QCD predictions in a broad region of x and Q^2 . The high-energy photon colliders allow to probe this quantity for very small values of x [157, 158].

Probing the QCD pomeron by J/Ψ production in $\gamma\gamma$ Collisions

The exchange of the hard QCD (or BFKL) pomeron is presumably the dominant mechanism of the process $\gamma\gamma \rightarrow J/\psi J/\psi$. Theoretical estimates of the cross-section presented in [159, 160] have demonstrated that measurement of the reaction $\gamma\gamma \rightarrow J/\psi J/\psi$ at the Photon Collider should be feasible.

1.2.8 Table of gold-plated processes

A short list of processes which we think are the most important ones for the physics program of the Photon Collider option of the LC is presented in Table 1.2.2.

Of course there exist many other possible manifestations of new physics in $\gamma\gamma$ and γe collisions which we have not discussed here. The study of resonant production of

Reaction	Remarks
$\gamma\gamma \rightarrow h^0 \rightarrow b\bar{b}$	SM (or MSSM) Higgs, $M_{h^0} < 160$ GeV
$\gamma\gamma \rightarrow h^0 \rightarrow WW(WW^*)$	SM Higgs, $140 \text{ GeV} < M_{h^0} < 190$ GeV
$\gamma\gamma \rightarrow h^0 \rightarrow ZZ(ZZ^*)$	SM Higgs, $180 \text{ GeV} < M_{h^0} < 350$ GeV
$\gamma\gamma \rightarrow H, A \rightarrow b\bar{b}$	MSSM heavy Higgs, for intermediate $\tan \beta$
$\gamma\gamma \rightarrow \tilde{f}\tilde{f}, \tilde{\chi}_i^+\tilde{\chi}_i^-, H^+H^-$	large cross sections, possible observations of FCNC
$\gamma\gamma \rightarrow S[\tilde{t}\tilde{t}]$	$\tilde{t}\tilde{t}$ stoponium
$\gamma e \rightarrow \tilde{e}^-\tilde{\chi}_1^0$	$M_{\tilde{e}^-} < 0.9 \times 2E_0 - M_{\tilde{\chi}_1^0}$
$\gamma\gamma \rightarrow W^+W^-$	anomalous W interactions, extra dimensions
$\gamma e^- \rightarrow W^-\nu_e$	anomalous W couplings
$\gamma\gamma \rightarrow WWWW, WWZZ$	strong WW scatt., quartic anomalous W, Z couplings
$\gamma\gamma \rightarrow t\bar{t}$	anomalous top quark interactions
$\gamma e^- \rightarrow \bar{t}b\nu_e$	anomalous Wtb coupling
$\gamma\gamma \rightarrow \text{hadrons}$	total $\gamma\gamma$ cross section
$\gamma e^- \rightarrow e^-X$ and $\nu_e X$	\mathcal{NC} and \mathcal{CC} structure functions (polarised and unpolarised)
$\gamma g \rightarrow q\bar{q}, c\bar{c}$	gluon distribution in the photon
$\gamma\gamma \rightarrow J/\psi J/\psi$	QCD Pomeron

Table 1.2.2: *Gold-plated processes at photon colliders*

excited electrons $\gamma e \rightarrow e^*$, the production of excited fermions $\gamma\gamma \rightarrow f^*f$, leptoquark production $\gamma e \rightarrow (eQ)\bar{Q}$ [161, 162], a magnetic monopole signal in the reaction of $\gamma\gamma$ elastic scattering [163, 164] etc. may be mentioned in this context.

To summarise, the Photon Collider will allow us to study the physics of the EWSB in both the weak-coupling and the strong-coupling scenarios. Measurements of the two-photon Higgs width of the h, H and A Higgs states provide a strong physics motivation for developing the technology of the $\gamma\gamma$ collider option. Polarised photon beams, large cross sections and sufficiently large luminosities allow to significantly enhance the discovery limits of many new particles in SUSY and other extensions of the Standard Model. Moreover, they will substantially improve the accuracy of the precision measurements of anomalous W boson and top quark couplings, thereby complementing and improving the measurements at the e^+e^- mode of TESLA. Photon colliders offer a unique possibility for probing the photon structure and the QCD Pomeron.

1.3 Electron to Photon Conversion

1.3.1 Processes in the conversion region

1.3.1.1 Compton scattering

Compton scattering is the basic process for the production of high energy photons at photon colliders. The fact that a high energy electron loses a large fraction of its energy in collisions with an optical photon was realized a long time ago in astrophysics [165]. The method of generation of high energy γ -quanta by Compton scattering of the laser light on relativistic electrons has been proposed soon after lasers were invented [166, 167] and has already been used in many laboratories for more than 35 years [168, 169]. In first experiments the conversion efficiency of electron to photons $k = N_\gamma/N_e$ was very small, only about 10^{-7} [169]. At linear colliders, due to small bunch sizes one can focus the laser to the electron beam and get $k \approx 1$ at rather moderate laser flash energy, about 1–5 J. Twenty years ago when photon colliders were proposed [1, 2] such flash energies could already be obtained but with a low rate¹ and a pulse duration longer than is necessary. Progress in laser technology since that time now presents a real possibility for the construction of a laser system for a photon collider.

Kinematics, photon spectrum

Let us consider the most important characteristics of Compton scattering. In the conversion region a laser photon with energy ω_0 scatters at a small collision angle α_0 off a high energy electron with energy E_0 . The energy of the scattered photon ω depends on the photon scattering angle as follows [2]:

$$\omega = \frac{\omega_m}{1 + (\vartheta/\vartheta_0)^2}, \quad \omega_m = \frac{x}{x+1}E_0, \quad \vartheta_0 = \frac{mc^2}{E_0}\sqrt{x+1}, \quad (1.3.1)$$

where

$$x = \frac{4E_0\omega_0}{m^2c^4} \cos^2\alpha_0/2 \simeq 15.3 \left[\frac{E_0}{\text{TeV}} \right] \left[\frac{\omega_0}{\text{eV}} \right] = 19 \left[\frac{E_0}{\text{TeV}} \right] \left[\frac{\mu\text{m}}{\lambda} \right], \quad (1.3.2)$$

ω_m is the maximum energy of scattered photons (in the direction of the electron, Compton “backscattering”).

For example: $E_0 = 250 \text{ GeV}$, $\omega_0 = 1.17 \text{ eV}$ ($\lambda = 1.06 \mu\text{m}$) (region of most powerful solid-state lasers) $\Rightarrow x = 4.5$ and $\omega_m/E_0 = 0.82$.

The energy spectrum of the scattered photons is defined by the Compton cross section

$$\frac{1}{\sigma_c} \frac{d\sigma_c}{dy} = \frac{2\sigma_0}{x\sigma_c} \left[\frac{1}{1-y} + 1 - y - 4r(1-r) + 2\lambda_e P_c r x (1-2r)(2-y) \right], \quad (1.3.3)$$

¹The proposed linear collider VLEPP (Novosibirsk) had initially only 10 Hz rep. rate with one bunch per “train”, in present projects the collision rate is about 10 kHz which is much more difficult.

$$y = \omega/E_0, \quad r = \frac{y}{(1-y)x}, \quad \sigma_0 = \pi r_e^2 = \pi \left(\frac{e^2}{mc^2} \right)^2 = 2.5 \cdot 10^{-25} \text{ cm}^2,$$

where λ_e is the mean electron helicity ($|\lambda_e| \leq 1/2$) and P_c is that of the laser photon ($|P_c| \leq 1$). It is useful to note that $r \rightarrow 1$ for $y \rightarrow y_m$.

The total Compton cross section is

$$\begin{aligned} \sigma_c &= \sigma_c^0 + 2\lambda_e P_c \sigma_c^1, \\ \sigma_c^0 &= \frac{2\sigma_0}{x} \left[\left(1 - \frac{4}{x} - \frac{8}{x^2} \right) \ln(x+1) + \frac{1}{2} + \frac{8}{x} - \frac{1}{2(x+1)^2} \right], \\ \sigma_c^1 &= \frac{2\sigma_0}{x} \left[\left(1 + \frac{2}{x} \right) \ln(x+1) - \frac{5}{2} + \frac{1}{x+1} - \frac{1}{2(x+1)^2} \right]. \end{aligned} \quad (1.3.4)$$

Polarisations of initial beams influence the differential and the total cross section only if both their helicities are nonzero, i.e. at $\lambda_e P_c \neq 0$. In the region of interest

$$x = 1 \div 5, \quad \sigma_c^0 = (1.5 \div 0.7) \sigma_0, \quad |\sigma_c^1|/\sigma_c < 0.1, \quad (1.3.5)$$

i.e. the total cross section only depends slightly on the polarisation.

On the contrary, the energy spectrum strongly depends on the value of $\lambda_e P_c$. The “quality” of the photon beam, i.e. the relative number of hard photons, is improved when one uses beams with a negative value of $\lambda_e P_c$. For $2\lambda_e P_c = -1$ the peak at $\omega = \omega_m$ nearly doubles, significantly improving the energy spread of the γ beam

$$\frac{d\sigma_c(y_m, 2\lambda_e P_c = -1)/dy}{d\sigma_c(y_m, 2\lambda_e P_c = 0)/dy} = \frac{2}{1 + (x+1)^{-2}}.$$

The full width of the spectrum at the half of maximum is $\Delta\omega_{1/2} \approx \omega_m/(x+2)$ for unpolarised beams, and even smaller at $\lambda_e P_c < 0$. Photons in this high energy peak have the characteristic angle $\theta_{\text{char}} = 1/\gamma = mc^2/E = 0.51/E_0[\text{TeV}] \mu\text{rad}$.

To increase the maximum photon energy, one should use a laser with a higher energy. This also increases the fraction of hard photons. Unfortunately, at large $x > 4.8$, a new phenomenon takes place: the high energy photons disappear from the beam, producing e^+e^- pairs in collisions with laser photons (see Section 1.3.1.3). Therefore, the value $x \approx 4.8$ is the most preferable.

The energy spectrum of the scattered photons for $x = 4.8$ is shown in Fig. 1.3.1 for various helicities of electron and laser beams. As was mentioned before, with the polarised beams at $2\lambda_e P_c = -1$, that the number of high energy photons nearly doubles and the luminosity in collisions of these photons is larger by a factor of 4. This is one of the important advantages of polarised electron beams.

The photon energy spectrum presented in Fig. 1.3.1 corresponds to the case of a small conversion coefficient. In the realistic case when the thickness of the laser target is about one collision length each electron may undergo multiple Compton scattering [5]. This probability is not small because, after a large energy loss in the first collision,

the Compton cross section increases and approaches the Thomson cross section $\sigma_T = (8/3)\sigma_0$. The secondary photons are softer and populate the low energy part of the spectrum. Multiple Compton scattering leads also to a low energy tail in the energy spectrum of the electron beam after the $e \rightarrow \gamma$ conversion. This creates a problem for the removal of the beams (see Section 1.4.2).

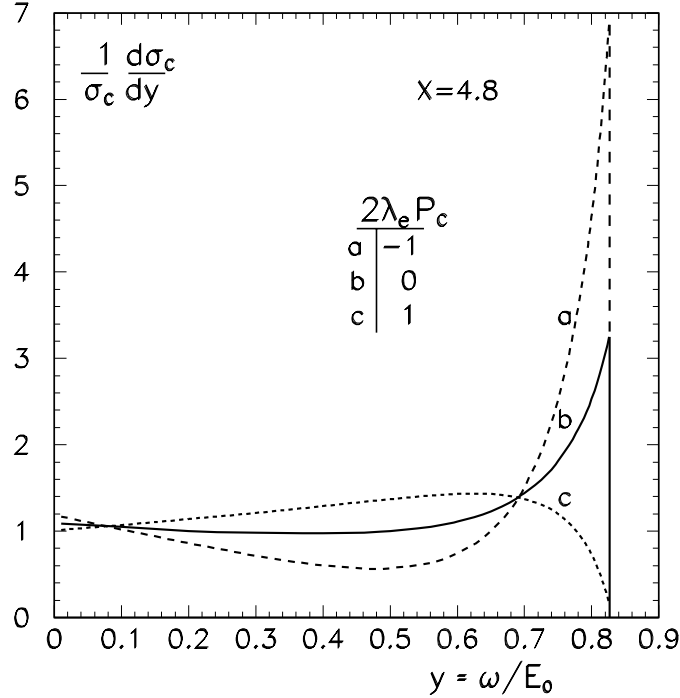


Figure 1.3.1: *Spectrum of the Compton scattered photons for different polarisations of the laser and electron beams.*

Polarisation of scattered photons

The averaged helicity of photons after Compton scattering is [3]

$$\langle \lambda_\gamma \rangle = \frac{-P_c(2r-1)[(1-y)^{-1} + 1-y] + 2\lambda_e x r [1 + (1-y)(2r-1)^2]}{(1-y)^{-1} + 1-y - 4r(1-r) - 2\lambda_e P_c x r (2-y)(2r-1)}. \quad (1.3.6)$$

The final photons have an averaged helicity $\langle \lambda_\gamma \rangle \neq 0$ if either the laser light has circular polarisation $P_c \neq 0$ or the electrons have mean helicity $\lambda_e \neq 0$. Moreover, $\langle \lambda_\gamma(\omega = \omega_m) \rangle = -P_c$ at $P_c = \pm 1$ or $\lambda_e = 0$.

The mean helicity of the scattered photons at $x = 4.8$ is shown in Fig. 1.3.2 for various helicities of the electron and laser beams [5]. For $2P_c\lambda_e = -1$ (the case with minimum energy spread) all photons in the high energy peak have a high degree of like-sign polarisation. This is the most valuable region for experiments. If the electron

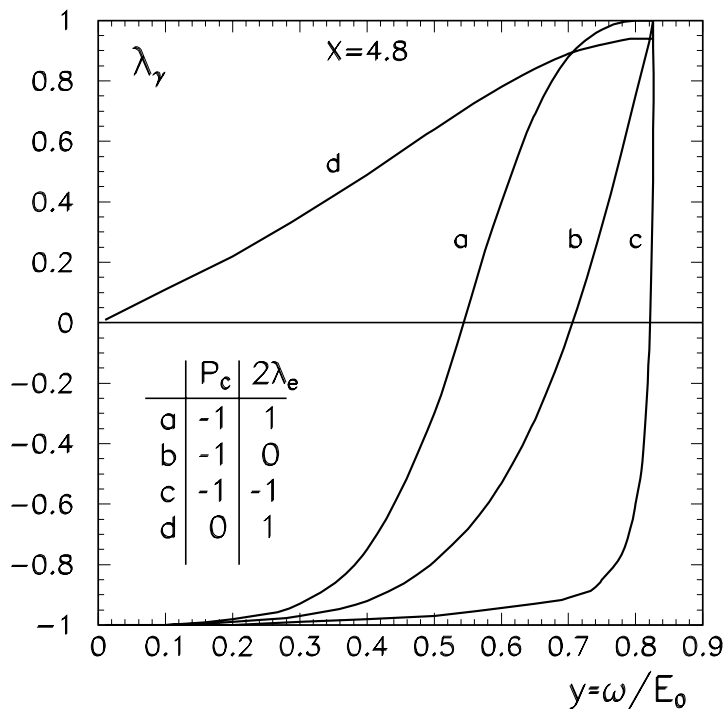


Figure 1.3.2: Mean helicity of the scattered photons.

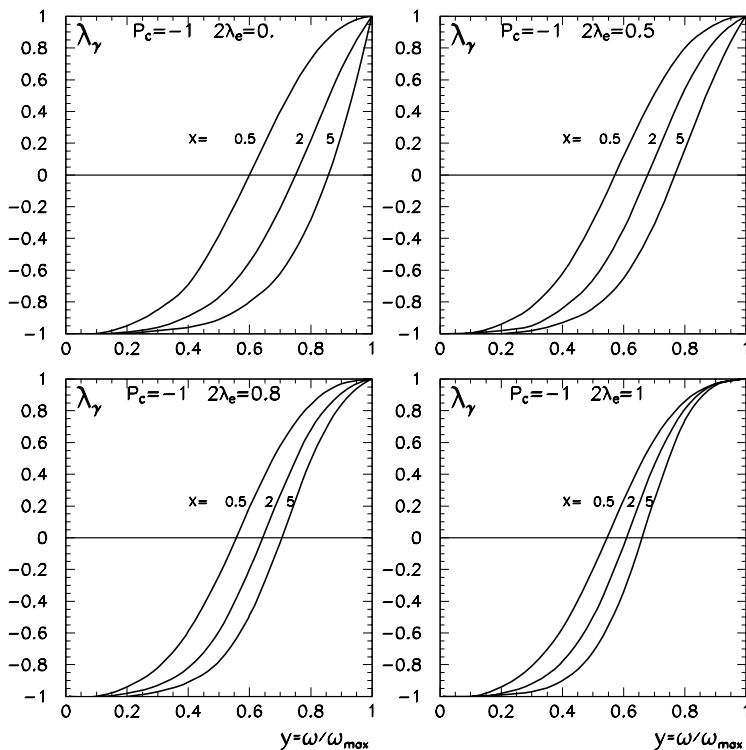


Figure 1.3.3: Mean helicity of the scattered photons for various x and degree of the longitudinal electron polarisation.

polarisation is not 100% and $|P_c| = 1$, the helicity of the photon with the maximum energy is still 100% but the energy region with a high helicity is reduced, see 1.3.3.

Low energy photons are also polarised (especially in the case $2\lambda_e P_c = +1$ which corresponds to the broad spectrum), but due to contribution of multiple Compton scattering and beamstrahlung photons produced during the beam collisions the low energy region is not attractive for polarisation experiments.

A high degree of longitudinal photon polarisation is essential for the suppression of the QED background in the study of the intermediate Higgs boson (Section 1.2). Note that at a 0.5 TeV linear collider the region of the intermediate Higgs can be studied with rather small x . In this case the helicity of scattered photons is almost independent of the polarisation of the electrons, and, if $P_c = 1$, the high energy photons have very high circular polarisation over a wide range near the maximum energy, even with $\lambda_e = 0$. Nevertheless, electron polarisation is very desirable even for rather low x because, as was mentioned before, it increases the relative number of high energy photons.

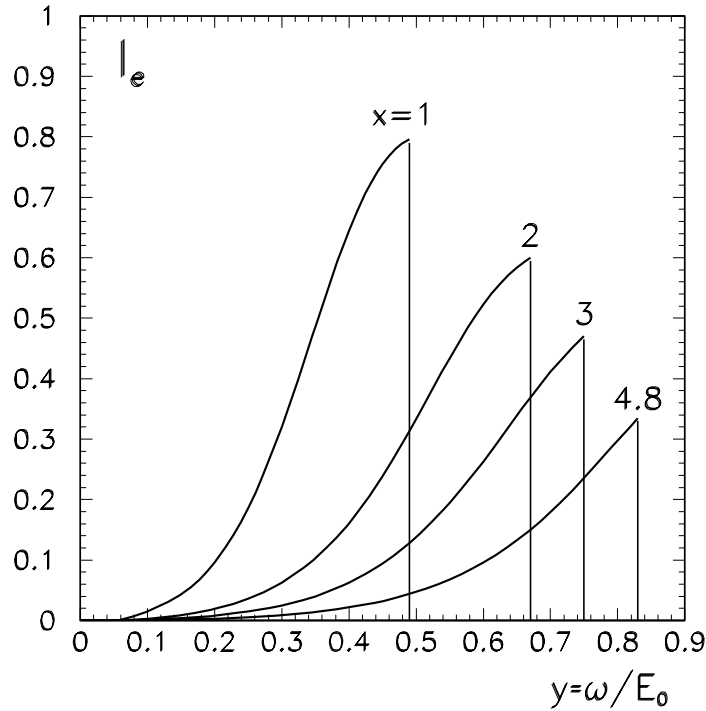


Figure 1.3.4: *Linear polarisation of the scattered photons for various x for unpolarised electrons and $P_l = 1$.*

The averaged degree of the linear polarisation of the final photons is [3]

$$\langle l_\gamma \rangle = \frac{2r^2 P_l}{(1-y)^{-1} + 1 - y - 4r(1-r) - 2\lambda_e P_c x r (2-y)(2r-1)}. \quad (1.3.7)$$

If the laser light has a linear polarisation, then the high-energy photons are polarised

in the same direction. The degree of this polarisation $\langle l_\gamma \rangle$ depends on the linear polarisation of laser photons P_l and $2\lambda_e P_c$. For $P_l = 1$ (in this case $P_c = 0$) the linear polarisation is maximum for the photons with the maximum energy. At $y = y_m$ the degree of linear polarisation for the unpolarised electrons

$$l_\gamma = \frac{2}{1 + x + (1 + x)^{-1}} \quad (1.3.8)$$

is 0.334, 0.6, 0.8 for $x = 4.8, 2, 1$ respectively. The dependence of the linear polarisation on the photon energy for unpolarised electron beams and 100% linear polarisation of laser photons is shown in Fig. 1.3.4

It is of interest that varying polarisations of laser and electron beams one can get larger $\langle l_\gamma \rangle$, up to $\langle l_\gamma \rangle = 1$. For example, at $P_t = 2(x + 1)/(x^2 + 2x + 2)$ and $2\lambda_e P_c = x(x + 2)/(x^2 + 2x + 2)$ the quantity $\langle l_\gamma \rangle$ at $y = y_m$ can reach 1. Unfortunately, in this case $2\lambda_e P_c \approx +1$, which corresponds to curve c in Fig. 1.3.1, when the number of photons with the energy ω near ω_m is small.

Linear polarisation is necessary for the measurement of the \mathcal{CP} -parity of the Higgs boson in $\gamma\gamma$ collisions (Section 1.2). Polarisation asymmetries are proportional to $l_{\gamma,1}l_{\gamma,2}$, therefore low x values are preferable.

1.3.1.2 Nonlinear effects

For the calculation of the $e \rightarrow \gamma$ conversion efficiency, beside the geometrical properties of the laser beam and the Compton effect, one has to consider also *nonlinear effects* in the Compton scattering. The field in the laser wave at the conversion region is very strong, so that the electron (or the high-energy photon) can interact simultaneously with several laser photons (so called nonlinear QED effects). These nonlinear effects are characterised by the parameter [170, 171, 172, 173]

$$\xi^2 = \frac{e^2 \bar{F}^2 \hbar^2}{m^2 c^2 \omega_0^2} = \frac{2n_\gamma r_e^2 \lambda}{\alpha}, \quad (1.3.9)$$

where \bar{F} is the r.m.s. strength of the electric (magnetic) field in the laser wave, n_γ is the density of laser photons. At $\xi^2 \ll 1$ the electron is scattered on one laser photon, while at $\xi^2 \gg 1$ on several (like synchrotron radiation in a wiggler). Nonlinear effects in Compton scattering at photon colliders are considered in detail in [174] and references therein.

The transverse motion of an electron in the electromagnetic wave leads to an effective increase of the electron mass: $m^2 \rightarrow m^2(1 + \xi^2)$, and the maximum energy of the scattered photons decreases: $\omega_m/E_0 = x/(1 + x + \xi^2)$. The relative shift $\Delta\omega_m/\omega_m \approx \xi^2/(x + 1)$. At $x = 4.8$ the value of ω_m/E_0 decreases by 5% at $\xi^2 = 0.3$ [5]. This value of ξ^2 can be taken as the limit. For smaller x it should be even lower.

The evolution of the Compton spectra as a function of ξ^2 for $x = 4.8$ and 1.8 (the latter case is important for the Higgs study) is shown in Fig. 1.3.5 [174]. One can see

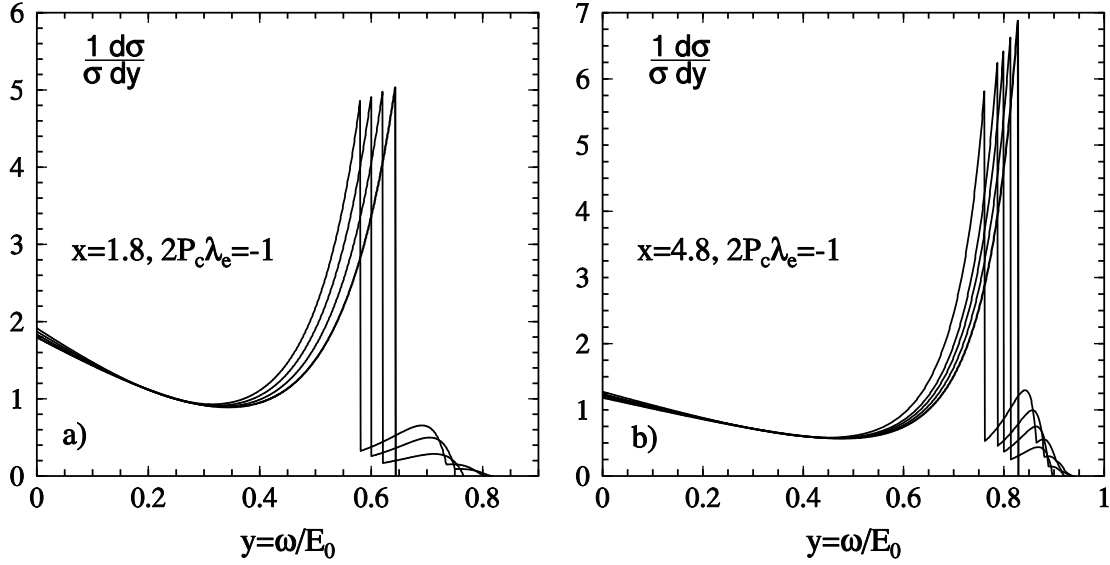


Figure 1.3.5: Compton spectra for various values of the parameter ξ^2 . Left figure is for $x = 1.8$, right for $x = 4.8$. Curves from right to left correspond to $\xi^2 = 0, 0.1, 0.2, 0.3, 0.5$ (the last for $x = 4.8$, only).

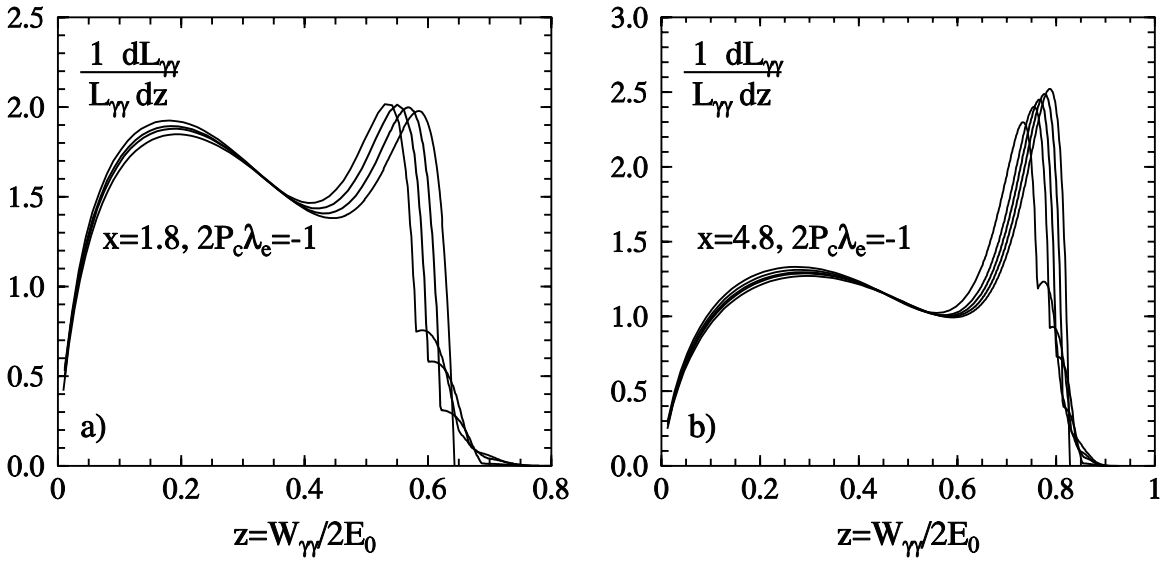


Figure 1.3.6: Idealised (see the text) $\gamma\gamma$ luminosity distributions for various values of the parameter ξ^2 . Left figure is for $x = 1.8$, right for $x = 4.8$. Curves from right to left correspond to $\xi^2 = 0, 0.1, 0.2, 0.3, 0.5$.

that with increasing ξ^2 the Compton spectrum becomes broader, is shifted to lower energies and higher harmonics appear. These effects are clearly seen also in the $\gamma\gamma$ luminosity distributions (Fig. 1.3.6) which, under certain conditions (Section 1.5), are a simple convolution of the photon spectra.

For many experiments (such as scanning of the Higgs) it is very advantageous to have a sharp edge of the luminosity spectrum. This requirement restricts the maximum values of ξ^2 to 0.1–0.3, depending on x .

1.3.1.3 e^+e^- Pair creation and choice of the laser wavelength

As it was mentioned with increasing x , the energy of the back-scattered photons increases and the energy spectrum becomes narrower. However, at high x , photons may be lost due to creation of e^+e^- pairs in the collisions with laser photons [2, 4, 5]. The threshold of this reaction is $\omega_m\omega_0 = m^2c^4$, which gives $x = 2(1 + \sqrt{2}) \approx 4.83$.

The cross section for e^+e^- production in a photon-photon collision is given by [52, 53, 175]

$$\sigma_{\gamma\gamma \rightarrow e^+e^-} = \sigma_{np} + \lambda_1\lambda_2\sigma_1, \quad (1.3.10)$$

$$\sigma_{np} = \frac{4\sigma_0}{x_\gamma} \left[2 \left(1 + \frac{4}{x_\gamma} - \frac{8}{x_\gamma^2} \right) \ln \frac{\sqrt{x_\gamma} + \sqrt{x_\gamma - 4}}{2} - \left(1 + \frac{4}{x_\gamma} \right) \sqrt{1 - \frac{4}{x_\gamma}} \right],$$

$$\sigma_1 = \frac{4\sigma_0}{x_\gamma} \left[2 \ln \frac{\sqrt{x_\gamma} + \sqrt{x_\gamma - 4}}{2} - 3\sqrt{1 - \frac{4}{x_\gamma}} \right], \quad (1.3.11)$$

where $x_\gamma = 4\omega_m\omega_0/m^2c^4 = x^2/(x+1)$, λ_1, λ_2 are photon helicities.

The ratio $\sigma_{\gamma\gamma \rightarrow e^+e^-}/\sigma_c$ and the maximum conversion efficiency is shown in Fig. 1.3.7 [4, 5].

One can see that above the threshold, ($x \approx 8-20$) the e^+e^- cross section is larger by a factor of 1.5–2, the maximum conversion coefficient is limited to 25–30%. Therefore, the value of k^2 which is proportional to the $\gamma\gamma$ luminosity is only 0.06–0.09. For these reasons it is preferable to work at $x \leq 4.8$ where $k^2 \approx 0.4$ (one collision length) or even higher values are possible.

The wavelength of the laser photons corresponding to $x = 4.8$ is

$$\lambda = 4.2E_0[\text{TeV}] \mu\text{m}. \quad (1.3.12)$$

For $2E_0 = 500 \text{ GeV}$ it is about $1 \mu\text{m}$, which is exactly the region of the most powerful solid state lasers. This value of $x \approx 4.8$ is preferable for most measurements. However, for experiments with linear photon polarisation (see above) lower values of x are preferable. Larger values of x may be useful, for example, for reaching somewhat higher energy.

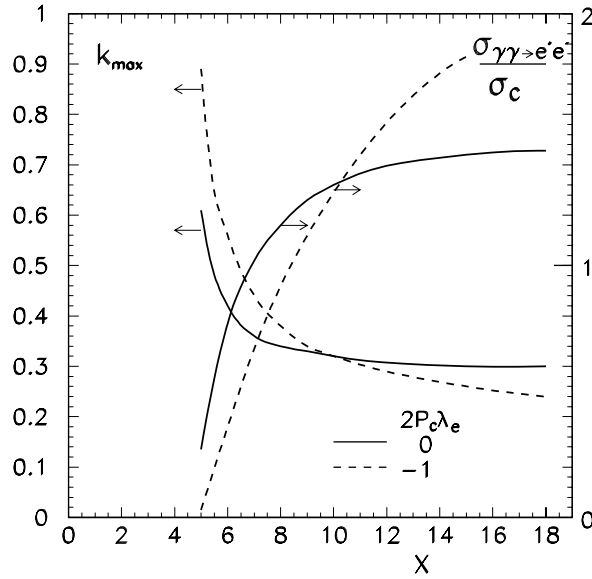


Figure 1.3.7: The ratio of cross sections for e^+e^- pair creation in the collision of laser and high energy photons and for Compton scattering; and the corresponding dependence of the maximum conversion efficiency on x assuming $\omega = \omega_m$.

The nonlinear effects, considered in the previous section for Compton scattering are important for the e^+e^- pair creation as well. First of all, due to the high photon density e^+e^- pairs can be produced in collisions of a high energy photon with several laser photons. This process is possible even at $x < 4.8$. For the considered values of ξ^2 such effect is not important for conversion, but the presence of positrons may be important for the beam removal.

It is even more important that the threshold for e^+e^- collision in the collision with one laser photon increases because the effective electron mass in the strong laser field increases: $m^2 \rightarrow m^2(1 + \xi^2)$ (see previous section). This means that the threshold value of x is shifted from $x = 4.8$ to

$$x_{eff} = 4.8(1 + \xi^2). \quad (1.3.13)$$

For example, for the maximum TESLA energy $2E_0 = 800 \text{ GeV}$ and $\lambda = 1.06 \mu\text{m}$ from (1.3.2) $x = 7.17$. For estimation of the e^+e^- production one can use Fig. 1.3.7 where all x values are multiplied by a factor of $1 + \xi^2$. Equivalently one can take the conversion probability in Fig. 1.3.7 (dashed lines) for $7.17/(1 + \xi^2)$. For $\xi^2 = 0.4$ (which is acceptable for such x values) we get $7.17/1.4 = 5.12$. One can see that the e^+e^- creation probability for such x is negligible. To be more accurate, the values of ξ^2 vary in the laser beam, but the main contribution to the e^+e^- probability comes from regions with values of ξ^2 close to maximum. Thus a laser with $\lambda = 1.06 \mu\text{m}$ can be used at all TESLA energies. This is confirmed by simulation (Section 1.4.5)

1.3.1.4 Low energy electrons in multiple compton scattering

For the removal of the disrupted electrons it is important to know the values of the maximum disruption angle and minimum energy of the electrons.

The disruption angles are created during beam collisions at the IP. Electrons with lower energies have larger disruption angles. The simulation code (to be described in the next section) deals with about 5000 (initial) macro-particles and can not describe the tails of distributions. But, provided that the minimum energy and the energy dependence of the disruption angle are known, we can correct the value of maximum disruption angle obtained by the simulation.

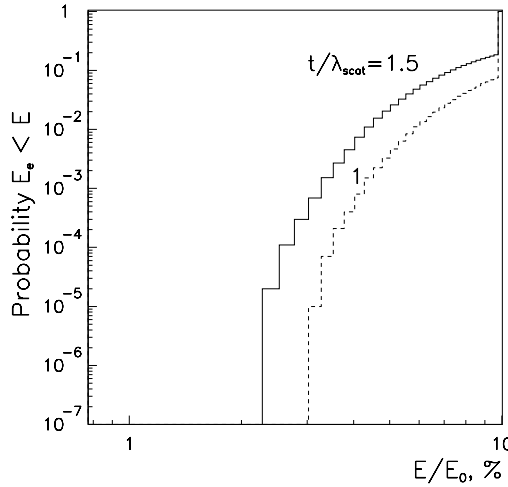


Figure 1.3.8: Probability for an electron to have an energy below E/E_0 after the conversion region.

Low energy electrons are produced at the conversion region due to multiple Compton scattering [4]. Fig. 1.3.8 [19] shows the probability that an electron which has passed the conversion region has an energy below E/E_0 . The two curves were obtained by simulation of 10^5 electrons passing the conversion region with a laser target thickness of 1 and 1.5 of the Compton collision length (at $x = 4.8$). Extrapolating these curves (by tangent line) to the probability 10^{-7} we can obtain the minimum electron energy corresponding to this probability: 2.5% and 1.7% of E_0 for $t/\lambda_{scat} = 1$ and 1.5 respectively. The ratio of the total energy of all these electrons to the beam energy is about $2 \cdot 10^{-9}$. This is a sufficiently low fraction compared with other backgrounds (see Section 1.5). We conclude that the minimum energy of electrons after the conversion region is about 2% of the initial energy, in agreement with the analytical estimate [4].

The minimum energy of electrons after n Compton collisions $E_{min} = E_0/(nx + 1) \approx E_0/nx$ [2]. The last approximation is done because the tails correspond to $n > 10$ [4]. After 1–2 collisions the Compton cross section approaches the Thompson one. This, together with the simulation result gives the scaling for the minimum energy as a function of the x and the thickness of the laser target in units of the collision length

(for electrons with the initial energy)

$$E_{min} \approx 6 \frac{\sigma_c(x)/\sigma_c(4.8)}{(\omega_0[\text{eV}]/1.25)(t/\lambda_{scat})} \text{ GeV.} \quad (1.3.14)$$

The results of this section will be used for calculation of the disruption angle (Section 1.4.2.5).

1.3.1.5 Other processes in the conversion region

Let us enumerate some other processes in the conversion region which are not dominant but nevertheless should be taken into account.

1. *Nonlinear e^+e^- pair creation $\gamma + n\gamma_0 \rightarrow e^+e^-$* below the single photon threshold $x = 4.8$ (see [171, 172, 173] and references therein). The probability of this process is not small and should be taken into account when the beam removal is considered.
2. *Variation of laser polarisation in the laser wave* [176]. It is well known that an electromagnetic field can be regarded as an anisotropic medium [170]. Strong laser fields also have such properties. As a result, the polarisation of high energy photons produced in the Compton scattering may be changed during the propagation through the polarised laser target. This effect is large only at $x \approx 4.8$ (the threshold for e^+e^- production). Note, that in the most important case, $2P_e\lambda_e = -1$, the polarisation of high energy circularly polarised photons propagating in the circularly polarised laser wave does not change. It also does not change for linearly polarised high energy photons propagating in a linearly polarised laser wave because they have the same direction.

In principle, using two adjacent conversion regions one can first produce circularly polarised photons (using a circularly polarised laser) and then change the circular polarisation to the linear one using a linearly polarised laser [177, 178]. However, it does not appear to be technically feasible and moreover the quality will be worse than in the ideal case due to a strong dependence of the rotation angle on the photon energy and the additional $e \rightarrow \gamma$ conversions on the second laser bunch.

A similar effect also exists at the interaction region of photon colliders (Section 1.4.2), the beam field influences the photon polarisation [177, 178].

3. *Variation of polarisation of unscattered electron* [179]. Compton scattering changes the electron polarisation. Complete formulae for the polarisation of the final electrons in the case of linear Compton scattering have been obtained in [180], for the nonlinear case in [181, 174]. However, additional effects have to be taken into account when simulating multiple Compton scattering.

Let us first consider a simple example: an unpolarised electron beam collides with a circularly polarised laser pulse. Some electrons pass this target without

Compton scattering. Their polarisation is changed, since the cross section of the Compton scattering depends on the product $P_c \lambda_e$ and the unscattered electron beam already contains unequal number of electrons with forward and backward helicities. When considering the multiple Compton scattering, this effect should be taken into account.

General formulae for this effect have been obtained in [179], where the variation in polarisation of the unscattered electrons was considered to be the result of the interference of the incoming electron wave with the wave scattered at zero angle.

1.3.2 The choice of laser parameters

For the $e \rightarrow \gamma$ conversion the following laser characteristics are important: wavelength, flash energy, duration, optimum focusing. The problem of optimum wavelength was considered in Section 1.3.1.3. The other items are considered below.

1.3.2.1 Conversion probability, laser flash energy

For the calculation of the conversion efficiency it is useful to remember the correspondence between the parameters of the electron and laser beams. The emittance of the Gaussian laser beam with diffraction limited divergence is $\epsilon_{x,y} = \lambda/4\pi$. The “beta-function” at a laser focus $\beta \equiv Z_R$, where Z_R is known as the Rayleigh length in optics literature.

The r.m.s. transverse radius of a laser near the conversion region depends on the distance z to the focus (along the beam) as [2]

$$\sigma_{L,r}(z) = \sigma_{L,r}(0) \sqrt{1 + z^2/Z_R^2}, \quad (1.3.15)$$

where the r.m.s. radius at the focus

$$a_\gamma \equiv \sigma_{L,r}(0) = \sqrt{\frac{\lambda Z_R}{2\pi}}. \quad (1.3.16)$$

We see that the effective length of the conversion region is about $2Z_R$. The r.m.s. beam sizes on x, y projections $\sigma_{L,i}(z) = \sigma_{L,r}(z)/\sqrt{2}$.

The r.m.s. angular divergence of the laser light in the focal point

$$\sigma_{L,x'} = \frac{\lambda}{4\pi\sigma_{L,x}} = \sqrt{\frac{\lambda}{4\pi Z_R}}. \quad (1.3.17)$$

The density of laser photons in a Gaussian laser beam

$$n_\gamma = \frac{A}{\pi\sigma_{L,r}^2(z)\omega_0} \exp(-r^2/\sigma_{L,r}^2(z)) F_L(z + ct), \quad (1.3.18)$$

$$\int F_L(z)dz = 1,$$

where A is the laser flash energy and the function $F_L(z)$ describes the longitudinal distribution (can be Gaussian as well).

Neglecting multiple scattering, the dependence of the conversion coefficient on the laser flash energy A can be written as

$$k = N_\gamma/N_e \approx 1 - \exp(-A/A_0), \quad (1.3.19)$$

where A_0 is the laser flash energy for which the thickness of the laser target is equal to one Compton collision length. The value of A_0 can be roughly estimated from the collision probability $p \approx n_\gamma \sigma_c l = 1$, where $n_\gamma \approx A_0/(\pi \omega_0 a_\gamma^2 l_\gamma)$, σ_c is the Compton cross section ($\sigma_c = 1.8 \cdot 10^{-25} \text{ cm}^2$ at $x = 4.8$), l is the length of the region with a high photon density, which is equal to $2Z_R$ at $Z_R \ll \sigma_{L,z} \approx \sigma_z$ (σ_z is the r.m.s. electron bunch length). This gives

$$A_0 \approx \frac{\pi \hbar c \sigma_z}{\sigma_c} \approx 5 \sigma_z [\text{mm}] \text{ J for } x = 4.8. \quad (1.3.20)$$

Note that the required flash energy decreases when the Rayleigh length is reduced to σ_z , and it hardly changes with further decreasing of Z_R . This is because the density of photons grows but the length having a high density decreases and as a result the Compton scattering probability is almost constant. It is not helpful to make the radius of the laser beam at the focus smaller than $\sigma_{L,x} \approx \sqrt{\lambda \sigma_z / 4\pi}$, which may be much larger than the transverse electron bunch size in the conversion region.

From (1.3.20) one can see that the flash energy A_0 is proportional to the electron bunch length and for TESLA ($\sigma_z = 0.3 \text{ mm}$) it is about 1.5 J.

More precise calculations of the conversion probability in head-on collision of an electron with a Gaussian laser beam can be found elsewhere [2, 4, 5]. However, this is not a complete picture, one should also take into account the following effects:

- *Nonlinear effects in Compton scattering.* In the laser focus the value of the parameter ξ^2 (Section 1.3.1.2) is given by

$$\xi^2 = \frac{4r_e \lambda A}{(2\pi)^{3/2} \sigma_{L,z} m c^2 Z_R}, \quad (1.3.21)$$

this follows from eqs (1.3.9,1.3.18). For example, for $A = 2 \text{ J}$, $\lambda = 1.06 \mu\text{m}$ and $\sigma_{L,z} = Z_R = \sigma_z = 0.3 \text{ mm}$, we get $\xi^2 \approx 0.2$. This is still acceptable, but for shorter bunches nonlinear effects will determine the laser flash energy.

- *Collision angle.* A maximum conversion probability for a fixed laser flash energy can be obtained in a head-on collision of the laser light with the electron beam. This variant was considered in the TESLA Conceptual Design [19]. In this case

focusing mirrors should have holes for the incoming and outgoing electron beams. From the technical point of view it is easier to put all laser optics outside the electron beams. In this case, the required laser flash energy is larger by a factor of 2 – 2.5, but on the other hand it is much simpler and this opens a way for a multi-pass laser system, such as an external optical cavity (Section 1.5.1). Below we assume that the laser optics is situated outside the electron beams.

- *Transverse size of the electron beam.* For the removal of disrupted beams at photon colliders it is necessary to use a crab-crossing beam collision scheme (see Fig. 1.1.1 and Section 1.4.1). In this scheme the electron beam is tilted relative to its direction of motion by an angle $\alpha_c/2 \approx 15$ mrad. Such a method allows to collide beams at some collision angle (to make easier the beam removal) without decrease of the luminosity.

Due to the tilt the electron beam at the laser focus has an effective size $\sigma_x = \sigma_z \alpha_c/2$ which is $4.5 \mu\text{m}$ for TESLA. This should be compared with the laser spot size (eq. 1.3.16), for $Z_R = \sigma_z = 0.3$ mm and $\lambda = 1.06 \mu\text{m}$ of $\sigma_{L,x} = \sqrt{\lambda Z_R/4\pi} \approx 5 \mu\text{m}$. The sizes are comparable, which leads to some increase of the laser flash energy.

The result of the simulation [21] of k^2 (k is the conversion coefficient) for the electron bunch length $\sigma_z = 0.3$ mm (TESLA project), $\lambda = 1.06 \mu\text{m}$, $x = 4.8$ as a function of the Rayleigh length Z_R for various flash energies and values of the parameter ξ^2 are shown in Fig. 1.3.9.

It was assumed that the angle between the laser optical axis and the electron beam line is $\theta = 2\sigma_{L,x'}$, where $\sigma_{L,x'}$ is the angular divergence of the laser beam in the conversion region (eq. 1.3.17), and the mirror system is situated outside the electron beam trajectories. One conversion length corresponds to $k^2 = (1 - e^{-1})^2 \approx 0.4$. One can see that $k^2 = 0.4$ at $\xi^2 = 0.3$ can be achieved with the minimum flash energy $A = 5$ J. The optimum value of Z_R is about 0.35 mm.

The r.m.s. duration of the laser pulse can be found from (1.3.21), for the considered case $\sigma_{L,z} = 0.44$ mm or 1.5 ps.

Above we have considered the requirements for the laser at $\lambda = 1.06 \mu\text{m}$, $x \approx 4.8$, which is the case for a $2E_0 = 500$ GeV collider. The required flash energy is about 5 J for $\xi^2 = 0.3$. Next we discuss what changes when the electron beam energy is decreased or increased?

When we decrease the energy to $E_0 = 100$ GeV, keeping the laser wavelength constant, the Compton cross section increases from $\sigma_C/\sigma_0 = 0.7$ ($x = 4.8$) to 1.24 ($x = 1.8$). This case corresponds to $W_{\gamma\gamma,m} \approx 130$ GeV. Calculations similar to the one presented in Fig. 1.3.9 show that for this case $k^2 = 0.4$ can be obtained with $A \approx 3.8$ J at $\xi^2 = 0.1$ (and $Z_r \approx 0.6$ mm) or with $A \approx 2.5$ J at $\xi^2 = 0.3$ (and $Z_r \approx 0.3$ mm). So, for the study of the low mass Higgs one needs a laser with somewhat lower flash energy and values of ξ^2 can be lower than that at $x \approx 4.8$.

Another variant for study of $W_{\gamma\gamma,m} \approx 130$ GeV involves decreasing the electron beam energy keeping $x = \text{const} = 4.8$. This requires $\lambda = 1.06/3 \mu\text{m}$. Calculations

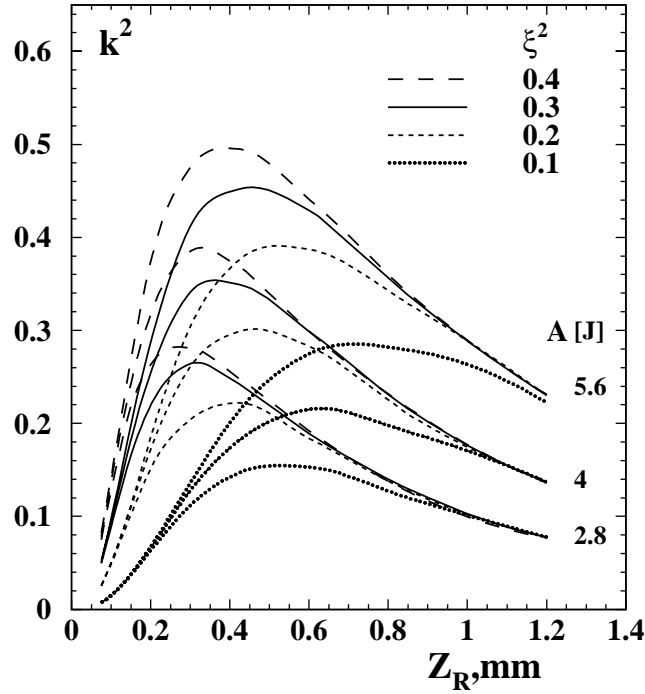


Figure 1.3.9: Square of the conversion probability (proportional to the $\gamma\gamma$ luminosity) as a function of the Rayleigh length for various parameters ξ^2 and laser flash energies; $x = 4.8$, $\lambda = 1.06 \mu\text{m}$ are assumed. The mirror system is situated outside the electron beam trajectories (collision angle $\theta = 2\sigma_{L,x'}$). The crab crossing angle 30 mrad is taken into account. See also the text.

show that using a 5 J laser flash one can obtain only $k^2 = 0.35$ at $\xi^2 = 0.3$. The conversion coefficient is lower than that for $x = 4.8$ and $\lambda = 1.06$. This result is quite surprising, because for the shorter wavelength the nonlinear effects are less important and according to (1.3.20) the minimum flash energy does not depend on the wavelength. Such behaviour is connected with the effective transverse electron bunch size due to the crab-crossing (see above) which restricts the minimum laser spot size, and to the fact that for shorter wavelength the energy of each photon is larger.

Comparing the two methods of reaching the low mass Higgs region we come to the conclusion that it is easier to use a $\lambda = \text{const} = 1.06 \mu\text{m}$ laser due to the lower flash energy, lower ξ^2 and the fact that this is the region of powerful solid state lasers (production of the second or third harmonics require 2–3 times larger initial flash energy). There are also some advantages for physics, namely, a high degree of linear polarisation.

In Section 1.3.1.3 it was shown that it is possible to work with a $\lambda = 1.06 \mu\text{m}$ laser even at the maximum TESLA energy of $2E_0 = 800 \text{ GeV}$, in spite of a value of $x = 7.17$. This is due to the nonlinear effects which increase the threshold for e^+e^- pair production from $x = 4.8$ to $x = 4.8(1 + \xi^2)$. The Compton cross section for the value of $x = 7.17$ is lower than at $x = 4.8$ by a factor of 1.32. Nevertheless, with 5 J flash energy and $\xi^2 = 0.4$, one can obtain $k^2 \approx 0.35$.

So, we can conclude that a laser with $\lambda \approx 1 \mu\text{m}$ is suitable for all TESLA energies.

1.3.2.2 Summary of requirements to the laser

From the above considerations it follows that to obtain a conversion probability of $k \approx 63\%$ at all TESLA energies a laser with the following parameters is required:

Flash energy	$\approx 5 \text{ J}$
Duration	$\tau(\text{rms}) \approx 1.5 \text{ ps}$
Repetition rate	TESLA collision rate, $\approx 14 \text{ kHz}$
Average power	$\approx 140 \text{ kW}$ (for one pass collision)
Wavelength	$\approx 1 \mu\text{m}$ (for all energies).

1.4 The Interaction Region

1.4.1 The collision scheme, crab-crossing

The basic scheme for photon colliders is shown in Fig. 1.1.1 (Section 1.1). The distance between the conversion point (CP) and the IP, b , is chosen from the relation $b \approx \gamma\sigma_y$, so that the size of the photon beam at the IP has equal contributions from the electron beam size and the angular spread from Compton scattering. At TESLA $\sigma_y \approx 4 \text{ nm}$ gives $b \approx 2 \text{ mm}$ at $2E_0 = 500 \text{ GeV}$. Larger b values lead to a decrease of the $\gamma\gamma$ luminosity, for smaller b values the low-energy photons give a larger contribution to the luminosity (which is not useful for the experiment but causes additional backgrounds).

In the TESLA Conceptual Design four years ago two schemes were considered: with magnetic deflection and without. At that time σ_y was assumed to be about 16 nm , and the distance $b \approx 1 \text{ cm}$ was sufficient for deflection of the electron beam from the IP using a small magnet with $B \approx 5 \text{ kG}$. With the new TESLA parameters with b about 5 times smaller this option is practically impossible (may be only for a special experiment with reduced luminosity). We now consider only one scheme: without magnetic deflection, when all particles after the conversion region travel to the IP producing a mixture of $\gamma\gamma$, γe , e^-e^- collisions. The beam repulsion leads to some reduction of the γe luminosity and a considerable suppression of the e^-e^- luminosity.

There are two additional constraints on the CP-IP distance. It should be larger than the half-length of the conversion region (which is about $Z_R \approx 0.35 \text{ mm}$ (Section 1.3)), and larger than about $2-3 \sigma_z$ (σ_z is the electron bunch length) because the $e \rightarrow \gamma$ conversion should take place before the beginning of electron beam repulsion. So, the minimum distance b for the TESLA is about 1 mm .

The removal of the disrupted beams can best be done using the crab-crossing scheme [182], Fig. 1.1.1, which is foreseen in the NLC and JLC projects for e^+e^- collisions. In this scheme the electron bunches are tilted (using an RF cavity) with respect to the direction of the beam motion, and the luminosity is then the same as for head-on collisions. Due to the collision angle the outgoing disrupted beams travel outside the final quads. The value of the crab-crossing angle is determined by the

disruption angles (see the next section) and by the final quad design (diameter of the quad and its distance from the IP). In the present TESLA design $\alpha_c = 34$ mrad.

1.4.2 Collision effects in $\gamma\gamma$, γe collisions

The luminosity in $\gamma\gamma, \gamma e$ collisions may be limited by several factors:

- geometric luminosity of the electron beams;
- collision effects (coherent pair creation, beamstrahlung, beam displacement);
- beam collision induced background (large disruption angles of soft particles);
- luminosity induced background (hadron production, e^+e^- pair production).

For optimisation of a photon collider it is useful to know qualitatively the main dependences. In this section we will consider collision effects which restrict the $\gamma\gamma$, γe luminosity.

Naively, at first sight, one may think that there are no collision effects in $\gamma\gamma$ and γe collisions because at least one of the beams is neutral. This is not correct because during the beam collision electrons and photons are influenced by the field of the opposite electron beam, which leads to the following effects [4, 5]:

$\gamma\gamma$ collisions: conversion of photons into e^+e^- pairs (coherent pair creation).

γe collisions: coherent pair creation; beamstrahlung; beam displacement.

Below we consider the general features of these phenomena and then present the results of simulations where all main effects are included.

1.4.2.1 Coherent pair creation

The probability of pair creation per unit length by a photon with the energy ω in the magnetic field B ($|B| + |E|$ for our case) is [4, 183]

$$\mu(\kappa) = \frac{\alpha^2 B}{r_e B_0} T(\kappa), \quad \kappa = \frac{\omega}{mc^2} \frac{B}{B_0}, \quad B_0 = \frac{\alpha e}{r_e^2} = 4.4 \cdot 10^{13} \text{ G}, \quad (1.4.1)$$

where B_0 is the the critical field, the function $T(\kappa) \approx 0.16\kappa^{-1} K_{1/3}^2(4/3\kappa)$. At $\kappa < 1$, it is small, $T \approx 0.23 \exp(-8/3\kappa)$, and $T \approx 0.1$ at $\kappa = 3-10$.

In our case, $\omega \approx 0.8E_0$, therefore one can put $\kappa \approx 0.8\Upsilon \equiv \gamma B/B_0$.

Coherent pair creation is exponentially suppressed for $\Upsilon < 1$, but for $\Upsilon > 1$ most high energy photons can convert to e^+e^- pairs during the beam collision. The detailed analyses of these phenomena at photon colliders are presented in [4, 5, 184].

Without disruption the beam field $B \approx eN/(\sigma_x\sigma_z)$ (we assume that $\sigma_x > \sigma_y$). Therefore, coherent e^+e^- creation restricts the minimum horizontal beam size.

For example, for $N = 2 \times 10^{10}$, $\sigma_x = 50$ nm, $\sigma_z = 0.3$ mm, $E_0 = 500$ GeV, we obtain $\kappa_{av} \approx 1.2$, $T \approx 0.01$ and the $\gamma \rightarrow e^+e^-$ conversion probability $p \approx \mu\sigma_z = 0.06$ (rather small). For $\sigma_x = 10$ nm it would be about 0.5 (40% loss of the $\gamma\gamma$ luminosity).

However, it turns out that at TESLA energies and beam parameters N, σ_z the coherent pair creation is further suppressed due to the repulsion of the electron beams [185, 184]. Due to the repulsion, the characteristic size of the disrupted beam $r \approx \sqrt{\sigma_z r_e N} / 8\gamma$, would be about 45 nm for the previous example. Therefore, with decreasing σ_x the field at the IP increases to a maximum value $B \approx 2eN / (r\sigma_z)$. The corresponding parameter $\Upsilon \propto (E_0/\sigma_z)^{3/2} N^{1/2}$. As a result, at a sufficiently low beam energy and long beams the field may be below the threshold for coherent pair creation even for zero initial transverse beam sizes. This fact allows, in principle, very high $\gamma\gamma$ luminosity to be reached. This interesting effect is confirmed by the simulation [184] (Section 1.4.4).

One comment on the previous paragraph: although the beam disruption helps to suppress the coherent pair creation and to keep the $\gamma\gamma$ luminosity close to the geometric one, there is, nevertheless, some restriction on the field strength due to background caused by coherent pair creation. One can show that the minimum energy of electrons (at the level of probability of $W \approx 10^{-7}$) in coherent pair creation is about $E_{min}/\omega \approx 0.05/\kappa$. Therefore at $\kappa > 2$ this energy is lower than the minimum energy of electrons after multiple Compton scattering and the resulting disruption angles will be determined by the coherent pair creation.

Electrons of similarly low energies are also produced in hard beamstrahlung with approximately similar probability. However, in the TESLA case, beamstrahlung is less important because electrons radiate inside the disrupted beam, while in the case of coherent pair creation the head of the Compton photon bunch travels in the field of the undisturbed oncoming electron beam and passes the region with the maximum (undisturbed) beam field. Simulation results for luminosity and disruption angles taking of all these effects into account are presented in Section 1.4.4.

1.4.2.2 Beamstrahlung

The physics of beamstrahlung (radiation during beam collisions) at linear e^+e^- colliders is very well understood [186, 187]. Consequences of beamstrahlung for $\gamma\gamma$, γe colliders have been considered in [4, 5].

For $\gamma\gamma$ collisions beamstrahlung is not important. However, beamstrahlung photons collide with opposing Compton and beamstrahlung photons, increasing the total $\gamma\gamma$ luminosity by a significant factor (mainly in the the region of rather low invariant masses, below the high energy luminosity peak.)

In the γe collisions beamstrahlung leads to a decrease of the electron energy and, as a result, the γe luminosity in the high energy peak also decreases. In addition, the beamstrahlung photon contribution to the γe luminosity considerably worsens the γe luminosity spectrum.

1.4.2.3 Beam–beam repulsion

During the collision opposing beams either attract or repulse each other. In e^+e^- collisions this effect leads to some increase of the luminosity (the pinch effect), while in e^-e^- collisions the attainable luminosity is reduced [188, 189, 190].

Photon colliders are based on e^-e^- beams. For $\gamma\gamma$ collisions the effects of the beam repulsion are only positive: the coherent pair creation is suppressed; the beamstrahlung photons emitted by the deflected electrons have a smaller probability of colliding with the Compton or beamstrahlung photons from the opposite electron beam; γe background is smaller due to the relative shift of the electron beams.

For γe collisions the effect of beam repulsion is negative. It leads to a displacement of the electron beam, and hence to a decrease of the γe luminosity.

The beam repulsion also leads to a considerable decrease of the e^-e^- “background” luminosity.

Beam–beam deflection is very useful for the diagnostics of beam collisions and for the stabilisation of the luminosity both at e^+e^- and photon photon colliders.

1.4.2.4 Depolarisation

Depolarisation effects are not included in our simulation code, therefore we give an estimation of these effects [4].

Depolarisation of electrons

When an electron is bent by the angle θ , its spin rotates, relative to its trajectory, by the angle [170]

$$\theta' = \frac{\mu'}{\mu_0} \gamma \theta \approx \frac{\alpha \gamma}{2\pi} \theta, \quad (1.4.2)$$

where μ_0 and μ' are the normal and the anomalous magnetic moments of the electron, $\alpha = e^2/\hbar c = 1/137$.

In the absence of disruption, the beam field

$$B \approx \frac{eN}{\sigma_z \sigma_x}. \quad (1.4.3)$$

The bending angle during beam collisions (on the length σ_z) is $\theta \approx eB\sigma_z/E_0 = r_e N/(\sigma_x \gamma)$. This gives

$$\theta' \approx \frac{\alpha r_e N}{2\pi \sigma_x}. \quad (1.4.4)$$

For example, for TESLA with $N = 2 \times 10^{10}$, $\sigma_x \approx 100$ nm, we get $\theta' = 0.65$. The corresponding polarisation (for $\lambda_{e,0} = 1$) is $\lambda_e \approx \cos \theta' \approx 0.8$. The effect is not small.

Let us now consider the same case with beam repulsion taken into account. In γe collisions, the electrons collide with the high energy photons until their vertical

displacement is smaller than σ_y (this is the case with the high energy photons for $b = \gamma\sigma_z$ (see Section 1.4.1)). The deflection angles are derived from $\rho\theta^2/2 \approx \sigma_y$ and $\rho \approx \gamma mc^2/eB$. This gives

$$\theta' \approx \frac{\alpha\gamma}{2\pi} \sqrt{\frac{2\sigma_y r_e N}{\sigma_x \sigma_z \gamma}}. \quad (1.4.5)$$

For the previous set of parameters and $\sigma_y = 4 \text{ nm}$, $2E_0 = 500 \text{ GeV}$, we obtain $\theta' = 0.1$ and $\lambda_e \approx \cos \theta' \approx 0.995$.

Although this estimate is rough, one can see that a factor of 2–3 will not change the conclusion that the Depolarisation of electrons in γe collisions is negligible.

Depolarisation of photons

It is well known that a strong electromagnetic field can be treated as an anisotropic medium with some refraction index n [170]. In fact, the conversion of photons to e^+e^- pairs (absorption) considered above is the manifestation of the imaginary part of the refraction index. The values n are different for photons with linear polarisation parallel and perpendicular to the field direction. As a result, the polarisation of photons travelling in this field can change. In Section 1.3.1.4 we mentioned already one such effect in the conversion region. Here we will consider the influence of the beam field on the polarisation of the high energy photons.

This problem was considered in detail in [177, 178]. The beam field can transform the circular photon polarisation into a linear polarisation and vice versa. The degree of Depolarisation as a function of E_γ/σ_z is shown in Fig. 1.4.1. Instead of the field strength each curve corresponds to a certain value of the coherent pair creation probability $W_{e^+e^-}$ which is defined in units of collision lengths. In this case, consideration of the beam disruption is not necessary, as it is included in the e^+e^- conversion probability which is kept under control at photon colliders.

For example, for TESLA beams $E_\gamma/\sigma_z \approx 10 \text{ TeV/cm}$. We see that even for 50% e^+e^- conversion probability the decrease of the photon polarisation is only about 1%. Moreover, as was mentioned before, due to the beam repulsion the coherent pair creation probability at TESLA is small, therefore the Depolarisation will be even smaller. Hence, the Depolarisation of photons is negligibly small.

1.4.2.5 Disruption angle

The maximum disruption angle is an important issue for photon colliders, it determines the value of the crab-crossing angle.

One source of large angle particles are low energy electrons from the conversion region. The minimum energy is about $0.02E_0$ (section 1.3.1.4). The second source of soft particles is hard beamstrahlung and coherent pair creation with the minimum energy of about $0.05/\Upsilon$. Particles from these sources can carry very large energies, therefore the crab-crossing angle should be sufficient for removal of all these particles from the detector without hitting the quads or detector components.

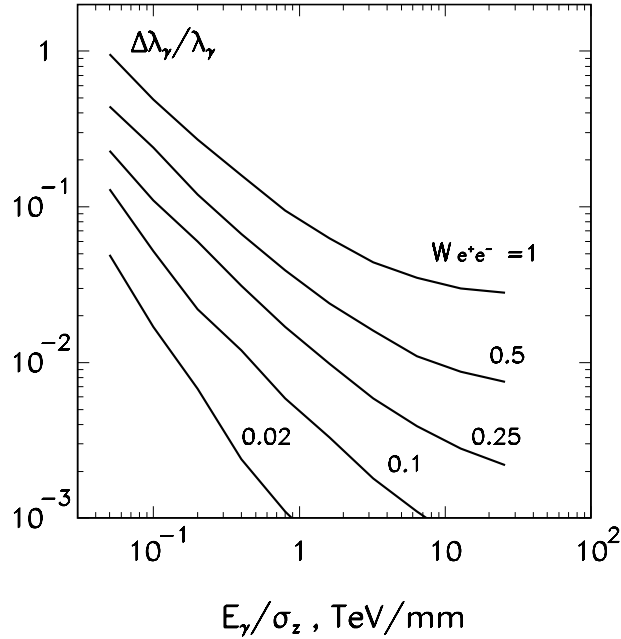


Figure 1.4.1: *Decrease in photon helicity during beam collisions for various beam parameters and probabilities of coherent pair creation $W_{e^+e^-}$ [177, 178]. See comments in the text.*

Another source of even lower energy particles are e^+e^- pairs produced incoherently in collisions of individual particles at the IP. This unavoidable background is proportional to the luminosity. A large fraction of these particles (with large energy and small angles) can also escape from the detector through the exit hole for disrupted beams. This source of background carries much less power than enumerated in the previous paragraph and can be handled without crab-crossing, as in the e^+e^- TESLA option.

The deflection angle for soft electrons in the field of the opposite beam is given approximately by [4, 19]

$$\vartheta_d \approx 0.7 \left(\frac{4\pi r_e N}{\sigma_z \gamma_{min}} \right)^{1/2} \approx 9 \left(\frac{N/10^{10}}{\sigma_z [\text{mm}] E_{min} [\text{GeV}]} \right)^{1/2} \text{ mrad.} \quad (1.4.6)$$

In the first approximation the deflection angle for very soft electrons does not depend on the transverse beam size. The coefficient 0.7 here was found by tracking particles in the field of the beam with a Gaussian longitudinal distribution for the TESLA range of parameters. For example: at $2E_0 = 500$ GeV, $E_{min}/E_0 = 0.02$ (Compton, $x = 4.8$), $N = 2 \times 10^{10}$, $\sigma_z = 0.3$ mm we get $\vartheta_d \approx 10.4$ mrad. This estimate will help us to understand results of the simulation.

The coefficient 0.7 in (1.4.6) corresponds to the collision of a low energy electron with the electron beam. If a low energy electron is produced near the centre of the opposing beam then it is more accurate to use the coefficient 1.2 instead of 0.7.

1.4.3 The simulation code

As we have seen, the picture of beam collisions at photon colliders is complicated and the best way to obtain final results is a simulation. In the present study we used the code described in [5].

It serves for simulation of e^+e^- , e^-e^- , γe , $\gamma\gamma$ beam collisions in linear colliders and the present version takes into account the following processes:

1. *Compton scattering in the conversion region.* At present we use the formulae for linear Compton scattering, including all polarisation effects. Nonlinear effects are considered approximately by smearing x ($x \rightarrow x/(1 + \xi^2)$) according to the variable density of laser photons in the conversion region.
2. e^+e^- pair creation in the conversion region for $x > 4.8$.
3. *Deflection by magnetic fields and synchrotron radiation* in the region between the CP and IP, due to special magnets or the solenoidal detector field (it has an effect due to the crab-crossing angle).
4. *Electromagnetic forces, coherent pair creation and beamstrahlung* during beam collisions at the IP.
5. *Incoherent e^+e^- creation* in $\gamma\gamma$, γe , e^+e^- collisions.

The initial electron beams are described by about 3000 macro-particles (m.p.) which have a shape of flat rectangular bars with the horizontal size equal to $0.4\sigma_x$ and zero vertical size. In the longitudinal direction the electron bunch has a Gaussian shape ($\pm 3\sigma$) and is cut into about 150 slices. It is assumed that the macro-particles have only a transverse field and influence macro-particles of the opposite bunch which have the same z -coordinate (this coordinate changes by steps). At initial positions macro-particles move to the collision region according to the beam emittances and beta functions. During the simulation new macro-particles (photons, electrons and positrons) are produced which are included in the calculation in the same way as the initial macro-particles.

Low energy particles can get too large a deflection during one step, therefore the maximum deflection angle is restricted for one step so the resulting angles will be simulated correctly. This occurs because the repulsion length for the soft electron is much shorter than the bunch length and the charge distribution (the beam field) in the next steps is approximately the same.

The code was used for simulation of photon colliders in NLC Zero Design and the TESLA Conceptual Design. The results are in agreement [191] with the code CAIN [192] written later for the same purpose.

1.4.4 Luminosity limitations due to beam collision effects

Beam collision effects in e^+e^- and $\gamma\gamma$, γe collisions are different. In particular, in $\gamma\gamma$ collisions there are no beamstrahlung or beam instabilities. Therefore, it was of

interest to study limitations of the luminosity at the TESLA photon collider due to beam collision effects. The simulation [9, 21] was done for the TESLA beams and the horizontal size of the electron beams was varied.

1.4.4.1 Ultimate luminosities

Fig. 1.4.2 shows the dependence of the $\gamma\gamma$ (solid curves) and the γe (dashed curves) luminosities on the horizontal beam size for several energies. The horizontal beam

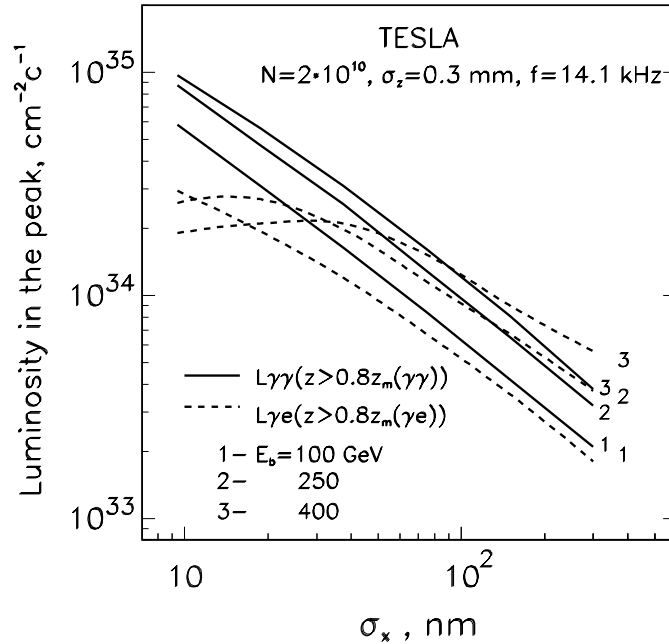


Figure 1.4.2: Dependence of $\gamma\gamma$ and γe luminosities in the high energy peak on the horizontal beam size for TESLA at various energies. See also comments in the text.

size was varied by changing the horizontal beam emittance keeping the horizontal beta function at the IP constant and equal to 1.5 mm.

One can see that all curves for the $\gamma\gamma$ luminosity follow their natural behaviour: $L \propto 1/\sigma_x$ (values of $\sigma_x < 10$ nm are not considered because too small horizontal sizes may introduce problems with the crab-crossing scheme). Note that while in e^+e^- collisions $\sigma_x \approx 500$ nm, in $\gamma\gamma$ collisions the attainable σ_x with the planned injector (damping ring) is about 100 nm (Section 1.4.5).

In γe collisions the luminosity at small σ_x is lower than follows from the geometric scaling due to beamstrahlung and displacement of the electron beam during the beam collision. So, we can conclude that for $\gamma\gamma$ collisions at TESLA one can use beams with a horizontal beam size down to 10 nm (maybe even smaller) which is much smaller than that in e^+e^- collisions. Note, that the vertical beam size could also be additionally decreased by a factor of two (for even smaller electron beam size the effective photon

beam size will be determined by the Compton scattering contribution). As a result, the $\gamma\gamma$ luminosity in the high energy peak can be, in principle, several times higher than the e^+e^- luminosity (Table 1.1.1).

Production of the polarised electron beams with emittances lower than those possible with damping rings is a challenging problem. There is one method, laser cooling [193, 194, 195] which allows, in principle, the required emittances to be reached. However this method requires a laser power one order of magnitude higher than is needed for $e \rightarrow \gamma$ conversion. This is not excluded, but since many years of R&D would be required, it should be considered as a second stage of the photon collider, maybe for a Higgs factory.

1.4.4.2 Disruption angles

As it was mentioned before, for small beam sizes one can expect the production of low energy particles in the processes of coherent pair creation and beamstrahlung. The luminosity may not be affected, but there is the problem with background due to the deflection of the low energy particles by the opposing electron beam. Fig. 1.4.3 shows

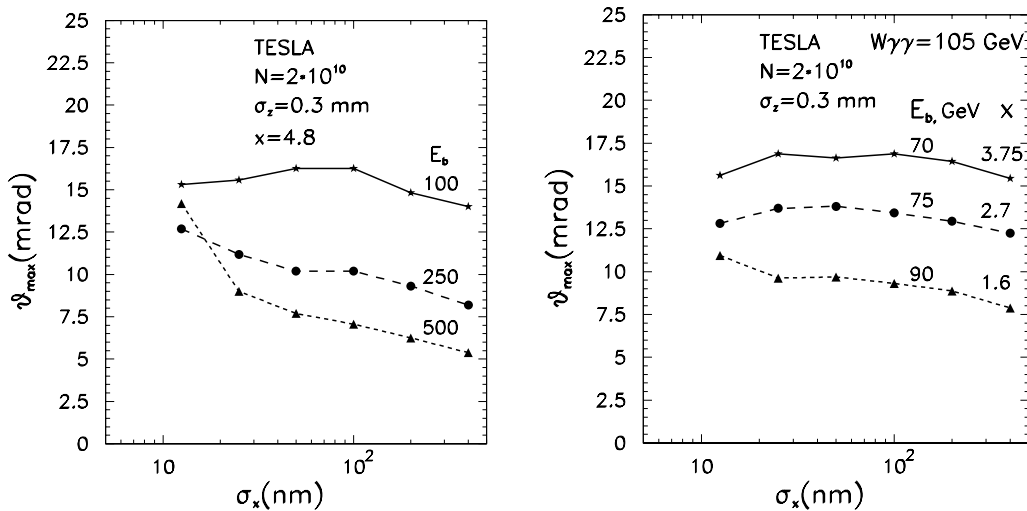


Figure 1.4.3: Dependence of the maximum disruption angle on the horizontal beam size for TESLA at various energies. Left figure for $x = 4.8$ and several beam energies. Right figure corresponds to the invariant mass $W_{\gamma\gamma} = 105$ GeV, x values 1.6, 2.7, 3.75 correspond to the laser wave lengths 1.06, 1.06/2, 1.06/3 μm , respectively.

the dependence of the maximum disruption angle on the horizontal beam size. In the left figure the parameter $x = 4.8$, the right figure corresponds to the c.m.s. energy of the $\gamma\gamma$ collider equal to 105 GeV. The total statistics in the simulation is about 10^5 particles, so the tails which can lead to background are not simulated. However, we know the scaling and therefore can make corrections. From the simulation we have found the angle corresponding to the probability 10^{-4} and multiplied it by a factor of

1.25. The angle shown in Fig. 1.4.3 is the angle above which the energy of background particles is less than about 10 TeV, that is less than the energy of the incoherent e^+e^- pairs (Section 1.4.7) which have larger angles and represent an unavoidable background.

In Fig. 1.4.3 (left) we see that at large σ_x the angle is smaller for higher beam energies, in agreement with (1.4.6). With decreasing σ_x the contribution of the low energy particles from coherent pair creation and beamstrahlung is seen.

Fig. 1.4.3 (right) shows that at the fixed $\gamma\gamma$ center-of-mass energy $W_{\gamma\gamma}$ the disruption angle is larger for larger x . It is easy to show that

$$\vartheta \propto \frac{x}{\sqrt{(x+1)\sigma_c(x)}}, \quad (1.4.7)$$

where the Compton cross section $\sigma_c(x)$ decreases with increasing x . This gives a factor of two difference between $x = 1.6$ and 3.75. We think that one can study the low mass Higgs with $\lambda \approx 1.06 \mu\text{m}$, i.e. with the same laser at all energies below $2E_0 = 500 \text{ GeV}$. Lower x have the advantage of a higher degree of linear polarisation (Section 1.3.1). As higher x values also have also some advantages (sharper edge) we can foresee the possibility of a frequency doubled laser. With these assumptions we conclude that the maximum disruption angle is about 14 mrad. For the laser with $\lambda \approx 1 \mu\text{m}$ 12 mrad will be sufficient. In the present design the crab-crossing angle in the second IP is 34 mrad. These values put restrictions on possible quadrupole designs.

1.4.5 $\gamma\gamma$ and γe luminosities at TESLA

1.4.5.1 Parameters of the electron beams

In this section we discuss what luminosities can be obtained with the technology presently available. It depends strongly on the emittances of the electron beams. There are two methods of production, low-emittance electron beams: damping rings and low-emittance RF-photo-guns (without damping rings). The second option is promising, but at the moment there are no such photo-guns producing polarised electron beams [196]. Polarisation of electron beams is very desirable for photon colliders (sect 1.2). So, there is only one choice now — damping rings.

Especially for a photon collider the possibility of decreasing the beam emittances at the TESLA damping ring has been studied [197] and it was found that the horizontal emittance can be reduced by a factor of 4 compared to the previous design. Now the normalised horizontal emittance is $\epsilon_{nx} = 2.5 \times 10^{-6} \text{ m}$.

The luminosity also depends on the β -functions at the interaction points: $L \propto 1/\sqrt{\beta_x\beta_y}$. The vertical β_y is usually chosen close to the bunch length σ_z (this is the design for e^+e^- collisions and can also be realized for $\gamma\gamma$ collisions). Some questions remain about the minimum horizontal β -function. For e^+e^- collisions, $\beta_x \approx 15 \text{ mm}$ which is larger than the bunch length $\sigma_z = 0.3 \text{ mm}$, because beams in e^+e^- collisions must be flat to reduce beamstrahlung. In $\gamma\gamma$ collisions, β_x could be about 1 mm (or even somewhat smaller). There are two fundamental limitations: the beam length and the Oide effects [198] (radiation in final quads). The latter is not important for the

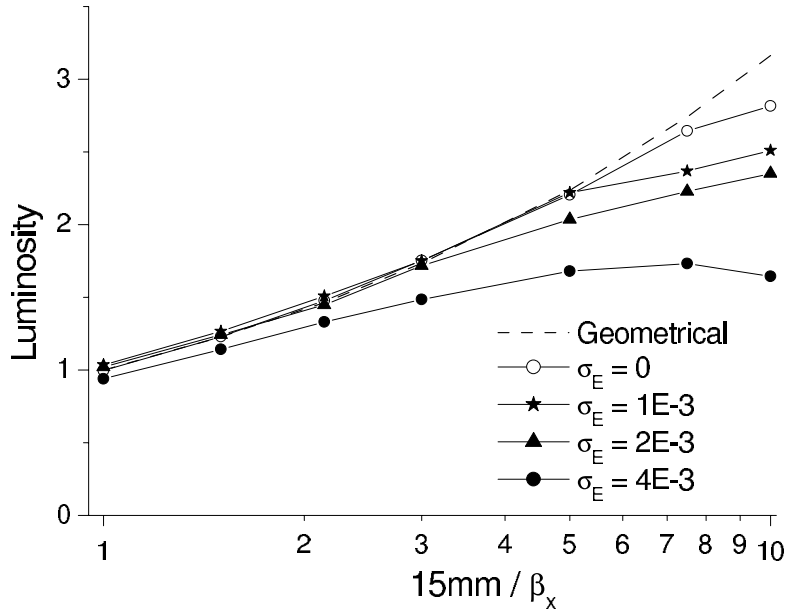


Figure 1.4.4: Dependence of the geometric e^-e^- luminosity on the horizontal β -function (SLAC design). For TESLA the relative energy spread (σ_E in the figure) is 10^{-3} .

beam parameters considered. There is also a certain problem with the angular spread of the synchrotron radiation emitted in the final quads. But, for the photon collider the crab-crossing scheme will be used and in this case there is sufficient clearance for the removal of the disrupted beams and synchrotron radiation.

Very preliminary studies of the existing scheme for the TESLA final focus have shown [199] that chromo-geometric aberrations dominate at $\beta \leq 6$ mm. However, this is not a fundamental limitation and it is very likely that after further study and optimisation a better solution will be found. At SLAC a new scheme for the final focus system has recently been proposed [200]. The first check without optimisation has shown [201] that, with the new scheme, one can obtain $\beta_x \approx 1.5$ mm with small aberrations, see Fig. 1.4.4, and further optimisation is possible. For the present study we assume $\beta_x = 1.5$ mm.

Some uncertainties remain for the operation of TESLA at low energies. For the low mass Higgs the minimum required energy is about 75 GeV. In this case TESLA should work either at reduced accelerating gradient or a bypass after about 100 GeV should be used. In the case of a bypass one can consider that the luminosity is approximately proportional to the beam energy (due to the adiabatic change of the beam emittances).

In principle, the loss of luminosity at low energies could be compensated by an increase of the repetition rate as $f \propto 1/E_0$. In this case the RF power (for the linac) is constant. However, for the present design of the TESLA damping ring, the repetition rate may be increased at most by a factor of 2. Further decrease of the damping time is possible but at additional cost (wigglers, RF-power). The factor of 2 is almost sufficient, but, unfortunately, at low gradients beam loading (RF efficiency) may be problem. Its adjustment requires the change of the coupler position, which for TESLA

is technically very difficult or even impossible.

For the present study we assume the bypass solution and use the same beam parameters (N, σ_z , normalised emittances, collision rate) for all energies, that gives $L \propto E_0$.

1.4.5.2 $\gamma\gamma, \gamma e$ luminosities, summary table

The resulting parameters of the photon collider at TESLA for $2E_0 = 200, 500$ and 800 GeV are presented in Table 1.4.1. It is assumed that the electron beams have 85% longitudinal polarisation and that the laser photons have 100% circular polarisation. The thickness of the laser target is one scattering length for $2E_0 = 500$ and 800 GeV and 1.35 scattering length for $2E_0 = 200$ GeV (the Compton cross section is larger), so that $k^2 \approx 0.4$ and 0.55 , respectively. The parameter $\xi^2 = 0.15, 0.3, 0.4$ for $2E_0 = 200, 500, 800$ GeV, as explained in Section 1.3.2. The laser wave length is $1.06 \mu\text{m}$ for all energies. The conversion point is situated at a distance $b = \gamma\sigma_y$ from the interaction point.

$2E_0$ [GeV]	200	500	800
λ_L [μm]/ x	1.06/1.8	1.06/4.5	1.06/7.2
t_L [λ_{scat}]	1.35	1	1
$N/10^{10}$	2	2	2
σ_z [mm]	0.3	0.3	0.3
$f_{\text{rep}} \times n_b$ [kHz]	14.1	14.1	14.1
$\gamma\epsilon_{x/y}/10^{-6}$ [m·rad]	2.5/0.03	2.5/0.03	2.5/0.03
$\beta_{x/y}$ [mm] at IP	1.5/0.3	1.5/0.3	1.5/0.3
$\sigma_{x/y}$ [nm]	140/6.8	88/4.3	69/3.4
b [mm]	2.6	2.1	2.7
$L_{ee}(\text{geom})$ [$10^{34} \text{ cm}^{-2}\text{s}^{-1}$]	4.8	12	19
$L_{\gamma\gamma}(z > 0.8z_{m,\gamma\gamma})$ [$10^{34} \text{ cm}^{-2}\text{s}^{-1}$]	0.43	1.1	1.7
$L_{\gamma e}(z > 0.8z_{m,\gamma e})$ [$10^{34} \text{ cm}^{-2}\text{s}^{-1}$]	0.36	0.94	1.3
$L_{e^+e^-}(z > 0.65)$ [$10^{34} \text{ cm}^{-2}\text{s}^{-1}$]	0.03	0.07	0.095

Table 1.4.1: Parameters of the $\gamma\gamma$ collider based on TESLA. two options.

As it was already mentioned in the introduction, for the same energy

$$L_{\gamma\gamma}(z > 0.8z_m) \approx \frac{1}{3}L_{e^+e^-}. \quad (1.4.8)$$

The relation (1.4.8) is valid only for the beam parameters considered. A more

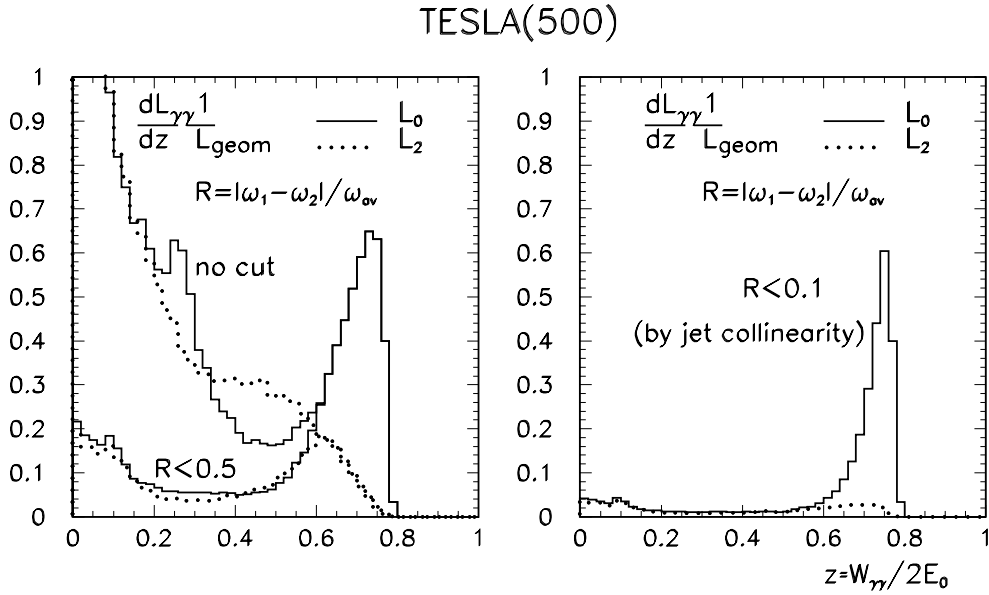


Figure 1.4.5: $\gamma\gamma$ luminosity spectra at TESLA(500) with various cuts on longitudinal momentum. Solid line for total helicity of the two photons 0 and dotted line for total helicity 2. See also Table 1.4.1.

universal relation is (for $k^2 = 0.4$)

$$L_{\gamma\gamma}(z > 0.8z_m) \approx 0.09L_{ee}(\text{geom}). \quad (1.4.9)$$

The normalised $\gamma\gamma$ luminosity spectra for $2E_0 = 500$ GeV are shown in Fig. 1.4.5 [21].

The luminosity spectrum is decomposed into two parts with the total helicity of the two photons 0 and 2. We see that in the high energy part of the luminosity spectra the photons have a high degree of polarisation. In addition to the high energy peak, there is a factor 5–8 higher luminosity at low energy. It is produced mainly by photons after multiple Compton scattering and beamstrahlung photons. These events have a large boost and can be easily distinguished from the central high energy events. Fig. 1.4.5 shows the same spectrum with an additional cut on the longitudinal momentum of the produced system, which suppresses the low energy luminosity to a low level. For two jet events ($H \rightarrow b\bar{b}$, $\tau\tau$, for example) one can restrict the longitudinal momentum using the acollinearity angle between the jets. The resulting energy spread of collisions can be about 7.5%, see Fig. 1.4.5 (right).

The high energy part of the $\gamma\gamma$ luminosity spectrum is almost independent of collision effects at the IP (beamstrahlung and multiple Compton scattering). For theoretical studies one can calculate the high energy part of the luminosity spectrum with sufficient accuracy by convolution of the Compton function [3]. Recently, a simple analytical formula for the Compton spectrum has been obtained [174] which takes into account nonlinear effects in the conversion region for sufficiently small values of ξ^2 .

The normalised γe luminosity spectra for $2E_0 = 500$ GeV are shown in Fig. 1.4.6 (left). Again, besides the high energy peak there is a several times higher γe luminosity at low invariant masses. Note, that the γe luminosity in the high energy peak is not

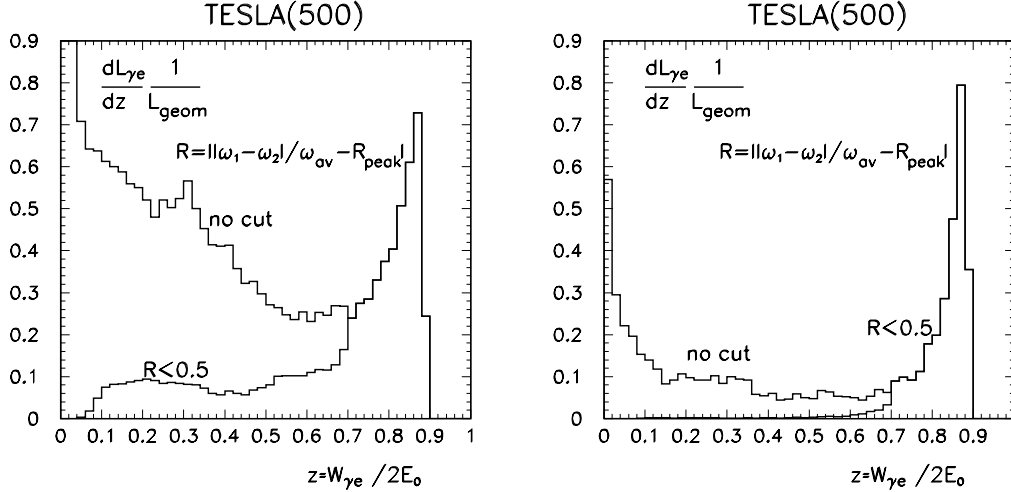


Figure 1.4.6: *Left: normalised γe luminosity spectra at TESLA(500) when the photon collider is optimised for $\gamma\gamma$ collisions and there is $\gamma \rightarrow e$ conversion for both electron beams, parameters are given in table 1.4.1. Right figure: there is $\gamma \rightarrow e$ conversion only for one electron beam and the distance between interaction and conversion point is 1.7 cm. See comments in the text.*

a simple geometric characteristic of the Compton scattering process (as it is in $\gamma\gamma$ collisions). For the case considered it is suppressed by a factor of 2–3, mainly due to the repulsion of the electron beams and beamstrahlung. The suppression factor depends strongly on the electron beam parameters.

For dedicated γe experiments one can convert only one electron beam, increase the distance between the conversion and the interaction points and obtain a much more monochromatic γe luminosity spectrum. One of such examples is shown in Fig. 1.4.6-right).

The luminosity distributions for $2E_0 = 800$ GeV is presented in Fig. 1.4.7 (left), and for $2E_0 = 200$ GeV on Fig. 1.4.7 (right). The latter case corresponds to $W_{\gamma\gamma,m} \approx 120$ GeV. At $2E_0 = 800$ GeV the value $x \approx 7.2 > 4.8$, however, due to nonlinear effects in the conversion region there is no suppression of the luminosity which might be due to e^+e^- creation (Section 1.3.1.3).

For the Higgs the production rate is proportional to $dL_0/dW_{\gamma\gamma}$ at $W_{\gamma\gamma} = M_H$. For the case considered, $M_H \approx 120$ GeV, and $x = 1.8$, $dL_0/dW_{\gamma\gamma} = 1.87 \times 10^{32} \text{ cm}^{-2}\text{s}^{-1}/\text{GeV}$, so that the coefficient in Fig. 1.1.5 characterising the width of the peak is about 5.3 (instead of 7).

Several other important accelerator aspects of the photon collider at TESLA are discussed in [199].

1.4.6 Monitoring and measurement of the $\gamma\gamma$ and γe luminosities

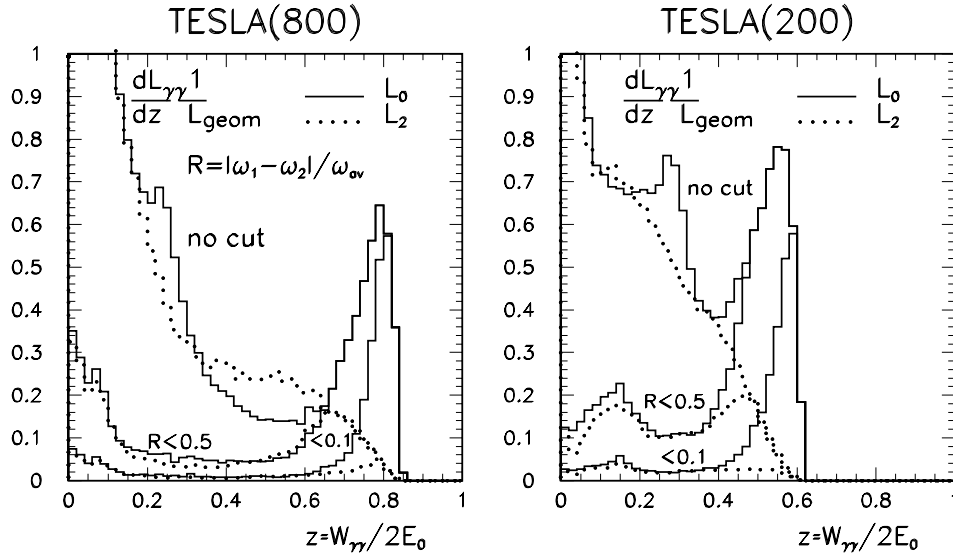


Figure 1.4.7: The $\gamma\gamma$ luminosity spectra at TESLA for $2E_0 = 800$ and 200 GeV (for Higgs(120)) with various cuts on longitudinal momentum (the case of $2E_0 = 500$ GeV is shown in Fig. 1.4.5). The solid line is for the total helicity of the two photons 0 and the dotted line for the total helicity 2. See also Table 1.4.1.

1.4.6.1 Luminosity measurement in $\gamma\gamma$ collisions

At photon colliders the luminosity spectrum is broad, photons and electrons may have various polarisations. One should have method to measure all luminosity characteristics. Let us start from $\gamma\gamma$ collisions.

We consider the head-on collisions of photons with 4-momenta $k_{1,2}$ and energies $\omega_{1,2}$. The z -axis is chosen along the momentum of the first photon, all the azimuthal angles are referred to one fixed orthogonal x -axis. The polarisation properties of the i -th photon are described by three parameters: λ_i the mean helicity (or degree of the circular polarisation), l_i and γ_i the mean degree of the linear polarisation and the azimuthal angle of its direction. The total cross section σ for the $\gamma\gamma$ collisions after summing over polarisations of final particles has the form [175]

$$\sigma = \sigma^{np} + \lambda_1 \lambda_2 \tau^c + l_1 l_2 \tau^l \cos 2(\gamma_1 - \gamma_2) \quad (1.4.10)$$

where σ^{np} is the total cross section for unpolarised photons and τ^c (τ^l) is the asymmetry related to the circularly (linearly) polarised photons. Besides, we use the notations $\sigma_0 = \sigma^{np} + \tau^c$ and $\sigma_2 = \sigma^{np} - \tau^c$ where 0 and 2 denote values of $|\lambda_1 - \lambda_2|$ — the total helicity of the produced system. The system produced in a $\gamma\gamma$ collision is characterised by its invariant mass $W_{\gamma\gamma} = \sqrt{4\omega_1\omega_2}$ and rapidity $\eta = 0.5 \ln(\omega_1/\omega_2)$.

Let us first consider the important case when both photons are circularly polarised. In this case we should have a method to measure a spectral luminosity $dL/dW_{\gamma\gamma}d\eta$ and the product of helicities $\lambda_1\lambda_2$ or, in other words, the spectral luminosities $dL_0/dW_{\gamma\gamma}d\eta$ and $dL_2/dW_{\gamma\gamma}d\eta$ with the total helicity 0 and 2.

These luminosities can be measured using the process $\gamma\gamma \rightarrow l^+l^-$, where $l = e$ or μ [2, 202, 5, 203, 204]. The cross section of this process for colliding photons with total helicity 0 and 2 and for $W_{\gamma\gamma}^2 \gg m^2$ is ($\hbar = c = 1$)

$$\begin{aligned}\sigma_0(|\cos\vartheta| < a) &\approx \frac{4\pi\alpha^2}{W_{\gamma\gamma}^2} \frac{8m^2}{W_{\gamma\gamma}^2} \left[\frac{1}{2} \ln\left(\frac{1+a}{1-a}\right) + \frac{a}{1-a^2} \right] \\ \sigma_2(|\cos\vartheta| < a) &\approx \frac{4\pi\alpha^2}{W_{\gamma\gamma}^2} \left[2 \ln\left(\frac{1+a}{1-a}\right) - 2a \right].\end{aligned}\quad (1.4.11)$$

One can see that $\sigma_0/\sigma_2 \sim m^2/W_{\gamma\gamma}^2 \ll 1$ (excluding the region of small angles). For photons with arbitrary circular polarisations the cross section is

$$\sigma_{\gamma\gamma \rightarrow e^+e^-} = \frac{1 + \lambda_1\lambda_2}{2}\sigma_0 + \frac{1 - \lambda_1\lambda_2}{2}\sigma_2, \quad (1.4.12)$$

where $\sigma_2 \gg \sigma_0$.

Hence the number of events

$$dN_{\gamma\gamma \rightarrow \mu^+\mu^-} \approx dL \frac{1 - \lambda_1\lambda_2}{2} \sigma_2 \equiv dL_2 \sigma_2, \quad (1.4.13)$$

and one can measure the luminosity $dL_2/dW_{\gamma\gamma}d\eta$. Measurement of $dL_0/dW_{\gamma\gamma}d\eta$ is done by inversion of the helicity of one photon beam simultaneously changing the signs of the helicities of the laser beam used for the $e \rightarrow \gamma$ conversion and that of the electron beam [202]. In this case the spectrum of scattered photons is not changed while the product $\lambda_1\lambda_2$ changes its sign. In other words, L_0 "becomes" now L_2 , which is measurable. The cross section for this process is $\sigma(|\cos\vartheta| < 0.9) \approx 10^{-36}/W_{\gamma\gamma}^2 [\text{TeV}] \text{cm}^2$. This process is very easy to select due to a zero coplanarity angle.

Linear photon polarisations can also be measured using the above processes. At large angles the cross section has a strong correlation between the plane of the final state particles and the directions of the photon polarisations. Let us consider the general case in more detail.

The differential cross section can be written in the form [3]

$$d\sigma = \frac{\alpha^2 T}{W_{\gamma\gamma}^2 (m^2 + \mathbf{p}_{-\perp}^2)^2} d\Gamma, \quad d\Gamma = \delta(k_1 + k_2 - p_- - p_+) \frac{d^3p_- d^3p_+}{E_- E_+} = \frac{dt d\varphi_-}{W_{\gamma\gamma}^2}, \quad (1.4.14)$$

where $\mathbf{p}_{-\perp}$ is the transverse momentum of the electron, $t = (k_1 - p_-)^2$ and φ_- is the azimuthal angle of the electron. The quantity T is

$$T = T_{00} + \lambda_1\lambda_2 T_{22} - 2T_\varphi, \quad (1.4.15)$$

with

$$\begin{aligned}T_{00} &= m^2(W_{\gamma\gamma}^2 - 2m^2) + \mathbf{p}_{-\perp}^2(W_{\gamma\gamma}^2 - 2\mathbf{p}_{-\perp}^2), \\ T_{22} &= m^2(W_{\gamma\gamma}^2 - 2m^2) - \mathbf{p}_{-\perp}^2(W_{\gamma\gamma}^2 - 2\mathbf{p}_{-\perp}^2),\end{aligned}\quad (1.4.16)$$

and

$$T_\varphi = l_1 l_2 [m^4 \cos(2\phi_1 - 2\phi_2) + (\mathbf{p}_{-\perp}^2)^2 \cos(2\phi_1 + 2\phi_2)] - 2m^2 \mathbf{p}_{-\perp}^2 [l_1 \cos 2\phi_1 + l_2 \cos 2\phi_2], \quad (1.4.17)$$

where $\phi_i = \varphi_- - \gamma_i$ is the (azimuthal) angle between the vector $\mathbf{p}_{-\perp}$ and the direction of the linear polarisation of i -th photon (therefore, the angle $\phi_2 - \phi_1 = \gamma_1 - \gamma_2$). From (1.4.15), ignoring the azimuthal term, the contribution of the total helicity 0 corresponds to the sum $T_{00} + T_{22}$ and the helicity 2 to the term $T_{00} - T_{22}$, which is smaller by a factor of m^2/p_\perp^2 , in agreement with our previous observation (see 1.4.12).

At high energy and not too small angles the cross section is

$$d\sigma = \frac{\alpha^2}{W_{\gamma\gamma}^2} \left[(1 - \lambda_1 \lambda_2) \left(\frac{W_{\gamma\gamma}^2}{\mathbf{p}_{-\perp}^2} - 2 \right) - 2l_1 l_2 \cos(2\phi_1 + 2\phi_2) \right] d\Gamma, \quad (1.4.18)$$

$$d\Gamma = \frac{2\omega_1 \omega_2}{[\omega_1(1 - \cos\theta_-) + \omega_2(1 + \cos\theta_-)]^2} d\Omega_-, \quad W_{\gamma\gamma}^2 \gg m^2, \quad \mathbf{p}_{-\perp}^2 \gg m^2$$

where $d\Omega_-$ is the electron solid angle. One sees that at large angles ($p_\perp \sim W_{\gamma\gamma}/2$) the cross section depends strongly on the degrees of both the circular and the linear photon polarisations.

The cross section of the calibration processes $\gamma\gamma \rightarrow e^+e^-(\mu^+\mu^-)$ is larger than those for most processes to be studied and only the processes $\gamma\gamma \rightarrow W^+W^-$ and $\gamma\gamma \rightarrow$ hadrons have larger cross sections. However, taking the detection efficiency for WW into account, the counting rate of WW pairs will be comparable with that of the calibration processes. As for hadrons, the expected number of calibration events is sufficient to measure the properties of hadronic reactions with high accuracy.

Note that the momenta of electrons (muons) in the processes under discussion can be measured with a high accuracy which is very important for the determination of the luminosity distribution near the high energy edge.

Other processes with large cross sections which can be used for the luminosity measurement are $\gamma\gamma \rightarrow W^+W^-$ [204] and $\gamma\gamma \rightarrow \mu^+\mu^-\mu^+\mu^-$ [2, 205]. The first process has a total cross section of 8×10^{-35} cm² the second one 1.6×10^{-34} cm². The first process depends on the photon polarisations especially in the region of large angles [112, 113]. The second processes is sensitive only to the linear photon polarisation. These processes may be useful, for an independent check and a fast monitoring of the luminosity.

1.4.6.2 Luminosity measurement in γe collisions

For the absolute γe luminosity measurement, one can use the process of Compton scattering, which is strongly polarisation dependent.

Let us consider the polarisation properties of Compton scattering at high energies. For an γe collider we consider the head-on collision of an electron with 4-momentum p and a photon with 4-momentum k , energies E and ω of the same order and the squared invariant mass of γe system $W_{\gamma e}^2 = (p + k)^2 \approx 4E\omega$. We choose the z -axis

along the momentum of the electron. The polarisation properties of the electron are described by its mean helicity λ_e ($|\lambda_e| \leq 1/2$), transverse polarisation ζ_\perp ($\zeta_\perp \leq 1$), and the azimuthal angle β of the direction of the transverse polarisation. The polarisation properties of the photon are described by three parameters: λ_γ the mean helicity (or degree of the circular polarisation), l_γ and γ the mean degree and the direction of the linear polarisation.

The total and differential cross sections for the process $e(p) + \gamma(k) \rightarrow e(p') + \gamma(k')$ and their dependence on the polarisation of the initial particles are discussed in [3]. We consider here the case of high energies $W_{\gamma e}^2 \gg m^2$ only. In this case the total cross section

$$\sigma \approx (1 + 2\lambda_e \lambda_\gamma) \frac{2\pi\alpha^2}{W_{\gamma e}^2} \ln \frac{W_{\gamma e}^2}{m^2}, \quad W_{\gamma e}^2 \gg m^2 \quad (1.4.19)$$

depends strongly on the circular photon polarisation and on the longitudinal electron polarisation only. Here the mean electron helicity is defined as a projection of its spin and 100% polarisation corresponds to $\lambda_e = 1/2$.

The differential cross section depends on the degrees of the circular and linear polarisations of the photon and on its angle γ which determines the direction of the linear photon polarisations as well as on the electron polarisation. It can be written in the the form

$$d\sigma = \frac{\alpha^2 F_0}{m^2 x} d\Gamma, \quad d\Gamma = \delta(p + k - p' - p') \frac{d^3 p' d^3 k'}{E' \omega'} = dy d\varphi_\gamma \quad (1.4.20)$$

where

$$x = \frac{2pk}{m^2} \approx \frac{4E\omega}{m^2} \gg 1, \quad y = 1 - \frac{pk'}{pk}, \quad r = \frac{y}{(1-y)x}$$

and φ_γ is the azimuthal angle of the final photon. The quantity F_0 is

$$F_0 = \frac{1}{1-y} + 1 - y - 4r(1-r) [1 + l_\gamma \cos 2(\varphi - \gamma)] - \quad (1.4.21)$$

$$-y\lambda_\gamma \left[2\sqrt{r(1-r)} \zeta_\perp \cos(\varphi - \beta) - \frac{2-y}{1-y} (1-2r) 2\lambda_e \right].$$

In the region of angles $\theta_\gamma \gg m/E$, we have

$$1 - y = \frac{E(1 - \cos \theta_\gamma)}{E(1 - \cos \theta_\gamma) + \omega(1 + \cos \theta_\gamma)}, \quad d\Gamma = \frac{2E\omega}{[E(1 - \cos \theta_\gamma) + \omega(1 + \cos \theta_\gamma)]^2} d\Omega_\gamma. \quad (1.4.22)$$

If the angle $\theta_\gamma \approx 1$ all terms in expression (1.4.21) have to be taken into account. Thus by detecting the final state particles at large angles, one can measure all polarisation parameters of the colliding particles.

In the region $m/E \ll \theta_\gamma \ll 1$, which corresponds to a large cross section, the expression for the differential cross section is

$$d\sigma = \frac{\alpha^2}{(E\theta_\gamma)^2} (1 + 2\lambda_e \lambda_\gamma) d\Gamma, \quad d\Gamma = \frac{E}{2\omega} d\Omega_\gamma \quad (1.4.23)$$

which depends strongly only on the circular photon polarisation and longitudinal electron polarisation only.

For the luminosity tuning in $\gamma\gamma$ and γe collisions one can use the beam–beam deflection (same as for e^+e^-) and “background” processes like incoherent e^+e^- and hadron production which are discussed in the next section.

1.4.7 Backgrounds

Backgrounds cause problems for recording data (complicating triggers) and data analysis (underlying background processes, overlapping of “interesting” and background events) and also damage of detectors. It is well known that at e^+e^- colliders background conditions are much less severe than at pp or $p\bar{p}$ colliders because the total $pp/p\bar{p}$ cross section is much larger.

The photon collider is based on electron–electron linear colliders and therefore has a lot of common with e^+e^- colliders as far as backgrounds are concerned. Like the electron, the photon interacts electromagnetically and does not participate directly in strong interactions. Photon colliders produce a mixture of e^-e^- , γe and $\gamma\gamma$ collisions. Electromagnetic interactions of these particles between each other (incoherently) as well as with the beam field (coherently) generate beamstrahlung photons, e^+e^- pairs and other reactions which are quite similar to those at e^+e^- colliders. These QED backgrounds have small transverse momenta and cause problems mainly for the vertex detector, the small angle calorimeter and the luminosity monitor. Many of these particles hit the final quads generating showers for which some of these particles may backscatter into the detector. These backgrounds at photon colliders are smaller than at e^+e^- colliders because of the crab–crossing collision scheme which provides a clear angle for disrupted beams and for the most energetic part of the luminosity–induced background.

On the other hand, due to virtual $q\bar{q}$ pairs the photon behaves as a hadron with the probability of about 1/200. The corresponding cross section $\sigma(\gamma\gamma \rightarrow \text{hadrons}) \approx 5 \times 10^{-31} \text{ cm}^2$ is smaller than the total pp cross section by 5 orders of magnitude. However, the TESLA bunch crossing rate ($\nu = 14 \text{ kHz}$) is about 3000 times lower than that at the pp collider LHC. For the same luminosity the probability of accidental coincidence (or the number of background events per bunch crossing) at the photon collider will be smaller by a factor of 30. At the $\gamma\gamma$ luminosity planned at TESLA the average number of hadronic background events per one bunch collision will be of the order of 1–3 and we should expect some problems with the analysis of certain physics processes.

However, there is very big difference between pp and $\gamma\gamma$ colliders because the rate of hadronic events per second at photon colliders is by 5 orders of magnitude smaller. Correspondingly there should be no problem with the radiation damage of the detector, nor the trigger.

In addition, photon colliders have several very specific background problems. Electrons after the Compton scattering have a very broad energy spectrum, $E \approx (0.02-1)E_0$, and an angular spread of about 5–10 mrad. Removal of the disrupted beams

requires the crab-crossing beam collision. This was discussed in Section 1.4.

Another specific problem is connected with the presence of the optical mirrors very close to the beams. The mirrors are bombarded by the large angle X-ray Compton scattered photons, by large angle beamstrahlung photons and by synchrotron radiation from beam tails. Also e^+e^- pairs produced at the interaction point will hit the mirrors.

Below the backgrounds are considered in the following order:

1. Particles with large disruption angles hitting the final quads and mirrors. The sources are multiple Compton scattering, hard beamstrahlung, Bremsstrahlung (in e^-e^-);
2. e^+e^- pairs created in the processes of $e^-e^- \rightarrow e^-e^-e^+e^-$ (Landau-Lifshitz, LL), $\gamma e \rightarrow ee^+e^-$ (Bethe-Heitler, BH), $\gamma\gamma \rightarrow e^+e^-$ (Breit-Wheeler, BW). This is the main source of low energy particles, which can cause problems in the vertex detector;
3. $\gamma\gamma \rightarrow$ hadrons;
4. X-ray background (for optical mirrors).

1.4.7.1 Low energy electrons

In Section 1.4 we considered already the disruption angles of low energy particles from multiple Compton scattering, hard beamstrahlung and coherent pair creation, and found that one can remove these particles from the detector with low backgrounds using the crab-crossing scheme with about 14 mrad (radius) holes for the disrupted beams. The low energy electrons after the hard bremsstrahlung may be sufficiently deflected by the opposite beam and hit the quads. A simple estimate shows that the total energy of these particles per bunch collision is of the order of one TeV which is much smaller than that of the e^+e^- pairs discussed below.

1.4.7.2 Incoherent e^+e^- pairs

This source of background at the photon collider is less important than for the TESLA e^+e^- collider because 1) one of the main sources (LL) is almost absent; 2) many particles with almost 99% of the total energy escape through the hole for the disrupted beams, while in e^+e^- collisions at TESLA (without crab-crossing) they almost all hit the quads.

Nevertheless, we will consider here the main characteristics of e^+e^- pairs which are important for designing the vacuum chamber near the IP and for the vertex detector design.

This background was considered in detail in the CDR on the photon collider at TESLA [19]. Since that time the geometric design luminosity has increased by one order of magnitude, but the γe luminosity/per bunch collision has increased only 2 times, while for e^-e^- even decreased 3 times. So, with a good accuracy we can use the previous numbers.

Most of the e^- and e^+ produced in LL, BH, BW processes travel in the forward direction, but due to the kick in the field of the opposing electron beam they get much larger angles and can cause problems in the detector.

In one bunch collisions about 50000 e^+e^- pairs are produced with a total energy of about 10^6 GeV. A large fraction of these particles escape the detector through the hole for the disrupted beams (about $10 - 15$ mrad) without interactions, and only particles with $\vartheta > 10$ mrad and $p \leq 1$ GeV (the latter due to crab-crossing in the solenoidal field) will hit the quads and mirrors. The total energy of these particles is much smaller: 2×10^4 GeV (we use the CDR number). We see that this energy is almost two orders of magnitude lower than in the case of e^+e^- collisions (without crab-crossing) where it was found that the backgrounds are acceptable for the detector. However, at the photon collider there are optical mirrors in the way of the large angle particles which may lead to differences in the flux of back scattered particles. This has to be simulated more accurately.

In the incoherent e^+e^- background there are two classes of particles: a) with large initial angles and b) with angles determined by the beam-beam interaction. The first class is an unavoidable background (and rather small), the second class of particles, which carry most of the total energy, can be suppressed by proper choice of the beam pipe and vertex detector geometry.

The shape of the zone occupied by the deflected electrons with an energy spectrum from 0 to E_0 is described by the formula [206, 19]

$$r_{max}^2 \simeq \frac{25Ne}{\sigma_z B} z \approx 0.12 \frac{N}{10^{10}} \frac{z [\text{cm}]}{\sigma_z [\text{mm}] B [\text{T}]}, \quad (1.4.24)$$

where r_{max} is the radius of the envelope at a distance z from the IP, B is the longitudinal detector field. For example, for TESLA with $N = 2 \times 10^{10}$, $\sigma_z = 0.3$ mm, and $B = 3$ T, $r = 0.52 \sqrt{z [\text{cm}]} \text{ cm}$. This simple formula can be used to define the vertex detector radius and the shape of the vacuum chamber.

1.4.7.3 $\gamma\gamma \rightarrow \text{hadrons}$

The cross section of this process is about 400–600 nb at $W_{\gamma\gamma} = 10\text{--}500$ GeV. The $\gamma\gamma$ luminosity at the TESLA Photon Collider (Table 1.4.1) is about $10^{35} \text{ cm}^{-2}\text{s}^{-1}$ in total, 5×10^{34} with $z = W_{\gamma\gamma}/2E_0 > 0.1$ and 1.2×10^{34} with $z > 0.65$. The corresponding numbers of hadronic events per bunch crossing at $2E_0 = 500$ GeV is about 3.5, 1.7 and 0.4, respectively.

We now discuss the consequences for the experiment and for the maximum luminosity. Detailed studies have been performed for the TESLA CDR using the PYTHIA code 5.720 [207]. At present there are new versions, but already at that time processes such as mini-jets from resolved photons were included approximately. In that study we considered different background levels, from 0.7 to 7 events/bunch collision. The present TESLA parameters are within this range. The change in the shape of the luminosity spectra is not essential.

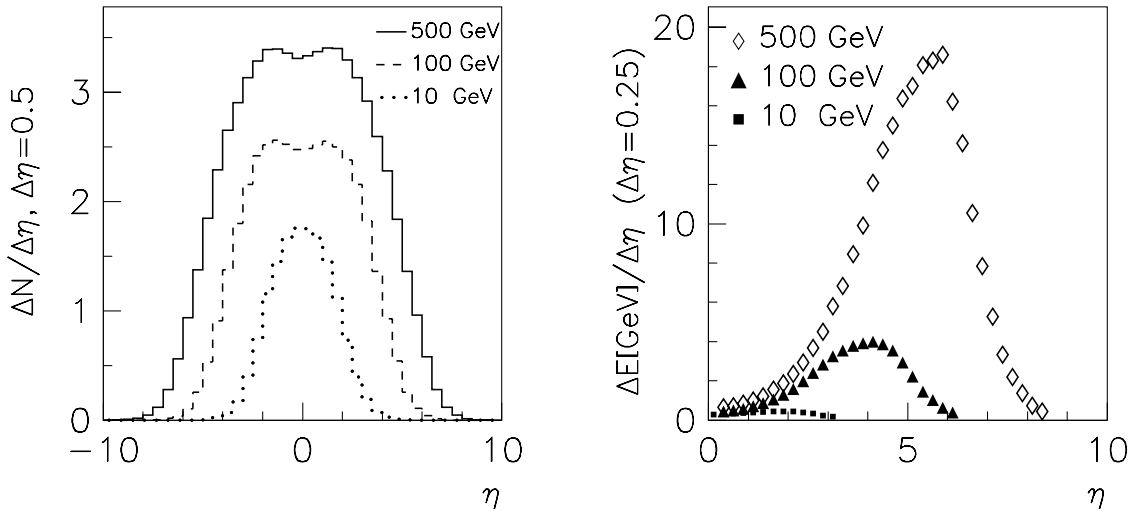


Figure 1.4.8: *Distribution of particle flow (left) and energy flow (right) in pseudo-rapidity in $\gamma\gamma \rightarrow$ hadrons events for various values of $W_{\gamma\gamma}$ assuming equal energies photons).*

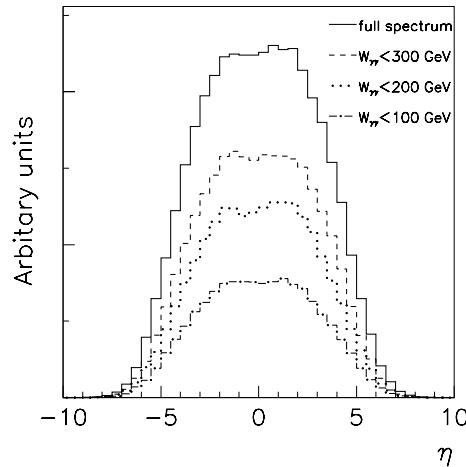


Figure 1.4.9: *Distribution of the number of particles in pseudo-rapidity for different ranges of $\gamma\gamma$ invariant mass for $2E_0 = 500$ GeV.*

Fig. 1.4.8 shows the flow of particles and their energies versus pseudo-rapidity ($\eta = -\ln \tan(\vartheta/2)$) in one $\gamma\gamma \rightarrow$ hadrons event at $W_{\gamma\gamma} = 10, 100$ and 500 GeV. Each 500 GeV hadronic event produces on the average 25 particles (neutral + charged) in the range of $-2 \leq \eta \leq 2$ ($\vartheta \geq 0.27$ rad) with a total energy of about 15 GeV. The average momentum of the particles is about 0.4 GeV. Note that the flux of the particles at large angles ($\eta \approx 0$) from a 10 GeV $\gamma\gamma$ collision is only twice smaller than that from a 500 GeV $\gamma\gamma$ collision.

In this respect it is of interest to check the background from different parts of the $\gamma\gamma$ luminosity spectra. Fig. 1.4.9 shows the distribution of particles in pseudo-rapidity

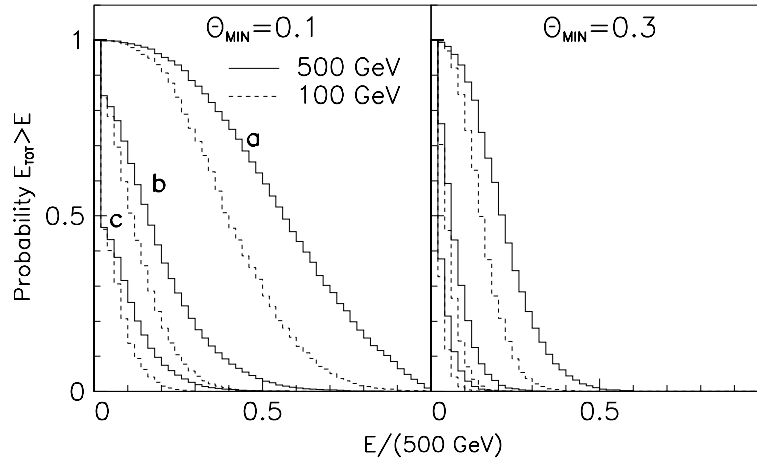


Figure 1.4.10: The probability of an energy deposition in the detector above the value E due to the process $\gamma\gamma \rightarrow \text{hadrons}$. The polar angle acceptance is $\vartheta > 0.1$ rad (left plot) and $\vartheta > 0.3$ rad (right plot). Curves a), b), c) correspond to 7, 2 and 0.7 hadronic events on the average per beam collision respectively. The collision energy $W_{\gamma\gamma}$ is 500 GeV (solid line) and 100 GeV (dashed line); both photons have equal energies.

for the TESLA $\gamma\gamma$ luminosity spectrum at $2E_0 = 500$ GeV. While the events with $W_{\gamma\gamma} < 100$ GeV contain more than 60% of the total luminosity, their contribution to the number of background particles is only about 30%, due to the smaller energy and large longitudinal boost of the produced system.

From figs. 1.4.8, 1.4.9 we see that the characteristics of events at large angles (small rapidities) do not depend strongly on the energy of the colliding photons. Rather than using the $W_{\gamma\gamma}$ dependence for hadronic events/bunch collision (see above), it is thus more convenient to use some “average” number of central collisions with energy $W_{\gamma\gamma} = 500$ GeV with equivalent background. Fig. 1.4.9 allows to make a reasonable approximation: events with $W_{\gamma\gamma} > 300$ GeV are similar to events at $W_{\gamma\gamma} = 500$ GeV and their contribution to the luminosity and background is known. The effective average rate is about 1.5 events per bunch collision.

The probability of an energy deposition in the detector above some value E is shown in Fig. 1.4.10. In the left figure the minimum angle of the detector is $\theta_{min} = 0.1$ rad, on the right one $\theta_{min} = 0.3$ rad. The curves a), b), c) correspond to 7, 2 and 0.7 hadronic events on average per collision; the solid curves are for $W_{\gamma\gamma} = 500$ GeV, the dashed for 100 GeV. For example, for 2 events per collision and $\theta_{min} = 0.1$ the probability of an energy deposition above 100 GeV is about 40%. This energy is produced by many soft particles and a smooth background can be subtracted during the jet reconstruction. More important are fluctuations in the background, which are discussed below.

In many experimental studies the important characteristic is missing transverse momentum. The probability to find an unbalanced transverse momentum above some p_t is shown in Fig. 1.4.11 for $\vartheta_{min} = 0.1$ and 0.3, for $W_{\gamma\gamma} = 500$ and 100 GeV $\gamma\gamma$ collisions. Again the 3 curves in each figure correspond to 7, 2 and 0.7 hadronic events on the average per collision. It is of interest that the curves for $\vartheta_{min} = 0.1$ and 0.3 are

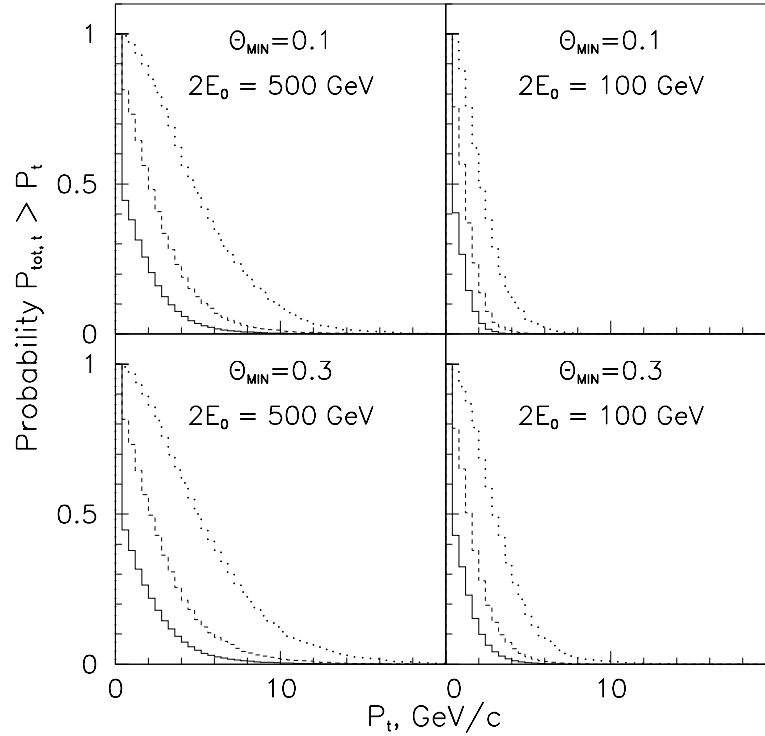


Figure 1.4.11: The probability to find an unbalanced transverse momentum above some p_t . Dotted, dashed and solid curves correspond to 7, 2, 0.7 $\gamma\gamma \rightarrow$ hadrons events on the average per beam collision. The polar angle acceptance is $\vartheta > 0.1$ rad (upper plots) and $\vartheta > 0.3$ rad (lower plots). The collision energy $W_{\gamma\gamma}$ is 500 GeV (left plots) and 100 GeV (right plots), both photons have equal energies.

quite similar. For 2 events (500 GeV) per collision the probability to get an unbalanced $p_{\perp} \geq 5$ GeV is about 15%. This is comparable with the detector resolution.

While calculating p_{\perp} , we summed all energy depositions in the detector, but “interesting” events usually have highly energetic particles or jets. The probability for the hadronic background adding energy to a jet is presented in Fig. 1.4.12. We have selected a cell $\Delta\varphi \leq 0.3$, $\Delta\eta \leq 0.3$, which corresponds to a characteristic jet transverse size at $\theta = \pi/2$, and calculated the probability of energy deposition in this region above some energy E . The curves correspond to one hadronic event on the average per bunch collision. For other levels of background, the probability should be multiplied by the average number of hadronic events per collision.

Note, that at the photon collider we are going to study events at rest in the lab. system, and the jet size is just $\Delta\Omega$. From the definition of the pseudorapidity follows $d\Omega = d\varphi d\eta \sin^2 \vartheta$. Therefore for obtaining the probability of background the value given in Fig. 1.4.12 should be divided by a factor of $\sin^2 \vartheta$.

A typical energy resolution for a 100 GeV jet is about 3 GeV. The probability to have such an energy deposition at $\eta = 0$ and 2 hadronic events per collision is 0.04%. For the $H(115) \rightarrow b\bar{b}$ decay the optimum angular cut is $\cos \vartheta = 0.7$, or pseudorapidity

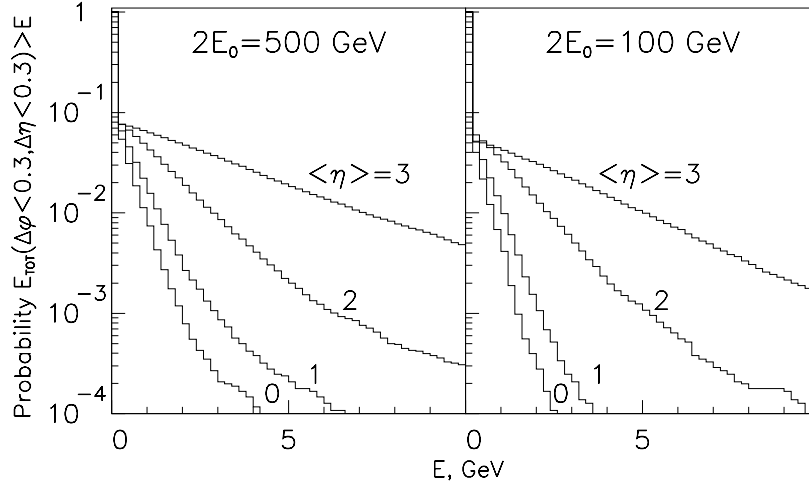


Figure 1.4.12: The probability to have the energy flow into $\Delta\phi \times \Delta\eta = 0.3 \times 0.3$ cell above some threshold (abscissa value) for 4 pseudo-rapidity points: $\eta = 0, 1, 2, 3$. $W_{\gamma\gamma}$ is 500 GeV (left) and 100 GeV (right).

$\eta = 0.87 \approx 1$. For such an angle the probability of 2 GeV energy deposition inside a jet from the Higgs decay is 1.5% and thus does not present a problem even for a 10 times larger luminosity.

However, the probability depends very strongly on the angle. For example, for $\eta = 2$ the probability of 2 GeV is already 60%. So, at low angles the hadronic background can worsen the resolution for low energy jets.

Of course, these estimates are very approximate and accurate simulation of certain processes is required.

1.4.7.4 Large angle compton scattering and beamstrahlung

X-ray radiation from beams can cause damage to multilayer dielectric mirrors. There are two main sources of such radiation [208]:

Large angle Compton scattering. The energies of these photons are $\omega = 4\omega_0/\theta^2$ at $\theta \gg 1/\gamma$, where ω_0 is the energy of the laser photon ($\approx 1\text{eV}$). At a distance l the flux of photons $dn/ds \propto N/\gamma^2 l^2 \theta^4$. The main contribution comes from Compton scattering on the low energy electrons. The simulation for $2E_0 = 500\text{ GeV}$ gives a power density $P \approx 10^{-7}\text{ W/cm}^2$, $\omega \approx 40\text{ keV}$ at $\theta = 10\text{ mrad}$ (the edge of the mirrors).

Large angle beamstrahlung. The simulation shows that X-ray photons have a wide spectrum, $P \approx 10^{-6}\text{ W/cm}^2$, $\omega \approx 1.5\text{ keV}$ at $\theta = 10\text{ mrad}$.

Note, that the X-ray power density on the mirrors is proportional to $1/\theta^6$ and, if necessary, the minimum angle can be increased, which is possible in the present scheme (Section 1.5) in which the mirrors are placed outside the electron beams.

1.4.8 The detector, experimentation issues

The detector for experimentation at the Photon Collider could be basically the same as for e^+e^- collisions. Some differences are connected only the optical system which should be placed inside the detector.

Optimum focusing of the laser beam determines the divergence of the laser beam at the conversion point (Section 1.3.2), it is $\sigma_{x'} = 0.0155$ and the angular radius $2.5\sigma_{x'}$ for the focusing mirror will be sufficient. As we consider the optics situated outside the electron beams, the required clear angle is $\pm 2 \times 2.5 \times 0.0155 = \pm 78$ mrad.

From the background consideration (previous section) follows that the vertex detector with a length of about ± 15 cm length should have a radius not smaller than 2 cm. This leaves the angular range ± 130 mrad inside the vertex for the laser beam, which is sufficient.

Beside the final focusing mirror the laser system has additional mirrors inside the detector (Section 1.5), at angles of about 120–140 mrad. This does not have a major impact for the experiment as the mirrors are situated close to the calorimeter, their diameter is 15–20 cm and the thickness will be less than one radiation length.

1.5 The Lasers and Optics

A key element of photon colliders is a powerful laser system which is used for the $e \rightarrow \gamma$ conversion. Lasers with the required flash energies (several J) and pulse durations (≈ 1 ps) already exist and are used in several laboratories. The main problem is the high repetition rate, about 10–15 kHz with the time structure of the electron bunches.

The requirements of the laser system for the Photon Collider at TESLA were discussed in Section 1.3.2. In summary, the required laser wavelength is about $1 \mu\text{m}$, the flash energy 5 J, and the repetition rate about 14 kHz. If two electron beams should be converted to photons the average power of the laser system should be about 140 kW. At TESLA the laser has to work only 0.5% of the time since the repetition rate is 5 Hz and duration of one train containing 3000 bunches is 1 msec. Thus the train structure of the LC is a very serious complication.

In this section we will consider possible optical schemes and lasers for the TESLA Photon Collider.

1.5.1 The laser optics at the interaction region

To overcome the “repetition rate” problem it is quite natural to consider a laser system where one laser bunch is used for the $e \rightarrow \gamma$ conversion many times. Indeed, a 5 J laser flash contains about 5×10^{19} laser photons and only 10^{10} – 10^{11} photons are knocked out per collision with the electron bunch. Below two ways of multiple use of one laser pulse are considered for the Photon Collider at TESLA: an optical storage ring and an external optical cavity.

1.5.1.1 The optical “trap”

The first approach is shown in Fig. 1.5.1 [21]. In Fig. 1.5.1a the laser pulse is used twice for the $e \rightarrow \gamma$ conversion. After the collision with the electron beam (number 1) the laser beam exits from the detector and after a 337 ns loop (the interval between beam collisions at TESLA) returns back and collides with the opposite electron beam (number 2). The second pass does not need any special optical elements, only mirrors. This is a very natural and simple solution. In this scheme the laser system should generate bunches with an interval of 337 ns.

In Fig. 1.5.1b the laser pulse is used for conversion four times. In this scheme one additional optical element is used, a thin film polariser (TFP), which is transparent for the light polarised in the plane of the plane of the drawing and reflects light with the orthogonal polarisation. Directions of the polarisation during the first cycle are shown in Fig. 1.5.1b. After the first cycle the polarisation is perpendicular to the plane of the drawing and the light is reflected from the TFP, while after the second cycle the polarisation will be again in the plane of the drawing and the laser pulse will escape the system via the TFP. The laser bunches are emitted by the laser at an average interval of 2×337 ns but not uniformly (337, 3×337), (337, 3×337), etc (see the next paragraph).

In Fig. 1.5.1c the laser pulse is sent to the interaction region where it is trapped in an optical storage ring, which can be built using Pockels cells (P), thin film polarisers (TFP) and $\lambda/4$ -wavelength plates ($\lambda/4$). Each bunch makes several (n) round trips (period of the round trip is $2T_0$, where $T_0 = 337$ ns is the interval between bunch collisions) and then is removed from the ring. All this can be done by switching one Pockels cell which can change the direction of linear polarisation by 90 degrees. The $\lambda/4$ plates are used for obtaining the circular polarisation at the collision point. For obtaining linear polarisation at the IP these plates should be replaced by $1/2$ wavelength plates. A similar kind of optical trap was considered as one of the options in the NLC Zero Design Report [22]. The number of cycles is determined by the attenuation of the pulse and by nonlinear effects in the optical elements. The latter problem is very serious for Terawatt (TW) laser pulses. During one total loop each bunch is used for conversion twice (see Fig. 1.5.1c). The laser bunch collides first with electron beam 1 travelling to the right and after a time equal to the interval between collisions (337 ns) it collides with beam 2 travelling to the left. For arbitrary number of the round trips, n , the laser pulse sequence is a sum of two uniform trains with the interval between neighbouring pulses in each train

$$\Delta T_t = 2nT_0 \quad (1.5.1)$$

and the trains are shifted by the time

$$\Delta T = kT_0, \quad k = 1, 3, \dots, 2n - 1. \quad (1.5.2)$$

In Fig. 1.5.1d the laser pulse is trapped in the same way as in Fig. 1.5.1d, but to avoid the problems of nonlinear effects (self-focusing) in the optical elements, the laser pulse is compressed using a grating pair before collision with the electron bunch

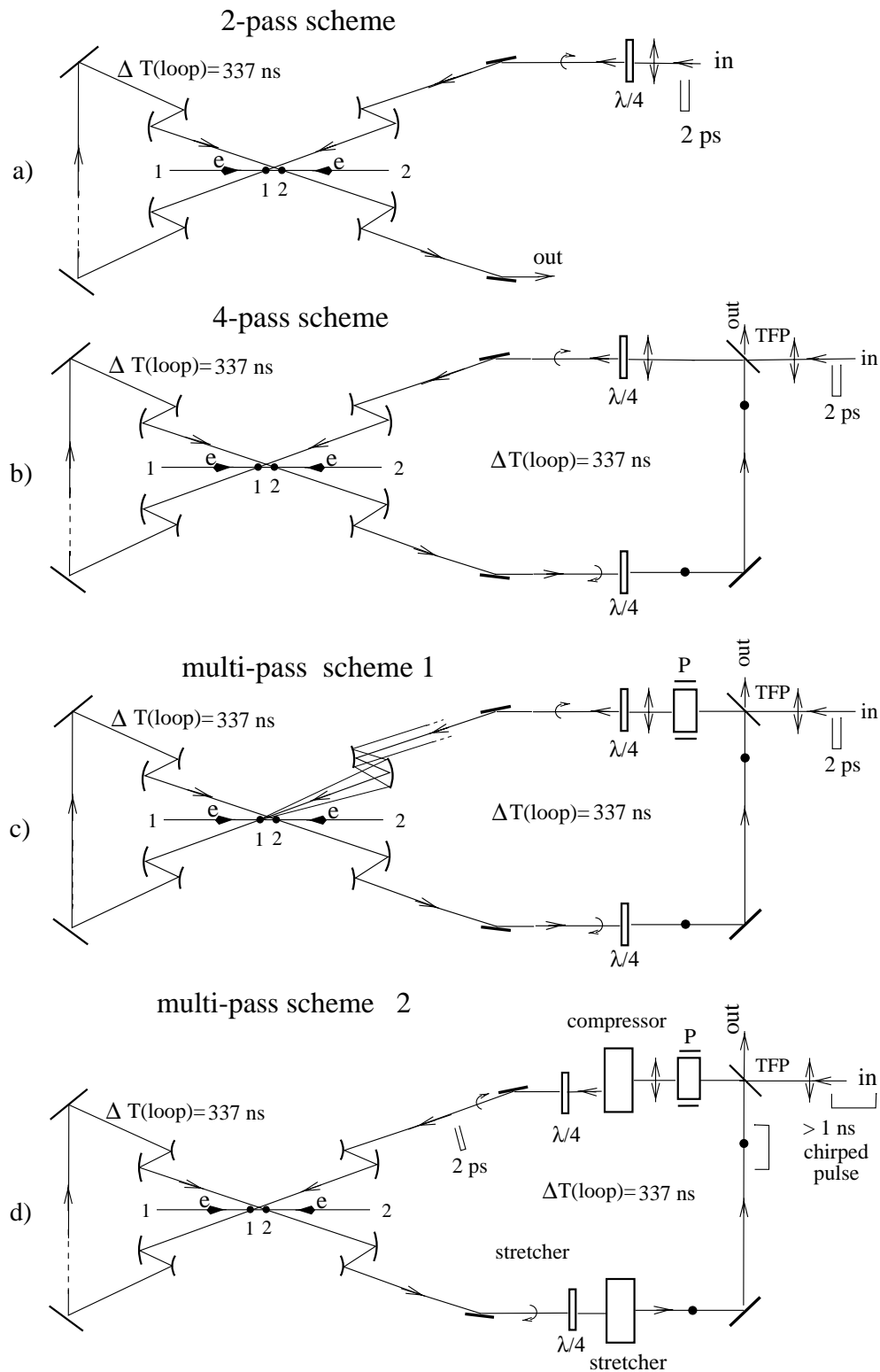


Figure 1.5.1: Optical trap: a) 2-pass optics for $e \rightarrow \gamma$ conversions; b) 4-pass optics; c) optical storage ring without stretching-compression; d) optical storage ring with stretching-compression; P is a Pockels cell, TFP is a thin film polariser, thick dots and double arrows show the direction of polarisation.

down to about 2–3 ps using grating pairs. It is then stretched again (decompressed) using another grating pair up to the previous length of about 11 ns just before passing through the optical elements.

Which system is the better one, 1.5.1b, 1.5.1c or 1.5.1d, is not clear a priori. The scheme (b) allows only 2 round trips, in the scheme (c) the number of cycles is limited by nonlinear effects, in the scheme (d) there is additional attenuation by the gratings used for compression and stretching. Optical companies suggest gratings for high powerful lasers with $R \approx 95\%$. One round trip requires four gratings, or a 20% loss/trip. So, the maximum number of trips for the scheme (c) is only about two. This presents no advantage compared to the scheme 1.5.1b which is much simpler and also allows two cycles, though it is not excluded that gratings with higher reflectivity will be available in future.

We next address the question how large the decrease of the laser energy per round trip can be in the scheme (c) without bunch compressor–stretchers. The minimum number of mirrors in the scheme is about 15–20. The reflectivity of multilayer dielectric mirrors for large powers suggested by optical companies is about 99.8% (or better). The total loss/cycle is thus about 3–4%. Let us add 1% attenuation in the Pockels cell. Due to the decrease of the laser flash energy the luminosity will vary from collision to collision. Calculations show that for attenuation factors of 1.3, 1.4, 1.5 for the laser pulse, the $\gamma\gamma$ luminosity will only vary by 14, 17, 21% (here we assumed that on average the thickness of the laser target is one collision length). For 5% loss/turn and 6 round trips the attenuation is 1.35, which is still acceptable.

Let us consider the problem of nonlinear effects for the scheme 1.5.1c. The refractive index of the material depends on the beam intensity

$$n = n_0 + n_2 I. \quad (1.5.3)$$

This leads to two types of a self focusing of the laser beam [209]. The first type is a self-focusing of the beam as a whole. The second one is self-focusing and amplification of non-uniformities which leads to break up of the beam into a large number of filaments with intensities exceeding the damage level. Both these effects are characterised by the parameter “B–integral” [209, 22]

$$B = \frac{2\pi}{\lambda} \int \Delta n dl = \frac{2\pi}{\lambda} n_2 I_{peak} \Delta l, \quad (1.5.4)$$

where Δl is the thickness of the material.

If the beam has a uniform cross section then nonlinear effects do not lead to a change of the beam profile, while for the Gaussian like beam, $B \approx 1$ corresponds to the self-focusing angle approximately equal to the diffraction divergence of the beam. This is not a problem since such distortions can be easily corrected using adaptive optics (deformable mirrors).

The second effect is more severe. Even for a uniform (in average) distribution of the intensity over the aperture a small initial perturbation δI_0 grows exponentially with a rate depending on the spatial wave number. The maximum rate is given in terms of

the same parameter B [209]

$$\delta I = \delta I_0 e^B. \quad (1.5.5)$$

This has been confirmed experimentally. To avoid amplification of small-scale non-uniformities, the parameter B should be smaller than 3–4 [209, 22], in other words

$$I_{peak} < \frac{\lambda}{2n_2\Delta l}. \quad (1.5.6)$$

Now we can evaluate the relationship between the diameter and the maximum thickness of the material. For $A = 5\text{ J}$, $\lambda = 1\text{ }\mu\text{m}$, $\sigma_{L,z} = 1.5\text{ ps}$, a typical value of $n_2 \approx 3 \times 10^{-16}\text{ cm}^2/\text{W}$ ¹ and a uniform beam we get

$$\Delta l[\text{cm}] < 0.1S[\text{cm}^2]. \quad (1.5.7)$$

For a beam diameter of 15 cm we obtain $l < 17\text{ cm}$. For Gaussian beams the maximum thickness is about two times smaller.

Next we address the question what value to insert for Δl . In the scheme 1.5.1c the dominant contribution to the total thickness is given by the Pockels cell. After the Pockels cell one can put a spatial filter (small hole in a screen) and thus suppress the growth of spikes. Δl in this case is the thickness of the Pockels cell and does not depend on the number of round trips. Moreover, the laser pulse is very short, has a broad spectrum and the corresponding coherence length is small, about $l_c \approx 4\pi\sigma_{L,z} \approx 0.5\text{ cm}$. The instabilities over a uniform high intensity background develop due to the interference of the fluctuation with the main power. However, this coherence is lost after one coherence length. Thus, the B-integral does not characterise the exponential growth of small scale non-uniformities once the coherence length is much lower than Δl (it will be suppressed even for small values of Δl , if the material is distributed over a long distance).

It turns out that the problem of nonlinear effects in the scheme 1.5.1c is not dramatic. The construction of a Pockels cells with an aperture of about 10–15 cm and a switching time of 300 ns is not very difficult. Quarter- and half-wave plates can be made thin or even combined with mirrors (retarding mirror).

In conclusion, a very preliminary analysis shows that the optical scheme 1.5.1c with about 6 round trips (12 collisions with electron beams) is a very attractive and realistic solution for the TESLA photon collider.

Now a few words on the laser system required for such an optical storage ring with 6 round trips. Schematically it is shown in Fig. 1.5.2. At the start (not shown) a low-power laser produces a train of 1 ms duration consisting of 500 chirped pulses with durations of several ns each. Then these pulses are distributed between 8 final amplifiers. Each of the 8 sub-trains has a duration of 1 msec and consists of 62 pulses. After amplification up to the energy of 5 J in one pulse these sub-trains are recombined to reproduce the initial time structure. The time spacing between bunches in the resulting train may be equal in average (see (1.5.2)) to the 6 intervals between beam collisions in TESLA in average (see 1.5.1).

¹it would be better to take n_2 for KD*P used for Pockels cells, but we have not found it in the literature

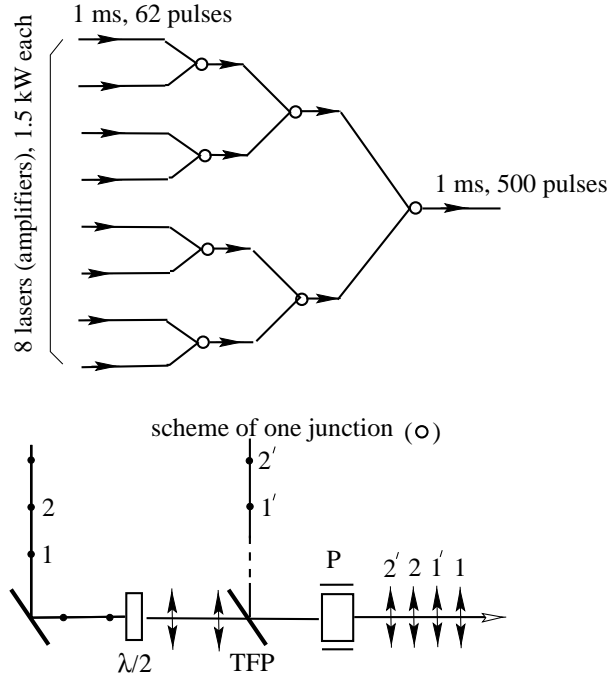


Figure 1.5.2: *Merging of pulses from several lasers (amplifiers)*

Due to the high average power the lasers should be based on diode pumping. Diodes have a much higher efficiency than flash lamps. It is about $\epsilon \approx 25\%$ for single pulses. For pulse trains, as in our case, the efficiency should be at least by a factor of two higher. Moreover, diodes are much more reliable. This technology has been developed very actively for other applications, such as inertial fusion.

The main problem with diodes are their cost. The present cost of diode lasers is about 5 EUR per Watt [210]. Let us estimate the required laser power. In the case of TESLA, the duration of the pulse train $T_0 = 1$ ms is approximately equal to the storage time ($\tau \approx 1$ msec) of the most promising powerful laser crystals, such as Yb:S-FAP. Therefore, the storage time does not help at TESLA. The required power of the diode pumping is

$$P_{diode} = \frac{A(\text{flash})N(\text{bunches})}{\epsilon T_0} = \frac{5\text{J} \times 500}{0.5 \times 10^{-3}} = 5\text{MW}. \quad (1.5.8)$$

Correspondingly, the cost of such diode system will be 25 MEUR. Here we assumed a 6-fold use of one laser bunch as described above.

Moreover, the Livermore laboratory is now working on a project of inertial confinement fusion with a high repetition rate and efficiency with the goal of building a power plant based on fusion. This project is based on diode pumped lasers. According to [211] they are currently working on the “integrated research experiment” for which “the cost of diodes should be reduced to 0.5 EUR/Watt and the cost of diodes for fusion should be 0.07 EUR/Watt or less.” Thus, the perspectives of diode pumped lasers for photon colliders are very promising. With 1 EUR/Watt the cost of diodes is 5 MEUR for the scheme with 6 round trips (with Pockels cell) and 15 MEUR for 2 round trips

without Pockels cell.

The average output power of all lasers in the scheme 1.5.1c is about 12kW, or 1.5kW for each laser.

1.5.1.2 The optical cavity

One problem with the optical storage ring at photon colliders is the self-focusing in optical elements due to the very high laser pulse power. There is another way to “create” a powerful laser pulse in the optical “trap” without any material inside: laser pulse stacking in an “external” optical cavity [9].

In short, the method is the following. Using a train of low energy laser pulses one can create in the external passive cavity (with one mirror having some small transmission) an optical pulse of the same duration but with an energy higher by a factor of Q (cavity quality factor). This pulse circulates many times in the cavity each time colliding with electron bunches passing the centre of the cavity. For more details see [9].

Such kind of cavity would allow to drastically reduce the overall costs of the laser system. Instead of several parallel working lasers it could be one table-top laser feeding the external optical cavity.

A possible layout of the optics scheme at the interaction region is shown in Fig. 1.5.3 [9, 21]. In this variant, there are two optical cavities (one for each colliding electron beam) placed outside the electron beams. Such a system has the minimum number of mirrors inside the detector. One of several possible problems in such a linear cavity is the back-reflection. In a ring type cavity this problem would be much easier to solve [212]. A possible scheme of such a ring cavity for photon colliders is shown in Fig. 1.5.4 [21] (only some elements are shown).

Some technical aspects of the external cavity approach are discussed in [212]. Such a cavity is operated already in MBI(Berlin) and $Q \approx 100$ has been demonstrated. A first view on technical problems of the optical cavities are given below.

The external resonant cavities have been used for comparable purposes for many years. A common application of those cavities is frequency conversion of the fundamental laser wavelength into its harmonics. Several optical laboratories have broad experience in application and design of those optical resonant enhancement cavities.

In order to provide an effective storage of the laser radiation, the length of the cavity has to be adjusted to an integer multiple of the laser wavelength with sub-micrometer accuracy. This ensures that the recirculating wave constructively interferes with the wave which is constantly fed into the cavity. An electronic feedback system is required for this task. Many different ways for obtaining the error signal are described in the scientific literature. The actual control of the resonator length is performed by means of piezoceramics which directly drive one of the resonator mirrors.

The quality factor Q of the cavity is typically limited by reflection losses at the optical elements. A cavity which has been operated at the Max-Born-Institute for several years for frequency doubling reaches a quality factor of 40 without difficulties, being determined by a nonlinear crystal. After removing the nonlinear crystal, an increase of the Q -factor to about 100 was observed.

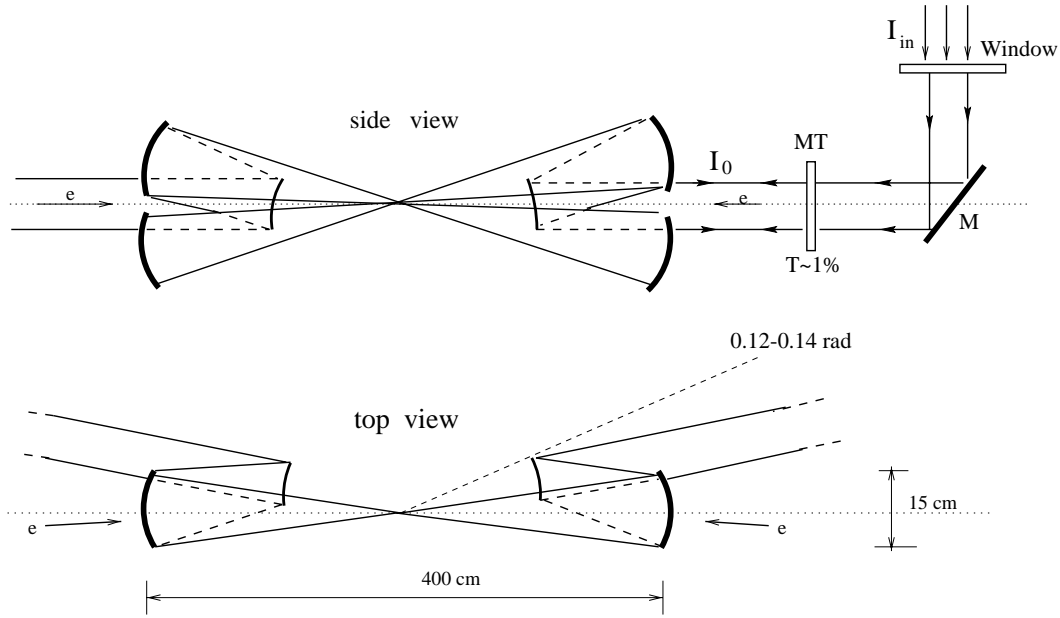


Figure 1.5.3: Principle scheme of “external” cavity for $e \rightarrow \gamma$ conversion. Laser beam coming periodically from the right semi-transparent mirror MT excites one cavity (includes left-down focusing mirror, right-up focusing mirror and the MT mirror). The second cavity (for conversion of the opposite electron beam) is pumped by laser light coming from the left (not shown) and includes the focusing mirrors left-up and right-down.

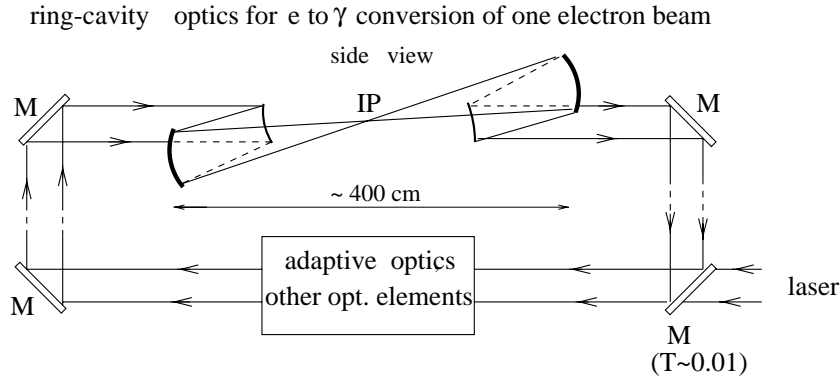


Figure 1.5.4: Ring type cavity. Only the cavity for one electron beam is shown. The top view is quite similar to that in Fig. 1.5.3

The majority of the cavities are used with uninterrupted cw laser radiation. Several laboratories have introduced appropriate extensions in order to use the cavities with pulses from mode locked lasers [213]. There are three major additional requirements to be fulfilled if the cavity has to store intensive laser pulses instead of cw radiation [214].

One of the problems in the optical cavity is temporal broadening of the pulse travelling in the cavity. This unfavourable effect may be caused by the wavelength

dependency of the refractive index (i.e. dispersion) which is experienced by the pulse passing through the optical elements. Appropriate compensation can be done using specially designed multilayer coatings (so called "chirped mirrors") [215], which are now commonly used in femtosecond laser oscillators. The chirped mirrors introduce particularly small optical losses and are therefore preferable for high- Q cavities. The maximum total thickness of the optical elements, whose dispersion can be compensated in one single reflection at a chirped mirror is limited to a few millimetres.

The design criteria for the resonant enhancement cavity follows:

- The cavity should have a ring-like geometry.
- The length of the cavity should be adjusted to the repetition rate of the electron bunches.
- The cavity length has to be stabilised to a very small fraction of the wavelength.
- Chirped mirrors can be used to compensate for dispersion in optical transmissive elements of up to several millimetres thickness. However, nonlinear perturbation of the wavefront by self-focusing limits this thickness to the millimetre or sub-millimetre range.
- Deformable mirrors should be used for maintaining the phase of the circulating light.
- Thin glass plates should be used for protection of individual mirrors from electrons and gamma radiation.
- The cavity cannot contain thick vacuum windows, i.e. the whole cavity has to be placed in a vacuum system.

Fig. 1.5.5 shows the basic elements of a possible resonant optical cavity for the TESLA Photon Collider (here two mirrors are missing which would allow to remove the laser beam from the IP region without passing the detector, as shown in Figs. 1.5.3, 1.5.4). The laser radiation is transferred to the cavity by means of two deformable mirrors M1 and M2. Those mirrors consist of a coated elastic glass plate which is bent by a number of piezo actuators. The purpose of the mirrors M1 and M2 is to adapt the incoming wavefront to the eigenmode to be excited in the cavity within a small fraction of the wavelength. This is essential in order to achieve constructive interference between the pulses from the laser and the pulses travelling inside the cavity. The actual coupling of the laser radiation into the cavity is performed by mirror M3 which should have a transmission of 1% (i.e. 99% reflectivity). All other mirrors M4 to M8 of the cavity are optimised for maximum reflectivity.

In order to maintain the phase of the circulating light wave across the complete beam profile, the optical path length should be adjusted locally at different positions in the beam. The required accuracy is the order of 0.1% of the wavelength. We propose to use the deformable mirrors M4 and M8 for this aim. The error signal for

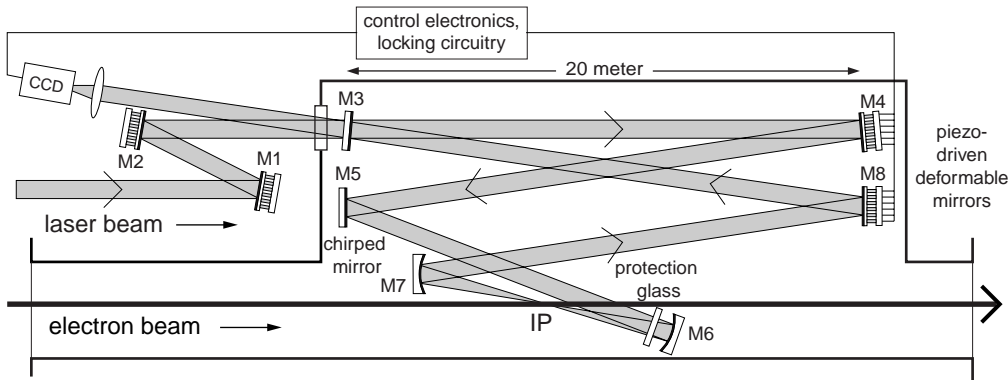


Figure 1.5.5: *External ring cavity for a TESLA photon collider. See comments in the text.*

driving the individual piezo actuators of these mirrors may be obtained by processing the image from a CCD camera located behind the resonator mirror M3. A feedback procedure optimises the coupling of the laser radiation into the cavity and minimises the losses of the stored laser field by adjusting the actuators of M4 and M8 for minimal leakage through M3. In addition, it allows for compensation of wavefront distortions by the optical elements of the cavity and ensures that the travelling optical wave can be focused in an optimum way

The Q factor of the cavity strongly depends on the reflectivity of the mirrors. Mirrors with multilayer coatings of reflectivity greater than 99.9% are already commercially available. The remaining loss in reflection of high-power mirrors is mainly caused by scattering at small impurities in the coatings. Therefore increasing the reflectivity requires to reduce the number of scattering impurities which can only be achieved by very special and expensive coating techniques.

A problem in the realisation of the cavity may be connected with a gradual damage of the coatings by synchrotron radiation and scattered electrons. This damage will lead to a slow reduction of the overall reflectivity of the mirrors thereby reducing the overall Q -factor of the cavity. The effect will be particularly important for the mirror located downstream the electron beam (M6 in Fig. 1.5.5). In order to avoid the damage we propose to protect this mirror with a thin glass plate. This plate should have antireflection coatings and easily exchangeable without misalignment of the cavity.

Taking into account these limitations we have estimated that a quality factor of $Q = 100$ should be within reach. This also complies with the value obtained in already operating external cavities for cw lasers. A $Q \approx 50$ would be sufficient for the photon collider at TESLA.

Because of the high average power and the high stability, the laser has to be laid out in MOPA (Master Oscillator – Power Amplifier) geometry. Probably only diode-pumped solid-state laser systems can reach the required reproducibility of the laser parameters. The most promising candidate for a laser suitable for the TESLA Photon Collider seems to be Ytterbium-doped YAG (Yb:YAG) which has already been used to generate pulses of 0.7 ps duration [216]. It has also been demonstrated that this

material can deliver a very high average laser power of up to 1 kW [217].

1.5.1.3 Laser damage of optics

The peak and average power in the laser system at the Photon Collider is very large. The damage threshold for multilayer dielectric mirrors depends on the pulse duration. The empirical scaling law is [209]

$$E_{th}[\text{J}/\text{cm}^2] \approx 10\sqrt{t[\text{ns}]} \quad (1.5.9)$$

for pulse durations ranging from picoseconds to milliseconds. At the LLNL the damage threshold for 1.8 ps single pulses of 0.7 to 2 J/cm² have been observed on commercial multilayer surfaces [22] with an average flux on the level of 3–5 kW/cm².

Comparing these numbers with the conditions at the TESLA Photon Collider (5 J for 1.5 ps, 6000×5 J for 1 ms and 140 kW average power) one finds that the average power requirements are most demanding. With a uniform distribution, the surface of the mirrors should be larger than 140/5 = 28 cm² and a factor of 2–3 larger for Gaussian laser beams with cut tails. So, the diameter of the laser beam on mirrors and other surfaces should be larger than 10 cm.

Short summary on the optical schemes

We have considered two possible options of laser optics for the TESLA photon collider:

1. Optical trap (storage ring) with about 8 diode pumped driving lasers (final amplifiers) with a total average power of about 12 kW. Beams are merged to one train using Pockels cells and thin-film polarisers. Each laser pulse makes 6 round trips in the optical trap colliding 12 times with the electron beams. This can be done now: all technologies exist.
2. External optical cavity is a very attractive approach which can additionally reduce the cost and complexity of the laser system. This scheme requires very small tolerances (of the order of $\lambda/(2\pi Q)$, where $Q \approx 50$) and very high mirror quality. R&D is required.

1.5.2 The lasers

In this proposal we do not present a detailed scheme of a laser for the TESLA Photon-Collider. It should be an additional R&D. However, we would like to consider briefly existing laser technologies which allow, in principle, the laser system required for the Photon Colliders to be built.

Development of laser technologies is being driven by several large programs, such as inertial fusion. This is a fortunate situation for photon colliders as we may benefit from the laser technology developments of the last 10–15 years which cost hundreds M\$ per year. Now practically all components exist and we can just design and build the

required system. Fortunately this possibility has appeared almost exactly in the time when the physics community is ready for construction of the TESLA Linear Collider. Of course, construction of the laser system for the Photon Collider is not a simple task and needs many efforts.

Two kind of lasers for photon colliders are feasible now: a solid state laser and a free electron laser (FEL).

The technology for production of picosecond pulses with terawatt power has been developed for solid state lasers. The wave length of the most powerful lasers about $1\ \mu\text{m}$ which is just optimum for the TESLA Photon Collider.

A free electron laser (FEL) is also attractive because it has a variable wave length and is based fully on the accelerator technology. The X-ray FEL with a wave length down to 1nm is a part of the TESLA project. The same technology can be used for the construction of an FEL with $1\ \mu\text{m}$ wave length for the Photon Collider. This task is much easier than the X-ray laser.

1.5.2.1 Solid state lasers

In the last decade the technique of short powerful lasers made an impressive step and has reached petawatt (10^{15}) power levels and few femtosecond durations [218]. Obtaining few joule pulses of picosecond duration is not a problem using modern laser techniques. For photon collider applications the main problem is the high repetition rate.

The success in obtaining picosecond pulses is connected with a chirped pulse amplification (CPA) technique [219]. “Chirped” means that the pulse has a time–frequency correlation. The main problem in obtaining short pulses is the limitation on peak power imposed by the nonlinear refractive index. This limit on intensity is about $1\ \text{GW}/\text{cm}^2$. The CPA technique successfully overcomes this limit.

The principle of CPA is demonstrated in Fig. 1.5.6. A short, low energy pulse is generated in an oscillator. Then this pulse is stretched by a factor about 10^4 in the grating pair which introduces a delay proportional to the frequency. This long nanosecond pulse is amplified and then compressed by another grating pair to a pulse with the initial or somewhat longer duration. As nonlinear effects are practically absent, the obtained pulses have a very good quality close to the diffraction limit.

One such laser worked since 1994 in the E–144 experiment at SLAC which studied nonlinear QED effects in the collision of laser photons with $50\ \text{GeV}$ electrons [220]. It has a repetition rate of $0.5\ \text{Hz}$, $\lambda = 1.06\ \mu\text{m}$ (Nd:Glass), $2\ \text{J}$ flash energy, $2\ \text{TW}$ power and $1\ \text{ps}$ duration. This is a table–top laser. Its parameters are very close to our needs, only the repetition rate was low due to overheating. In this laser a flashlamp pumping was used.

The latter problem can be solved using another very nice technique: diode pumping (the diode is a semiconductor laser with high efficiency). Since the frequency of photons from diode lasers coincides almost with the pump frequency of the $1\ \mu\text{m}$ lasers they are very efficient in converting wall plug power to laser light: efficiencies of 10% have been achieved. But even more important the heating of the laser medium with diode

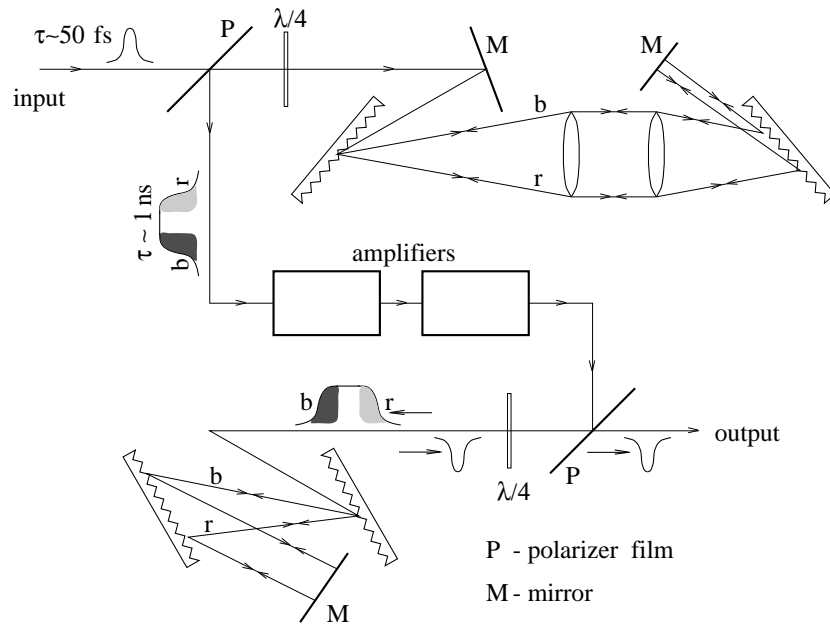


Figure 1.5.6: *Chirped pulse amplification.*

pumping is much lower than with flashlamps. This gives one to two orders increase in repetition rate. Moreover, the flashlamps have a limited lifetime of $< 10^6$ shots, while the lifetime of diodes is many orders of magnitude higher.

The main problem of diodes is their cost. But it decreases very fast. As it was mentioned, their cost is 5 EUR/Watt, the next step in the inertial fusion program assumes the reduction of the cost down to 0.5 EUR/Watt and the final goal is 0.07 EUR/Watt. The cost of diodes for TESLA photon colliders would be about 25 MEUR already with the present cost and a further significant decrease is very likely.

Below is a list of laser technologies important for photon colliders:

- chirped-pulse technique;
- diode pumping;
- laser materials with high thermo-conductivity;
- adaptive optics (deformable mirrors);
- disk amplifiers with gas (helium) cooling;
- large Pockels cells, polarisers;
- high power and high reflectivity multilayer dielectric mirrors;
- anti-reflection coatings.

Non-uniform, train structure of electron bunches at TESLA makes the task somewhat more difficult than it would be for a uniform pulse structure. This leads to rather

high power of pumping diodes (high power inside one train), but as we mentioned this is not a serious problem.

However, generating a 1ms long train with $3000/6 = 500$ pulses, 5 J energy each, is not the same as generation of one 2.5 kJ pulse (4 kJ diode pumped units are developed for laser fusion) for the same time, because the volume of the laser crystal in the first case may be 500 times smaller. Beside, we consider 8 lasers working in parallel.

It is very convenient that the distance between electron bunches at TESLA is large, 337 ns (1.4 ns at NLC and JLC). This time allows to use large Pockels cells for manipulations of high power laser pulses.

At TESLA the train is very long and storage time of laser materials can not be used for pumping the laser medium in advance, but on the other hand, in this case, one can use a large variety of laser materials optimising other parameters (thermal conductivity etc.).

The development of the optimum design of the laser system for the Photon Collider requires special R&D. Solutions should be different for TESLA and NLC/JLC colliders.

1.5.2.2 Free electron lasers

Potential features of a free electron laser (FEL) allow one to consider it as an ideal source of primary photons for a $\gamma\gamma$ collider. Indeed, FEL radiation is tunable and has always minimal (i.e. diffraction) dispersion. The FEL radiation is completely polarised either circularly or linearly for the case of the helical or planar undulator, respectively. A driving accelerator for the FEL may be a modification of the main linear accelerator, thus providing the required time structure of laser pulses. The problem of synchronisation of the laser and electron bunches at the conversion region is solved by means of traditional methods used in accelerator techniques. A FEL amplifier has the potential to provide a high conversion efficiency of the kinetic energy of the electron beam into coherent radiation. At sufficient peak power of the driving electron beam the peak power of the FEL radiation could reach the required TW level.

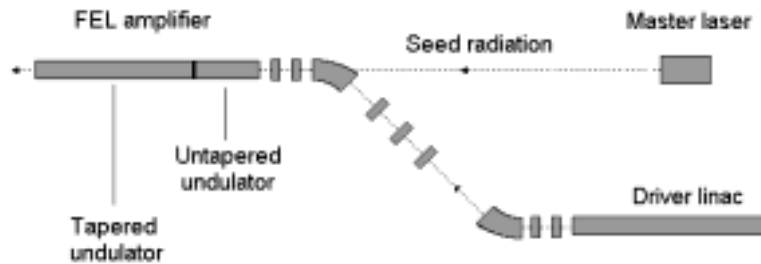


Figure 1.5.7: *Basic scheme of the MOPA laser system for a photon collider.*

The idea to use a FEL as a laser for the $\gamma\gamma$ collider has been proposed in [221]. The present view on FEL systems for the photon collisions at TESLA is discussed in [222]. The FEL system is built as a master oscillator–power amplifier (MOPA) scheme where the low–power radiation from a Nd glass laser ($\lambda = 1 \mu\text{m}$) is amplified in a long tapered

undulator by an electron beam (see Fig. 1.5.7). The driving accelerator has the same pulse structure as the main TESLA linac.

The driving electron beam for the FEL is produced by the accelerator based on TESLA technology and similar to the TTF (TESLA Test Facility) accelerator [223]. Parameters of the accelerator are presented in Table 1. The beam with a charge of 12 nC and normalised emittance of 30π mm mrad is generated in the photoinjector, accelerated in superconducting modules with the gradient 20–25 MV/m and compressed down to a 2 ps duration in the bunch compressors. Note that the emittance is not a critical parameter for the considered FEL. The number of bunches per macropulse is about 3 times lower than that in the TESLA train, but as discussed in the previous section one laser bunch can be used several times for $e \rightarrow \gamma$ conversion.

Energy	1.5 GeV
Charge per bunch	12 nC
Peak current	2.4 kA
Bunch length (RMS)	0.6 mm
Normalised emittance	30π mm mrad
Energy spread (RMS)	1 MeV
Repetition rate	$5H^0$
Macropulse duration	800 μ s
# of bunches per macropulse	1130
Bunch spacing	708 ns
Average beam power	102 kW

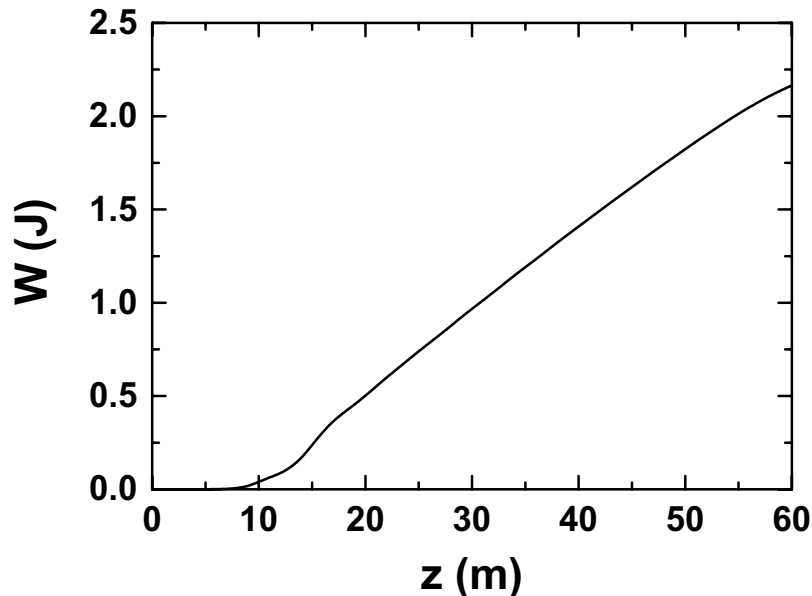
Table 1.5.1: *Parameters of the driving accelerator*

The peak power of the master laser with the wavelength of $1\ \mu\text{m}$ is assumed to be $1m_W$ with a pulse duration of several picoseconds, so that the average power will be below 0.1 W. This means that only a small fraction of the power can be taken from the 2 W of infrared radiation generated in the laser system of the photoinjector. Then this radiation can be transported to the undulator entrance. The problem of synchronisation of electron and optical bunches is therefore solved naturally.

To obtain reasonable luminosity of the $\gamma\gamma$ collider at TESLA, the energy in the radiation pulse at the FEL amplifier exit should be above 2 J and the peak power should reach sub-terawatt level. For the chosen parameters of the electron beam this means that the FEL efficiency must exceed 10%. In an FEL amplifier with a uniform undulator the efficiency is limited by saturation effects and is below 1% in the considered case. Saturation of the radiation power in the FEL amplifier occurs due to the energy loss by the particles which fall out of the resonance with the electromagnetic wave. Nevertheless, effective amplification of the radiation is possible in the nonlinear regime by means of using a tapered undulator. In this case a large fraction of particles is trapped in the effective potential of the interaction with the electromagnetic wave and is decelerated.

Parameters of the FEL amplifier with the tapered undulator are presented in Ta-

<u>Undulator</u>	
Type	Helical
Period	10 cm
Magnetic field (entr./exit)	1.4 T/ 1.08 T
Total length	60 m
Length of untapered section	10.7 m
Beam size in the und. (RMS)	230 μm
<u>Radiation</u>	
Wavelength	1 μm
Dispersion	Dif. limit
Pulse energy	2.2 J
Pulse duration (HWHM)	1.6 ps
Repetition rate	5 Hz
Macropulse duration	800 μs
# of pulses per macropulse	1130
Peak output power	0.7 TW
Average power	12.5 kW
Efficiency	12.2%

Table 1.5.2: *Parameters of the FEL amplifier*Figure 1.5.8: *Energy in the radiation pulse versus the undulator length.*

ble 1.5.2. The tapering can be done by decreasing the magnetic field at fixed undulator period. The undulator is helical to provide polarised radiation and is superconducting. The resonance is maintained by decreasing the magnetic field at fixed period of the undulator.

The dependence of the radiated energy versus the undulator length is shown in Fig. 1.5.8. The efficiency 12.2%, reached in the end of the undulator, corresponds to

2.2 J in the optical pulse.

Use of a free electron laser as a source of primary photons for the $\gamma\gamma$ collider at TESLA seems to be a natural solution. TESLA already includes an integrated X-ray FEL facility. Powerful VUV radiation has been produced at DESY in a SASE FEL with 15 m long undulator [224]. The FEL for the photon colliders is simpler than the X-ray FEL.

Scale and cost of the FEL facility for the Photon Collider can be estimated in a simple way. It requires a 1.5 GeV linear accelerator similar to the main TESLA accelerator and a 60 m long undulator.

Summary on lasers

We have considered briefly two kinds of lasers for the photon collider at TESLA: a solid state laser and a FEL. Both approaches are technically feasible. However, the first one looks somewhat more attractive, because it might be a large room-size system, while a FEL includes a 160 m long accelerator (with wiggler) which would be a large facility. For energies $2E_0 \geq 800$ GeV where longer laser wave length will be required, a FEL may be the best choice.

1.6 Summary

The Photon Collider presents a unique opportunity to study $\gamma\gamma$ and γe interactions at high energies and luminosities, which can considerably enrich the physics program of the e^+e^- linear collider TESLA. The parameters of the super-conducting collider TESLA: the energy, the interval between electron bunches are particularly suited for design and performance of the Photon Collider.

This novel option requires only one new additional element: the powerful laser, which can be built using modern laser technologies. The optimum laser wave length for TESLA is about $1 \mu\text{m}$, which is exactly the region of the most powerful developed solid state lasers.

The second interaction region and the detector may be very similar to those for e^+e^- collisions and can be also be used for study of e^-e^- or e^+e^- interactions.

Bibliography

- [1] I. F. Ginzburg, G. L. Kotkin, V. G. Serbo, and V. I. Telnov. *Pizma ZhETF*, 34:514, 1981. *JETP Lett.* 34:491, 1982. Preprint INP 81-50, Novosibirsk, 1981.
- [2] I. F. Ginzburg, G. L. Kotkin, V. G. Serbo, and V. I. Telnov. *Nucl. Instrum. Meth.*, 205:47, 1983. Preprint INP 81-102, Novosibirsk, 1981.
- [3] I. F. Ginzburg, G. L. Kotkin, S. L. Panfil, V. G. Serbo, and V. I. Telnov. *Nucl. Instrum. Meth.*, A219:5–24, 1984.
- [4] V. I. Telnov. *Nucl. Instrum. Meth.*, A294:72–92, 1990.
- [5] V. I. Telnov. *Nucl. Instrum. Meth.*, A355:3, 1995.
- [6] M. Baillargeon, et al. In P. Zerwas (ed.), *e^+e^- Collisions at TeV Energies: The Physics Potential, Part D*, DESY 96-123D. DESY, 1995.
- [7] I. Ginzburg and V. Serbo. In *Proc. of 23rd Winter School of LINP*, vol. 2, p. 132, 1988.
- [8] I. F. Ginzburg. Physical Potential of Photon-Photon and Electron - Photon Colliders in TeV Region. In D. Caldwell and H. Paar (eds.), *Proc. IX Intern. Workshop on Photon - Photon Collisions, San Diego, CA, USA*, p. 474, 1992. World Scientific.
- [9] V. I. Telnov. In *Proc. of International Conference on the Structure and Interactions of the Photon (Photon 99), Freiburg, Germany*, 2000. Nucl. Phys. Proc. Suppl. 82. hep-ex/9908005.
- [10] V. Telnov. *Int. J. Mod. Phys.*, A13:2399–2410, 1998. hep-ex/9802003.
- [11] A. N. Skrinsky. *Sov. Phys. Usp.*, 25:639–661, 1982.
- [12] V. I. Telnov. $\gamma\gamma$, γe Collision at Linear Colliders. In *Physics and Experiments with Linear Colliders, Saariselka, Finland*, 1992. Ed. R. Orava et al., World Scientific.
- [13] D. L. Borden, D. Bauer, and D. O. Caldwell. *Phys. Rev.*, D48:4018–4028, 1993.
- [14] V. I. Telnov. $\gamma\gamma$, γe at Linear Colliders. In D. Caldwell and H. Paar (eds.), *Proc. IX Intern. Workshop on Photon - Photon Collisions, San Diego, CA, USA*, p. 369, 1992. World Scientific.
- [15] S. J. Brodsky and P. M. Zerwas. *Nucl. Instrum. Meth.*, A355:19–41, 1995. hep-ph/9407362.
- [16] M. Baillargeon, G. Belanger, and F. Boudjema. Electroweak Physics Issues at a High-Energy Photon Collider. 1994. hep-ph/9405359.
- [17] D. J. Miller. Other Options: e^-e^- , $e^-\gamma$ and $\gamma\gamma$ Physics at a Linear Collider. In *3rd Workshop on Physics and Experiments with e^+e^- Linear Colliders (LCWS 95), Iwate, Japan*, p. 305, 1995.

-
- [18] I. Watanabe, et al. $\gamma\gamma$ Collider as an Option of JLC. KEK-REPORT-97-17.
- [19] R. Brinkmann et al. *Nucl. Instrum. Meth.*, A406:13, 1998. hep-ex/9707017.
- [20] A. M. Sessler. *Phys. Today*, 51:48–53, 1998.
- [21] V. Telnov. Photon Collider at TESLA. In *Intern. Workshop on High-Energy Photon Colliders, Hamburg, Germany*, 2000. submitted to Nucl. Instrum. Meth. A. hep-ex/0010033.
- [22] The NLC Design Group. *Zeroth-Order Design Report for the NLC*. LBNL-5424, SLAC-474, UCBL-ID-124161, UC-414. SLAC, <http://www-project.slac.stanford.edu/lc/ZDR/>, 1996.
- [23] R. Brinkmann, G. Materlik, J. Rossbach, and A. Wagner (eds.). *Conceptual Design of a 500 GeV e^+e^- Linear Collider with Integrated X-Ray Laser Facility*. DESY 1997-048, ECFA 1997-182. DESY, 1997.
- [24] N. Akasaka et al. JLC Design Study. KEK-REPORT-97-1.
- [25] *Nucl. Instrum. Meth.*, A355, 1995. Proc. of Workshop on $\gamma\gamma$ Colliders. Berkeley CA, USA, 1994.
- [26] *International Workshop On High-Energy Photon Colliders (GG 2000), Hamburg, Germany*, 2000. To be published in Nucl. Instrum. Meth. A, <http://www.desy.de/gg2000/>.
- [27] I. Ginzburg. In *Proc. of International Conference on the Structure and Interactions of the Photon (Photon 99), Freiburg, Germany, 23-27 May 1999*, 2000. Nucl. Phys. Proc. Suppl. 82:367. hep-ex/9907549.
- [28] B. Pietrzyk. The Global Fit to Electroweak Data. In *Proc. 30th International Conference on High-Energy Physics (ICHEP 2000), Osaka, Japan*, 2000. LAPP-EXP-2000-06.
- [29] P. Igo-Kemenes. For the LEP Working Group on Higgs boson search, talk at the LEPC open session on Nov. 3rd, 2000, <http://lephiggs.web.cern.ch/LEPHIGGS/talks/index.html>.
- [30] ALEPH-Collaboration: R. Barate et al. *Phys. Lett.*, B495:1–17, 2000. hep-ex/0011045.
- [31] L3-Collaboration: M. Acciarri et al. *Phys. Lett.*, B495:18–25, 2000. hep-ex/0011043.
- [32] S. Heinemeyer, W. Hollik, and G. Weiglein. *Eur. Phys. J.*, C9:343, 1999. hep-ph/9812472.
- [33] H. E. Haber. How well can we predict the Mass of the Higgs Boson of the Minimal Supersymmetric Model? In *Proceedings of 4th International Symposium on Radiative Corrections (RADCOR 98): Applications of Quantum Field Theory to Phenomenology, Barcelona, Spain*, 1999. hep-ph/9901365.
- [34] T. Barklow. In *Research Directions for the Decade. Proceedings, Summer Study*

- on *High-Energy Physics, Snowmass, USA*, p.440, 1990.
- [35] J. F. Gunion and H. E. Haber. In *Research Directions for the Decade. Proceedings, Summer Study on High-Energy Physics, Snowmass, USA*, p. 206, 1990.
- [36] J. F. Gunion and H. E. Haber. *Phys. Rev.*, D48:5109–5120, 1993.
- [37] D. L. Borden, D. A. Bauer, and D. O. Caldwell. *Phys. Rev.*, D48:4018–4028, 1993.
- [38] T. Ohgaki. *Int. J. Mod. Phys.*, A15:2587, 2000. physics/0002020.
- [39] V. I. Telnov. Gamma Gamma, Gamma Electron Colliders. In *17th International Conference on High-Energy Accelerators (HEACC 98), Dubna, Russia*, p. 98, 1998. hep-ex/9810019.
- [40] J. F. Gunion, L. Poggioli, R. V. Kooten, C. Kao, and P. Rowson. Higgs Boson Discovery and Properties. In *1996 DPF / DPB Summer Study on New Directions for High-Energy Physics (Snowmass 96), Snowmass, CO, USA*, 1996. hep-ph/9703330.
- [41] H. E. Haber. Challenges for Non-Minimal Higgs Searches at Future Colliders. In *Beyond the Standard Model Conf., Lake Tahoe, CA, Dec 13-18, 1994 and Ringsberg Workshop on Perspectives for Electroweak Interactions in e^+e^- Collisions, Ringsberg, Germany, 5-8 Feb 1995.*, 1995. Published in Ringsberg Electroweak 1995:219-232. hep-ph/9505240.
- [42] A. Djouadi, V. Driesen, W. Hollik, and J. I. Illana. *Eur. Phys. J.*, C1:149–162, 1998. hep-ph/9612362.
- [43] B. Grzadkowski and J. F. Gunion. *Phys. Lett.*, B294:361–368, 1992. hep-ph/9206262.
- [44] J. F. Gunion and J. G. Kelly. *Phys. Lett.*, B333:110–117, 1994. hep-ph/9404343.
- [45] M. Krämer, J. Kühn, M. L. Stong, and P. M. Zerwas. *Z. Phys.*, C64:21–30, 1994. hep-ph/9404280.
- [46] S. Söldner-Rembold and G. Jikia. Light Higgs production at a Photon Collider. In *Intern. Workshop on High-Energy Photon Colliders, Hamburg, Germany*, 2000. submitted to Nucl. Instrum. Meth. A. See [26].
- [47] M. Melles, W. J. Stirling, and V. A. Khoze. *Phys. Rev.*, D61:054015, 2000. hep-ph/9907238.
- [48] T. Ohgaki, T. Takahashi, and I. Watanabe. *Phys. Rev.*, D56:1723–1729, 1997. hep-ph/9703301.
- [49] T. Ohgaki, T. Takahashi, I. Watanabe, and T. Tauchi. *Int. J. Mod. Phys.*, A13:2411, 1998.
- [50] M. Melles. Precision Higgs Physics at a $\gamma\gamma$ Collider. In *Intern. Workshop on High-Energy Photon Colliders, Hamburg, Germany*, 2000. submitted to

- Nucl. Instrum. Meth. A. hep-ph/0008125.
- [51] M. Melles. In *International Conference on the Structure and Interactions of the Photon (Photon 99), Freiburg, Germany and 4th International Workshop on Linear Colliders (LCWS 99), Sitges, Spain*, p. 379, 2000. Nucl. Phys. Proc. Suppl. 82. hep-ph/9906467.
- [52] K. A. Ispirian, I. A. Nagorskaya, A. G. Oganessian, and V. A. Khoze. *Yad. Fiz.*, 11:1278–1283, 1970.
- [53] K. A. Ispirian, I. A. Nagorskaya, A. G. Oganessian, and V. A. Khoze. *Sov. J. Nucl. Phys.*, 11:712, 1970.
- [54] G. Jikia and S. Söldner-Rembold. *Nucl. Phys. Proc. Suppl.*, 82:373–378, 2000. hep-ph/9910366.
- [55] G. Jikia and A. Tkabladze. *Nucl. Instrum. Meth.*, A355:81–83, 1995. hep-ph/9406428.
- [56] G. Jikia and A. Tkabladze. *Phys. Rev.*, D54:2030–2042, 1996. hep-ph/9601384.
- [57] D. L. Borden, V. A. Khoze, W. J. Stirling, and J. Ohnemus. *Phys. Rev.*, D50:4499–4507, 1994. hep-ph/9405401.
- [58] V. A. Khoze. On Measuring the Gamma Gamma Width of the Intermediate Mass Higgs at a Photon Linear Collider. In *Photon '95. 10th International Workshop on Gamma Gamma Collisions and Related Processes, Sheffield, UK*, p. 392, 1995. World Scientific, Singapore. hep-ph/9504348.
- [59] M. Melles and W. J. Stirling. *Nucl. Phys.*, B564:325–342, 2000. hep-ph/9903507.
- [60] M. Melles and W. J. Stirling. *Eur. Phys. J.*, C9:101–106, 1999. hep-ph/9810432.
- [61] M. Melles and W. J. Stirling. *Phys. Rev.*, D59:094009, 1999. hep-ph/9807332.
- [62] M. Battaglia. Measuring Higgs Branching Ratios and Telling the SM from a MSSM Higgs Boson at the e^+e^- Linear Collider. In E. Fernández and A. Pacheco (eds.), *Proceedings of the Worldwide Study on Physics and Experiments with Future Linear e^+e^- Colliders*, p. 163, Sitges, Spain, 1999. Universitat Autònoma de Barcelona. hep-ph/9910271.
- [63] D. A. Morris, T. N. Truong, and D. Zappala. *Phys. Lett.*, B323:421–426, 1994. hep-ph/9310244.
- [64] I. F. Ginzburg and I. P. Ivanov. *Phys. Lett.*, B408:325–330, 1997. hep-ph/9704220.
- [65] E. Boos, et al. *Phys. Lett.*, B427:189–196, 1998. hep-ph/9801359.
- [66] E. Boos, et al. Higgs to WW^* in Gamma Gamma Collisions. In E. Fernández and A. Pacheco (eds.), *Proceedings of the Worldwide Study on Physics and Experiments with Future Linear e^+e^- Colliders*, vol. I, p. 498, Sitges, Spain, 1999. Universitat Autònoma de Barcelona.

- [67] G. V. Jikia. *Phys. Lett.*, B298:224–229, 1993.
- [68] G. Jikia. *Nucl. Phys.*, B405:24–54, 1993.
- [69] M. S. Berger. *Phys. Rev.*, D48:5121–5126, 1993. hep-ph/9307259.
- [70] D. A. Dicus and C. Kao. *Phys. Rev.*, D49:1265–1271, 1994. hep-ph/9308330.
- [71] E. Boos, J. C. Brient, D. W. Reid, H. J. Schreiber, and R. Shanidze. Measuring the Higgs Branching Fraction into Two Photons at Future Linear e^+e^- Colliders. 2000. hep-ph/0011366.
- [72] D. W. Reid. Measurement of the Branching Ratio $B(H \rightarrow \gamma\gamma)$. In E. Fernández and A. Pacheco (eds.), *Proceedings of the Worldwide Study on Physics and Experiments with Future Linear e^+e^- Colliders*, vol. I, p. 179, Sitges, Spain, 1999. Universitat Autònoma de Barcelona.
- [73] M. M. Mühlleitner. Production of MSSM Higgs Bosons in Gamma-Gamma Collisions. In *Intern. Workshop on High-Energy Photon Colliders, Hamburg, Germany*, 2000. submitted to Nucl. Instrum. Meth. A. See [26].
- [74] M. M. Mühlleitner, M. Krämer, M. Spira, and P. M. Zerwas. Production of MSSM Higgs bosons in photon photon collisions. 2001. hep-ph/0101083.
- [75] ATLAS Collaboration. ATLAS: Detector and Physics Performance Technical Design Report. *CERN*, LHCC 99-14, 1999. <http://atlasinfo.cern.ch/Atlas/GROUPS/PHYSICS/TDR/access.html>.
- [76] CMS Collaboration. The Compact Muon Solenoid, Technical Proposal. *CERN*, LHCC 94-38, 1994. <http://cmsinfo.cern.ch/TP/TP.html>.
- [77] A. Djouadi, J. Kalinowski, P. Ohmann, and P. M. Zerwas. *Z. Phys.*, C74:93–111, 1997. hep-ph/9605339.
- [78] ECFA/DESY LC Physics Working Group-Collaboration: E. Accomando et al. *Phys. Rept.*, 299:1–78, 1998. hep-ph/9705442.
- [79] P. M. Zerwas. Physics with an e^+e^- Linear Collider at High Luminosity. In B. B. Levchenko and V. I. Savrin (eds.), *14th International Workshop On High Energy Physics And Quantum Field Theory*, Moscow, Russia, 2000. hep-ph/0003221.
- [80] M. M. Mühlleitner. *Higgs Particles in the Standard Model and Supersymmetric Theories*. Ph.D. thesis, 2000. hep-ph/0008127.
- [81] C. N. Yang. *Phys. Rev.*, 77:242–245, 1950.
- [82] S. Y. Choi and K. Hagiwara. *Phys. Lett.*, B359:369–374, 1995. hep-ph/9506430.
- [83] J. I. Illana. Resonant Production of Heavy MSSM Higgs Bosons at the Photon Collider. In *4th Workshop on Physics and Detectors for a Linear Electron Positron Collider (2nd Joint ECFA / DESY Study)*, Oxford, England, 1999. hep-ph/9912467.

-
- [84] I. F. Ginzburg and I. P. Ivanov. CP Odd Anomalous Interactions of Higgs Boson in its Production at Photon Colliders. 2000. hep-ph/0004069.
- [85] E. Asakawa. Heavy Higgs Productions at Gamma Gamma Colliders. In E. Fernández and A. Pacheco (eds.), *Proceedings of the Worldwide Study on Physics and Experiments with Future Linear e^+e^- Colliders*, Sitges, Spain, 1999. Universitat Autònoma de Barcelona. hep-ph/9908457.
- [86] E. Asakawa, J. Kamoshita, A. Sugamoto, and I. Watanabe. *Eur. Phys. J.*, C14:335–345, 2000. hep-ph/9912373.
- [87] I. F. Ginzburg, M. Krawczyk, and P. Osland. Potential of Photon Colliders in Resolving SM-like Scenarios. In *Intern. Workshop on High-Energy Photon Colliders, Hamburg, Germany*, 2000. submitted to Nucl. Instrum. Meth. A. See [26].
- [88] I. F. Ginzburg, M. Krawczyk, and P. Osland. In *Linear Collider Workshop, FNAL, Batavia, IL, USA*, 2000. American Institute of Physics. To be published, see <http://www-lc.fnal.gov/lcws2000>.
- [89] E. Asakawa, S. Y. Choi, K. Hagiwara, and J. S. Lee. *Phys. Rev.*, D62:115005, 2000. hep-ph/0005313.
- [90] M. Klasen. Sfermion Production at Photon Colliders. In *Intern. Workshop on High-Energy Photon Colliders, Hamburg, Germany*, 2000. submitted to Nucl. Instrum. Meth. A. hep-ph/0008082.
- [91] T. Mayer and H. Fraas. Chargino Production and Decay in Photon-Photon-Collisions. In *Intern. Workshop on High-Energy Photon Colliders, Hamburg, Germany*, 2000. submitted to Nucl. Instrum. Meth. A. hep-ph/0009048.
- [92] F. Cuypers, G. J. van Oldenborgh, and R. Rückl. *Nucl. Phys.*, B383:45–57, 1992. hep-ph/9205209.
- [93] F. Cuypers, G. J. van Oldenborgh, and R. Rückl. *Nucl. Phys.*, B409:144–160, 1993. hep-ph/9302302.
- [94] F. Cuypers. *Phys. Rev.*, D49:3075–3078, 1994. hep-ph/9310327.
- [95] A. Goto and T. Kon. *Europhys. Lett.*, 19:575–580, 1992.
- [96] T. Kon and A. Goto. *Phys. Lett.*, B295:324–329, 1992.
- [97] C. Blöchinger, F. Franke, and H. Fraas. Distinguishing between MSSM and NMSSM with e Gamma Scattering. In *Intern. Workshop on High-Energy Photon Colliders, Hamburg, Germany*, 2000. submitted to Nucl. Instrum. Meth. A. hep-ph/0008167.
- [98] C. Blöchinger and H. Fraas. Possible test of the GUT relation between M_1 and M_2 in Electron-Photon scattering. LC-TH-2000-017.
- [99] D. S. Gorbunov, V. A. Ilyin, and V. I. Telnov. TESLA: Potentials of Gamma

- Gamma and e^+e^- Options in Stopped Searches. In *Intern. Workshop on High-Energy Photon Colliders, Hamburg, Germany*, 2000. submitted to Nucl. Instrum. Meth. A. hep-ph/0012175.
- [100] N. Arkani-Hamed, S. Dimopoulos, and G. Dvali. *Phys. Lett.*, B429:263–272, 1998. hep-ph/9803315.
- [101] N. Arkani-Hamed, S. Dimopoulos, and G. Dvali. *Phys. Rev.*, D59:086004, 1999. hep-ph/9807344.
- [102] I. Antoniadis, N. Arkani-Hamed, S. Dimopoulos, and G. Dvali. *Phys. Lett.*, B436:257–263, 1998. hep-ph/9804398.
- [103] G. F. Giudice, R. Rattazzi, and J. D. Wells. *Nucl. Phys.*, B544:3–38, 1999. hep-ph/9811291.
- [104] T. Han, J. D. Lykken, and R.-J. Zhang. *Phys. Rev.*, D59:105006, 1999. hep-ph/9811350.
- [105] E. A. Mirabelli, M. Perelstein, and M. E. Peskin. *Phys. Rev. Lett.*, 82:2236–2239, 1999. hep-ph/9811337.
- [106] J. L. Hewett. *Phys. Rev. Lett.*, 82:4765–4768, 1999. hep-ph/9811356.
- [107] T. G. Rizzo. Indirect Collider Tests for Large Extra Dimensions. In H. Klapdor-Kleingrothaus and I. Krivosheina (eds.), *2nd International Conference Physics Beyond the Standard Model: Beyond the Desert 99: Accelerator, Nonaccelerator and Space Approaches*, Bristol, England, 1999. IOP. hep-ph/9910255.
- [108] T. G. Rizzo. New Physics Beyond the Standard Model at Gamma Gamma Colliders. In *Intern. Workshop on High-Energy Photon Colliders, Hamburg, Germany*, 2000. submitted to Nucl. Instrum. Meth. A. hep-ph/0008037.
- [109] T. G. Rizzo. *Phys. Rev.*, D60:115010, 1999. hep-ph/9904380.
- [110] K. Cheung. *Phys. Rev.*, D61:015005, 2000. hep-ph/9904266.
- [111] H. Davoudiasl. *Int. J. Mod. Phys.*, A15:2613, 2000. hep-ph/0001248.
- [112] I. F. Ginzburg, G. L. Kotkin, S. L. Panfil, and V. G. Serbo. *Nucl. Phys.*, B228:285, 1983.
- [113] I. F. Ginzburg, G. L. Kotkin, S. L. Panfil, and V. G. Serbo. *Nucl. Phys.*, B243:550, 1984.
- [114] T. Takahashi. In *Workshop on Physics and Experiments with Linear Colliders, Marioka-Appi, Japan*, p. 681, 1996. World Scientific.
- [115] I. F. Ginzburg. In F. Harris, S. Olsen, S. Pakvasa, and X. Tata (eds.), *Physics and Experiments with Linear e^+e^- Colliders, Waikoloa, USA*, vol. v, II, p. 739, 1993. World Scientific.
- [116] I. F. Ginzburg, V. A. Ilyin, A. E. Pukhov, V. G. Serbo, and S. A. Shichanin.

- Phys. Atom. Nucl.*, 56:1481–1486, 1993.
- [117] I. F. Ginzburg. *Nucl. Instrum. Meth.*, A355:63–74, 1995.
- [118] I. F. Ginzburg. Why Photon Colliders are Necessary in a Future Collider Program. In *Intern. Workshop on High-Energy Photon Colliders, Hamburg, Germany*, 2000. submitted to *Nucl. Instrum. Meth. A*. hep-ph/0101029.
- [119] M. Baillargeon, G. Belanger, and F. Boudjema. *Nucl. Phys.*, B500:224, 1997. hep-ph/9701372.
- [120] F. Boudjema. In *Workshop on e^+e^- Collisions at 500 GeV: The Physics Potential*, 1992.
- [121] M. Baillargeon, G. Belanger, and F. Boudjema. Electroweak Physics Issues at a High-Energy Photon Collider. 1994. hep-ph/9405359.
- [122] S. J. Brodsky. Photon-Photon Collisions at the Next Linear Collider: Theory. In F. A. Harris, S. Olsen, S. Pakvasa, and X. Tata (eds.), *Physics and Experiments with Linear e^+e^- Colliders, Waikoloa, HI, USA*, p. 295, 1993. World Scientific.
- [123] G. Jikia. *Nucl. Instrum. Meth.*, A355:84–88, 1995. hep-ph/9406395.
- [124] G. Jikia. *Nucl. Phys.*, B437:520–540, 1995. hep-ph/9407393.
- [125] K. Cheung. *Phys. Lett.*, B323:85–89, 1994. hep-ph/9310340.
- [126] K. Cheung. *Phys. Rev.*, D50:4290–4298, 1994. hep-ph/9406228.
- [127] R. D. Peccei and X. Zhang. *Nucl. Phys.*, B337:269–283, 1990.
- [128] R. D. Peccei, S. Peris, and X. Zhang. *Nucl. Phys.*, B349:305–322, 1991.
- [129] J. L. Hewett. *Int. J. Mod. Phys.*, A13:2389–2398, 1998. hep-ph/9803369.
- [130] E. E. Boos. Top Quarks at Photon Colliders. In *Intern. Workshop on High-Energy Photon Colliders, Hamburg, Germany*, 2000. submitted to *Nucl. Instrum. Meth. A*. hep-ph/0009100.
- [131] A. Djouadi, J. Ng, and T. G. Rizzo. New Particles and Interactions. In T. Barklow, S. Dawson, H. Haber, and J. Seigrist (eds.), *Electroweak Symmetry Breaking and Beyond the Standard Model*, 1995. World Scientific. hep-ph/9504210.
- [132] P. Poulose and S. D. Rindani. *Phys. Lett.*, B452:347–354, 1999. hep-ph/9809203.
- [133] S. Y. Choi and K. Hagiwara. *Phys. Lett.*, B359:369–374, 1995. hep-ph/9506430.
- [134] M. S. Baek, S. Y. Choi, and C. S. Kim. *Phys. Rev.*, D56:6835–6855, 1997. hep-ph/9704312.
- [135] E. Boos, M. Dubinin, A. Pukhov, M. Sachwitz, and H. J. Schreiber. In preparation.

-
- [136] G. V. Jikia. *Nucl. Phys.*, B374:83–98, 1992.
- [137] E. Yehudai, S. Godfrey, and K. A. Peterson. Single Top Production in e Gamma Collisions. In F. Harris, S. Olsen, S. Pakvasa, and X. Tata (eds.), *Physics and Experiments with Linear e^+e^- Colliders, Waikoloa, HI, USA*, 1993. World Scientific. hep-ph/9308281.
- [138] E. Boos, A. Pukhov, M. Sachwitz, and H. J. Schreiber. Single Top and Light Higgs at TeV Energy Gamma e Colliders. In *4th Workshop on Physics and Detectors for a Linear Electron Positron Collider (1st Joint ECFA / DESY Study)*, Hamburg, Germany, 1996. hep-ph/9711253.
- [139] E. Boos, A. Pukhov, M. Sachwitz, and H. J. Schreiber. *Phys. Lett.*, B404:119–123, 1997. hep-ph/9704259.
- [140] J.-J. Cao, J.-X. Wang, J. M. Yang, B.-L. Young, and X.-M. Zhang. *Phys. Rev.*, D58:094004, 1998. hep-ph/9804343.
- [141] E. Boos, L. Dudko, and T. Ohl. *Eur. Phys. J.*, C11:473–484, 1999. hep-ph/9903215.
- [142] E. Boos, M. Dubinin, M. Sachwitz, and H. J. Schreiber. *Eur. Phys. J.*, C16:269–278, 2000. hep-ph/0001048.
- [143] R. Godbole and G. Pancheri. Gamma-Gamma Cross Section at Gamma-Gamma Colliders. In *Intern. Workshop on High-Energy Photon Colliders, Hamburg, Germany*, 2000. submitted to Nucl. Instrum. Meth. A. hep-ph/0101320.
- [144] I. F. Ginzburg, S. L. Panfil, and V. G. Serbo. *Nucl. Phys.*, B284:685–705, 1987.
- [145] I. F. Ginzburg, S. L. Panfil, and V. G. Serbo. *Nucl. Phys.*, B296:569–581, 1988.
- [146] I. F. Ginzburg, D. Y. Ivanov, and V. G. Serbo. *Phys. Atom. Nucl.*, 56:1474–1480, 1993.
- [147] A. Vogt. *Nucl. Phys. Proc. Suppl.*, 82:394–399, 2000. hep-ph/9908315.
- [148] A. Gehrmann-De Ridder, H. Spiesberger, and P. M. Zerwas. *Phys. Lett.*, B469:259–262, 1999. hep-ph/9909230.
- [149] P. Aurenche et al. *Prog. Theor. Phys.*, 92:175–188, 1994. hep-ph/9401269.
- [150] M. Klasen, T. Kleinwort, and G. Kramer. *Eur. Phys. J. Direct*, C1:1–105, 1998. hep-ph/9712256.
- [151] M. Drees, M. Krämer, J. Zunft, and P. M. Zerwas. *Phys. Lett.*, B306:371–378, 1993.
- [152] T. Wengler and A. D. Roeck. The Gluon Content of the Photon from Di-Jet Production at the Photon Photon Collider. In *Intern. Workshop on High-Energy Photon Colliders, Hamburg, Germany*, 2000. submitted to Nucl. Instrum. Meth. A. hep-ph/0010293.

- [153] P. Jankowski, M. Krawczyk, and A. D. Roeck. Charm Production at a Linear e^+e^- and Photon Collider and its Sensitivity to the Gluon Content of the Photon. In *Intern. Workshop on High-Energy Photon Colliders, Hamburg, Germany*, 2000. submitted to Nucl. Instrum. Meth. A. See [26].
- [154] M. Stratmann and W. Vogelsang. *Phys. Lett.*, B386:370–378, 1996. hep-ph/9606346.
- [155] M. Stratmann. *Nucl. Phys. Proc. Suppl.*, 82:400–406, 2000. hep-ph/9907467.
- [156] M. Stratmann. Determining the Spin Structure of the Photon at Future Colliders. 2000. hep-ph/0006285.
- [157] J. Kwiecinski and B. Ziaja. QCD Predictions for Spin Dependent Photonic Structure Function $g_1(\gamma)(x, Q^2)$ in the Low x Region of Future Linear Colliders. 2000. hep-ph/0006292.
- [158] J. Kwiecinski and B. Ziaja. QCD Predictions for the Spin Dependent Structure Function $g_1(\gamma)(x, Q^2)$ of the Photon in the Low x Region of $e\gamma$ Colliders. In *Intern. Workshop on High-Energy Photon Colliders, Hamburg, Germany*, 2000. submitted to Nucl. Instrum. Meth. A. See [26].
- [159] J. Kwiecinski and L. Motyka. *Phys. Lett.*, B438:203–210, 1998. hep-ph/9806260.
- [160] J. Kwiecinski, L. Motyka, and A. D. Roeck. The QCD Pomeron at TESLA: Motivation and Exclusive j/ψ Production. In *5th Workshop on Physics and Detectors for a Linear Electron Positron Collider (2nd Joint ECFA / DESY Study)*, Obernai, France, 1999. hep-ph/0001180.
- [161] J. Blümlein and A. Kryukov. In *Intern. Workshop on High-Energy Photon Colliders, Hamburg, Germany*, 2000. submitted to Nucl. Instrum. Meth. A. hep-ph/0008097.
- [162] A. F. Zarnecki. In *Intern. Workshop on High-Energy Photon Colliders, Hamburg, Germany*, 2000. submitted to Nucl. Instrum. Meth. A. hep-ph/0006335.
- [163] I. F. Ginzburg and S. L. Panfil. *Yad. Fiz.*, 36:1461, 1982.
- [164] I. F. Ginzburg and A. Schiller. *Phys. Rev.*, D60:075016, 1999. hep-ph/9903314.
- [165] E. Feenberg and H. Primakoff. *Phys. Rev.*, 73:449, 1948.
- [166] F. R. Arutyunian and V. A. Tumanian. *Phys. Lett.*, 4:176, 1963.
- [167] R. H. Milburn. *Phys. Rev. Lett.*, 10:75, 1963.
- [168] O. F. Kulikov et al. *Phys. Lett.*, 13:344, 1964.
- [169] J. Ballam et al. *Phys. Rev. Lett.*, 23:498, 1969.
- [170] V. B. Berestetskii, E. M. Lifshitz, and L. P. Pitaevskii. *Quantum electrodynamics*. Pergamon Press, Oxford, 1982.
- [171] I. F. Ginzburg, G. L. Kotkin, and S. I. Polityko. *Sov. J. Nucl. Phys.*, 37:222,

- 1983.
- [172] I. F. Ginzburg, S. I. Polityko, and G. L. Kotkin. *Yad. Fiz.*, 40:1495, 1984.
- [173] I. F. Ginzburg, G. L. Kotkin, and S. I. Polityko. *Phys. Atom. Nucl.*, 56:1487–1493, 1993.
- [174] M. Galynskii, E. Kuraev, M. Levchuk, and V. I. Telnov. In *Intern. Workshop on High-Energy Photon Colliders, Hamburg, Germany, 2000*. submitted to Nucl. Instrum. Meth. A. hep-ph/0012338.
- [175] V. M. Budnev, I. F. Ginzburg, G. V. Meledin, and V. G. Serbo. *Phys. Rept.*, 15:181–281, 1974.
- [176] G. L. Kotkin and V. G. Serbo. *Phys. Lett.*, B413:122–129, 1997. hep-ph/9611345.
- [177] V. I. Telnov. In *Proc. of Intern. Vavilov’s Conference on Nonlinear Optics, Novosibirsk*, 1998. Proc. SPIE Int. Soc. Opt. Eng. 3485:13-24. physics/9710014.
- [178] V. I. Telnov. *Physics of Vibration*, 6:168, 1998.
- [179] G. L. Kotkin, H. Perl, and V. G. Serbo. *Nucl. Instrum. Meth.*, A404:430, 1998. hep-ph/9706405.
- [180] G. L. Kotkin, S. I. Polityko, and V. G. Serbo. *Nucl. Instrum. Meth.*, A405:30, 1998.
- [181] M. V. Galynskii and S. M. Sikach. *Zh. Eksp. Teor. Fiz.*, 101:828–837, 1992.
- [182] R. B. Palmer. Energy Scaling, Crab Crossing and the Pair Problem. In *DPF Summer Study Snowmass ’88: High Energy Physics in the 1990’s, Snowmass, Colo., Jun 27 - Jul 15, 1988*, SLAC-PUB 4707.
- [183] P. Chen and V. I. Telnov. *Phys. Rev. Lett.*, 63:1796, 1989.
- [184] V. I. Telnov. In *Proc. of ITP Workshop “Future High Energy Colliders, Santa Barbara, CA, USA, 1996*. AIP Conf. Proc. 397:259-273. physics/9706003.
- [185] V. I. Telnov. *Proc. of Workshop ‘Photon 95’, Sheffield, UK*, 1995.
- [186] R. J. Noble. *Nucl. Instrum. Meth.*, A256:427, 1987.
- [187] K. Yokoya and P. Chen. Beam-Beam Phenomena in Linear Colliders. In *1990 US-CERN School on Particle Accelerators, Hilton Head Isl., SC, USA*. Tsukuba KEK - KEK-Prepr.-91-002 (91/04,rec.Jul.) 36 p.
- [188] V. Balakin and N. Solyak. Preprint INF 82-123, Novosibirsk,1982.
- [189] V. Balakin and N. Solyak. In *8th All Union Workshop on Ch. Part. Accel., Dubna, Russia*, vol. 2, p. 263, 1983.
- [190] V. Balakin and N. Solyak. In *8th Int. Conf. on High Energy Accel., Novosibirsk, Russia*, p. 151, 1987.
- [191] T. Takahashi, K. Yokoya, V. I. Telnov, M. Xie, and K. Kim. *Proc. of Snowmass*

- Workshop*, 1996.
- [192] P. Chen, T. Ohgaki, A. Spitkovsky, T. Takahashi, and K. Yokoya. *Nucl. Instrum. Meth.*, A397:458, 1997. physics/9704012.
- [193] V. I. Telnov. *Phys. Rev. Lett.*, 78:4757–4760, 1997. Erratum: *Phys. Rev. Lett.* 80:2747, 1998, hep-ex/9610008.
- [194] V. I. Telnov. Electron Photon Interactions in High Energy Beam Production and Cooling. In *Proc. Advanced ICFE Workshop on Quantum aspects of beam physics, Monterey, CA, USA*, p. 173, 1998. hep-ex/9805002.
- [195] V. I. Telnov. *Nucl. Instrum. Meth.*, A455:63–69, 2000. hep-ex/0001029.
- [196] M. Ferrario. In *Intern. Workshop on High-Energy Photon Colliders, Hamburg, Germany*, 2000. submitted to Nucl. Instrum. Meth. A. See [26].
- [197] W. Decking. In *Intern. Workshop on High-Energy Photon Colliders, Hamburg, Germany*, 2000. submitted to Nucl. Instrum. Meth. A. See [26].
- [198] K. Hirata, K. Oide, and B. Zotter. *Phys. Lett.*, B224:437, 1989.
- [199] N. Walker. In *Intern. Workshop on High-Energy Photon Colliders, Hamburg, Germany*, 2000. submitted to Nucl. Instrum. Meth. A. See [26].
- [200] P. Raimondi and A. Seryi. A Novel Final Focus Design for Future Linear Colliders. SLAC-PUB-8460.
- [201] A. Seryi. private communication.
- [202] V. I. Telnov. In *Workshop on Physics and Exper. with Linear e^+e^- Colliders, Waikoloa, USA*, p. 323, 1993. World Scientific.
- [203] D. J. Miller. *Nucl. Instrum. Meth.*, A355:101, 1995.
- [204] Y. Yasui, I. Watanabe, J. Kodaira, and I. Endo. *Nucl. Instrum. Meth.*, A335:385–396, 1993. hep-ph/9212312.
- [205] C. Carimalo, W. da Silva, and F. Kapusta. In *Intern. Workshop on High-Energy Photon Colliders, Hamburg, Germany*, 2000. submitted to Nucl. Instrum. Meth. A. See [26].
- [206] M. Battaglia, A. Andreazza, M. Caccia, and V. I. Telnov. Studies on the Vertex Tracker Design and Backgrounds at the High Energy e^+e^- Linear Collider. In *2nd Workshop on Backgrounds at Machine Detector Interface, Honolulu, HI*, 1997. HIP-1997-522-exp.
- [207] G. A. Schuler and T. Sjostrand. *Z. Phys.*, C73:677, 1997. hep-ph/9605240.
- [208] V. I. Telnov. Gamma Gamma, Gamma Electron Colliders: Physics, Luminosities, Backgrounds. In E. Fernández and A. Pacheco (eds.), *Proceedings of 4th International Workshop on Linear Colliders (LCWS 99), Sitges, Spain*, 1999. Universitat Autònoma de Barcelona. hep-ex/9910010.
- [209] W. Koechner. *Solid State Laser Engineering*. Springer-Verlag.

-
- [210] J. Gronberg. In *Intern. Workshop on High-Energy Photon Colliders, Hamburg, Germany*, 2000. submitted to Nucl. Instrum. Meth. A. See [26].
- [211] S. A. Payne, C. Bibeau, C. D. Marshall, and H. T. Powell. *UCRL-JC-119366*, 1998.
- [212] I. Will, T. Quast, H. Redlin, and W. Sandner. In *Intern. Workshop on High-Energy Photon Colliders, Hamburg, Germany*, 2000. submitted to Nucl. Instrum. Meth. A. See [26].
- [213] M. Persaud, J. Tolchard, and A. Ferguson. *IEEE J. Quantum. Electron*, 26:1253, 1990.
- [214] S. Tiedwell, J. Seamans, D. Lowenthal, G. Matone, and G. Giordano. *Opt. Lett.*, 18:1517, 1993.
- [215] O. Martinez, J. Gordon, and R. Fork. *Opt. Soc. Am.*, A1:1003, 1984.
- [216] J. A. der Au, et al. *Opt. Lett.*, 25:859, 2000.
- [217] E. Honea, et al. *Opt. Lett.*, 25:805, 2000.
- [218] M. Perry and G. Mourou. *Science*, 264:917, 1994.
- [219] D. Strickland and G. Mourou. *Opt. Commun.*, 56:219, 1985.
- [220] C. Bamber et al. *Phys. Rev.*, D60:092004, 1999.
- [221] A. M. Kondratenko, E. V. Pakhtusova, and E. L. Saldin. *Sov. Phys. Dokl.*, 27:476, 1982.
- [222] E. L. Saldin, E. A. Schneidmiller, and M. V. Yurkov. In *Intern. Workshop on High-Energy Photon Colliders, Hamburg, Germany*, 2000. submitted to Nucl. Instrum. Meth. A. See [26].
- [223] D. A. Edwards (ed.). TESLA Test Facility Linac - Design Report. *TESLA 95-01*, 1995.
- [224] TESLA-Collaboration: J. Andruszkow et al. *Phys. Rev. Lett.*, 85:3825–3829, 2000. physics/0006010.

2 THERA

Electron–Proton Scattering at $\sqrt{s} \sim 1\text{TeV}$



H. Abramowicz⁴⁰, S.P. Baranov²¹, J. Bartels¹⁷, W. Bialowons¹³, R. Brinkmann¹³, O. Çakır⁴, A. Caldwell¹², V. Chekelian^{32,31}, A.K. Çiftçi⁴, J.G. Conteras¹⁴, M. Corradi⁷, J.A. Crittenden⁸, J. Dainton²³, K. Daum⁴⁴, A. Deshpande⁴⁵, D. Eckstein¹³, E. Elsen¹³, B. Foster⁹, L. Frankfurt⁴⁰, E. Gabathuler²³, J. Gassner³⁸, U. Gensch¹³, I. Ginzburg³³, L. Gladilin⁴³, M. Glück¹⁴, N. Gogitidze²¹, K. Golec-Biernat¹⁷, E. Gotsman⁴⁰, T. Greenshaw²³, V. Guzey², P. Jankowski, U. Jezuita-Dabrowska⁴¹, H. Jung¹³, U.F. Katz⁸, R. Klanner^{13,17}, M. Klasen¹⁷, M. Klein¹³, B. Kniehl¹⁷, H. Koru⁵, P. Kostka¹³, H. Kowalski¹³, M. Krawczyk⁴¹, T. Kurča²⁰, M. Kuze¹⁹, P. Landshoff¹⁰, T. Laštovička³⁷, B. Levchenko³⁰, E. Levin⁴⁰, A. Levy⁴⁰, K. Long²⁴, L. Lönnblad²⁵, U. Maor⁴⁰, M. McDermott²³, K. Nagano¹⁹, T. Naumann¹³, W. van Neerven²², P. Newman⁶, N. Nikolaev¹⁸, C. Pascaud³⁴, E. Perez³⁹, D. Pitzl¹³, B. Pötter³², G. Rädcl¹, V. Ravindran³, I. Redondo²⁶, E. Reya¹⁴, A. De Roeck¹¹, E. Rondio⁴², J. Ruan¹⁵, W. Schäfer¹⁸, S. Schlenstedt¹³, P. Schleper¹³, U. Schneekloth¹³, S. Söldner-Rembold^{16,11}, H. Spiesberger²⁷, U. Stösslein¹³, M. Strikman³⁶, S. Sultansoy⁵, K. Tuchin⁴⁰, W.K. Tung²⁹, R. Wallny⁴⁶, D. Waters³⁵, P. Wesolowski¹³, F. Willeke¹³, M. Wing²⁸, Ö. Yavaş⁴, M. Yılmaz⁵, A.F. Żarnecki⁴¹, A. Zembrzuski⁴¹, A. Zhokin³¹, V. Zoller³¹, N.P. Zotov³⁰.

-
- ¹ RWTH Aachen, Germany
 - ² University of Adelaide, Australia
 - ³ Mehta Research Institute of Mathematics and Mathematical Physics, Allahabad, India
 - ⁴ Ankara University, Turkey
 - ⁵ Gazi University, Ankara, Turkey
 - ⁶ University of Birmingham, UK
 - ⁷ INFN Bologna, Italy
 - ⁸ Universität Bonn, Germany
 - ⁹ University of Bristol
 - ¹⁰ Cambridge University, UK
 - ¹¹ CERN, Geneva, Switzerland
 - ¹² Columbia University, Nevis Labs, Irvington, USA
 - ¹³ DESY, Hamburg and Zeuthen, Germany
 - ¹⁴ Universität Dortmund, Germany
 - ¹⁵ East China Normal University, Shanghai, P.R. China
 - ¹⁶ Universität Freiburg, Germany
 - ¹⁷ Universität Hamburg, Germany
 - ¹⁸ Forschungszentrum Jülich, Germany
 - ¹⁹ KEK, Tsukuba, Japan
 - ²⁰ Institute of Experimental Physics, Košice, Slovak Republic
 - ²¹ Lebedev Physical Institute, Moscow, Russia
 - ²² University of Leiden, The Netherlands
 - ²³ University of Liverpool, UK
 - ²⁴ Imperial College London, UK
 - ²⁵ Lund University, Sweden
 - ²⁶ Universidad Autónoma de Madrid, Spain
 - ²⁷ Universität Mainz, Germany
 - ²⁸ McGill University, Montreal, Canada
 - ²⁹ Michigan State University, East Lansing, USA
 - ³⁰ Moscow State University, Russia
 - ³¹ ITEP, Moscow, Russia
 - ³² MPI für Physik, München, Germany
 - ³³ Institute of Mathematics, Novosibirsk, Russia
 - ³⁴ LAL, Orsay, France
 - ³⁵ University of Oxford, UK
 - ³⁶ Pennsylvania State University, New Kensington, USA
 - ³⁷ Charles University, Prague, Czech Republic
 - ³⁸ PSI, Villingen, Switzerland
 - ³⁹ DAPNIA-CEA/Saclay, Gif sur Yvette, France
 - ⁴⁰ Tel Aviv University, Israel
 - ⁴¹ Warsaw University, Poland
 - ⁴² Institute for Nuclear Studies, Warsaw, Poland
 - ⁴³ Weizmann Institute, Rehovot, Israel
 - ⁴⁴ Universität Wuppertal, Germany
 - ⁴⁵ Yale University, Prospect, USA
 - ⁴⁶ Universität Zürich, Switzerland

Contents

2	THERA: Electron–Proton Scattering at $\sqrt{s} \sim 1$ TeV	99
2.1	Introduction	103
2.2	Physics with THERA	105
2.2.1	Low- x physics	105
2.2.2	Proton structure and quantum chromodynamics	113
2.2.3	Searches for new particles or phenomena	123
2.2.4	Resolving the partonic structure of the photon	126
2.3	Experimentation at THERA	130
2.3.1	Collision of TESLA electrons with HERA protons	130
2.3.2	A detector for THERA	136
2.4	Further Options	140
2.4.1	Electron–nucleus scattering	140
2.4.2	Real photon–proton scattering	144
2.4.3	Polarised protons	146
2.5	Summary	149
	Bibliography	152

2.1 Introduction

The elementary nature of the electron makes it a good probe to study the structure of the proton in deep inelastic ep interactions [1]. Previous fixed-target deep inelastic scattering (DIS) experiments have discovered the partonic structure of the nucleon and established Quantum Chromodynamics (QCD) as the correct field theory of quark–gluon interactions at small distances.

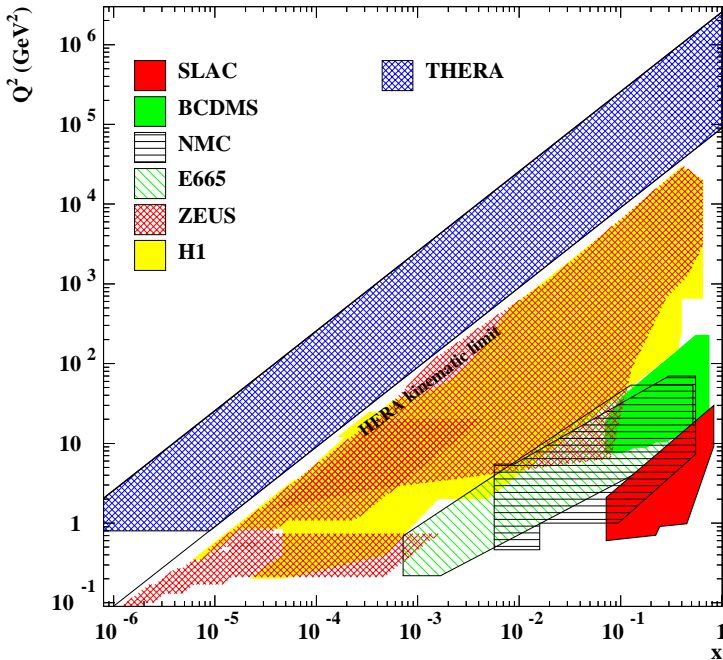


Figure 2.1.1: *The kinematic plane in deep inelastic lepton–proton scattering, showing the regions covered by fixed-target scattering experiments and by the HERA experiments, and the extension of the kinematic range by the THERA collider with an ep centre-of-mass energy squared of $s = 2.56 \times 10^6 \text{ GeV}^2$. The variables x and Q^2 denote the Bjorken scaling variable and the negative square of the four-momentum transfer between lepton and proton, respectively.*

HERA [2], the first electron–proton collider, has been a major step forward in accelerator technology and has resulted in a number of fundamental physics observations: the discovery of the rise of the proton structure function $F_2(x, Q^2)$ towards low Bjorken x , which is related to a large gluon density in the proton; the discovery of hard diffractive scattering in DIS and the confirmation of the pointlike nature of the partons down to distances of about 10^{-18} m . The HERA measurements at low Q^2 have initiated intense studies of the transition between QCD radiation at small distances and non-perturbative parton dynamics at large transverse distances, which has become a central issue in modern strong interaction theory.

THERA¹ uses polarised electrons or positrons from the linear accelerator TESLA at energies of 250–800 GeV and brings them into collision with high-energy protons (500 GeV to 1 TeV) from HERA in the West Hall on the DESY site. THERA will thus extend the investigation of deep inelastic scattering into an as yet unexplored kinematic region (Fig. 2.1.1), yielding complementary information to hadron–hadron and e^+e^- colliders in the TeV energy range.

At low x , THERA offers the possibility of uncovering a new strong-interaction do-

¹The acronym THERA symbolises a combination of TESLA and HERA. It also is the name of a Greek island, which in the Doric period was called Kalliste, most beautiful.

main of parton saturation, which would be a substantial step towards an understanding of confinement. Processes such as jet production in the proton beam direction or heavy flavour production at low x , studies of the partonic structure of the photon and a precision measurement of the strong interaction coupling constant α_s make THERA an excellent facility for investigating strong and electroweak interaction dynamics. Finally, the high centre-of-mass energy will open a new window for the observation of new particles or interactions, such as leptoquarks, supersymmetric particles or contact interactions, the helicity structure of which could be particularly well investigated at THERA.

With centre-of-mass energies beyond 1 TeV, structures in the proton with sizes down to 10^{-19} m will be resolved. In the history of the exploration of the basic structure of matter, illustrated in Fig. 2.1.2, THERA thus represents a new major step.

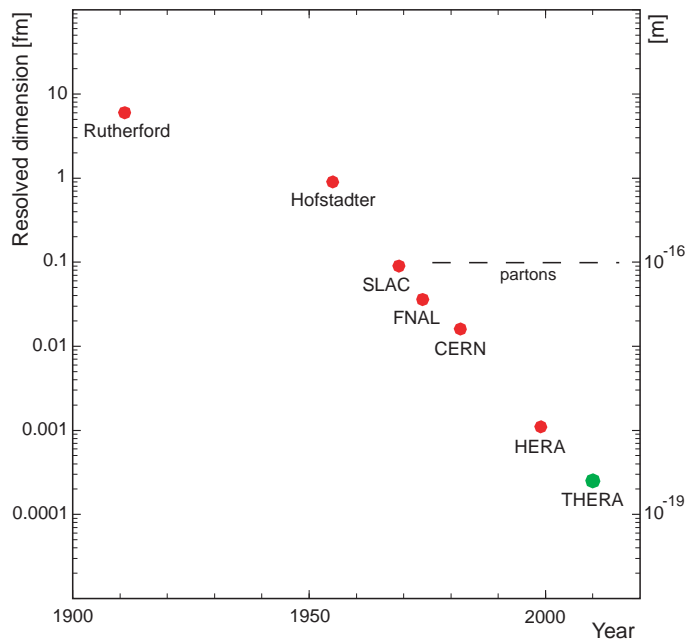


Figure 2.1.2: *The development over time of the resolution power of experiments exploring the inner structure of matter, from the Rutherford experiment to THERA.*

The electron–proton scattering programme at THERA can be greatly extended by accelerating nuclei or polarised protons in the HERA ring, or with real photon–proton scattering using laser light backscattered off the electron beam. Thus THERA can be a unique long-term, cost-effective facility for inelastic lepton–hadron scattering in an unexplored range.

The structure of this appendix¹ is the following: In Sect. 2.2 the physics subjects studied are discussed, and the major physics possibilities are highlighted. In Sect. 2.3 the THERA machine layout and luminosity estimates, as well as the concept of a THERA detector, are presented. Sect. 2.4 presents briefly the physics options of running the THERA facility in $\vec{e}A$, $\vec{\gamma}p$ and $\vec{e}\vec{p}$ mode. A brief summary is given in Sect. 2.5.

¹This appendix summarises studies of a group of about one hundred physicists. Most of the results are available on the web (<http://www.ifh.de/thera>) and will be documented in more detail in a separate volume [3].

2.2 Physics with THERA

2.2.1 Low- x physics

From the measurement of the differential cross section $d^2\sigma/dx dQ^2$ in inclusive deep-inelastic lepton–proton scattering, $\ell p \rightarrow \ell X$, the proton structure function $F_2(x, Q^2)$ is determined. In the naive Quark Parton Model (QPM), F_2 is interpreted as the sum of the momentum densities of quarks and anti-quarks in the proton, weighted with their charge squares. The variable x is interpreted as the fraction of the proton’s longitudinal momentum carried by the struck quark. According to the relation $x = Q^2/sy$ (where y is the fractional energy carried by the exchanged current), every step towards higher centre-of-mass energy, \sqrt{s} , leads deeper into the unexplored region of low x .

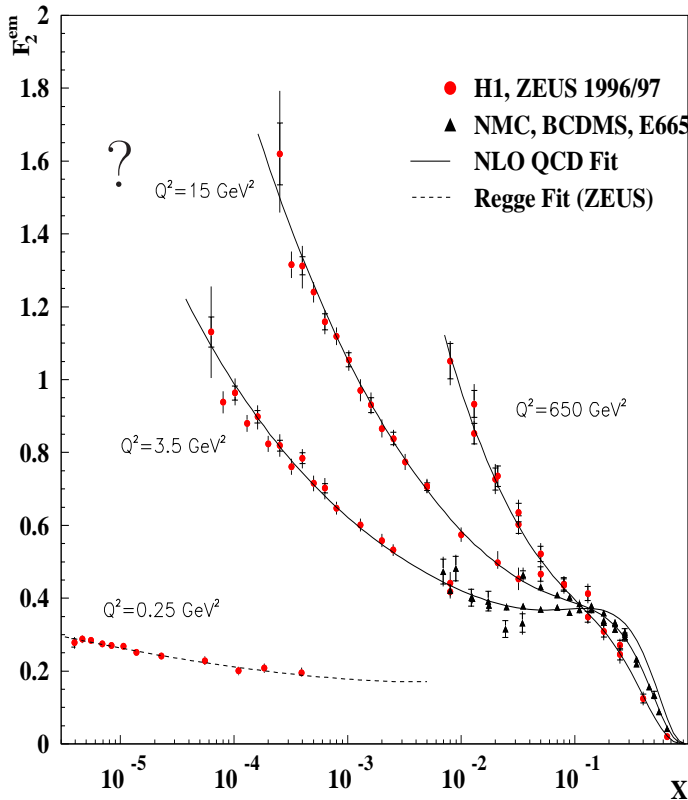


Figure 2.2.1: The proton structure function $F_2(x, Q^2)$ as measured in fixed-target μp scattering at large x , and in ep scattering at HERA. The solid curves show a fit using the next-to-leading order QCD evolution equations. The dashed curve for the lowest- Q^2 data is a fit using Regge theory. The structure function in the low- x region represents the sea-quark component of the proton. With THERA, the kinematic range will be extended by a further order of magnitude towards lower x . The expected behaviour of F_2 in this new region is hotly debated.

The high-energy collider HERA and its experiments have extended the kinematic (x, Q^2) region for DIS by about two orders of magnitude. As can be seen in Fig. 2.2.1, the structure function F_2 as measured at HERA [4, 5] and thus the sea-quark density rises by a large factor towards low x , and the increase becomes stronger with increasing Q^2 . The data in the DIS region were found to be well described by the QCD evolution equations [6], which are based on the renormalisation group equations and the operator product expansion. Figure 2.2.1 also illustrates that the behaviour of the data [7] at low $Q^2 < 1 \text{ GeV}^2$ is completely different, showing a slower, logarithmic rise, which is typical for the energy dependence of soft hadronic processes.

Much of the understanding of strong interaction dynamics is derived from the study

of Q^2 dependences in DIS. The HERA experiments have found that $F_2(x, Q^2)$ at fixed small values of x strongly rises with Q^2 . In the standard QCD evolution equations, the derivative $(\partial F_2 / \partial \ln Q^2)_x$ at fixed low x is, at leading order, proportional to the product of the strong interaction coupling constant, α_s , and the gluon momentum density, xg . Thus the rise of F_2 with Q^2 as measured at HERA implies a large gluon density in the proton, which increases towards low x (see Fig. 2.2.2). However, it remains an open question whether the underlying evolution equations strictly hold at the lowest x values, in spite of neglecting large logarithms of the type $\ln(1/x)$ and possible unitarity effects. Data at lower x and larger Q^2 are required to resolve this issue. Theoretical QCD developments regarding DIS at low x are discussed in Sect. 2.2.2.1.

In the HERA collider experiments a number of observables have been studied which provide insight into strong interaction dynamics independently of F_2 and are also sensitive to the behaviour of the gluon distribution at low x . Examples are the longitudinal structure function $F_L \propto \alpha_s xg$ [4], the production of vector mesons like J/ψ [8, 9] ($\propto (\alpha_s xg)^2$) and the charm structure function F_2^c [10, 11]. The successful description of these and further measurements with a single set of parton distribution functions of the proton has been a major success of perturbative QCD.

Due to the high density of quarks and gluons, qualitatively new signatures are expected in the low- x region of THERA. An extrapolation of the rise of F_2 to lower x , as indicated by Fig. 2.2.1, would at some point violate the unitarity limit of virtual photon–proton scattering. An upper limit on xg is obtained from the unitarity require-

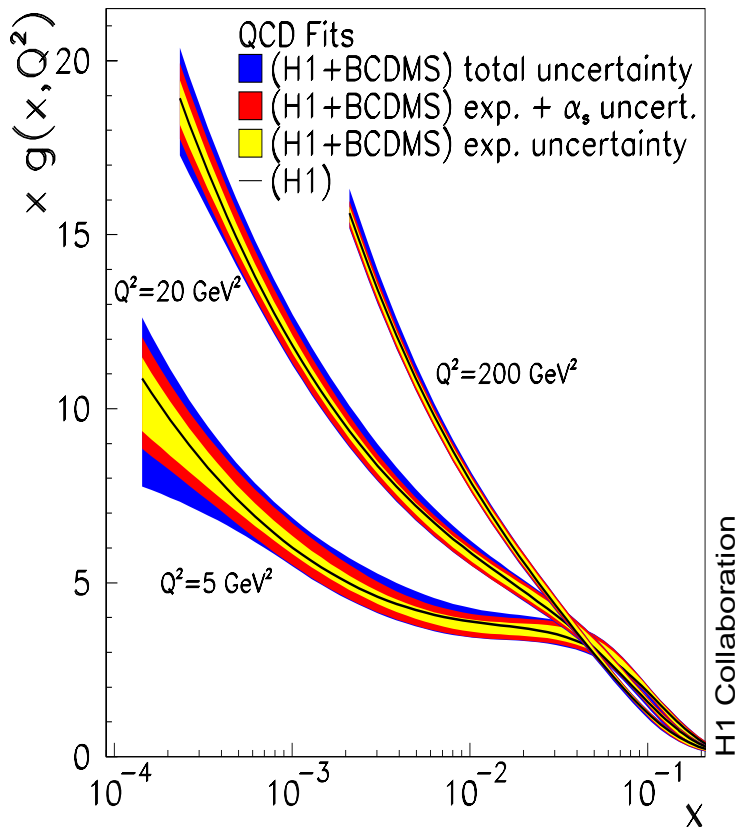


Figure 2.2.2: *Gluon momentum distribution measured at HERA, extracted within the framework of the conventional evolution equations of perturbative QCD. The gluon distribution is sensitive to the understanding of heavy flavour production at low x and Q^2 . The behaviour of the gluon density in the kinematic range of THERA is a hotly debated issue which has to be resolved experimentally.*

ment that the inelastic cross section of the interaction of a small dipole¹ [13,14] with the proton may not exceed the transverse proton size πR^2 . This leads to an approximate constraint [15,16]

$$xg(x, Q^2) \leq \frac{1}{\pi N_c \alpha_s(Q^2)} Q^2 R^2 \simeq \frac{Q^2}{\alpha_s}, \quad (2.2.1)$$

where N_c is the number of colours and Q^2 is given in GeV^2 . Given the strong rise of xg towards low x (Fig. 2.2.2), it seems likely that the unitarity limit is reached in the THERA kinematic range and that therefore this rise eventually becomes tamed. As discussed in Sect. 2.4.1, it is possible that these effects are amplified in electron–nucleus scattering. In any case, understanding deep inelastic structure functions in the THERA range is of crucial relevance for the description of high-energy cross sections at hadron colliders and astro-particle physics experiments [17,18].

Saturation may be connected with a novel, high parton density state of QCD, between the low-density region of partons and the region of confinement. The transition from the perturbative range of small distances to the physics at large distances is currently being intensively studied, using data from the HERA collider experiments on the total virtual-photon proton cross section as well as on elastic vector meson production and diffraction. Despite the success of phenomenological models, however, a consistent theoretical description remains elusive [19]¹, and a significant extension of the kinematic range in deep inelastic scattering is required.

2.2.1.1 The high-density QCD phase and confinement

The deep inelastic scattering process can be viewed as a fluctuation of the incoming proton into a cloud of constituents which is subsequently scanned by the virtual photon. The life-time of the cloud, $\tau \approx 1/Mx$, is considerably longer than the photon interaction time (M being the proton mass). Therefore the photon takes ‘snapshots’ of the ‘frozen’ proton cloud with a resolution $\Delta r \approx 1/\sqrt{Q^2}$. The x and Q^2 dependence of the proton structure may be viewed as sketched in Fig. 2.2.3.

HERA data and theoretical studies suggest that hadrons have a qualitatively different structure in three domains:

¹Theoretical descriptions of DIS at low x frequently use a frame in which the proton is at rest. In the high-energy limit, low- x processes factorise into a virtual photon fluctuation to a hadronic system at large distances from the proton target, which is followed by a brief interaction with the target and subsequent hadronic final state formation over a longer period. The simplest fluctuation, which dominates for systems with small transverse size, is a quark–antiquark state which forms a colour-triplet dipole. This view is attractive for describing inclusive DIS at low x as well as suitable for vector meson production and diffractive processes. It has been successfully used and developed much further in recent years, as is reviewed in [12].

¹This is reminiscent of a situation about 100 years ago before Planck successfully solved the black-body radiation problem bridging the gap between Wien’s law and the Rayleigh–Jeans formula. In analogy to the ultraviolet catastrophe, i.e. the divergence of the Rayleigh–Jeans law at small wavelengths, the proton structure function F_2 cannot grow indefinitely as x approaches zero.

1. The *domain of perturbative QCD* with small-size constituents which are distributed in a hadron with rather low density (the region below the solid line in Fig. 2.2.3). Reacting partons are resolved with a resolution determined as $\Delta r \approx 1/Q$.
2. The *QCD domain of high parton density* [20] but small coupling, where the density is too large to use the established perturbative QCD methods (the region above the solid line). Theoretical studies suggest that the size of the partons in this region is effectively determined by an x dependent resolution scale, $Q_S(x)$: $\Delta r \approx 1/Q_S(x)$ [21].
3. The *non-perturbative QCD domain*, in which the QCD coupling α_s is large, Regge theory applies and the confinement of quarks and gluons occurs. New theoretical methods must be developed to explore this region (left of the dash-dotted line).

According to [22, 16] the HERA data suggest the existence of the high-density QCD domain in which a new scaling law for the virtual photon–proton cross section may apply [23]. However, the HERA data can also be described without such an assumption [16, 24]. At THERA, such investigations can be performed at larger Q^2 for a given x , i.e. more safely inside the region of small α_s . Thus the extension of the kinematic range is crucial to the distinction and analysis of these states of matter.

It is well known that in the short-distance limit (i.e. in the perturbative QCD domain), quarks and gluons are the proper degrees of freedom of the QCD Lagrangian. To describe the transition from short to long distances, however, one needs to consider degrees of freedom beyond quarks and gluons. Approaches based on colour dipole formation as the first stage in this transition are promising.

Understanding the confinement of quarks and gluons is still a challenge to theorists. Deep inelastic scattering provides two approaches to study this phenomenon. Firstly,

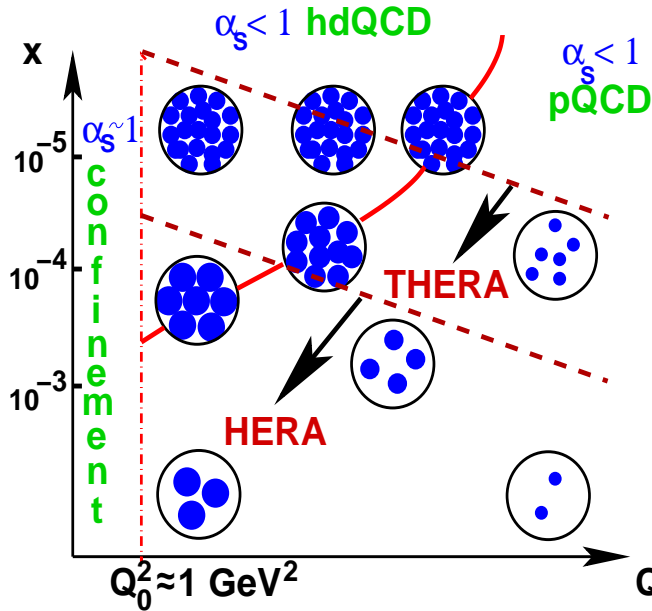


Figure 2.2.3: Snapshots of the proton constituents (full dots) taken with different resolution ($\Delta r \approx 1/Q$) at different values of x . The solid line shows the estimated position of the transition from the perturbative region to the high-density phase of QCD (hdQCD). The resolution scale diminishes with Q^2 in the pQCD region but with x in the hdQCD region. The vertical dash-dotted line delimits the confinement region. The dashed lines and the corresponding arrows indicate the HERA and THERA measurement ranges. The observation of signatures allowing the identification of the various regions is a challenge for THERA.

the experimental data at high energies suggest some properties of confinement, such as factorisation, the space-time picture or the quark model. These hint at the effective degrees of freedom and at which type of effective Lagrangian may be used for developing a microscopic theory at high energies. Secondly, DIS data allow the matching of perturbative and non-perturbative QCD domains to be studied by investigating low- Q^2 virtual-photon proton scattering. Clearly, a solution to the confinement problem of hadrons has fundamental implications.

2.2.1.2 Vector-meson production

Investigations of vector meson production at HERA have provided insights into the dynamics of both soft and hard diffractive processes [25] (for a review see [26]). The high flux of quasi-real photons from the electron beam permitted detailed measurements of both elastic and proton-dissociative photoproduction of ρ^0 , ω , ϕ , J/ψ , and Υ mesons. Power-law scaling with the photon–proton centre-of-mass energy, W , was observed, as is illustrated by Fig. 2.2.4. The steep energy dependence measured for J/ψ mesons inspired a number of theoretical approaches based on perturbative QCD [27, 28, 29].

In the theory of light vector mesons, the photon virtuality [31, 32, 33, 15, 34] and the momentum transferred to the proton [35, 36, 37, 38] were introduced as hard scales. These calculations demonstrated remarkable sensitivity to the gluon density, since the cross sections were shown to be proportional to $(xg)^2$. With large THERA data

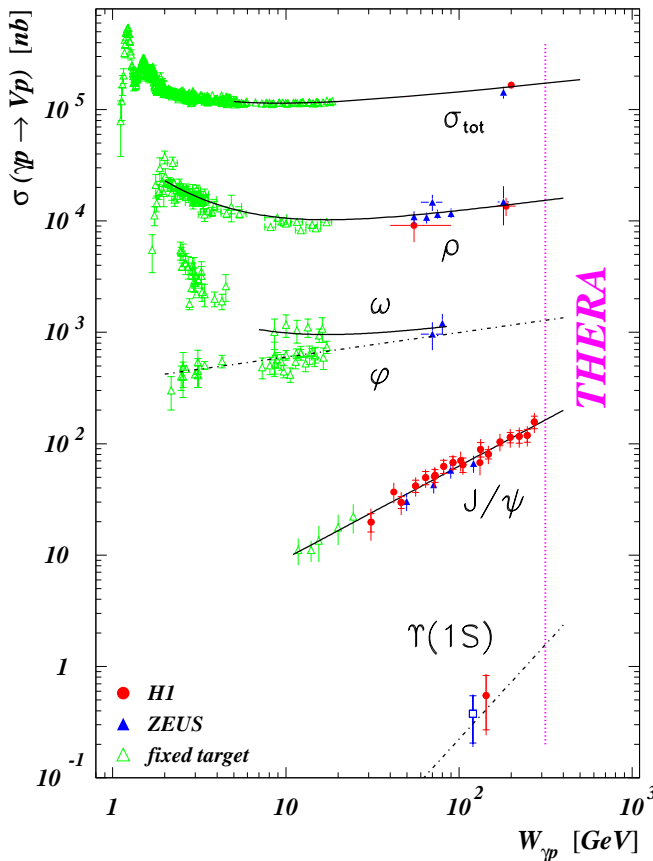


Figure 2.2.4: Energy dependence of the total γp cross section and the elastic vector meson photoproduction cross sections for ρ^0 , ω , ϕ , J/ψ , and Υ mesons. Here W is the photon–proton centre-of-mass energy. The plot is reproduced from [30]. Since the production cross section of heavy vector mesons is proportional to $(xg)^2$, measurements in the THERA range of W up to 1 TeV may be sensitive to saturation.

samples, covering a variety of vector meson species, remaining theoretical uncertainties can be tackled, such that elastic vector meson production could become a competitive means of extracting the gluon density. Of particular interest is the question whether the rise of the J/ψ cross section towards large W (Fig. 2.2.4) is tamed, for example by unitarity effects, or indeed persists [24]. Because of the enlarged cross section and W range, the investigation of Υ meson production [39, 40] will become an important topic at THERA.

Whereas perturbative QCD is applicable where hard scales are present, long-range strong-interaction dynamics apply to the forward production of light vector mesons at low Q^2 . The transition between these two regimes is studied by scanning Q^2 or the square of the four-momentum transfer at the proton vertex, t , allowing comparisons to hadronic interactions. Of particular interest is the possibility of determining the transverse interaction size which may grow with energy [24, 41, 16], as given by the slope of the Pomeron trajectory, α' . Due to the weakness of the energy dependence in such long-distance processes, the extension of the energy reach is essential to provide sensitivity to α' .

The programme of vector meson measurements will benefit not only from the extended kinematic reach but as well from the improved coverage of the THERA detector at small angles and from tagging systems in both the proton and electron beam directions, designed with the benefit of the experience obtained at HERA.

2.2.1.3 Hard diffractive scattering

A striking result at HERA has been the abundance of diffractive processes of the type $ep \rightarrow eXp$ [42, 43] in DIS, where the proton remains intact with only a small loss in momentum. Deep inelastic scattering at low x thus became, rather unexpectedly, an important process for the understanding of one of the oldest puzzles of high energy physics, the nature of diffraction [44]. The mechanism responsible for diffraction remains unsettled, and its investigation will profit enormously from the extended phase space available at THERA. Since total, elastic and diffractive cross sections are closely related via the optical theorem, it is clear that a correct description of diffractive processes must be an integral part of any consistent theory of low- x physics [45, 46, 47].

The diffractive contribution to F_2 has been measured in the form of a structure function $F_2^{D(3)}(x_P, \beta, Q^2)$. Here, as illustrated in Fig. 2.2.5a, x_P is the fractional proton longitudinal momentum loss and $\beta = x/x_P$ is the fraction of the exchanged longitudinal momentum carried by the quark coupling to the virtual photon. Figures 2.2.5b,c show the kinematic regions in which diffractive processes can be measured at HERA and at THERA. An extension of approximately an order of magnitude towards lower β or x_P is obtained at fixed Q^2 .

The hard scale supplied by the photon virtuality has encouraged perturbative QCD approaches to diffractive DIS. A QCD factorisation theorem has recently been proven for the process [48], implying that diffractive parton densities at fixed x_P can be defined, which should describe both the scaling violations of $F_2^{D(3)}$ and exclusive final state cross sections such as those for high- p_t jet production. HERA data have shown that

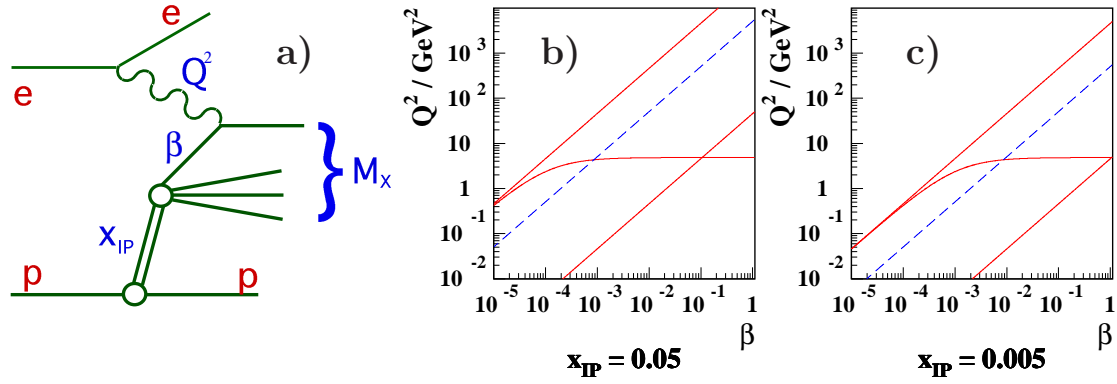


Figure 2.2.5: (a) Feynman diagram of diffractive ep scattering, with the kinematic quantities indicated in blue. (b,c) The accessible kinematic plane in β and Q^2 for diffractive DIS at two different values of $x_{\mathbb{P}}$. The solid red lines show the limits imposed by the cuts $0.001 < y < 1$ and $\theta_e < 179.5^\circ$ for THERA, with electrons of 250 GeV and protons of 920 GeV. The dashed blue lines show the kinematic limit at HERA.

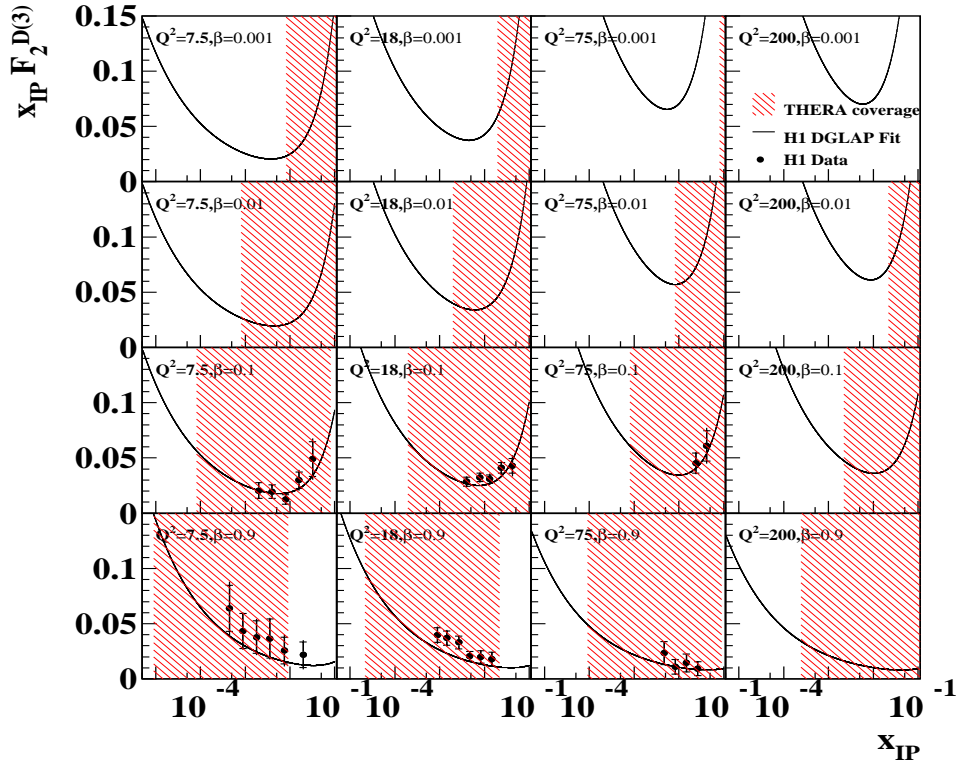


Figure 2.2.6: Illustration of the kinematic coverage for measurements of $F_2^{D(3)}(x_{\mathbb{P}}, \beta, Q^2)$ at HERA and at THERA. The accessible $x_{\mathbb{P}}$ range is shown for selected values of β and Q^2 . Appropriate HERA data points from [42] are also shown. The curves are extrapolations of QCD fits to data with $\beta < 0.65$ from [42]. The shaded areas show the region of extended coverage at THERA (920 GeV protons, 250 GeV electrons).

the diffractive parton densities are dominated by gluons at large β [49]. The region $\beta \lesssim 0.05$ remains poorly explored at HERA.

In the proton rest-frame approach, diffractive DIS is considered as the elastic scattering of the proton with $q\bar{q}$ and $q\bar{q}g$ partonic fluctuations of the virtual photon. The scattering has been modelled either in terms of multiple interactions in the non-perturbative colour field of the proton [50, 51] or in terms of the exchange of a pair of perturbative gluons [52, 53, 22]. THERA data in an extended phase space will be very powerful in distinguishing between these different approaches.

From combined analyses of diffractive and inclusive γ^*p cross sections, it has been suggested that the regime of parton saturation, expected as the unitarity limit is approached, is already reached at HERA [22]. Diffractive data are crucial for this sort of analysis, since for fixed x , saturation is expected to set in at larger Q^2 values in the diffractive than in the inclusive cross section. Although the presence or absence of saturation effects in diffraction at HERA is hotly debated, it is likely that the effect will be clearly visible in the extended low- x range at THERA.

Figure 2.2.6 indicates the regions in which measurements of $F_2^{D(3)}$ will be possible at THERA, together with selected data points from HERA. Extrapolations of a QCD fit to HERA data [42] based on DGLAP evolution of the diffractive parton distributions are also shown. THERA measurements at lower β will allow the precise determination

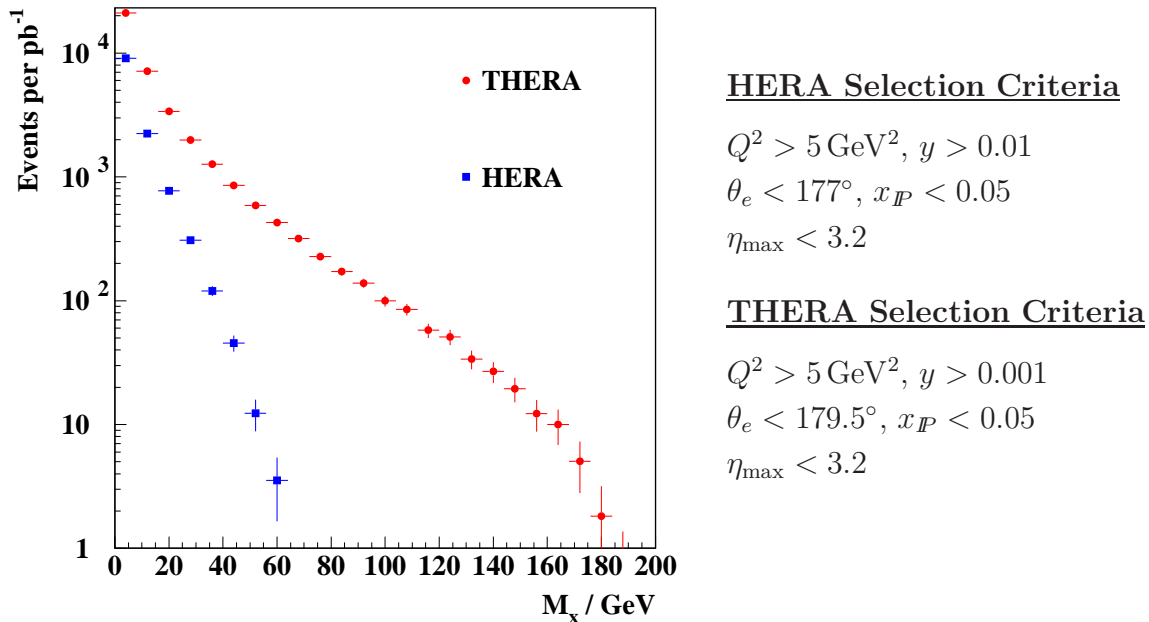


Figure 2.2.7: *Event yields per unit luminosity for the process $ep \rightarrow eXp$ after applying the quoted selection criteria at THERA (920 GeV protons, 250 GeV electrons) and HERA. The yields are shown as a function of the mass M_X and are based on an ad hoc extrapolation of a QCD fit to HERA data [42].*

of diffractive parton densities in the region of low momentum fraction. The extended range in $x_{\mathcal{P}}$ will allow an improved determination of the energy dependence of diffractive DIS from the combined HERA and THERA data. This will lead to detailed tests of the hypothesis of ‘Regge’ factorisation of the $x_{\mathcal{P}}$ dependence from the Q^2 and β dependences, as would be expected for a universal pomeron exchange [54].

Further tests of QCD models of diffraction and an improved understanding of the gluonic degrees of freedom are achievable by studies of hadronic final state cross sections involving additional hard scales due to the presence of charm or high- p_t jets. At HERA, the limited reach in M_X (see Fig. 2.2.5a) seriously restricts the phase space for charm and dijet production and implies that these final states can only be studied at rather large $x_{\mathcal{P}}$. As can be seen from Fig. 2.2.7, the values of M_X reached at THERA for $x_{\mathcal{P}} < 0.05$ are larger by a factor of around 3 than in the HERA case.

In diffractive events the proton can remain intact or dissociate into a low-mass hadronic system. In this sense diffractive events are directly sensitive to the conditions required to preserve the hadronic bound state. A detailed comparative study of diffractive events with and without proton dissociation could reveal information about confinement. Such an analysis can be performed if the outgoing proton beam-line is instrumented with detectors to tag the final-state protons (leading-proton spectrometer).

2.2.2 Proton structure and quantum chromodynamics

Deep-inelastic scattering has been crucial in the development of Quantum Chromodynamics since the observation of the logarithmic pattern of scaling violations in $F_2(x, Q^2)$. Over the past decades, precision measurements of structure functions and studies of final state characteristics have deepened the understanding of QCD. With the access to very low values of Bjorken x in the deep inelastic region, the exploration of extremely high Q^2 values at high luminosity, and an extension of the transverse momentum phase space, THERA promises new insights into the structure of QCD.

2.2.2.1 Perturbative QCD and structure functions

The measurements of structure functions in DIS have been accompanied by remarkable progress in QCD calculations. Both the splitting functions, to second order in α_s , and the coefficient functions, to order α_s^3 , are calculated [55], and the NNLO calculation of the splitting functions is in progress. The current measurements of $F_2(x, Q^2)$ in the kinematic range of HERA are very well described by the twist-2 evolution equations, even in a range in which significant higher-twist effects and specific higher-order small- x effects were previously expected. The phenomenological success of joint determinations of the coupling constant α_s and the gluon distribution xg , together with the quark distributions, is impressive [56, 4] and has led to precise measurements of these quantities. Parton densities to NLO have been extracted over a wide kinematic range from HERA F_2 and other cross section data [57, 58, 59]. With data in the kinematic domain of THERA, both at lower x and larger Q^2 , the precision of these quantities will further improve significantly (see below).

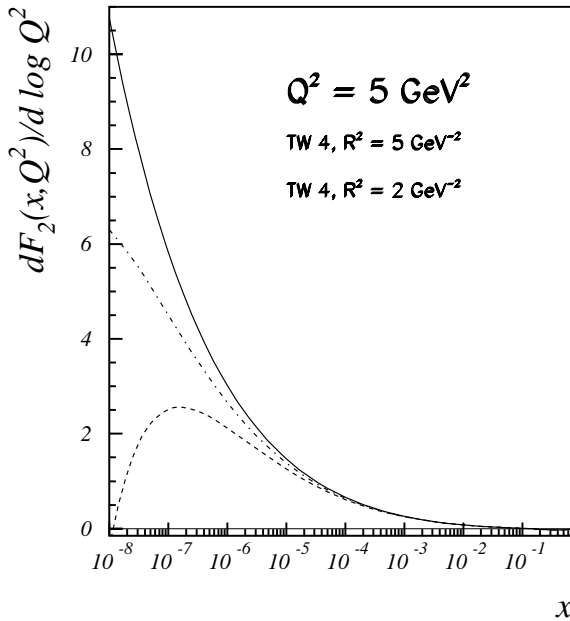


Figure 2.2.8: The slope $\partial F_2(x, Q^2)/\partial \log Q^2$ at $Q^2 = 5 \text{ GeV}^2$ [60]. Full line: leading-order twist-2 contributions (parameterisation [59]); dash-dotted line: slope including the twist-4 contribution with a screening radius of $R^2 = 5 \text{ GeV}^{-2}$; dashed line: $R^2 = 2 \text{ GeV}^{-2}$.

As was discussed above, an important question is how the low- x growth in F_2 as observed at HERA is tamed to satisfy the unitarity bound. Higher-order corrections to the twist-2 terms diminish the growth but do not lead to a saturation as $x \rightarrow 0$. One can expect that unitarity is restored by higher-twist contributions. First studies of these effects have been performed [61, 60] in approaches based on the light-cone expansion. Numerical results on the slope $\partial F_2/\partial \log Q^2$ for specific choices of twist-4 screening radii R are depicted in Fig. 2.2.8, showing that one may indeed probe these effects in the kinematic domain of THERA, $x \gtrsim 10^{-6}$ (see also [62]). Rather large higher twist effects [63, 64] may be seen in measurements of the longitudinal structure function F_L .

The apparent success of the complete fixed-order calculations in describing F_2 in the small- x domain is puzzling theoretically. Starting from the BFKL approximation and resumming the most singular pieces, large corrections were predicted both for the anomalous dimensions [65] and for the coefficient functions [66]. Recently, large next-to-leading order resummed gluon anomalous dimensions were found [67], however with opposite sign. This led to the conclusion that they have to be stabilised by resumming even higher orders [68, 69, 70]. Formally, sub-leading terms were found to be quantitatively as important as the resummed ‘leading’ terms due to the strong rise of the gluon and sea quark densities in the small- x domain. This requires the knowledge of the coefficient functions also for the range of medium values of x [68, 70], where resummations are not possible. More theoretical work is needed to further develop perturbative QCD. This will be stimulated by a continuing experimental programme and data in an extended range.

Ultimately, in the regime of extremely low values of x and small Q^2 , one expects that the light-cone expansion does not apply anymore. For this kinematic domain new theoretical concepts have still to be developed.

2.2.2.2 Forward jet production

In order to understand strong-interaction dynamics, inclusive cross section measurements and their interpretations have to be complemented by the investigation of the hadronic final state. At HERA, the description of details of the final states, for example in forward jet production at low x , requires to consider resolved photon structure effects in addition to the pure DGLAP evolution. However, an extension of the phase space as provided by THERA is necessary to distinguish between a DGLAP-based calculation with an additional resolved virtual photon contribution, which mimics non- k_t -ordered (i.e. non-pure-DGLAP) contributions at present energies, and small- x evolution as modelled by the BFKL [65] or CCFM [71] equations. The CCFM evolution equation, based on the principle of colour coherence, is equivalent to BFKL for $x \rightarrow 0$ and reproduces the DGLAP equation for large x .

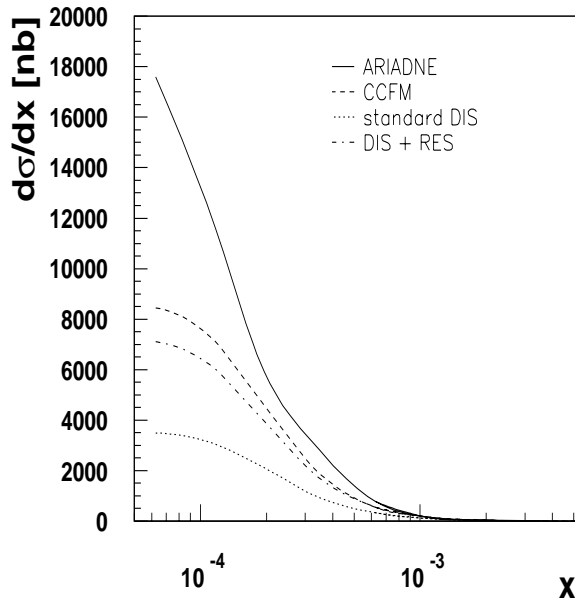


Figure 2.2.9: *Forward-jet cross section as a function of x in different models for $0.5 < p_t^2/Q^2 < 2$ and a minimum polar jet angle of 1° . The measurements at HERA are limited to $x \gtrsim 2 \times 10^{-3}$.*

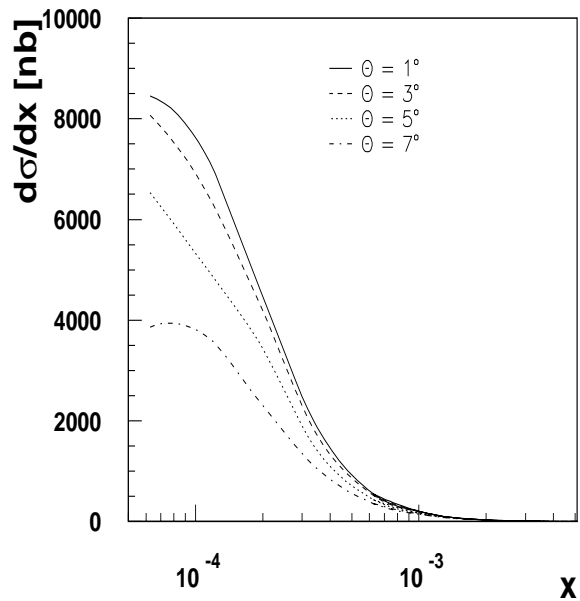


Figure 2.2.10: *Forward-jet cross section as a function of x obtained from CCFM for $0.5 < p_t^2/Q^2 < 2$, for different values of the minimum jet angle.*

At THERA the differences between these approaches become striking. In Fig. 2.2.9 the cross section for forward jet production [72] is shown as a function of x . Whereas the measurement at HERA is limited to $x \gtrsim 2 \times 10^{-3}$, the available x range at THERA is extended by one order of magnitude towards lower x . At THERA the CCFM approach predicts a much larger cross section than the model with resolved virtual photon contributions added, giving the unique opportunity to identify a new QCD regime, which can only be described by new small- x evolution equations. This not only allows us

to distinguish between the different approaches, but also to study details of the QCD cascade, which at small x includes unintegrated parton densities [46]. THERA will be the only place where these parton densities can be measured, and where the small- x parton dynamics can be clearly studied.

In Fig. 2.2.10 the forward jet cross section is shown for different minimal jet angles. On the experimental side this requires complete acceptance both in the electron and proton direction down to the lowest possible angles. From the size of the cross section $d\sigma/dx$ one would like to reach at least $\theta \sim 3^\circ$ for the forward jet measurement, desirably even $\theta \sim 1^\circ$. The luminosity required for such measurements is of the order of 10 pb^{-1} .

2.2.2.3 Measurement of the strong coupling constant α_s

The accurate determination of α_s has been a central issue in many high-energy experiments which revealed a logarithmic dependence of α_s with Q^2 , thereby confirming the property of asymptotic freedom of QCD (for a review see [73]). A precise measurement of this coupling constant is very important for the calculation of strong interaction processes and for unified field theories [74]. Inclusive deep inelastic scattering is particularly suitable to determine $\alpha_s(Q^2)$ because the predictions of QCD at large space-like momentum transfer can be derived in a rigorous way, based on the operator product expansion, and are free of additional assumptions like quark–hadron duality, assumptions concerning the behaviour of quark and gluon condensates, or assumptions regarding the absence or parametrisation of power corrections. The precision of QCD predictions in inclusive DIS is only limited by the present ability to evaluate perturbative corrections to sufficiently high orders. DIS measurements are therefore a unique opportunity to test QCD in a stringent way which is superior to e^+e^- annihilation and pp collisions.

Present DIS measurements of α_s [4, 56, 75] have about the accuracy of and are consistent with the world-averaged determinations of α_s . Improving these analyses is a challenge to the experimental precision and the theoretical calculations. The extension of the (x, Q^2) range and the envisaged cross section uncertainties at THERA of 1–3% lead to an estimated error [76] on $\alpha_s(M_Z^2)$ of about 0.3–0.5%, which is smaller than the current theoretical uncertainty [77] dominated by the choice of the renormalisation scale.

Reduction of the theoretical uncertainty requires the calculation of the complete 3-loop anomalous dimensions needed for NNLO QCD analyses. First results for a series of fixed moments have been obtained already [78] on the way to the complete solution. Based on these results, numerical investigations have been performed on the 3-loop splitting functions [79, 77].

Since THERA extends the Q^2 range and provides p_T values up to almost 100 GeV for jet production [80], the predictions of perturbative QCD become more reliable. Thus measurements of dijet cross sections promise to yield complementary and more accurate information on α_s and the gluon distribution than has presently been achieved at HERA [81, 82].

2.2.2.4 Heavy-flavour physics

In the last years, heavy-flavour production in ep scattering has become a subject of intense research in perturbative QCD (see [83,84] and references therein).

Heavy quarks are produced copiously in ep collisions. The total charm and beauty cross sections at HERA are of the order of $1\mu\text{b}$ and 10nb , respectively. Charm production at HERA has been studied by the H1 and ZEUS collaborations in both the photoproduction and DIS regimes [85,10]. General agreement with pQCD expectations was observed in the DIS case, while a description of the charm photoproduction cross sections is more problematic for present pQCD calculations. The first measured beauty photoproduction cross sections at HERA [86] lie above the fixed-order next-to-leading order (NLO) QCD predictions [87]. No measurements of beauty production in the DIS regime at HERA have been performed so far.

An increase of the centre-of-mass energy of ep collisions from about 300GeV at HERA to $\sim 1\text{TeV}$ at THERA will result in an increase of the total charm and beauty production cross sections by factors ~ 3 and ~ 5 , respectively [88,89].

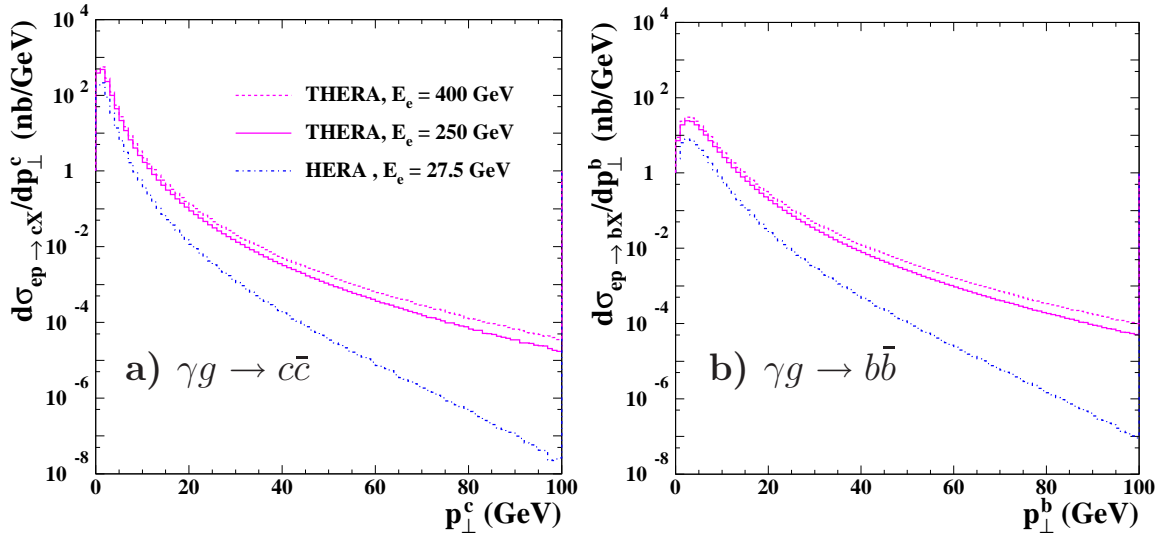


Figure 2.2.11: The contribution of photon–gluon fusion to the differential cross sections $d\sigma/dp_{\perp}$ for (a) charm and (b) beauty production calculated in NLO QCD for $Q^2 < 1\text{GeV}^2$. The solid and dashed violet curves show the predictions for THERA operation with an electron energy of 250GeV and 400GeV , respectively, and $E_p = 920\text{GeV}$. The predictions for the HERA case are indicated by the dash-dotted blue curves.

Figure 2.2.11 compares the contributions of photon–gluon fusion to the differential cross sections $d\sigma/dp_{\perp}^{c,b}$ ($p_{\perp}^{c,b}$ denoting the quark transverse momentum) at HERA and THERA, calculated within NLO QCD [87] for $Q^2 < 1\text{GeV}^2$. The difference between the heavy quark production cross sections at THERA and HERA increases with increasing $p_{\perp}^{c,b}$, thereby creating the opportunity to measure charm and beauty quarks at THERA in a wider transverse momentum range. Such measurements will provide a solid basis for testing the fixed-order, resummed, and k_t -factorisation [90] pQCD calculations.

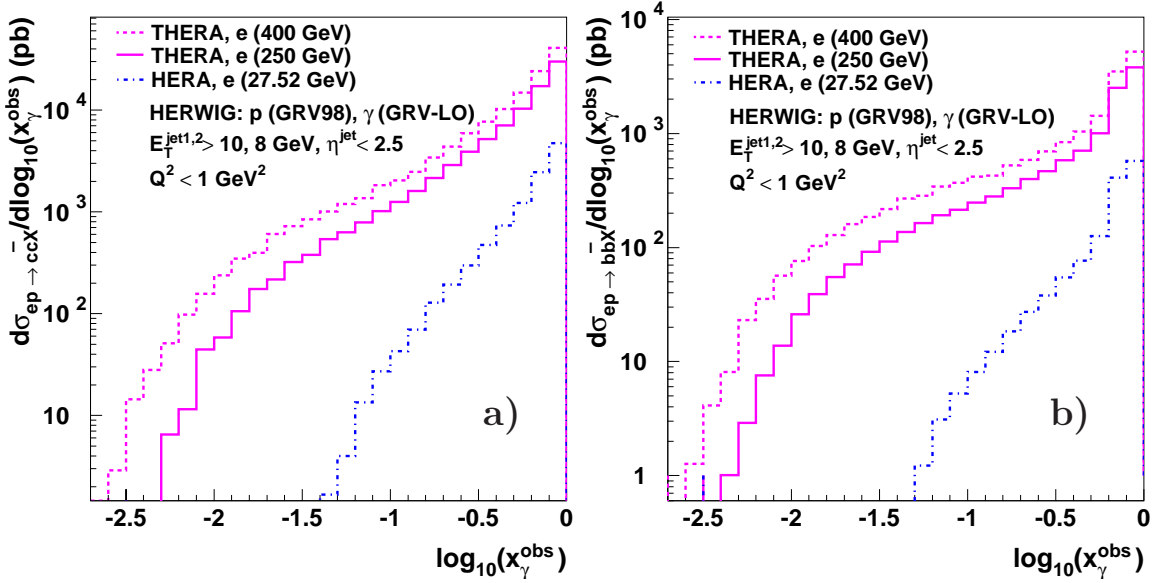


Figure 2.2.12: The differential cross sections $d\sigma/d\log_{10} x_{\gamma}^{\text{obs}}$ for (a) charm and (b) beauty dijet photoproduction as calculated in LO with the Monte Carlo generator HERWIG. The cross sections are shown for THERA, for a proton beam energy of 920 GeV and electrons with 250 GeV (solid magenta) and 400 GeV (dashed magenta), and for HERA (dashed blue).

The reconstruction of two jets in heavy-quark photoproduction events provides an opportunity to study the gluon and heavy-quark structure of the photon [85, 10]. The fraction of the photon energy contributing to the dijet photoproduction,

$$x_{\gamma}^{\text{obs}} = \frac{\sum_{\text{jet}1,2} (E_T^{\text{jet}} e^{-\eta^{\text{jet}}})}{2E_{\gamma}}, \quad (2.2.2)$$

has been found a useful observable for the investigation of the photon structure function. Here, E_T^{jet} and η^{jet} are the jet transverse energy and pseudorapidity, respectively, and the summation is over the two jets with highest E_T^{jet} within the accepted η^{jet} range. Figure 2.2.12 compares $d\sigma/d\log_{10} x_{\gamma}^{\text{obs}}$ for charm and beauty photoproduction ($Q^2 < 1 \text{ GeV}^2$) at HERA and THERA. The cross sections have been calculated in LO with the Monte Carlo generator HERWIG [91]. The difference between the heavy-quark dijet photoproduction cross sections at THERA and HERA increases towards smaller x_{γ}^{obs} values. The gluon and heavy quark structure of the photon can be studied only for $x_{\gamma}^{\text{obs}} \gtrsim 0.1$ at HERA. The transition to the THERA energy regime will provide an opportunity to probe the structure down to at least $x_{\gamma}^{\text{obs}} = 10^{-2}$ [88]. The gluon and heavy quark structure of the photon at THERA will be measured at rather large scale values stemming from the high E_T values of two reconstructed jets. Thus the measurements will provide complementary information to the results of future e^+e^- and $\gamma\gamma$ colliders [88].

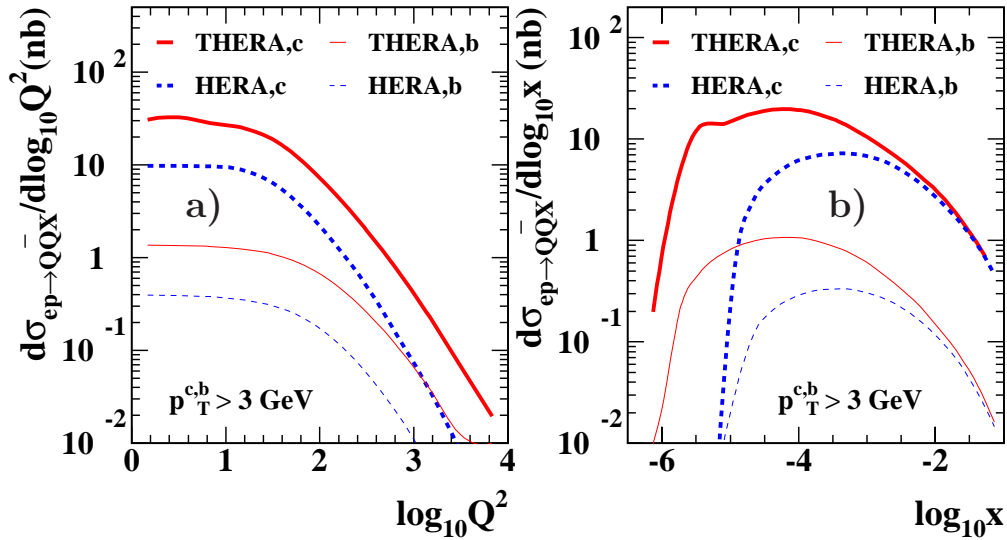


Figure 2.2.13: The differential cross sections for charm (thick curves) and beauty (thin curves) production in neutral current DIS calculated in NLO QCD, (a) $d\sigma/d\log_{10} Q^2$ and (b) $d\sigma/d\log_{10} x$. The cross sections at THERA (solid curves) and HERA (dashed curves) are compared.

The kinematic limits of DIS at THERA are one order of magnitude higher in Q^2 and one order smaller in x with respect to those at HERA. Figure 2.2.13 shows the differential cross sections $d\sigma/d\log_{10} Q^2$ and $d\sigma/d\log_{10} x$ for charm and beauty production in neutral current (NC) DIS calculated with the NLO code of [92]. The THERA cross sections are shifted towards smaller x values with respect to those at HERA. They are significantly above the HERA cross sections at all Q^2 . Thus THERA will open new kinematic regions where the charm and beauty contributions to the proton structure function, F_2^c and F_2^b , can be extracted [89]. The measurement of charm production at large Q^2 will provide an opportunity to test the resummed pQCD calculations which treat the charm quark as a massless parton [93]. Charm production in the process of photon–gluon fusion at low Q^2 values will serve for the determination of the gluon structure of the proton in the as yet unexplored kinematic range $10^{-5} < x_g < 10^{-4}$ [89].

The theoretical description of charm production in charged current (CC) DIS is challenging [94]. The special interest in this process is caused by its sensitivity to the proton strange-quark density which is rather poorly known [95]. However, no measurement of CC charm production has been performed so far at HERA due to the small signal cross section (~ 10 pb). According to a HERWIG calculation, the cross sections for both LO CC charm production processes, $W^+s \rightarrow c$ and $W^+g \rightarrow c\bar{s}$, will be more than 6 times larger at THERA than at HERA. The differential cross sections $d\sigma/d\log_{10} Q^2$ for CC charm production are shown in Fig. 2.2.14. The THERA cross sections are shifted towards larger Q^2 with respect to those at HERA. They are one order of magnitude larger than the HERA cross sections at large Q^2 values, thereby creating the opportunity to study charm production in CC DIS at THERA [89].

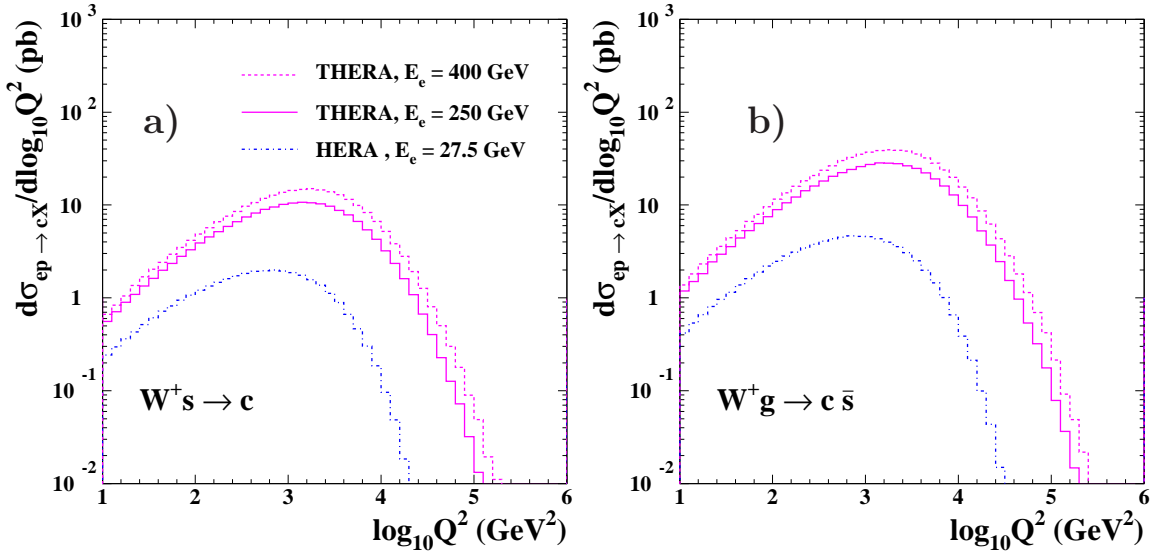


Figure 2.2.14: *The differential cross sections $d\sigma/d\log_{10} Q^2$ for charm production in charged current DIS, (a) from the strange sea and (b) from boson–gluon fusion, calculated with the LO Monte Carlo generator HERWIG. The cross sections are shown for THERA for a proton beam energy of 920 GeV and electrons with 250 GeV (solid magenta) and 400 GeV (dashed magenta), and for HERA (dashed blue).*

In conclusion, studies of charm and beauty production at THERA will provide unique new information about the proton and photon structures in as yet unexplored kinematic ranges.

2.2.2.5 Electroweak structure functions

In the THERA range of very high $Q^2 > M_Z^2$, the NC cross section receives comparable contributions from the exchange of photons, of Z bosons and from their interference. This is illustrated in Fig. 2.2.15 showing the reduced NC cross section, $\sigma_r = \sigma_{NC}/Y_+$, defined by the relation

$$\sigma_{NC} = \frac{d^2\sigma_{NC}^\pm}{dx dQ^2} \frac{Q^4 x}{2\pi\alpha^2} = Y_+ \mathbf{F}_2^\pm + Y_- \mathbf{xF}_3^\pm \quad (2.2.3)$$

with $Y_\pm = (1 \pm (1-y)^2)$ and the fine structure constant α . Due to the Z exchange contribution, a new structure function combination \mathbf{xF}_3 occurs in NC [96, 97] (for a comprehensive review see [98]), which in the QPM measures a combination of the u and d valence quark distributions $q_v = q - \bar{q}$. Therefore deep inelastic NC scattering at very high Q^2 is sensitive to the quark flavours, in contrast to low Q^2 , where the structure function F_2 measures only the weighted sum $\sum_q Q_q^2 (q + \bar{q})$ of quark and anti-quark distributions.

Similarly, in CC scattering, the double differential cross section is given by

$$\frac{d^2\sigma_{CC}^\pm}{dxdy} = \frac{G_F^2}{2\pi} \cdot \left(\frac{M_W^2}{Q^2 + M_W^2} \right)^2 \cdot s \cdot \frac{1 \pm \lambda}{2} \cdot [Y_+ W_2^\pm \mp Y_- x W_3^\pm], \quad (2.2.4)$$

where M_W is the CC propagator mass and G_F the Fermi constant. For a given beam charge, the cross section contains two structure functions which, in the QPM, are given by the following sums over the u - and d -type parton distributions:

$$\begin{aligned} W_2^{+(-)} &= 2x \sum (q_{d(u)} + \bar{q}_{u(d)}) \\ xW_3^{+(-)} &= 2x \sum (q_{u(d)} - \bar{q}_{d(u)}). \end{aligned} \quad (2.2.5)$$

The cross section is proportional to s (which at THERA is equivalent to a beam energy of about 10^3 TeV in a neutrino fixed-target experiment). Combining NC and CC

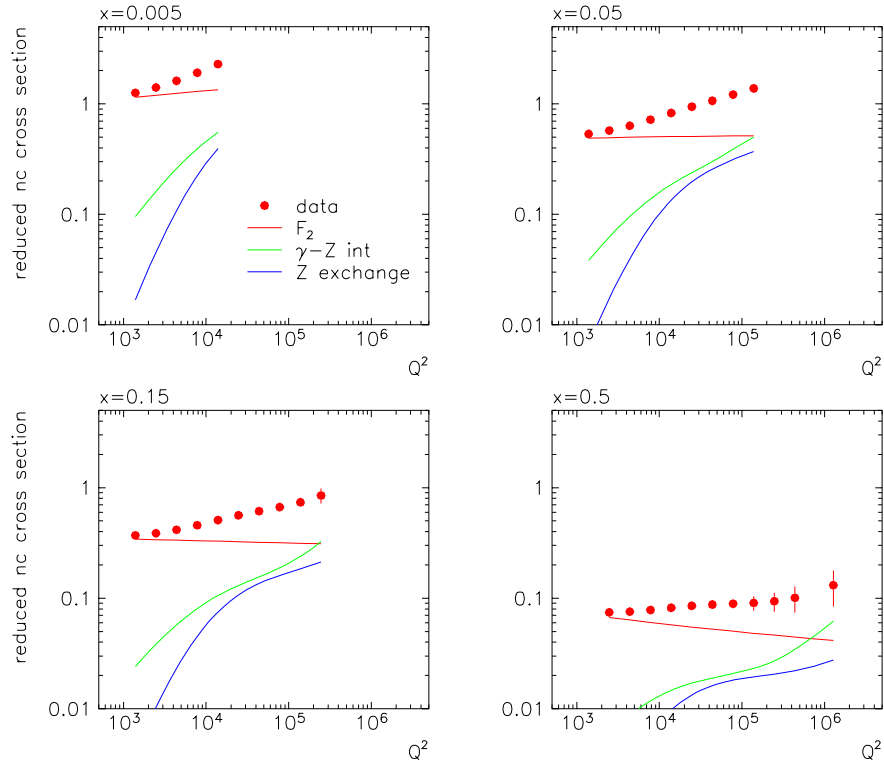


Figure 2.2.15: Simulation of a measurement of the reduced NC DIS cross section at THERA in unpolarised electron scattering, for an integrated luminosity of 200 pb^{-1} . The error bars are a convolution of statistical and estimated systematic uncertainties. The curves represent the fraction of the one-photon exchange (red, top), of the γZ interference (green, middle) and of the pure Z exchange (blue, bottom). Towards very high Q^2 , depending on the lepton beam charge and polarisation, the Z exchange contributions become increasingly important.

$e^\pm p$ cross sections for different lepton polarisations, a complete unfolding [99] of the up and down quark and anti-quark distributions can be envisaged at THERA, with much higher accuracy than at HERA due to the extended Q^2 range which enhances the electroweak contributions to the cross section. The approximate symmetry of the electron and proton beam energies furthermore allows access to the up and down valence quark distributions up to very large x . This is of advantage over the standard method to access d_v at large x which relies on a comparison of proton and neutron structure functions and thus is subject to uncertain nuclear binding corrections, see [100]. The combination with the results of future high-statistics neutrino experiments [101] will permit important, flavour dependent tests of QCD.

The coverage of the full x range from about 0.005 to 1 in the region of high Q^2 at THERA is also essential for testing rigorous theoretical predictions in CC scattering [102], such as the Adler sum rule, $\int_0^1 (W_2^+ - W_2^-) dx/x = 2$, the Bjorken sum rule, $\int_0^1 (W_1^+ - W_1^-) dx = 1$, and the Gross-Llewellyn-Smith sum rule, $\int_0^1 (W_3^+ + W_3^-) dx = 6$. While the Adler sum rule holds independently of QCD, the two latter relations test QCD and are subject to higher-twist corrections which are negligible in the very high Q^2 range of THERA.

Various measurements of electroweak quantities can be performed at THERA, e.g. of the light-quark couplings, of the gauge boson masses in the space-like region and of parity violation at very high Q^2 via polarisation asymmetries in NC scattering, similarly to the pioneering experiment [103]. Utilising the high degree of lepton-beam polarisation at TESLA, one can search with much increased sensitivity for the existence of right handed currents in the new energy range which would prevent the CC cross section σ^\pm from vanishing at $\lambda \rightarrow \mp 1$ (cf. eq. 2.2.4). Such a measurement at THERA for a luminosity of 100 pb^{-1} is illustrated in Fig. 2.2.16 for $\sqrt{s} = 1 \text{ TeV}$.

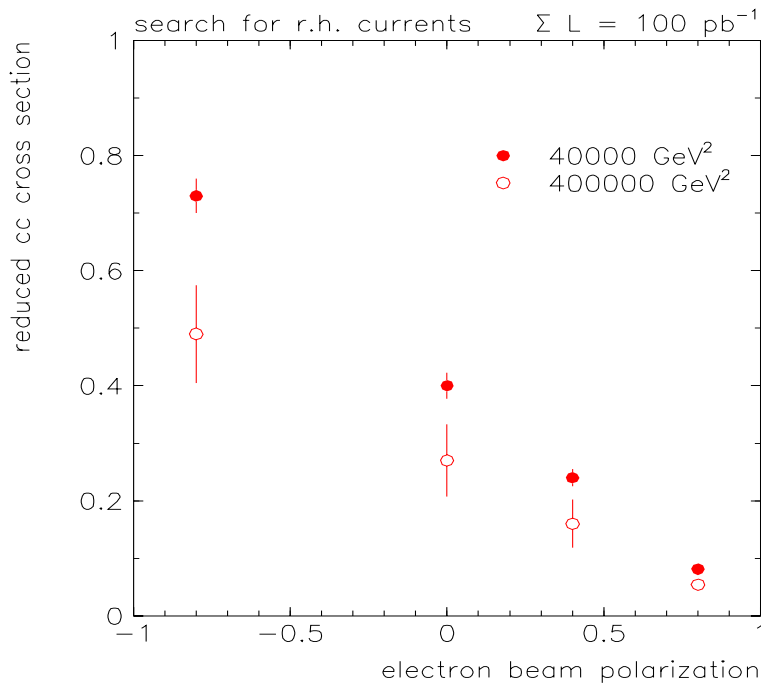


Figure 2.2.16: Search for right-handed currents in CC scattering at THERA using a measurement of the electron-proton CC cross section as a function of the electron beam polarisation, λ . This simulation assumes a total integrated luminosity of 100 pb^{-1} distributed over four measurements at different λ .

The extension towards the electroweak region of very high $Q^2 \sim 10^5 \text{ GeV}^2$ and the coverage of the full x range make THERA an excellent facility for the exploration of the partonic nucleon structure and the test of the electroweak theory. If new interactions and particles will be found in the TeV range of energy, THERA will not only explore these but as well be crucial in accurately determining the parton distributions which have to be known for the interpretation of the new phenomena.

2.2.3 Searches for new particles or phenomena

2.2.3.1 Leptoquarks and squarks

The ep collider THERA, providing both baryonic and leptonic quantum numbers in the initial state, naturally offers the possibility to search for new bosons possessing couplings to an electron–quark pair. Such particles could be squarks in supersymmetry with R -parity violation (\mathcal{R}_p), or leptoquark (LQ) bosons [104] which appear in various unifying theories beyond the Standard Model (SM).

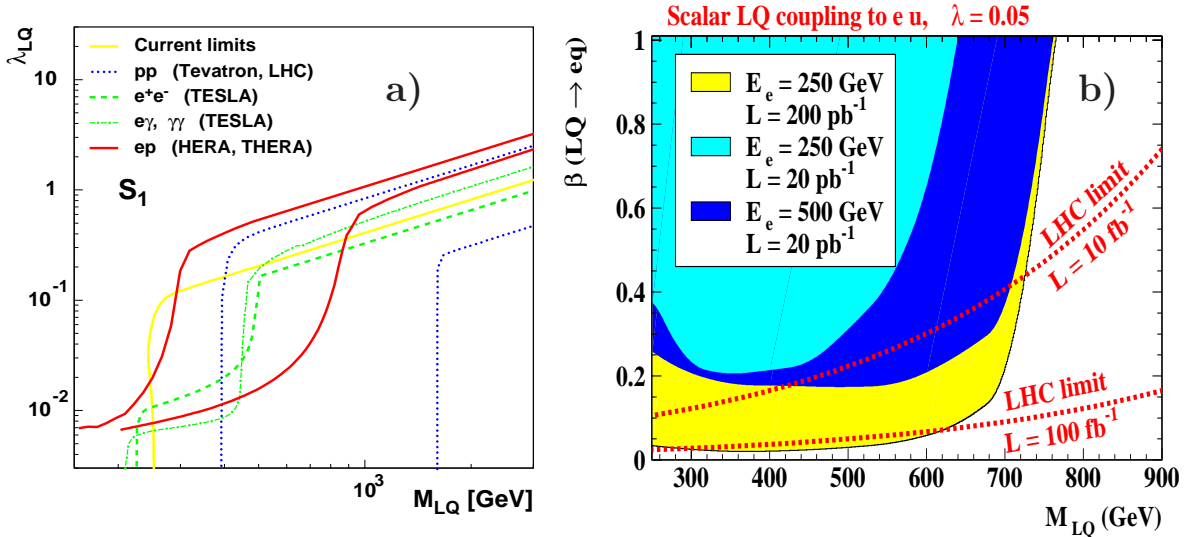


Figure 2.2.17: (a) Mass-dependent upper bounds on the LQ coupling λ as expected at THERA (lower solid red curve, $E_e = 250 \text{ GeV}$, $E_p = 920 \text{ GeV}$, 100 pb^{-1} of e^-p data), HERA (upper solid red curve, $2 \times 400 \text{ pb}^{-1}$ of $e^\pm p$ data), TESLA ($E_e = 250 \text{ GeV}$, 100 fb^{-1} of ee , $e\gamma$ or $\gamma\gamma$ data), Tevatron (upper dotted curve, 10 fb^{-1}) and LHC (lower dotted curve, $\sqrt{s} = 14 \text{ TeV}$, 100 fb^{-1}). Upper limits as obtained from a global fit of various existing data sets [104] are also shown by the solid yellow curve. (b) Typical expected mass-dependent sensitivities on the branching ratio $\beta(LQ \rightarrow eq)$ of a LQ decaying to eq , at THERA for two different values of the lepton beam energy and at LHC; the coloured regions (the domains above the dashed red curves) would be probed by THERA (LHC).

Leptoquarks (or \mathcal{R}_p squarks) with masses up to the kinematic limit, \sqrt{s} , could be singly produced as s -channel resonances by the fusion of the incoming electron with

a quark coming from the proton, with largest cross section when a valence quark in the proton participates in the fusion. For LQs decaying into an electron and a quark, the final state is similar to that of high- Q^2 NC DIS. For masses above the kinematic limit, LQ exchange can be parameterised by a contact interaction and could affect the measured high- Q^2 NC DIS cross section.

The sensitivity to LQs is discussed here either in the strict context of the BRW phenomenological ansatz [105], where the decay branching ratios are fixed by the model, or in the context of generic models allowing for arbitrary branching ratios.

For one of the scalar LQs described by the BRW model, with fermion number $F = 2$ (i.e. coupling to an e^- and a valence quark), the expected THERA sensitivity on the Yukawa coupling λ at the LQ- e - q vertex is illustrated in Fig. 2.2.17a as a function of the LQ mass, and compared to that of HERA-II, TESLA and hadron colliders [106]. THERA will improve the bounds expected from the full data sample of HERA by typically one order of magnitude, and its sensitivity will be significantly better than that of TESLA in the mass range 0.5–1 TeV, for a lepton beam energy of 250 GeV. However, the sensitivity of the LHC to pair-produced LQs should extend up to LQ masses of ~ 2 TeV, independently of λ . The LHC will thus probe the mass domain where resonant LQ production could be possible at THERA. This statement remains valid in ‘generic’ models, where the branching ratio $\beta(\text{LQ} \rightarrow eq)$ of the LQ to decay into eq is not fixed but treated as a free parameter, as shown in Fig. 2.2.17b.

	$S_{0,L}$	$S_{1,L}$	$\tilde{S}_{0,R}$	$S_{0,R}$	$S_{1/2,L}$	$\tilde{S}_{1/2,L}$	$S_{1/2,R}$
$\tilde{S}_{0,L}$		β_ν	P_e	P_e	e^+/e^-		
$S_{1,L}$	β_ν		P_e	P_e			
$\tilde{S}_{0,R}$	P_e	P_e		P_p			
$S_{0,R}$	P_e	P_e	P_p				
$S_{1/2,L}$	e^+/e^-					P_p	P_e
$\tilde{S}_{1/2,L}$					P_p	P_e	
$S_{1/2,R}$					P_e	P_e	

Table 2.2.1: *Discrimination between LQs with different quantum numbers by using the lepton beam charge (e^+/e^-) or e/p polarisation (P_e, P_p). The nomenclature of [107] has been used to label the different scalar LQ species described by the BRW model, in which the branching ratio β_ν of the LQs is known.*

If a LQ directly accessible at THERA is discovered elsewhere, THERA will be the ideal machine to disentangle the quantum numbers of this resonance and to study its properties, as illustrated in table 2.2.1: the angular distribution of the final-state lepton easily discriminates between a scalar or vector resonance; the fermion number is obtained by comparing the signal cross section in e^+p and e^-p collisions; the polarisation P_e of the lepton beam determines the chirality structure of the LQ coupling. In addition, the fact that a signal in the CC channel could also be observed provides another

discriminating variable in LQ models where the branching ratio $\beta_\nu = \beta(\text{LQ} \rightarrow \nu q)$ is known. Further discrimination between LQs coupling to eu or ed would need e.g. proton beam polarisation, P_p [108].

Finally, THERA allows direct measurements of LQ couplings in the range 10^{-1} – 10^{-2} for given LQ branching ratios. In contrast, pp and $p\bar{p}$ colliders are only sensitive to larger couplings via lepton-pair production induced by t -channel LQ exchange.

2.2.3.2 Contact interactions

The sensitivity of THERA to generic $eeqq$ four-fermion contact interactions (CI) has been studied in detail. Besides the exchange of very massive LQs, such CI terms can be used to parameterise any new physics process (e.g. exchange of new bosons, compositeness) appearing at an energy scale above the centre-of-mass energy. At THERA, $eeqq$ four-fermion terms would interfere (constructively or destructively) with NC DIS and thus affect the measured NC DIS Q^2 distribution. Various CI models can be considered, depending on the chiral structure of the new interaction and on the flavours of the involved quarks. CI models which violate parity are already severely constrained by the precise measurements of atomic parity violation. For models conserving parity, scales up to ~ 18 TeV could be probed at THERA, extending considerably beyond the existing bounds. The LHC collider should be able to probe even larger scales. However, should an $eeqq$ CI be within its reach, THERA would give deeper insights on the chiral structure of this new interaction by exploiting the lepton beam polarisation. For general CI models involving all possible flavour and chiral structures, searches at THERA and LHC will be to a large extent complementary.

2.2.3.3 Large extra dimensions

The t -channel exchange of Kaluza–Klein gravitons in models with large extra dimensions [109] would also affect the Q^2 distribution of the observed NC DIS events. Compactification scales up to ~ 2.8 TeV could be probed at THERA. However, the existence of extra dimensions corresponding to much larger scales should be detected by the analysis of dijet events at the LHC. It has been conjectured that fermions with different gauge quantum numbers are localised on different ‘branes’ in the full space-time [110]. For accessible compactification scales, relevant and complementary information on this fermion localisation could be provided by TESLA and THERA, in contrast to the LHC, where the two-gluon initial state would dominate the cross section.

2.2.3.4 Excited leptons

The single production of excited leptons (electrons, e^* , and neutrinos, ν^*) at THERA can proceed via the t -channel exchange of a gauge boson. Assuming an equal coupling, f , of the e^*e pair to $U(1)$ and $SU(2)$ bosons, the expected sensitivity to f/Λ has been studied as a function of the e^* mass M_{e^*} (here Λ denotes the compositeness scale [111]). For $f/\Lambda = 1/M_{e^*}$, excited electrons could be detected up to masses of ~ 1 TeV at THERA with a luminosity of 200 pb^{-1} and beam energies of 800 GeV.

A similar sensitivity is expected for excited neutrinos. This extends far beyond the current bounds of HERA and LEP. Pair production of e^* and ν^* at the LHC should probe this mass domain independently of the unknown couplings.

2.2.4 Resolving the partonic structure of the photon

In high-energy processes, the photon exhibits a “hadronic structure”. At low Bjorken x , the photon structure function $F_2^\gamma(x, \hat{Q}^2)$ is expected to behave like the proton F_2 , i.e. to increase towards lower x at sufficiently large \hat{Q}^2 , where \hat{Q}^2 is the scale used to probe the quasi-real photon. Unique expectations for the photon are the logarithmic rise of the hadronic structure function with the scale, \hat{Q}^2 , and a large quark density at large x . Observations of these phenomena are basic tests of QCD and essential to understanding the structure of the photon.

The ep collider THERA offers the opportunity to study the partonic structure of the photon in terms of the variable x_γ , which measures the fraction of the photon momentum participating in the hard interaction. At lowest order, x_γ is equal to unity for ‘direct process’ (Fig. 2.2.18a), whereas ‘resolved processes’ (Fig. 2.2.18b) are characterised by a smaller x_γ . THERA extends the kinematic range in x_γ by approximately one order of magnitude towards smaller values with respect to existing colliders (HERA and LEP) and significantly increases the accessible hard scale $\hat{Q}^2 = p_T^2$, i.e. the square of the parton transverse momenta (corresponding to Q^2 in deep inelastic $e\gamma$ scattering).

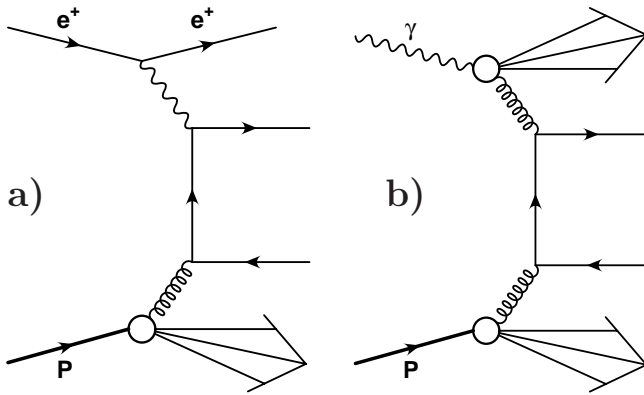


Figure 2.2.18: Examples of LO (a) direct photon and (b) resolved photon processes in ep collisions.

Photoproduction ($Q^2 < 1 \text{ GeV}^2$) of particles (hadrons or prompt photons) or jets at high transverse momenta provides information on the gluonic content of the quasi-real photon (Fig. 2.2.18b), complementary to that from deep inelastic $e\gamma$ scattering. The photoproduction of dijets, heavy quarks and prompt photons has been studied [112, 88, 113], with the emphasis on the potential of THERA to yield information on the structure of the real photon. The possibility of measuring the structure of the virtual photon at THERA has also been considered [114]. In addition, it has been demonstrated that a first determination of the spin structure of the photon at THERA appears feasible for luminosities significantly exceeding $\mathcal{O}(10 \text{ pb}^{-1})$ [115].

Good knowledge of the hadronic interactions of the photon is important for future

high energy physics investigations, e.g. for determining the Standard Model background in searches for new particles. The present situation is not satisfactory, as data for some processes, such as photoproduction of dijets at HERA, are not in agreement with existing NLO QCD calculations [116, 117]. The level of agreement for processes involving resolved virtual photons is even more problematic.

2.2.4.1 Kinematics and comparison with other colliders

A first estimate of the benefits of THERA can be obtained by comparing the kinematic reach of THERA ($\sqrt{s} \approx 1$ TeV) with that of LEP ($\sqrt{s} \approx 200$ GeV), HERA ($\sqrt{s} \approx 300$ GeV) and a future linear e^+e^- collider, TESLA, ($\sqrt{s} \approx 500$ GeV). Of interest for this section are the minimal accessible x_γ ,

$$x_\gamma^{\min}|_{e^+e^-} = \frac{p_T e^{\pm\eta_{\text{CM}}}}{2E_e - p_T e^{\mp\eta_{\text{CM}}}}, \quad x_\gamma^{\min}|_{ep} = \frac{E_p p_T e^{-\eta_{\text{LAB}}}}{2E_e E_p - E_e p_T e^{\eta_{\text{LAB}}}}, \quad (2.2.6)$$

the range of the hard scale, \hat{Q}^2 , and the pseudorapidity, η , of the jets in resolved-photon events which determines the geometrical acceptance of the detector.

In Fig. 2.2.19a, the minimum photon momentum fraction, x_γ^{\min} , for a fixed transverse momentum of $p_T = 10$ GeV, is shown as a function of the laboratory-frame pseudorapidity for e^+e^- and ep colliders. It can be seen that for a given η , THERA accesses x_γ^{\min} values that are an order of magnitude smaller than at HERA. The minimum x_γ at TESLA would also be beyond the reach of LEP and HERA. However, smaller values of x_γ can be accessed at THERA than at TESLA in the very forward direction ($\eta_{\text{LAB}}^{ep} > 2$), reaching a minimum for the given transverse momentum at $\eta_{\text{LAB}}^{ep} \approx 4.6$. This demonstrates the need for an instrumentation of the very forward direction at THERA which allows an accurate measurement of jets up to the rapidities discussed here.

The accessible regions in \hat{Q}^2 and x or x_γ are shown in Fig. 2.2.19b, taking into account restrictions imposed by limited detector acceptance. Typical kinematic selection criteria are imposed, as indicated in Fig. 2.2.19b for LEP and HERA. The same cuts have also been applied for the TESLA and THERA studies, although it is hoped that the future experiments would have improved acceptance in the very forward and backward regions. Although the e^+e^- machines will yield the lowest values of x , the ep machines can probe smaller values of x_γ for a given \hat{Q}^2 . In particular, THERA will provide valuable additional information on the structure of the photon down to $x_\gamma \sim 0.01$ at high p_T , thus complementing TESLA and the current experiments.

2.2.4.2 Jet production

Inclusive dijet and charm production at THERA have been studied and compared with what is currently achievable at HERA [112, 88, 118]. Heavy quark production at THERA is discussed in Sect. 2.2.2.4. Here the focus is on the potential of the THERA collider in testing the partonic content of the photon using jets and heavy quarks as tools. In dijet production, the observable x_γ^{obs} , defined as the fraction of the photon

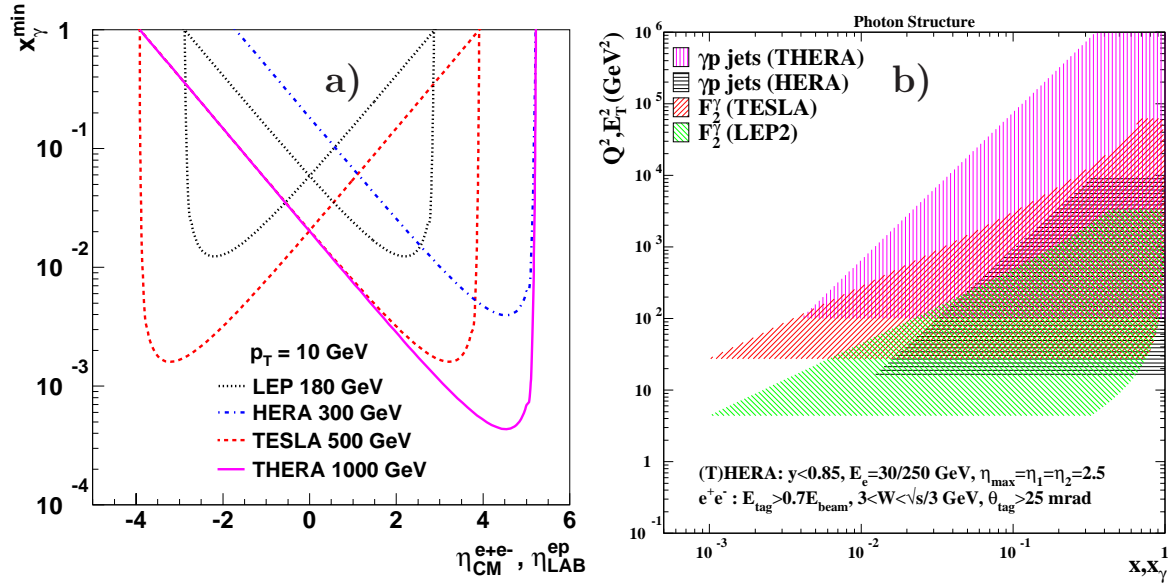


Figure 2.2.19: (a) The minimum photon momentum fraction, x_γ^{\min} , as a function of the rapidity in the centre-of-mass frame for e^+e^- colliders and in the laboratory frame for ep colliders. (b) Range in \hat{Q}^2 (Q^2 or p_T^2) versus x or x_γ with kinematic cuts reflecting a realistic detector acceptance (indicated at the bottom of the figure). The kinematic reach of THERA is compared with that of TESLA, HERA and LEP2.

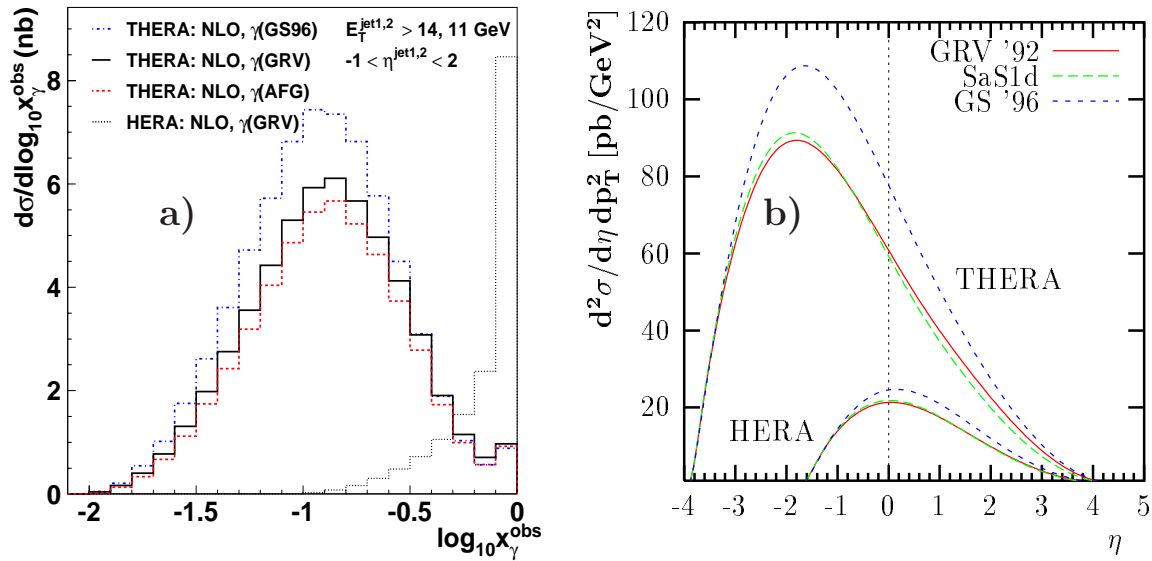


Figure 2.2.20: (a) The differential cross section, $d\sigma/d\log_{10} x_\gamma^{\text{obs}}$, for inclusive dijet photoproduction at HERA and THERA as predicted by a NLO calculation. (b) The differential cross section for photoproduction of charm in ep reactions, $ep \rightarrow e c \bar{c} X$, at $p_T = 10$ GeV calculated in LO in the massless (VFNS) scheme.

energy producing the two jets of highest transverse energy (see eq. 2.2.2), is used as an estimator for x_γ [119]. The cross section $d\sigma/d\log_{10} x_\gamma^{\text{obs}}$ in NLO [120] is shown in Fig. 2.2.20a. It can be seen that the prediction for HERA is strongly peaked at x_γ^{obs} close to unity, whereas the predictions for THERA peak at $x_\gamma^{\text{obs}} \sim 0.1$. Differences of up to 50% between the results for different structure function sets [121] are observed. The charm cross section $d^2\sigma/d\eta dp_T^2$ from a LO calculation for $p_T = 10$ GeV is peaked at $\eta \approx 0$ for HERA and at $\eta \approx -2$ for THERA (see Fig. 2.2.20b). The cross section maximum at THERA is enhanced by a factor of about 5 as compared to HERA. Again, some sensitivity to the choice of the photon parton parametrisation is evident. For THERA, the cross section ratio of resolved to direct photoproduction of charm exceeds unity at $\eta > -3.5$ and rapidly increases with growing η (see Fig. 2.2.21).

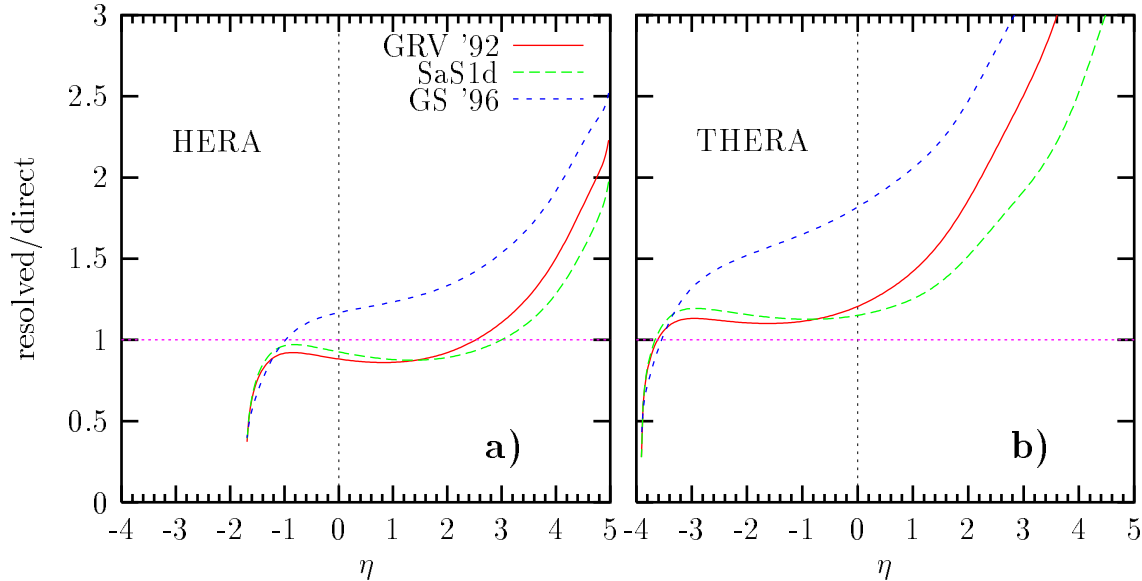


Figure 2.2.21: The ratio of the resolved to the direct contributions to the charm photoproduction cross sections $d^2\sigma/d\eta dp_T^2$ in ep reactions at $p_T = 10$ GeV, (a) for HERA and (b) for THERA. The cross sections have been calculated to LO in the massless (VFNS) scheme, using the CTEQ5L parton distribution set for the proton and three different LO parton distribution sets for the photon.

2.2.4.3 Prompt photon production

Prompt photon photoproduction, $ep \rightarrow \gamma X$ (the deep inelastic Compton scattering process), allows the photon structure to be studied in yet another way [113]. For example, calculations demonstrate that in the forward region ($\eta_\gamma > 0$) the Compton process is dominated by the reaction ($gq \rightarrow \gamma q$) with a cross section nearly ten times larger than at HERA and extending to larger transverse momenta of the photon. Thus prompt photon production will allow the gluonic content of the photon to be probed.

2.3 Experimentation at THERA

2.3.1 Collision of TESLA electrons with HERA protons

The achievable luminosity for THERA, the TESLA–HERA electron proton collider, is constrained by the electron beam power, the intra-beam scattering which limits the emittance of the proton beam, and the β -function of the protons which is achievable within the practical limits of focusing at the interaction point (IP). In the limit of ultra-short bunches and assuming head-on collisions, round beams, and equal transverse beam sizes for electrons and protons at the crossing point, the luminosity L is given by

$$L = \frac{N_e N_p f_b \gamma_p}{4\pi \varepsilon_p \beta^*}, \quad (2.3.1)$$

where ε_p is the normalised proton beam emittance or mean square beam size divided by the betatron parameter β^* , N_e and N_p are the numbers of electrons and protons per bunch, f_b is the collision frequency, and γ_p is the proton Lorentz factor. Once the energy of the electron beam is chosen, the total electron beam current ($I_e = N_e \cdot e \cdot f_b$) is limited by the allowed electron beam power or $I_e = e \cdot P_e / E_e$. The luminosity L is independent of the bunch charge N_e and the collision frequency f_b as long as their product, expressed by the beam power P_e , is constant. The luminosity can thus be written in the following form:

$$L = 4.8 \times 10^{30} \text{ cm}^{-2} \text{ s}^{-1} \cdot \frac{N_p}{10^{11}} \frac{10^{-6} \text{ m}}{\varepsilon_p} \frac{\gamma_p}{1066} \frac{10 \text{ cm}}{\beta^*} \frac{P_e}{22.6 \text{ MW}} \frac{250 \text{ GeV}}{E_e}. \quad (2.3.2)$$

2.3.1.1 Proton phase space density

The ratio N_p/ε_p is called beam brightness. In conjunction with a certain bunch length and energy spread of the protons it is a measure of the phase space density. The beam brightness is limited by space charge forces in the low-energy part of the accelerator chain. But also at high energy, the beam brightness is subject to slow decay due to Coulomb scattering of protons within the bunch, the so-called intra-beam scattering (IBS) [122], which, in the presence of dispersion, leads to emittance growth. The limitation of beam brightness depends on the longitudinal charge density and thus on the bunch length σ_p . This is, however, also a critical parameter at collision since it limits the effective size of the proton beam at the IP. For long bunches (large σ_p compared to β^*), collisions occur at significantly increased cross sections due to the quadratic increase of β as a function of the distance s from the IP (hourglass effect). In addition, the finite bunch length reduces the effective proton beam cross section in case of a crossing angle. For given radio-frequency (RF) focusing forces, the bunch length is given by the longitudinal emittance, which is also subject to limitation by space charge effects at low energy and to slow growth due to IBS at high energy. Due to practical limitations of the RF focusing system and dynamical stability considerations, there is only a limited range for optimising the bunch length within these constraints. At low energy, one wants to maximise the bunch length to achieve maximum brightness. At

high energies, at collisions, one wants minimum bunch length to achieve the minimum effective beam cross section.

Taking these general limitations into account, an IBS growth time of 2.9 hours results for a 1 TeV proton beam in HERA with an initial transverse normalised emittance of $\varepsilon_p = 1 \times 10^{-6}$ m, an initial bunch length of $\sigma_p = 10$ cm, and an initial relative energy spread of $\sigma_{p\epsilon} = 1.1 \times 10^{-4}$. The longitudinal growth time is just 2 hours. This determines the luminosity lifetime and must be considered as an upper limit for the proton density. In order to achieve smaller proton beam emittance, emittance cooling is required. For example, to reduce the emittance by a factor of five, cooling times of 12 min must be achieved to balance the IBS emittance growth. Up to this point, no such powerful cooling systems are available. This leads to the conclusion, that a proton beam normalised emittance in the order of $\varepsilon_p = 1 \times 10^{-6}$ m with $N_p = 10^{11}$ has to be considered as a minimum for HERA. It represents quite a challenge to achieve the corresponding beam brightness in the injector chain. At present, the best beam brightness values achieved in the DESY III synchrotron are in the range of $N_p/\varepsilon_p = 1.3 \times 10^{11}/3 \times 10^{-6}$ m [123] which falls short by a factor of 2.3 to the target value of $10^{11}/10^{-6}$ m. Electron cooling in the lower energy stages [124] may be necessary to achieve the target value. Active feedback to damp injection oscillations might be needed in the higher energy stages. The conclusion is that the target values of $N_p = 10^{11}$, $\varepsilon_p = 10^{-6}$ m, $\sigma_p = 16$ cm and $\sigma_{p\epsilon} = 1.1 \times 10^{-4}$ constitute an ambitious but maybe not unrealistic goal for the phase space density of an LC-ring electron-proton collider at HERA.

2.3.1.2 Interaction region layout

Small values of the β -function β^* at the IP are essential for high luminosity. The β -function is limited by the chromaticity of the protons which is generated in the low- β quadrupole magnets, by aperture limitations in connection with a maximum achievable field gradient in the quadrupole magnets and by the proton bunch length. As chromaticity and maximum beam size grow linearly with the final focus quadrupole distance from the IP, for fixed β^* , it is desirable to focus electrons and protons simultaneously, thereby minimising the distance of the quadrupole magnets to the IP. At 1 TeV proton energy, the bunch length should be 10 cm or longer for adequate IBS life times. In addition, in order to avoid the excitation of synchro-betatron resonances of the protons by the electrons the crossing angle must be limited to a few mrad. This is supported by recent tracking calculations [125]. Additional beam separation technique is thus required, possibly using soft magnetic separation.

Figure 2.3.1 shows a component layout and the resulting envelope functions that meet the requirements. The layout has been designed for a ratio of proton to electron energies of 1 TeV/300 GeV and is taken from previous work on electron-proton colliders based on a LC-ring combination [126]. The electron beam is focused by a superconducting quadrupole triplet which is placed at 5 m from the IP and two doublets which give a β^* of 97 cm at the IP and also low β at 25 m and 50 m from the IP. At these latter positions strong quadrupoles for the protons are placed which, because of the low

The trajectory of the TESLA beam line is planned to be tangential to the HERA Straight Section West. The beam separation scheme is designed such that no bends in the electron beam lines are necessary for the incoming electron beam. However, the outgoing protons receive a kick of 14 mrad and a radial displacement of 468 mm. This could be compensated by disabling the first superconducting dipole magnet for the outgoing protons, accompanied by a small correction kick of 1 mrad and a radial shift of the IP by approximately 524 mm away from the centre of the ring. The final geometry of the TESLA tunnel and beam line should take this into account. The outgoing electrons are allowed to receive a bending angle which would shorten the separation section on the other side considerably. The additional space made available in this way is needed to restore the proton orbit for incoming protons, making use of the now available dipole magnet from the other side. A complete layout of the geometry has not yet been designed.

2.3.1.3 Luminosity estimate

In Table 2.3.1, the parameters of an (e -LC)-(p -ring) collider based on TESLA and HERA parameters are summarised. In calculating the luminosity, the limitations in β and proton beam brightness as discussed in the previous sections as well as the hourglass effect and the effect of a crossing angle have been taken into account. Assuming a bunch length of 10 cm to be possible, the hourglass reduction factor is 0.9. Even a tiny crossing angle of $\theta = 0.05$ mrad changes the cross section and thus the luminosity by 6%. Combining all these numbers yields a luminosity of $L = 4.1 \times 10^{30} \text{ cm}^{-2} \text{ s}^{-1}$ when operating TESLA at $E_e = 250 \text{ GeV}$ and HERA at $E_p = 1 \text{ TeV}$. In a year of running this luminosity corresponds to about 40 pb^{-1} assuming an efficiency of 60% and 200 days of operation.

If THERA is operated with equal electron and proton energies, the focusing could be made much more efficient. Such an energy setting is not favourable for low x physics because the electron would be scattered even closer to the electron beam direction than in the asymmetric energy case. This constraint, however, is not important for high- Q^2 studies, for which, on the other hand, maximising the luminosity is of utmost importance.

With equal beam energies, a single low-beta doublet could be used to focus the beam to beta functions as small as 1 cm. The superconducting quadrupole magnets need to have a length of $l = 3 \text{ m}$, and would be placed starting at 2 m from the IP. An aperture of 20 mm would correspond to 10 times the r.m.s. beam size in these magnets. A peak field of 5 T would be required to produce the gradients needed in this setup. The magnet cryostat would have an estimated outer diameter of 40 cm. The detector would have to provide space for these magnets by giving up small-angle detector acceptance. The strong hourglass effect in this situation, with 16 cm bunch length and 1 cm beta function, must be overcome following a proposal by Dohlus and Brinkmann [127] which features a moving β -waist around the IP due to time-dependent focusing by introduction of RF quadrupoles. This way, the minimum β -function occurs at the location and time where the e -beam collides with a slice of the proton beam

electron beam parameters	
electron energy	$E_e = 250 \text{ GeV}$
number of electrons per bunch	$N_e = 2 \times 10^{10}$
bunch length	$\sigma_{se} = 0.3 \text{ mm}$
invariant emittance	$\varepsilon = 100 \times 10^{-6} \text{ m}$
beta function at IP	$\beta_{x,y} = 0.5 \text{ m}$
electron tune shift	$\Delta\nu_y = 0.228$
disruption	$D = 0.02$
bunch spacing	$t_{be} = t_{bp} = 211.37 \text{ ns}$
RF frequency	$f = 1301 \text{ MHz}$
accelerating gradient	$g = 23.4 \text{ MV/m}$
beam pulse length	$T_p = 1.19 \text{ ms}$
number of bunches	$56 \times (94 + 6 \text{ empty bunches})$
duty cycle	$d = 0.5\%$
repetition rate	$f_r = 5 \text{ Hz}$
beam power	$P_b = 22.6 \text{ MW}$
proton beam parameters	
proton energy	$E_p = 1 \text{ TeV}$
number of protons per bunch	$N_p = 10^{11}$
number of bunches	$N_{pb} = 94$
beam current	$I_p = 71 \text{ mA}$
bunch length	$\sigma_p = 10 \text{ cm}$
beta functions at IP	$\beta_{xp}^* = 10 \text{ cm}$
normalised emittance	$\varepsilon_p = 1 \times 10^{-6} \text{ m}$
IBS growth time transv./long.	$\tau_s = 2.88 \text{ h}, \tau_x = 2.0 \text{ h}$
collider parameters	
hourglass reduction factor	$R = 0.9$
crossing angle	$\theta = 0.05 \text{ mrad}$
luminosity	$L = 4.1 \times 10^{30} \text{ cm}^{-2} \text{ s}^{-1}$

Table 2.3.1: *Main parameters of an electron–proton collider based on HERA and TESLA.*

and the beam size remains uniform during the whole collision time. In the horizontal plane, the beam size would be dominated by the crossing angle and the β -function can be relaxed to 3 cm. The luminosity which can be achieved in this scenario is estimated to be $L = 2.5 \times 10^{31} \text{ cm}^{-2} \text{ s}^{-1}$ for $E_e = E_p = 500 \text{ GeV}$. This scenario uses both arms of TESLA, which is possible due to the standing-wave type cavities in the superconducting LC. With the TESLA machine upgraded in power, energies as high as 400 GeV per arm are envisaged, which for THERA opens the possibility to run at $E_e = E_p = 800 \text{ GeV}$. This provides a maximum energy in ep scattering of $\sqrt{s} = 1.6 \text{ TeV}$ at an estimated luminosity of $1.6 \times 10^{31} \text{ cm}^{-2} \text{ s}^{-1}$. Thus with equal beam energies and a dynamic focusing system, integrated luminosities of about 200 pb^{-1} per year are in reach for THERA.

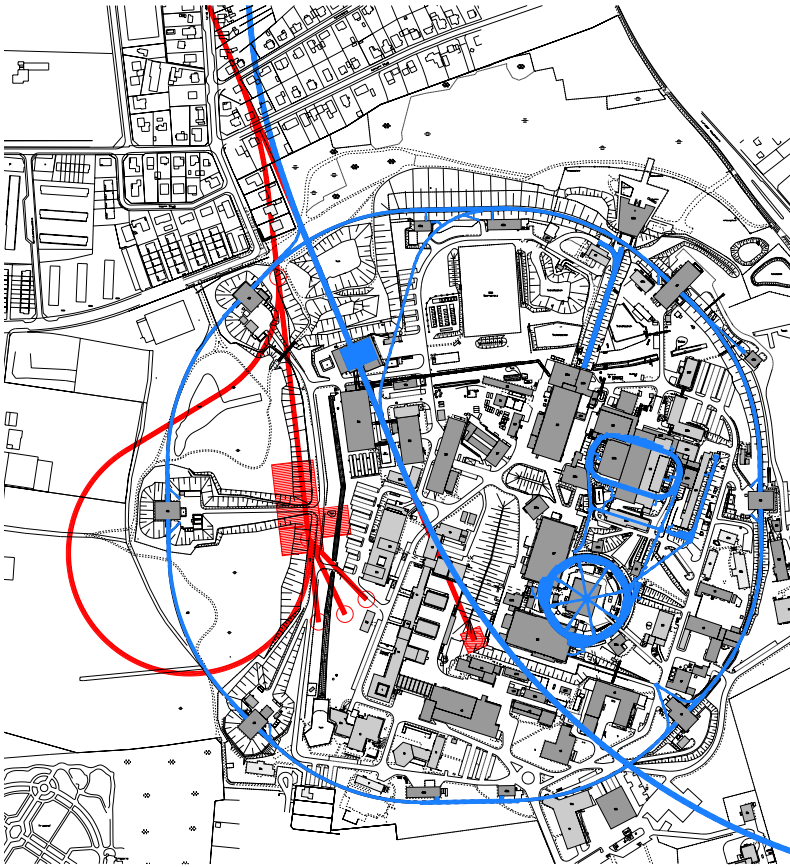


Figure 2.3.2: *Site of THERA: TESLA (red) is foreseen to be built tangentially to the HERA ring (blue) such that electrons from North hit protons in the West Hall on the DESY site. The PETRA ring is seen which serves as a pre-accelerator for HERA protons. The PETRA lepton injection line will be instrumented with superconducting magnets to arrange protons travelling clockwise in HERA. After collision the TESLA electrons will be dumped on site.*

2.3.1.4 Auxiliary systems

The THERA accelerator site at DESY is shown in Fig. 2.3.2. Electrons or positrons are injected at the far North end into the linac and accelerated up to full energy. A dedicated THERA electron gun and a short injector unit will be necessary. In order to operate the ep collider, the protons have to travel clockwise around HERA. For injecting the proton beam, the current lepton injection line has to be used, whose strong bends require superconducting magnets for a 40 GeV proton beam. The slope of the line is a problem for the cryogenic supply of these magnets, which however can presumably be solved. The electron beam lines into and out of HERA require civil engineering work including two long slits of the HERA tunnel. A beam dump similar to the TESLA beam dump has to be foreseen, which would fit on the DESY site. Two types of superconducting quadrupoles for the new interaction region have to be provided with five magnets each and cryogenic supply. Beam pipes, support, power supplies, beam diagnostics and controls are required. In addition, faster kicker magnets are needed to provide the desired bunch spacing. In order to achieve the envisaged beam brightness, electron cooling in PETRA will most likely be required.

2.3.2 A detector for THERA

The electron–proton scattering kinematics governs the design of the THERA detector. Roughly speaking, there are three detector regions which have to match different requirements: the forward¹ part, where the final-state energies are limited by the proton beam energy, E_p ; the central part, where particles with transverse momenta up to $\sqrt{s}/2$ can be produced; the backward part, where the final-state energies are limited by the electron beam energy, E_e . The forward part thus has to match similar criteria as at HERA, whereas the backward part has to cope with much higher energies. The central part bridges these two extremes.

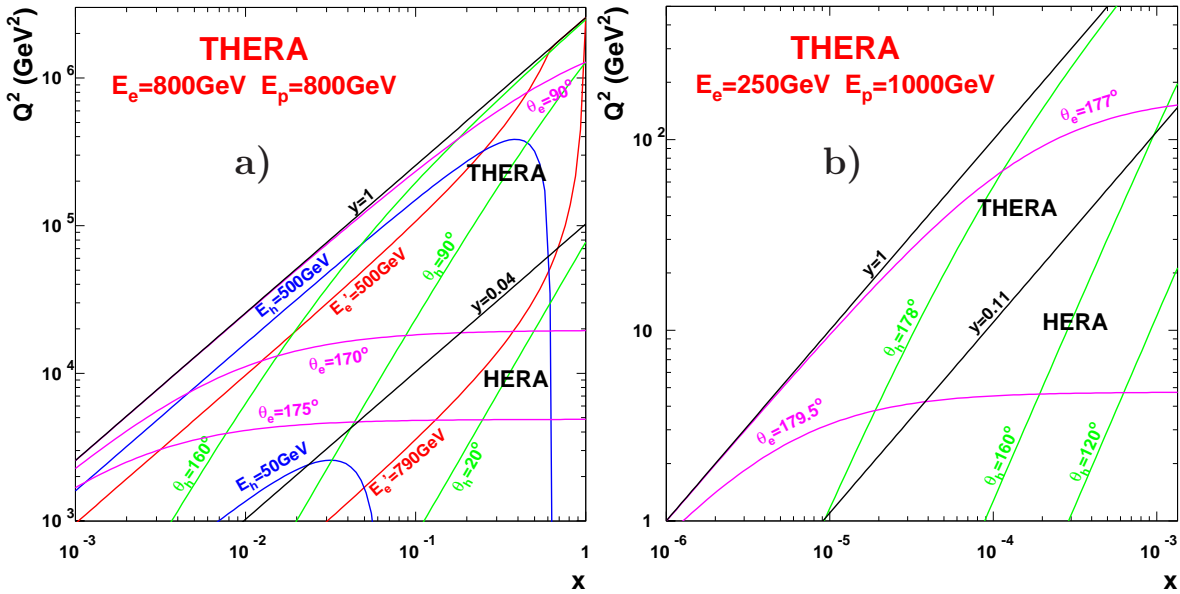


Figure 2.3.3: Kinematic range covered by THERA, (a) at high x and Q^2 for $E_e = E_p = 800$ GeV ($\sqrt{s} = 1.6$ TeV), and (b) at low x and Q^2 for beam energies of $E_e = 250$ GeV and $E_p = 1$ TeV ($\sqrt{s} = 1$ TeV). The lines for $y = 0.04$ in (a) and $y = 0.11$ in (b) indicate the kinematic limit of HERA. Lines of constant E'_e (red), E_h (blue), θ_e (magenta) and θ_h (green) are indicated. In (b), E_h and E'_e are given approximately by yE_e and $(1 - y)E_e$, respectively. Note that for low x both the electron and the jet are scattered into the backward region, illustrating the strong boost of the electron–quark system in this kinematic region.

The coverage of the (x, Q^2) plane for DIS at large $Q^2 > 10^3$ GeV^2 is shown in Fig. 2.3.3a for the maximum THERA centre-of-mass energy envisaged (see Sect. 2.3.1.3). The final-state electrons have energies, E'_e , of hundreds of GeV and are scattered at backward and central angles, θ_e . The current jets emerge at a broad spectrum of angles, θ_h , hitting the forward, central and backward detector parts with energies, E_h , which

¹A coordinate system is defined according to the HERA conventions, with the origin in the interaction point (IP) and the z axis pointing in the proton beam direction, referred to as forward.

are approaching E_p at highest x and E_e at highest y .

The kinematic properties of low- x reactions are illustrated in Fig. 2.3.3a. The most striking features of such events are the very small deflection of the electrons and their large energies of $E'_e \approx (1 - y) E_e$, exceeding the corresponding values in the HERA backward region by one order of magnitude. As can be seen from this figure, Q^2 values of a few GeV^2 can be accessed only with electron scattering angles close to 180° (θ_e as large as 179.5° is e.g. required to reach $Q^2 = 4E_e E'_e \cos^2(\theta_e/2) \simeq 2 \text{ GeV}^2$ at $y = 0.5$ for $E_e = 250 \text{ GeV}$). Simultaneously, the current jets are also scattered into the backward direction, with energies $E_h \approx y E_e$.

The backward region of the THERA detector is therefore of central importance for low- x investigations and has to be newly designed, since the corresponding HERA detector components cannot provide the required energy containment and angular coverage. The extension in z of the very backward detector part (i.e. at largest θ) depends critically on the beam-pipe radius which can be as small as 2 cm because of the absence of synchrotron radiation from bends of the incoming electron beam near the interaction region. The beam-pipe will have exit windows with 2π azimuthal coverage to minimise shower development and multiple scattering.

Based on the experience of experimentation at HERA and a simulations of THERA DIS events and kinematics, a design study of the THERA detector has been performed [128].

The *operation* of the THERA experiment is envisaged in two phases aiming at low- x physics and high- Q^2 physics, respectively. Accordingly, the THERA detector is foreseen to be modular in its structure. Detectors near the beam-pipe and the extended backward part should be removable for high-luminosity operation, which will require the installation of focusing magnets as close as possible to the interaction point. Characteristic parameters of both phases are summarised in Table 2.3.2.

Magnetic field: A homogenous solenoidal magnetic field, extending over almost 10 m in z could be provided by the H1 and ZEUS coils which can be operated at 1–1.5 T. The mechanical stability of such an arrangement and the design of the support structure have not yet been investigated.

The *calorimeter* has to be almost 4π -hermetic in order to be able to reconstruct the longitudinal energy-momentum balance, $E - p_z$, which is essential for DIS event identification and reconstruction. The required energy resolutions are roughly $15\%/\sqrt{E(\text{GeV})}$ for electromagnetic and $40\%/\sqrt{E(\text{GeV})}$ for hadronic energy measurements, with additional constant terms of about 1%. These resolution requirements can be met by presently available calorimeter technology as e.g. employed by the HERA collaborations. In particular, one might consider to equip the forward and central calorimeter regions with the H1 LAr calorimeter, and to use the instrumented iron structure of the H1 detector. The reconstruction of forward-jet final states requires position reconstruction and energy flow measurements down to polar scattering angles of about 1° . Thus, a new calorimeter with enhanced granularity will have to be constructed for the very forward region, i.e. $\theta < 5^\circ$ ('forward plug').

In the backward direction, the calorimeter must be able to provide energy and position measurement for the scattered electrons with energies close to the electron

	low- x configuration	high- Q^2 configuration	
electron beam energy, E_e	250 GeV	500 GeV	800 GeV
proton beam energy, E_p	1 TeV	500 GeV	800 GeV
c.m.s. energy, \sqrt{s}	1.0 TeV	1.0 TeV	1.6 TeV
luminosity [$10^{30} \text{ cm}^{-2} \text{ s}^{-1}$]	4	25	16
distance focusing magnet – IP	5 m	2 m	2 m
backward electron acceptance	$\theta_e < 179.7^\circ$	$\theta_e < 175^\circ$	$\theta_e < 175^\circ$
forward calorimetric acceptance	$\theta_h > 1^\circ$	$\theta_h > 5^\circ$	$\theta_h > 5^\circ$

Table 2.3.2: *Operation parameters of THERA. The first phase with standard beam energies and luminosity will focus on low- x physics. A subsequent, higher-luminosity phase is envisaged which will concentrate on high- Q^2 physics. In this high- Q^2 phase, both arms of TESLA are used for acceleration of electrons to achieve maximum energy. Note that the maximum Q^2 is given by $s = 4E_e E_p$. Choosing $E_e = E_p$ is favourable for maximising the luminosity (see Sect. 2.3.1). An electron energy of 800 GeV energy can be obtained after the TESLA power upgrade, while 500 GeV are available already in the first stage of TESLA.*

beam energy, at angles up to 179.7° . Furthermore, hadronic energy measurement and reliable electron/hadron separation are required in the same energy and angular range to fully cover low- x reactions, in which both the electron and the hadronic state are scattered into a narrow cone in the e beam direction (see Fig. 2.3.3a). These requirements necessitate a high-resolution, fine-grain calorimeter with sufficient depth to contain electron and hadronic energy deposits of several 100 GeV. Particularly stringent constraints are present for the calorimeter part close to the beam-pipe, which is envisaged to be constructed as a separate module (‘backward plug’).

Tracking: Tracks will be reconstructed in silicon strip detector telescopes near the beam-pipe and an arrangement of outer tracking detectors. These may consist of a cylindrical central chamber and, for example, of planes of straw-tube or drift-chamber detectors in the forward and the extended backward regions, with hit resolutions of about $150 \mu\text{m}$.

Electron identification near $\theta_e = 179.5^\circ$ will be achieved using a combination of the calorimetric information and the data from a track detector which has sufficient resolution to determine the charge of particles with momenta up to E_e and will be positioned in front of the backward plug calorimeter. Low- x charm and beauty physics requires the reconstruction of tracks with momenta of a few GeV at scattering angles up to 179° . It has been verified with simulation studies [129] that the required angular acceptance and momentum resolution can be provided using 6-inch silicon strip detectors with hit resolutions of about $20 \mu\text{m}$. These detectors will be arranged in 5-plane modules, which are mounted around the beam pipe and cover the full range of polar and azimuthal angles. The backward tracker response was simulated in some detail, and resolutions of about 15 MeV for the $D^0 \rightarrow K\pi$ mass reconstruction and of about

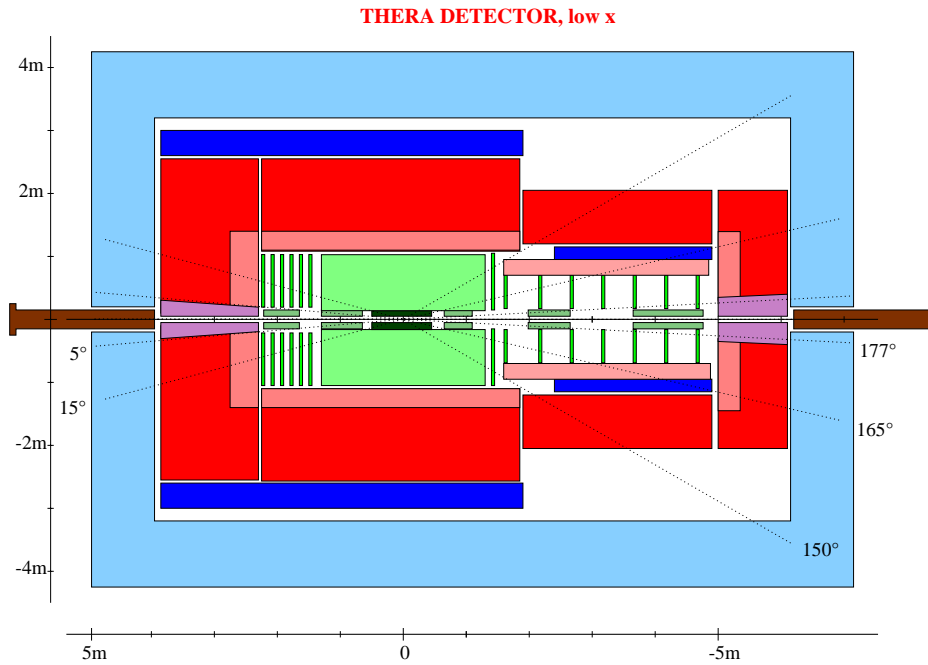


Figure 2.3.4: Basic design of the THERA detector in the low- x configuration. The electrons enter from left, the protons from right. Around the beam-pipe, modules of 6-inch silicon strip detectors are positioned (dark-green). Tracking is complemented by planar and circular track chambers (light-green). Electromagnetic (pink) and hadronic (red) calorimetry ensures hermetic, accurate reconstruction of the final-state energy depositions. A homogenous, solenoidal field over 9 m length is provided by the large-diameter H1 coil and the smaller ZEUS coil (blue). The return yoke iron structure (light-blue) is instrumented for shower tail catching and muon detection. The focusing magnets (brown) are placed near the plug calorimeters (magenta).

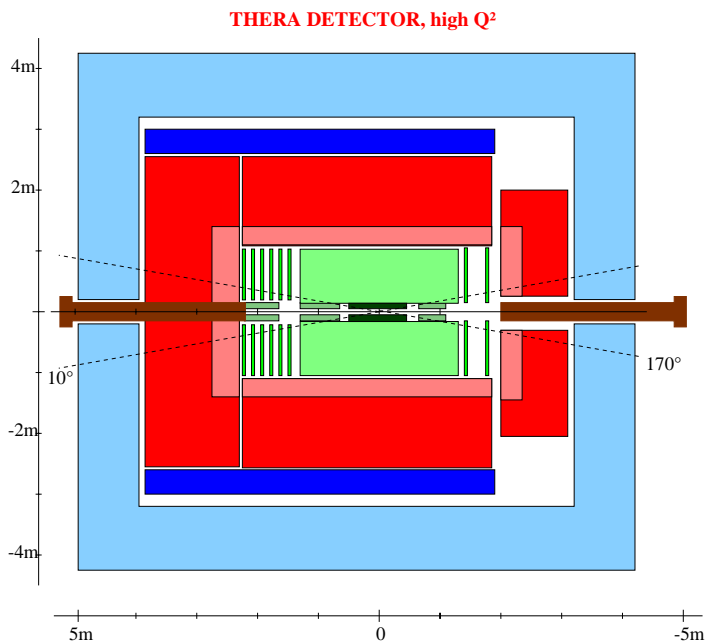


Figure 2.3.5: Basic design of the THERA detector in the high- Q^2 configuration. This detector is similar in its basic layout to Figure 2.3.4, with the backward detector part and the ZEUS coil removed and the iron structure shortened correspondingly. Removal of the large/small angle trackers and the forward/backward plug calorimeters permits the focusing magnets to be placed much nearer to the interaction point than in the low- x phase.

0.5 MeV for the $D^* - D^0$ mass difference were obtained. The tiny transverse size of the interaction spot (roughly $20 \mu\text{m}$ diameter) is of great advantage for momentum measurement and in particular for tagging heavy-flavour decays by reconstructing impact parameters and secondary vertices.

Muon chambers outside the calorimeter are required in the full acceptance range of the detector, preferentially also backwards at small angles for heavy-flavour physics.

Tagging of electrons and photons in the electron beam direction is necessary for luminosity measurements, control of radiative corrections and for identifying photoproduction events, in particular in the context of exclusive measurements. The detection of protons and neutrons in the proton beam direction is needed, or at least supportive, for investigations of diffractive reaction channels. It appears feasible to include these different tagging detectors in the interaction region; however, no effort has been made to design them at this stage.

It is concluded that low- x physics at THERA, while representing the challenge of measuring the scattered electron so close to the beam-pipe, can be studied with a detector design following the above considerations, as shown in Fig. 2.3.4. The design is sufficiently modular to allow for a detector reconfiguration suitable for the THERA high- Q^2 phase (see Fig. 2.3.5).

The construction of the THERA detector can be based on the large experience with the collider detectors at HERA and is not expected to exceed their cost.

2.4 Further Options

2.4.1 Electron–nucleus scattering

Deep inelastic scattering of nuclei is a classical way of studying the space-time picture of strong interactions, (see [130] for a recent review). So far DIS data on nuclei are only available for $x \gtrsim 0.003$, see e.g. Fig. 2.4.1 (reproduced from [130]).

The prime motive for using nuclear beams at THERA is to advance much deeper into the region of high parton densities than it would be possible in the electron–proton mode. Based on the dependence of various observables on the nucleon number, A , measurements at THERA would provide decisive tests and a number of valuable cross checks of various ideas about the QCD state in the high-density limit (for a summary see [132, 133, 134]). Effects to be investigated would include the saturation of gluon and quark densities [135, 136] (discussed in Sect. 2.2.1) or a large reduction of the nuclear gluon density [137], g_A , as compared to the incoherent sum $g_A = Ag_N$ of the individual nucleon densities, g_N (*leading-twist shadowing*). Indeed, the small- x gluon densities per unit area at central impact parameters in nuclei (i.e. at small transverse distances from the centre of the nucleus) are enhanced as compared to the nucleon case by a factor $(g_A/\pi R_A^2)/(g_N/\pi r_N^2) \approx A^{1/3}g_A/Ag_N$, which is as large as 6 for $A = 200$ if $g_A \approx Ag_N$ is assumed. The unitarity constraint (see eq. 2.2.1 for a nucleon target), requiring that the total inelastic cross section of the interaction of a small dipole with the nucleus cannot exceed πR_A^2 (*the black body limit*), implies the presence of large screening effects and nonlinear dynamics in eA scattering at THERA. In particular,

it implies that in the interaction of small colour-octet dipoles with nuclei at central impact parameters the gluon density per nucleon (i.e. the ratio of the gluon density averaged over a small range of central impact parameters and the number of nucleons, A_{eff} , in the corresponding nuclear volume) cannot exceed [15, 138]

$$\left. \frac{xg_A(x, Q^2)}{A_{\text{eff}}} \right|_{\text{central}} \leq 3A^{-1/3}Q^2 (\text{GeV}^2) \stackrel{A=200}{\approx} 0.5Q^2 (\text{GeV}^2). \quad (2.4.1)$$

Note that this ratio would be equal to xg_N if the nucleon fields would add incoherently. The upper bound in eq. 2.4.1 can be compared e.g. with $xg_N(x=10^{-3}, Q^2=4 \text{ GeV}^2) \geq 5$ in the current parton distribution fits. One concludes that strong modifications of the gluon field in heavy nuclei (as compared to the incoherent sum of the nucleon fields) appear to be unavoidable in a wide (x, Q^2) range to be covered by THERA.

A significant part of these modifications required to satisfy the unitarity constraints is the leading-twist reduction of the gluon and quark parton densities (shadowing) related to the leading-twist diffraction observed at HERA [137]. The rest should be due to nonlinear effects. The kinematic range where nonlinear effects are expected to be large is illustrated in Fig. 2.4.2 for scattering of small-size colour-triplet and colour-octet dipoles off nuclei, taking into account the leading-twist shadowing. For central impact parameters the limits are much stronger – the limit for the inclusive scattering off a nucleus with a given A corresponds to the limit at central impact parameters for a nucleus with $A' \approx A/3.5$, so that the inclusive curves for $A = 40$ are the same as the curves for central scattering off carbon (the subtraction of the contribution from scattering at peripheral impact parameters can be performed by studying cross sections for a series of nuclei, e.g. for $A, A/4, \dots$ [132]). The interaction strength in this domain may reach values close to the black body limit and can be studied at THERA in a wide x range as a function of the parton density (i.e. the number of nucleons at the impact parameter

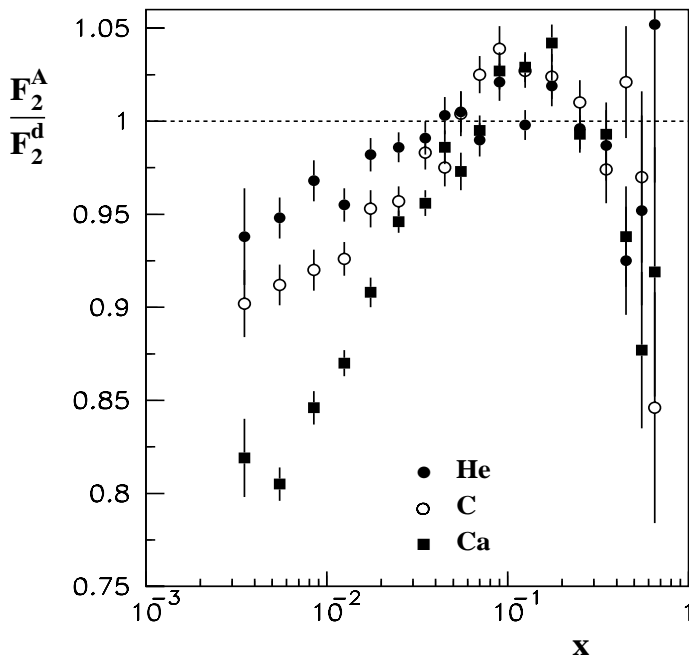


Figure 2.4.1: NMC data [131] for the structure function ratio F_2^A/F_2^d per nucleon for ${}^4\text{He}$, ${}^{12}\text{C}$ and ${}^{40}\text{Ca}$ for $Q^2 \geq 0.7 \text{ GeV}^2$. THERA would extend these measurements by three orders of magnitude to $x \simeq 10^{-5}$.

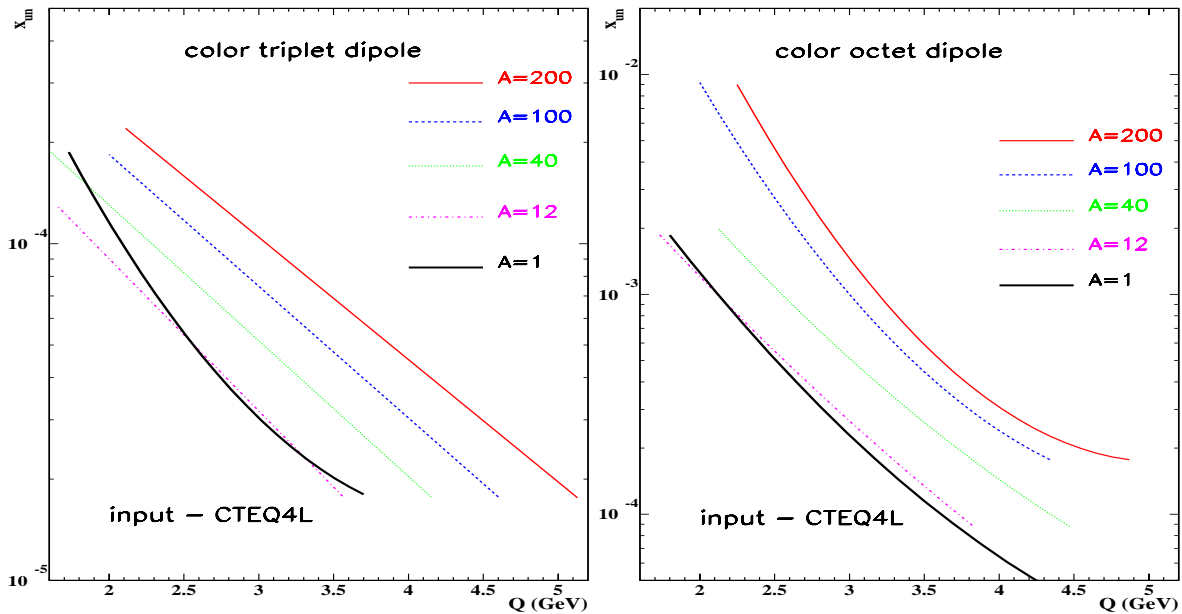


Figure 2.4.2: Unitarity boundaries in the $(x, \sqrt{Q^2})$ -plane for (a) the inelastic $q\bar{q}$ (colour triplet)–nucleus and (b) the $q\bar{q}g$ (colour octet)–nucleus cross sections for nuclei with $A = 12, 40, 100$ and 200 . The unitarity boundaries for the inelastic $q\bar{q}$ – and $q\bar{q}g$ –nucleon cross sections are indicated as black solid lines.

of the probe), which is impossible for the case of ep scattering. In a number of models [139, 140] the shadowing in the leading twist is assumed to be small, resulting in a much larger range of (x, Q^2) where nonlinear effects should dominate (see plots in [133]).

One can see from the figure that the measurement of central scattering for $A = 40$ (which requires data from a set of isoscalar nuclei with $A \leq 40$ for the subtraction of the peripheral part) would access limits corresponding to inclusive scattering off nuclei with $A \sim 200$ and hence extend the Q^2 unitarity boundary by a at least a factor of two at x values of $\sim 10^{-4}$. This gain would allow the observation of nonlinear effects in a Q^2 range which is indisputably perturbative, at least for ep scattering.

It will be possible to reveal unambiguously the new high-density regime of DIS at small- x eA collisions via studies of a number of inclusive observables and the A -dependence of the properties of the final states. Several gold-plated observables are listed in the following. For illustration, expectations based on the black body limit scenario [141, 15, 138, 142] are considered (which is rather closely related to the saturation scenario [135, 136, 139, 140, 143]), though nonlinear effects could tame the increase of the interaction strength before this limit is reached.

Inclusive observables

In the black body limit, the relation $F_2^A \propto 2\pi R_A^2 Q^2 \ln(1/x)$ holds for $Q^2 \leq Q_{\text{bb1}}^2(x)$, where $Q_{\text{bb1}}^2(x)$ denotes the maximal value of Q^2 for which the total inelastic cross section of the interaction of a small colour dipole of transverse size $\propto 1/Q$ with a heavy nucleus is equal to the black body limit, πR_A^2 . The scale $Q_{\text{bb1}}^2(x)$ increases with

A. The measurement of the scaling violation of $F_2^A(x, Q^2)$ provides direct access to the dynamics of the interaction of the small dipoles with nuclei and hence yields detailed information about the relevance of the black body limit for γ^*A scattering. Direct tests of the onset of the black body regime in the gluon channel may be possible via measurements of $\sigma_L(eA)$ and the study of dijet production in γ^*A scattering.

Another signal for approaching the black body limit would be an A dependence of the transverse momentum (p_t) spectrum of the partons: the average p_t rises with $Q_{\text{bbi}}^2(x)$, $\langle p_t \rangle \sim Q_{\text{bbi}}$ [139, 140], resulting in an A dependence of the leading hadron spectrum in the current fragmentation region at values of Feynman x close to one: the multiplicity will decrease with A [142] and the average p_t^2 at $x_F \sim 1$ should be proportional to Q_{bbi}^2 . Such a gross violation of the QCD factorisation theorem for leading hadron production in DIS will provide one of the model independent signals for the onset of the black body regime.

Diffractive observables

For experimental investigations, three classes of diffractive electron–nucleus interactions have to be considered: *diffractive dissociation* with meson production in the nucleus fragmentation region, *nuclear break-up* producing nuclear fragments (mostly neutrons and protons) in the forward direction, and *coherent scattering*, where the nucleus stays intact. The separation of these three classes from non-diffractive reactions is very similar to the selection of diffractive events in the ep case. The contribution of diffractive dissociation to the overall diffractive cross section is significantly smaller than in the ep case. The experimental signatures for this reaction class are similar to ep scattering since the energy flow in the forward direction is expected to have almost the same topology. Calorimetric coverage down to $\theta \lesssim 1^\circ$ in the forward region (see Sect. 2.3.2) will allow the detection of most dissociative reactions. Nuclear break-up is expected to constitute about 10% of the coherent diffraction for a wide range of model parameters. Forward detectors similar to the forward neutron calorimeters (FNC) of the HERA collider experiments will be needed to distinguish these two processes [133].

Inclusive DIS diffraction provides a direct test of how close the interaction is to the black body limit, where the probability of coherent diffraction is close to 50% of the total cross section [141, 144, 145, 146]. The same is true for partial cross sections such as for charm production or dijet production in γA scattering. Moreover, since the interaction is stronger in the gluon channel, the diffractive cross section should be close to 50% of the corresponding total cross section in a wider (x, Q^2) range [137]. The differential cross section of diffractive production of states with mass $M_X^2 \leq Q_{\text{bbi}}^2$ is also predicted in a model-independent way, see [142]. Another signature of the black body limit is that for $M_X^2 \leq Q_{\text{bbi}}^2$ the production of high- p_t jets is strongly enhanced: $\langle (p_t^{\text{jet}})^2 \rangle = 3M_X^2/20$.

Exclusive DIS diffraction, the production of vector mesons in the process $\gamma^* + A \rightarrow V + A$, provides a clean experimental signature if the V decay products are in the detector acceptance. This will be the case for light vector mesons if either Q^2 or $|t|$ (the square of the momentum transfer at the nucleon vertex) are sufficiently high, and for J/ψ and Υ mesons over the full kinematic range. The separation of coherent and

incoherent events will require the same experimental techniques as for inclusive studies and can in addition make use of the very steep diffractive peak expected for coherent processes. Exclusive DIS diffraction yields a direct answer to the fundamental question: Are heavy nuclei transparent for high-energy small objects like J/ψ or Υ mesons? In the region of $x \sim 0.02$, evidence for colour transparency was obtained [147] by the observation that the coherent J/ψ production amplitude is proportional to $AF_A(t)$, where $F_A(t)$ is the nuclear form factor. This colour transparency regime corresponds to the propagation of a small dipole through a thick target with very small absorption. At small $x \lesssim 0.01$, a qualitatively new phenomenon – colour opacity – is expected: a strong absorption of the small dipoles propagating through the nuclei. In the black body limit the increase of the cross section with A will be reduced to $A^{2/3}$ as compared to $A^{4/3}$ in the colour transparency limit. QCD also predicts the absolute cross section for the vector meson production in the black body limit. The THERA kinematic range would allow for studying the interplay of colour transparency and colour opacity in a wide (x, Q^2) range and distinguishing between various models of shadowing for the interaction of small dipoles. In particular, the eikonal model [135] leads to a much smaller colour opacity effect than the leading-twist models of gluon shadowing based on the dominance of gluons in the diffractive structure functions [137].

Measurements with deuteron beams (which probably can be polarised without installation of Siberian snakes using a novel technique suggested by A. Skrinky [148]) would allow the investigation of low- x physics in reaction channels which cannot be induced by Pomeron exchange (‘non-vacuum channels’) by combining inclusive measurements and techniques of neutron tagging [132]. Measurements of non-vacuum exchange would be given by the structure function differences $F_2^p - F_2^n$ or $g_1^p - g_1^n$. Electron–deuteron scattering would also allow an interesting test of the Gottfried sum rule, $\int_0^1 (F_2^p - F_2^n) dx/x = 1/3 + 2/3 \int_0^1 (\bar{u} - \bar{d}) dx$, in a new kinematic range.

To summarise, the use of nuclear beams would increase in a major way the THERA potential for the study of nonlinear QCD phenomena. Several measurements, especially in the diffractive channels, will determine in an unambiguous way whether the black body regime is reached and explore in detail a new QCD state of matter produced at small x . Most of these measurements will require rather modest luminosities of 1–10 pb⁻¹ per nucleus [132]. It would be possible to explore the nonlinear regime in a Q^2 range extended by at least a factor of 2 with respect to ep scattering by performing measurements on a series of nuclei with $A \leq 40$, e.g. $A = 2, 4, 16, 40$.

2.4.2 Real photon–proton scattering

At a linear collider, laser light can be Compton-backscattered off the high-energy electron beam, offering the unique opportunity [149, 150, 151] to run THERA as a real-photon nucleon collider. As has been studied in detail in [149, 152], the luminosity for a γp machine depends on the distance z between the conversion region and the interaction point and also on the laser and electron beam helicities. An increase of z reduces the luminosity but also reduces the energy spread of the photon beam. A careful optimisation of the operation parameters such as the photon and electron beam

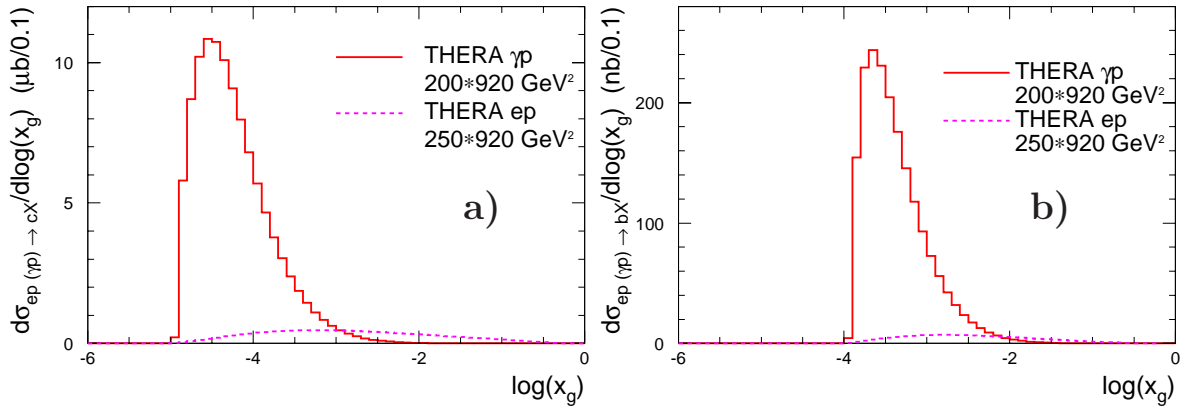


Figure 2.4.3: *Dependence of the differential cross section of (a) charm and (b) beauty production on x_g in γp and ep scattering at THERA.*

helicities and the collision angle between the photon and proton beams is required. The basic scheme for converting the TESLA electron beam into a high-energy photon beam is described in appendix I, *The Photon Collider at TESLA*, of this Technical Design Report. Given the much larger beam size of the protons, the interaction of the laser with the electron beam can happen several meters away from the photon–proton interaction point and thus outside of the detector. Photon–proton luminosities of order 30% of the electron–proton luminosities can be achieved.

Compton backscattering yields a beam of photons with about 80% of the electron beam energy on average, with a full width of approximately 15%. The resulting photon–proton interactions allow studies of many of the physics issues discussed above, e.g. heavy flavour production or photon structure, with much enhanced sensitivity. This is illustrated in Fig. 2.4.3 which compares the differential cross sections of charm and beauty production in γp scattering and in ep scattering as functions of the gluon fractional momentum in the proton, x_g . The cross section gain at low x_g is striking. A similar observation holds for the differential cross section with respect to the photon energy fraction, x_γ^{obs} (see eq. 2.2.2), carried by the produced dijet system in charm and beauty events as is shown in Fig. 2.4.4.

The main physics goals of a THERA-based γp collider [150, 153] are:

- a measurement of the total γp cross section at the TeV scale;
- high-statistics studies of heavy-quark production (roughly 10^8 , 10^6 , 10^2 events per year for $c\bar{c}$, $b\bar{b}$, $t\bar{t}$ production);
- investigation of the partonic structure of real photons;
- single production of W bosons and top quarks;
- search for excited quarks (u^* and d^*) with masses up to 1 TeV;

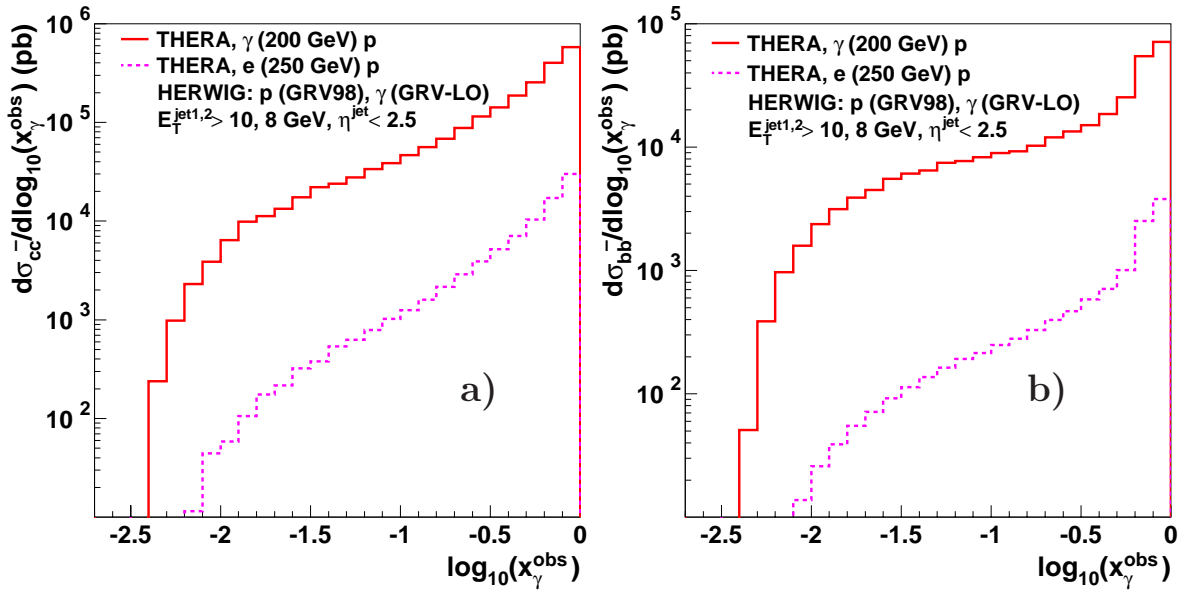


Figure 2.4.4: Differential cross sections with respect to x_γ^{obs} for (a) charm and (b) beauty production for the γp and ep options of THERA.

- search for fourth-family quarks, Q , produced via anomalous γcQ , γuQ ($Q=t_4, u_4$), γsd_4 or γdd_4 couplings.

The photon polarisation will provide important additional information in all these measurements. In addition, a γp collider with a longitudinally polarised proton beam will be a powerful tool for investigating the spin structure of the proton.

Of particular interest is the photon–nucleus (γA) collider option of THERA (see Sect. 2.4.1 and [150, 153]) which, besides all the investigations mentioned above for the γp mode, allows for example detailed studies of quark–gluon plasma formation at very high temperature but relatively low nuclear density, or of multi-quark clusters in nuclei.

2.4.3 Polarised protons

The detailed study of the nucleon spin structure was initiated by the EMC muon experiment [154], which found that the quark contribution to the nucleon spin is surprisingly small and that hence the nucleon spin cannot be understood within the naive quark parton model. Since then a wealth of data from fixed-target experiments on spin structure has been accumulated and spin theory became much more sophisticated. The puzzling question of the nucleon spin composition is still unresolved (for the present status see [155]). The importance of extending the kinematic range of spin physics by an ep collider has been investigated and emphasised in a series of workshops on polarised ep physics at HERA [156, 157, 158].

In polarised DIS, the spin-dependent terms only make a small contribution to the total cross section. They can be extracted from measurements of cross section differ-

ences for interactions with opposite relative orientations of lepton and nucleon helicities, in which the spin-independent contributions cancel. A classic quantity is the spin structure function g_1 , which measures the weighted sum of polarised quark distribution functions Δq and is approximately related to the cross section asymmetry, $A_{\parallel} = (\sigma_{\uparrow\downarrow} - \sigma_{\uparrow\uparrow})/(\sigma_{\uparrow\downarrow} + \sigma_{\uparrow\uparrow})$, by:

$$g_1 \simeq \frac{F_2}{2x} \cdot \frac{A_{\parallel}}{\lambda_e \lambda_p} \cdot \frac{y^2 + 2(1-y)}{y(2-y)}. \quad (2.4.2)$$

Eq. 2.4.2 illustrates the need for high polarisations, λ_e and λ_p , and a preference for measurements at large values of y . The electron polarisation at TESLA will be high, $\lambda_e \simeq 0.8$. Polarisation $\lambda_p \simeq 0.6$ may be achieved in the HERA proton ring. From eq. 2.4.2 it can be deduced that integrated luminosities exceeding 100 pb^{-1} per polarisation state are necessary for studying the proton spin structure in a quantitative manner. Therefore, dedicated high-luminosity e -nucleus ring facilities are under discussion [159, 160] with typical energies of $\sqrt{s} \simeq 50 \text{ GeV}$. High-statistics fixed target experiments are being carried out at CERN, DESY and SLAC and proposed to be pursued at TESLA [161].

The outstanding advantage of the THERA facility is the large extension of the kinematic range. Due to the very large centre-of-mass energy, $\sqrt{s} \simeq 1 \text{ TeV}$, the Q^2 evolution can be tested, the x range expanded to much lower x and exploratory measurements be performed. In spin physics these comprise for example inclusive polarised deep inelastic scattering and spin asymmetries in jet and dijet production. For the first time, spin effects will be measurable in polarised DIS through electroweak asymmetries in CC and NC scattering.

The study of spin-dependent effects would be extended to low x and allow for a test of the Q^2 evolution of g_1 towards highest $Q^2 \simeq 10^4 \text{ GeV}^2$. Important information on the spin structure can be obtained from data on the asymmetry in the production of two jets (dijets) or of two hadrons. The polarised gluon distribution ΔG can be accessed with dijet events, as was demonstrated in [162] for HERA operation with polarised protons. For THERA, the asymmetries, calculated with MEPJET and GSA, are about 6% at $x = 0.05$ and smaller than 0.5% for $x < 0.001$. A further source of information about gluon polarisation at low x is charm production which occurs with high cross section at THERA (see Sect. 2.2.2.4).

Inclusive measurements in DIS are sensitive to the sum of all quark flavours. To extract flavour-dependent spin information, one presently uses semi-inclusive scattering, an area being actively pursued in fixed-target experiments [155]. In the very high Q^2 range of THERA, however, CC interactions are a new and promising way to access flavour-specific spin information, independently of fragmentation effects which hinder semi-inclusive analyses. Thus CC scattering has been considered here as an example to illustrate the THERA potential for investigating the polarised proton structure at high Q^2 .

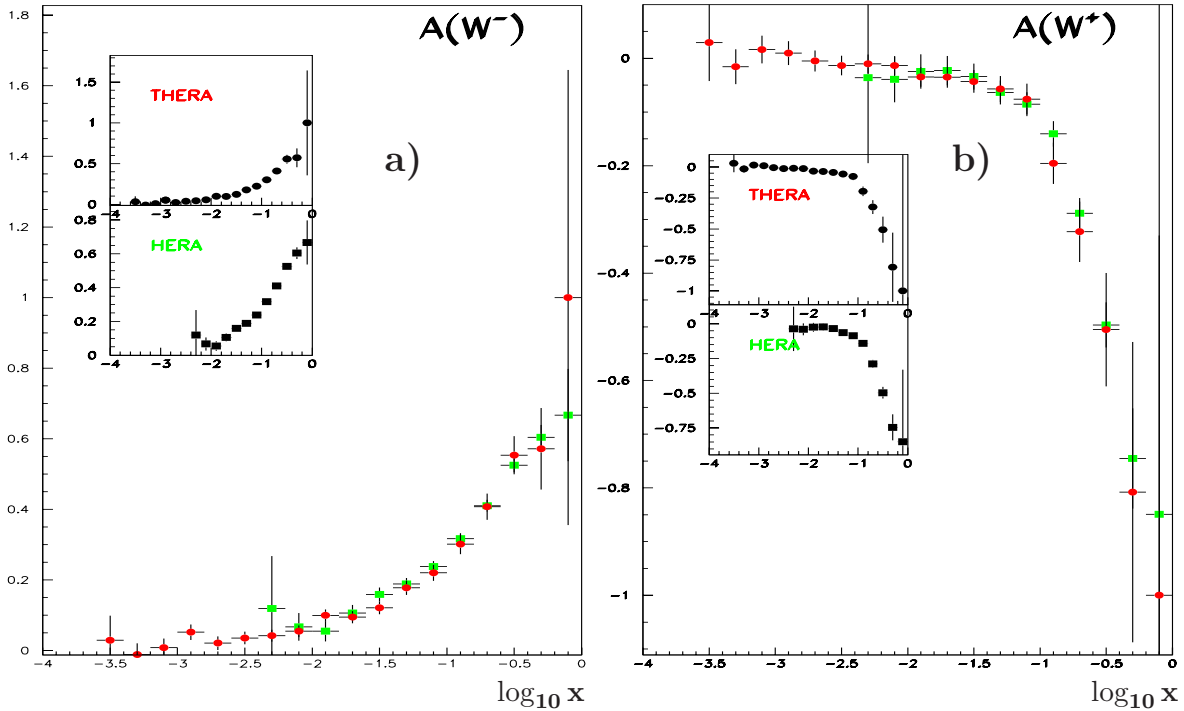


Figure 2.4.5: Simulated measurements of (a) the asymmetry A^{W^-} and (b) of A^{W^+} in CC scattering as functions of x , as expected at the HERA and THERA facilities with polarised proton beams. Note that this representation hides the large differences in the Q^2 range of the HERA and THERA measurements, respectively.

In the CC e^+p and e^-p scattering cross sections, asymmetries can be defined as

$$A^{W^\mp} = \frac{d\sigma_{\uparrow\downarrow}^{W^\mp} - d\sigma_{\uparrow\uparrow}^{W^\mp}}{d\sigma_{\uparrow\downarrow}^{W^\mp} + d\sigma_{\uparrow\uparrow}^{W^\mp}} = \frac{\pm 2bg_1^{W^\mp} + ag_5^{W^\mp}}{aF_1^{W^\mp} \pm bF_3^{W^\mp}} \approx \frac{g_5^{W^\mp}}{F_1^{W^\mp}} \quad (2.4.3)$$

with $a = 2(y^2 - 2y + 2)$ and $b = y(2 - y)$, $g_5^{W^-} = \Delta u + \Delta c - \Delta \bar{d} - \Delta \bar{s}$ and $g_5^{W^+} = \Delta d + \Delta s - \Delta \bar{u} - \Delta \bar{c}$. A simulation study has been performed for the measurement of this asymmetry, requiring the total missing transverse momentum to exceed 12 GeV. From A^{W^\mp} measurements, the new structure functions g_5 [163] can be extracted following the method used in [164]. The results for A^{W^\pm} are shown in Fig. 2.4.5, for a luminosity of 100 pb^{-1} for each polarisation combination, assuming full polarisation. The error bars indicate the statistical precision of the measurement. The results are compared with simulated asymmetry measurements for polarised HERA operation, which will access lower Q^2 at a given x . THERA will allow such asymmetry measurements to be performed in the CC channel for x values down to below 10^{-3} , thus extending the range accessible to HERA by one order of magnitude in x and by even more compared to the projected electron–nucleus colliders. It is expected that $g_5^{W^+}$ can be measured at THERA in the region $x \gtrsim 10^{-2}$, while for electron scattering the asymmetries are large enough to allow for a measurement of $g_5^{W^-}$ down to $x \simeq 10^{-3}$. Both g_5 structure functions are related by a Bjorken sum rule which is valid for very large Q^2 [102].

If any deviation from the Standard Model is found, such as R -parity violating SUSY [165], leptoquarks [108] or instantons [166], it will be particularly interesting to study the helicity-specific properties of the corresponding objects in $\vec{e}\vec{p}$ scattering at THERA.

2.5 Summary

A new electron–proton collider, THERA, based on the linear accelerator TESLA and the proton ring HERA, can be built at DESY. With electron energies between 250 and 800 GeV and proton energies between 500 GeV and 1 TeV, THERA opens a new, unexplored energy range in deep inelastic lepton–nucleon scattering. Design considerations of the THERA facility lead to preliminary estimates of the achievable luminosity between 4 and $25 \times 10^{30} \text{ cm}^{-2} \text{ s}^{-1}$ (corresponding to annual luminosities between about 40 pb^{-1} and 250 pb^{-1}), depending on the beam energies. Relying on the experience and some components of the H1 and ZEUS experiments at HERA, a detector design is presented which promises to allow successful experimentation at THERA at the required level of accuracy and in the full kinematic range. Operation of THERA can be envisaged to proceed in two phases, one dedicated to the physics at very low Bjorken x and the other to extremely high momentum transfers Q^2 .

A study is presented of those physics subjects which, based on present results of HERA and theoretical extrapolations, are considered to most likely govern the future physics of deep inelastic scattering and photoproduction in the TeV energy range. Important aims of THERA are the understanding of strong interactions in the presence of high parton densities, a coherent description of the transition from small to large distances and the exploration of new particles and phenomena. The detection of the complete final state and high accuracy in the measurements allow a rich experimental and theoretical programme of research to be performed in the unexplored region. This will test QCD as the theory of strong interactions in much more depth than could be reached so far.

The results of the THERA studies [3] can be summarised as follows:

- The extension of the kinematic range down to $x \simeq 10^{-6}$ allows access to the high-parton-density domain and its detailed exploration in the deep-inelastic regime. Studies of the saturation phase of matter are expected to yield insight into the question of confinement. These studies require the measurements of inclusive DIS, of light and heavy vector meson production and of diffraction. These results will allow the transition from the perturbative to the non-perturbative QCD regime to be understood much better than presently.
- The measurement of proton structure functions at THERA will be essential for determining quark and gluon distributions in the proton in an unexplored kinematic region. This will be crucial for a consistent theoretical description of low- x phenomena, which so far is elusive, and also for understanding the interactions at hadron colliders and of highest-energy cosmic particles.

- The nature of diffraction will be studied in a much extended phase space region of the fractional proton longitudinal momentum loss, x_{IP} , and the ratio $\beta = x/x_{IP}$. The rise of the diffractive structure function $F_2^{D(3)}$ will be explored accurately, which, together with the inclusive F_2 , constitutes one of the key measurements to investigate the properties of the saturation region.
- The study of forward-going jets at THERA is expected to reveal the mechanism for the evolution of QCD radiation at low x . The increased range for the Q^2 evolution of parton densities will allow a precision measurement of α_s to the level of 0.5%. This is accompanied by major theoretical efforts to calculate QCD to next-to-next-to-leading order.
- The total cross sections for charm and beauty production are expected to increase by factors of three and five, respectively, as compared to HERA. This will allow the structure functions F_2^c and F_2^b to be measured precisely, heavy-quark QCD predictions to be tested and the gluon distribution in the proton to be determined from the photon–gluon fusion process at much lower x .
- THERA will operate beyond the electroweak unification scale and is thus a truly ‘electroweak interaction machine’. The measurement of neutral and charged current cross sections will allow the flavour content of the proton to be unfolded at very high Q^2 and large x , including the region near $x = 1$.
- THERA will probe physics beyond the Standard Model. In particular, leptoquarks or squarks in supersymmetry with R -parity violation can be produced and their couplings determined in a rather complete manner. THERA is very sensitive to four-fermion contact interactions and probes compactification scales up to about 2.8 TeV via t -channel exchange of Kaluza–Klein gravitons in models with large extra dimensions. THERA will extend the searches for excited fermions to masses of up to 1 TeV.
- The photon structure will be resolved at harder scales and lower x_γ . The higher cross section for heavy-flavour production will permit the charm and bottom content of the quasi-real and virtual photon to be explored. Photon structure studies at THERA will be complementary to the investigations in $\gamma\gamma$ and $e\gamma$ reactions at TESLA.
- The acceleration of nuclei in HERA allows the investigation of electron–nucleus scattering in a very high energy range. This may lead deep into the region of high parton densities at low x and to phenomena such as saturation or large leading-twist shadowing. In eA collisions, coherent diffraction is expected to represent about half of the total interaction cross section.
- A further option of THERA consists in colliding a high-energy quasi-monochromatic beam of real photons, produced by backscattering laser light off the TESLA electron beam, with the proton beam from HERA. This would extend the field

of real-photoproduction studies into the TeV range and would allow for high-statistics studies of heavy-quark production at low x .

- Polarised proton–electron scattering at THERA allows the study of the spin structure of the proton and its theoretical interpretation in QCD to be extended into an hitherto unexplored kinematic range of low x and large Q^2 .

THERA represents a unique, cost-effective facility for investigating the structure of matter down to distances of about 10^{-19} m. As such it continues the long tradition of lepton–nucleon scattering experiments. Similarly to HERA, which has been the ep companion of the pp and e^+e^- colliders Tevatron and LEP, the THERA facility will yield information complementary to the LHC and to TESLA, utilising the rich physics potential of deep inelastic scattering in the TeV range of energy.

Bibliography

- [1] R.P. Feynman, *Photon-Hadron Interactions*. Benjamin, New York, 1972.
- [2] G.A. Voss and B.H. Wiik, *Ann. Rev. Nucl. Part. Sci.* **44**, 413 (1994).
- [3] *The THERA Book*, Report DESY-LC-REV-2001-062, 2001.
<http://www.desy.de/~lcnotes>.
- [4] H1 Coll., C. Adloff et al., *Deep inelastic inclusive ep scattering at low x and a determination of α_s* . Preprint DESY-00-181 (hep-ex/0012053), 2000. Subm. to *Eur. Phys. J.*
- [5] ZEUS Coll., *Measurement of the proton structure function F_2 in e^+p collisions at HERA*. Subm. to *ICHEP2000, Osaka*, abstract 1048, 2000.
- [6] G. Altarelli and G. Parisi, *Nucl. Phys.* **B 126**, 298 (1977);
V.N. Gribov and L.N. Lipatov, *Sov. J. Nucl. Phys.* **15**, 438 (1972);
Yu.L. Dokshitzer, *Sov. Phys. JETP* **46**, 641 (1977).
- [7] ZEUS Coll., J. Breitweg et al., *Phys. Lett.* **B 487**, 53 (2000).
- [8] ZEUS Coll., J. Breitweg et al., *Eur. Phys. J.* **C 6**, 603 (1999).
- [9] H1 Coll., C. Adloff et al., *Phys. Lett.* **B 483**, 23 (2000).
- [10] ZEUS Coll., J. Breitweg et al., *Eur. Phys. J.* **C 12**, 35 (2000).
- [11] H1 Coll., *Measurement of D^* production and F_2^c in DIS*. Subm. to *ICHEP2000, Osaka*, abstract 984, 2000.
- [12] M.F. McDermott, *The dipole picture of small x physics: A summary of the Amirim meeting*. Preprint DESY-00-126 (hep-ph/0008260), 2000.
- [13] A.H. Mueller, *Nucl. Phys.* **B 415**, 373 (1994).
- [14] N.N. Nikolaev and B.G. Zakharov, *Z. Phys.* **C 49**, 607 (1991);
N.N. Nikolaev and B.G. Zakharov, *Z. Phys.* **C 64**, 631 (1994).
- [15] L. Frankfurt, W. Koepf and M. Strikman, *Phys. Rev.* **D 54**, 3194 (1996).
- [16] E. Gotsman et al., *Has HERA reached a new QCD regime? (Summary of our view)*. Preprint DESY-00-149 (hep-ph/0010198), 2000.
- [17] M. Glück, S. Kretzer and E. Reya, *Astropart. Phys.* **11**, 327 (1999).
- [18] J. Kwiecinski, A.D. Martin and A.M. Stasto, *Penetration of the earth by ultrahigh-energy neutrinos and the parton distributions inside the nucleon*. Preprint hep-ph/9905307, 1999. Talk at *34th Rencontres de Moriond: QCD and Hadronic Interactions*, Les Arcs, France.
- [19] J. Bartels and H. Kowalski, *Diffraction at HERA and the confinement problem*. Preprint DESY-00-154 (hep-ph/0010345), 2000.
- [20] L.V. Gribov, E.M. Levin and M.G. Ryskin, *Phys. Rept.* **100**, 1 (1983);
A.H. Mueller and J. Qiu, *Nucl. Phys.* **B 268**, 427 (1986).

-
- [21] E. Levin, *Low-x physics*. Preprint hep-ph/0010272, 2000. Talk at *Diffraction 2000, Centraro, Italy*.
- [22] K. Golec-Biernat and M. Wüsthoff, Phys. Rev. **D 60**, 114023 (1999).
- [23] A.M. Stasto, K. Golec-Biernat and J. Kwiecinski, Phys. Rev. Lett. **86**, 596 (2001).
- [24] L. Frankfurt, M. McDermott and M. Strikman, *A fresh look at diffractive J/ψ photoproduction at HERA, with predictions for THERA*. Preprint hep-ph/0009086, 2000.
- [25] B. Naroska, *New results on vector meson production at HERA*. Preprint hep-ex/0006010, 2000. Contrib. to *35th Rencontres de Moriond: QCD and High Energy Hadronic Interactions*, Les Arcs, France.
- [26] J.A. Crittenden, *Exclusive Production of Neutral Vector Mesons at the Electron-Proton Collider HERA*, Springer Tracts in Modern Physics, Vol. 140. Springer, Berlin, Heidelberg, 1997.
- [27] M.G. Ryskin, Z. Phys. **C 57**, 89 (1993).
- [28] L.Frankfurt, W. Koepf and M. Strikman, Phys. Rev. **D 57**, 512 (1998).
- [29] M.G. Ryskin et al., Z. Phys. **C 76**, 231 (1997).
- [30] P. Merkel, *Diffractive Photoproduction of Heavy Vector Mesons at HERA*. Ph.D. Thesis, University of Hamburg, Report DESY-THESIS-1999-030, 1999.
- [31] S.J. Brodsky et al., Phys. Rev. **D 50**, 3134 (1994).
- [32] J.C. Collins, L. Frankfurt and M. Strikman, Phys. Rev. **D 56**, 2982 (1997).
- [33] A.D. Martin, M.G. Ryskin and T. Teubner, Phys. Rev. **D 55**, 4329 (1997).
- [34] J. Nemchik et al., Phys. Lett. **B 374**, 199 (1996).
- [35] D.Yu. Ivanov, Phys. Rev. **D 53**, 3564 (1996).
- [36] I.F. Ginzburg and D.Yu. Ivanov, Phys. Rev. **D 54**, 5523 (1996).
- [37] S.J. Brodsky et al., Phys. Lett. **B 449**, 306 (1999).
- [38] J.R. Forshaw and M.G. Ryskin, Z. Phys. **C 68**, 137 (1995).
- [39] A.D. Martin, M.G. Ryskin and T. Teubner, Phys. Lett. **B 454**, 339 (1999).
- [40] L.L. Frankfurt, M.F. McDermott and M. Strikman, JHEP **9902**, 002 (1999).
- [41] A. Levy, Phys. Lett. **B 424**, 191 (1998).
- [42] H1 Coll., C. Adloff et al., Z. Phys. **C 76**, 613 (1997).
- [43] ZEUS Coll., J. Breitweg et al., Eur. Phys. J. **C 6**, 43 (1999).
- [44] E.L. Feinberg and I.Y. Pomerantchuk, Nuov. Cim. Suppl. **III(4)**, 652 (1956);
F.E. Low, Phys. Rev. **D 12**, 163 (1975);
S. Nussinov, Phys. Rev. Lett. **34**, 1286 (1975).

- [45] J. Bartels, J. Phys. **G 26**, 481 (2000).
- [46] J. Kwiecinski, *Introduction to low x physics and diffraction*. Preprint hep-ph/0102018, 2001.
- [47] P.V. Landshoff, *Pomeron physics: An update*. Preprint DAMTP-2000-122 (hep-ph/0010315), 2000. Talk at *Diffraction 2000*, Centrarò, Italy.
- [48] J.C. Collins, Phys. Rev. **D 57**, 3051 (1998). Erratum in Phys. Rev. **D 61** 019902 (2000).
- [49] ZEUS Coll., J. Breitweg et al., Eur. Phys. J. **C 5**, 41 (1998); H1 Coll., C. Adloff et al., *Diffraction jet production in deep-inelastic e^+p collisions at HERA*. Preprint DESY-00-174 (hep-ex/0012051), 2000. Subm. to Eur. Phys. J.
- [50] W. Buchmüller, M.F. McDermott and A. Hebecker, Nucl. Phys. **B 487**, 283 (1997). Erratum in Nucl Phys. **B 500**, 621 (1997).
- [51] W. Buchmüller, T. Gehrmann and A. Hebecker, Nucl. Phys. **B 537**, 477 (1999).
- [52] J. Bartels, H. Lotter and M. Wüsthoff, Phys. Lett. **B 379**, 239 (1996). Erratum in Phys. Lett. **B 382**, 449 (1996); J. Bartels, H. Jung and M. Wüsthoff, Eur. Phys. J. **C 11**, 111 (1999).
- [53] E. Gotsman, E. Levin and U. Maor, Nucl. Phys. **B 493**, 354 (1997).
- [54] G. Ingelman and P.E. Schlein, Phys. Lett. **B 152**, 256 (1985).
- [55] E. Zijlstra and W. van Neerven, Nucl. Phys. **B 417**, 61 (1994). Erratum in Nucl. Phys **B 426**, 245 (1994); J. Blümlein and S. Kurth, Phys. Rev. **D 60**, 014018 (1999); E. Remiddi and J.A.M. Vermaseren, Int. J. Mod. Phys. **A 15**, 725 (2000); J. Blümlein, Comput. Phys. Comm. **133**, 76 (2000); S. Moch and J.A.M. Vermaseren, Nucl. Phys. **B 573**, 853 (2000).
- [56] J. Santiago and F.J. Ynduráin, Nucl. Phys. **B 563**, 45 (1999).
- [57] CTEQ Coll., H.L. Lai et al., Eur. Phys. J. **C 12**, 375 (2000).
- [58] A.D. Martin et al., Eur. Phys. **C 4**, 463 (1998).
- [59] M. Glück, E. Reya and A. Vogt, Eur. Phys. J. **C 5**, 461 (1998).
- [60] J. Blümlein et al., *Twist-4 gluon recombination corrections for deep inelastic structure functions*. Preprint DESY-01-007 (hep-ph/0102025), 2000.
- [61] J. Bartels and C. Bontus, Phys. Rev. **D 61**, 034009 (2000); J. Bartels, C. Bontus and H. Spiesberger, *Factorization of twist four gluon operator contributions*. Preprint DESY-99-118 (hep-ph/9908411), 1999.
- [62] M.A. Kimber, J. Kwiecinski and A.D. Martin, *Gluon shadowing in the low x region probed by the LHC*. Preprint PPP-01-01 (hep-ph/0101099), 2001.
- [63] J. Bartels, K. Golec-Biernat and K. Peters, Eur. Phys. J. **C 17**, 121 (2000).

-
- [64] E. Gotsman et al., *Higher twists and maxima for DIS on proton in high density QCD region*. Preprint TAUP-2644-2000 (hep-ph/0008280), 2000.
- [65] E.A. Kuraev, L.N. Lipatov and V.S. Fadin, Sov. Phys. JETP **44**, 443 (1976);
E.A. Kuraev, L.N. Lipatov and V.S. Fadin, Sov. Phys. JETP **45**, 199 (1977);
I.I. Balitski and L.N. Lipatov, Sov. J. Nucl. Phys. **28**, 822 (1978).
- [66] S. Catani and F. Hautmann, Nucl. Phys. **B 427**, 475 (1994).
- [67] V.S. Fadin and L.N. Lipatov, Phys. Lett. **B 429**, 127 (1998).
- [68] J. Blümlein, J. Phys. **G 19**, 1695 (1993);
J. Blümlein and W.L. van Neerven, Phys. Lett. **B 450**, 412 (1999);
J. Blümlein, *QCD evolution of structure functions at small x*. Preprint hep-ph/9909449, 1999. Lectures at *Ringberg Workshop: New Trends in HERA Physics*, Ringberg Castle, Tegernsee, Germany.
- [69] G. Altarelli, R.D. Ball and S. Forte, Nucl. Phys. **B 575**, 313 (2000).
- [70] R.K. Ellis, F. Hautmann and B.R. Webber, Phys. Lett. **B 348**, 582 (1995).
- [71] M. Ciafaloni, Nucl. Phys. **B 296**, 49 (1988);
S. Catani, F. Fiorani and G. Marchesini, Phys. Lett. **B 234**, 339 (1990);
S. Catani, F. Fiorani and G. Marchesini, Nucl. Phys. **B 336**, 18 (1990);
G. Marchesini, Nucl. Phys. **B 445**, 49 (1995).
- [72] H. Jung and L. Lönnblad, *Forward jet production at THERA*, in *The THERA Book* [3].
- [73] S. Bethke, J. Phys. **G 26**, R27 (2000).
- [74] C. Quigg, *Perspectives in high-energy physics*. Preprint hep-ph/0002080, 2000. Review Lecture at ICFA School on Instrumentation in Elementary Particle Physics, Istanbul, Turkey.
- [75] S.I. Alekhin and A.L. Kataev, Nucl. Phys. **A 666**, 179 (2000).
- [76] M. Klein, C. Pascaud and R. Wallny, *QCD analysis of structure function measurements*, in *The THERA Book* [3].
- [77] W.L. van Neerven and A. Vogt, Nucl. Phys. **B 568**, 263 (2000).
- [78] S. Larin, T. van Ritbergen and J.A.M. Vermaseren, Nucl. Phys. **B 427**, 41 (1994);
S. Larin et al., Nucl. Phys. **B 492**, 338 (1997);
A. Retey and J.A.M. Vermaseren, *Some higher moments of deep inelastic structure functions at next-to-next-to-leading order of perturbative QCD*. Preprint NIKHEF-2000-018 (hep-ph/0007294), 2000.
- [79] W. van Neerven and A. Vogt, Nucl. Phys. **B 588**, 345 (2000);
W.L. van Neerven and A. Vogt, Phys. Lett. **B 490**, 111 (2000).
- [80] B. Pötter, *High- p_t jet production*, in *The THERA Book* [3].

- [81] H1 Coll., C. Adloff et al., *Measurement and QCD analysis of jet cross-sections in deep inelastic positron-proton collisions at \sqrt{s} of 300 GeV*. Preprint DESY-00-145 (hep-ex/0010054), 2000. Subm. to Eur. Phys. J.
- [82] ZEUS Coll., *Measurement of differential cross sections for dijet production in neutral current DIS at high Q^2 and determination of α_s* . Subm. to ICHEP2000, Osaka, abstract 891, 2000.
- [83] W.-K. Tung, *The heavy quark parton oxymoron – a mini-review of heavy quark production theory in pQCD*, in *Proc. 5th Int. Workshop on Deep Inelastic Scattering and QCD (DIS97), Chicago, IL, USA*, eds. J. Repond and D. Krakauer, p. 1014. American Institute of Physics, Woodbury, NY, 1997. Also in preprint hep-ph/9706480.
- [84] A. Chuvakin, J. Smith and B.W. Harris, *Variable flavor number schemes versus fixed order perturbation theory for charm quark electroproduction*. Preprint YITP-SB-00-68 (hep-ex/0010350), 2000.
- [85] H1 Coll., C. Adloff et al., Nucl. Phys. **B 545**, 21 (1999);
ZEUS Coll., J. Breitweg et al., Eur. Phys. J. **C 6**, 67 (1999).
- [86] H1 Coll., C. Adloff et al., Phys. Lett. **B 467**, 156 (1999);
ZEUS Coll., J. Breitweg et al., *Measurement of open beauty production in photoproduction at HERA*. Preprint DESY-00-166 (hep-ex/0011081), 2000. Subm. to Eur. Phys. J.
- [87] S. Frixione et al., Nucl. Phys. **B 412**, 225 (1994);
M.L. Mangano, P. Nason and G. Ridolfi, Nucl. Phys. **B 373**, 295 (1992).
- [88] P. Jankowski, M. Krawczyk and M. Wing, *Heavy quark production at THERA*, in *The THERA Book* [3].
- [89] L Gladilin and I. Redondo, *Heavy quark production measurements at THERA*, in *The THERA Book* [3].
- [90] S.P. Baranov and N.P. Zotov, *Heavy quark production in the semihard approach at THERA*, in *The THERA Book* [3].
- [91] G. Marchesini et al., Comp. Phys. Comm. **67**, 465 (1992).
- [92] B.W. Harris and J. Smith, Phys. Rev. **D 57**, 2806 (1998).
- [93] J. Amundson et al., JHEP **0010**, 031 (2000). Also in hep-ph/0005221;
A. Chuvakin, J. Smith and B.W. Harris, *Variable flavor number schemes versus fixed order perturbation theory for charm quark electroproduction*. Preprint YITP-SB-00-68 (hep-ph/0010350), 2000.
- [94] M. Buza and W.L. van Neerven, Nucl. Phys. **B 500**, 301 (1997);
R.S. Thorne and R.G. Roberts, *A variable number flavor scheme for charged current heavy flavor structure functions*. Preprint RAL-TR-2000-048 (hep-ph/0010344), 2000.

-
- [95] V. Barone, C. Pascaud and F. Zomer, *A new global analysis of DIS data and the strange sea distribution*, in *Proc. Workshop on Light-Cone QCD and Nonperturbative Hadron Physics, Adelaide, Australia, 1999*, p. 167. 2000. Also in preprint hep-ph/0004268.
- [96] E. Derman, *Phys. Rev. D* **7**, 2755 (1973).
- [97] M. Klein and T. Riemann, *Z. Phys. C* **24**, 151 (1984).
- [98] U.F. Katz, *Deep-Inelastic Positron-Proton Scattering in the High-Momentum-Transfer Regime of HERA*, Springer Tracts in Modern Physics, Vol. 168. Springer, Berlin Heidelberg, 2000.
- [99] J. Blümlein et al., *Z. Phys. C* **45**, 501 (1990).
- [100] S. Kuhlmann et al., *Phys. Lett. B* **476**, 291 (2000).
- [101] J.G. Morfin, *Nucl. Phys. Proc. Suppl.* **79**, 664 (1999);
C. Albright et al., *Physics at a neutrino factory*. Report FERMILAB-FN-492 (hep-ex/0008064), 2000.
- [102] W. van Neerven, *Precision tests of perturbative QCD at THERA*. Talk at THERA meeting, Hamburg, 2000.
http://www.ifh.de/thera/agenda_18oct.html.
- [103] C.Y. Prescott et al., *Phys. Lett. B* **77**, 347 (1978).
- [104] A.F. Żarnecki, *Eur. Phys. J. C* **17**, 695 (2000).
- [105] W. Buchmüller, R. Rückl and D. Wyler, *Phys. Lett. B* **191**, 442 (1987).
Erratum in *Phys. Lett. B* **448** 320 (1999).
- [106] A.F. Żarnecki, *Leptoquark searches at future colliders*. Subm. to *ICHEP2000, Osaka*, abstract 193, 2000.
- [107] A. Djouadi et al., *Z. Phys. C* **46**, 679 (1990).
- [108] P. Taxil, E. Tuğcu and J.M. Virey, *Eur. Phys. J. C* **14**, 165 (2000).
- [109] N. Arkani-Hamed, S. Dimopoulos and G. Dvali, *Phys. Lett. B* **429**, 263 (1998);
N. Arkani-Hamed, S. Dimopoulos and G. Dvali, *Phys. Rev. D* **59**, 086004 (1999).
- [110] N. Arkani-Hamed and M. Schmaltz, *Phys. Rev. D* **61**, 033005 (2000).
- [111] K. Hagiwara, D. Zeppenfeld and S. Komamiya, *Z. Phys. C* **29**, 115 (1985).
- [112] M. Wing, *Inclusive dijet photoproduction and the resolved photon at THERA*, in *The THERA Book* [3].
- [113] M. Krawczyk and A. Zembrzuski, *Prompt photon production at THERA*, in *The THERA Book* [3].
- [114] U. Jezuita-Dabrowska and M. Krawczyk, *On the importance of the interference terms and longitudinal virtual photon contribution at THERA*, in *The THERA*

- Book* [3].
- [115] M. Stratmann, *Determining the spin structure of the photon at future colliders*. Preprint hep-ph/0006285, 2000. Contrib. to *DIS2000*, Liverpool.
 - [116] ZEUS Coll., J. Breitweg et al., Euro. Phys. J. **C 11**, 35 (1999);
ZEUS Coll., *The structure of the photon and the dynamics of resolved-photon processes in dijet photoproduction*. Subm. to *ICHEP2000, Osaka*, abstract 1066, 2000;
ZEUS Coll., *Measurement of dijet photoproduction at high transverse energies at HERA*. Subm. to *EPS-HEP99*, Tampere, Finland, paper 540, 1999.
 - [117] M. Krawczyk, A. Zembrzuski and M. Staszal, *Survey of present data on photon structure functions and resolved photon processes*. Preprint IFT-99-15 (hep-ph/0011083), 2000. Subm. to Phys. Rept.
 - [118] M. Klasen, *Jet photoproduction at THERA*, in *The THERA Book* [3].
 - [119] ZEUS Coll., M. Derrick et al., Phys. Lett. **B 348**, 665 (1995).
 - [120] S. Frixione, Z. Kunszt and A. Signer, Nucl. Phys. **B 467**, 399 (1996);
S. Frixione, Nucl. Phys. **B 507**, 295 (1997);
S. Frixione and G. Ridolfi, Nucl. Phys. **B 507**, 315 (1997).
 - [121] L.E. Gordon and J.K. Storrow, Nucl. Phys. **B 489**, 405 (1997);
M. Glück, E. Reya and A. Vogt, Phys. Rev. **D 45**, 3986 (1992);
M. Glück, E. Reya and A. Vogt, Phys. Rev. **D 46**, 1973 (1992);
P. Aurenche, J.P. Guillet and M. Fontannaz, Z. Phys. **C 64**, 621 (1994);
G.A. Schuler and T. Sjöstrand, Z. Phys. **C 68**, 607 (1995).
 - [122] A. Piwinski, *Intrabeam scattering*, in *Proc. 9th Int. Conf. on High Energy Accelerators, Stanford (1974)*, p. 405. 1975.
 - [123] J. Maidment. Private communication, 2001.
 - [124] K. Balewski et al., Nucl. Instrum. Meth. **A 441**, 274 (2000).
 - [125] T. Sen, *Crossing angle option for HERA*. Report DESY-HERA-96-02, 1996.
 - [126] M. Tigner, B. Wiik and F. Willeke, *An electron-proton collider in the TeV range*, in *Proc. IEEE Particle Accelerator Conference, San Francisco*, p. 2910. 1991.
 - [127] R. Brinkmann and M. Dohlus, *A method to overcome the bunch length limitations on β_p^* for electron-proton colliders*. Report DESY-M-95-11, 1995.
 - [128] J. Crittenden et al., *A detector for THERA*, in *The THERA Book* [3].
 - [129] L. Gladilin et al., *The backward silicon tracker for THERA*, in *The THERA Book* [3].
 - [130] G. Piller and W. Weise, Phys. Rept. **330**, 1 (2000).
 - [131] New Muon Coll., P. Amaudruz et al., Nucl. Phys. **B 441**, 3 (1995).

-
- [132] M. Arneodo et al., *Nuclear beams in HERA*, in *Proc. Workshop on Future Physics at HERA*, eds. G. Ingelman, A. De Roeck and R. Klanner, p. 887. Hamburg, Germany, DESY, 1996.
- [133] L. Frankfurt and M. Strikman, *Small- x phenomena in eA collisions*, in *The THERA Book* [3].
- [134] *Proc. Nuclear Theory Summer Meeting on eRHIC*, eds. L. McLerran and R. Venugopalan, 2000. Report BNL-52606.
- [135] A.H. Mueller, Nucl. Phys. **B 335**, 115 (1990).
- [136] E. Iancu, A. Leonidov and L. McLerran, *Nonlinear gluon evolution in the color glass condensate. I*. Preprint SACLAY-T00-166 (hep-ph/0011241), 2000.
- [137] L. Frankfurt and M. Strikman, Eur. Phys. J. **A 5**, 293 (1999).
- [138] L. Frankfurt, V. Guzey and M. Strikman, J. Phys. **G 27**, R23 (2001).
- [139] L. McLerran and R. Venugopalan, Phys. Rev. **D 50**, 2225 (1994).
- [140] L. McLerran and R. Venugopalan, Phys. Rev. **D 59**, 094002 (1999).
- [141] V.N. Gribov, Sov. Phys. JETP **30**, 709 (1970).
- [142] M. McDermott et al., Eur. Phys. J. **C 16**, 641 (2000).
- [143] A.H. Mueller, Nucl. Phys. **B 558**, 285 (1999);
Y.V. Kovchegov, A.H. Mueller and S. Wallon, Nucl. Phys. **B 507**, 367 (1997).
- [144] N.N. Nikolaev, B.G. Zakharov and V.R. Zoller, Z. Phys. **A 351**, 435 (1995).
- [145] L.L. Frankfurt and M.I. Strikman, Phys. Lett. **B 382**, 6 (1996).
- [146] E. Gotsman et al., Phys. Lett. **B 492**, 47 (2000).
- [147] B.H. Denby et al., Phys. Rev. Lett. **52**, 795 (1984).
- [148] A. Skrinsky, *Prospects for polarized electron nuclei colliders*, in *Proc. Workshop on Physics With Electron Polarized Ion Collider (EPIC99)*, eds. L.C. Bland, J.T. Londergan and A.P. Szczepaniak. 1999.
- [149] A.K. Çiftçi et al., Nucl. Instrum. Meth. **A 365**, 317 (1995).
- [150] R. Brinkmann et al., *Linac-ring type colliders: Fourth way to TeV scale*. Preprint DESY-97-239 (physics/9712023), 1997.
- [151] S. Sultansoy, *The post-HERA era: Brief review of future lepton hadron and photon hadron colliders*. Preprint DESY-99-159 (hep-ph/9911417), 1999.
- [152] S.F. Sultanov, *Prospects of the future ep and γp colliders: Luminosity and physics*. Report IC/89/409, ICTP, Trieste, 1989.
- [153] S. Sultansoy, Turkish J. Phys. **22**, 575 (1998).
- [154] EMC Coll., J. Ashman et al., Phys. Lett. **B 206**, 364 (1988);
EMC Coll., J. Ashman et al., Nucl. Phys. **B 328**, 1 (1989).

-
- [155] N.C.R. Makins, *Spin physics*. Talk at *DIS2000*, Liverpool, hep.ph.liv.ac.uk/~disproc/plenary1/makins.ps.gz, 2000; U. Stösslein, *Summary of the spin programme (PWG1)*. Talk at *DIS2000*, Liverpool, hep.ph.liv.ac.uk/~disproc/plenary2/PWG1/stoesslein, 2000.
- [156] *Proc. Workshop on Future Physics at HERA*, eds. G. Ingelman, A. De Roeck and R. Klanner, 1996.
- [157] *Proc. Workshop Deep Inelastic Scattering off Polarized Targets: Theory Meets Experiment*, ed. J. Blümlein et al., Report DESY-97-200, 1997.
- [158] A. Deshpande, *The physics case for polarized protons at HERA*, in *Proc. Workshop on Polarized Protons at High Energies – Accelerator Challenges and Physics Opportunities*, eds. A. De Roeck, D. Barber and G. Rädcl. 1999.
- [159] *An electron ring collider at RHIC*. Proc. 2nd eRHIC Workshop, Yale, 2000. Report BNL-52592.
- [160] *An electron ring at RHIC and EIC*. Proc. 2nd Workshop on an Electron Ion Collider (EIC), Boston, 2000.
- [161] TESLA-N Study Group, M. Anselmino et al., *Electron scattering with polarized targets at TESLA*. Preprint DESY-00-160 (hep-ph/0011299), 2000. Also in this volume.
- [162] A. De Roeck et al., Eur. Phys. J. C **6**, 121 (1999).
- [163] J. Blümlein, RIKEN Rev. **28**, 126 (2000). Also in hep-ph/9912550.
- [164] J.G. Contreras, A. De Roeck and M. Maul, *A study on Δu and Δd in charged current events using polarized beams at HERA*, in *Proc. Workshop on Physics with Polarized Protons at HERA, Hamburg*, p. 103. 1998. Also in preprint hep-ph/9711418.
- [165] J. Ellis, S. Lola and K. Sridhar, Phys. Lett. B **408**, 252 (1997).
- [166] N. Kochelev, *Instantons, spin crisis and high Q^2 anomaly at HERA*, in *Proc. Workshop on Physics with Polarized Protons at HERA, Hamburg*, p. 225. 1997. <http://www.desy.de/~gehrt/heraspin/proclist.html>.

3 TESLA-N: Electron Scattering with Polarised Targets

The TESLA-N Study Group

M. Anselmino¹², E.C. Aschenauer⁴, S. Belostotski¹⁰, W. Bialowons⁴, J. Blümlein⁴, V. Braun¹¹, R. Brinkmann⁴, M. Düren², F. Ellinghaus⁴, K. Goeke³, St. Goertz³, A. Gute⁵, J. Harmsen³, R. Jakob¹⁴, E.M. Kabuss⁸, R. Kaiser⁴, V. Korotkov⁴, P. Kroll¹⁴, E. Leader⁷, B. Lehmann-Dronke¹¹, L. Mankiewicz¹³, A. Meier³, W. Meyer³, N. Meyners⁴, D. Müller¹¹, P.J. Mulders¹, W.-D. Nowak⁴, L. Niedermeier¹¹, K. Oganessyan⁴, P.V. Pobilitza³, M.V. Polyakov³, G. Reicherz³, K. Rith⁵, D. Ryckbosch⁶, A. Schäfer¹¹, K. Sinram⁴, E. Steffens⁵, J. Steijger⁹, G. van der Steenhoven⁹, D. von Harrach⁸, C. Weiss³.

¹Vrije Universiteit Amsterdam, The Netherlands

²Universität Bayreuth, Germany

³Ruhr-Universität Bochum, Germany

⁴DESY Hamburg and Zeuthen, Germany

⁵Friedrich-Alexander-Universität Erlangen-Nürnberg, Germany

⁶Université Gent, Belgium

⁷Imperial College, London, UK

⁸Johannes Gutenberg-Universität Mainz, Germany

⁹NIKHEF, Amsterdam, The Netherlands

¹⁰University of St.Petersburg, Russia

¹¹Universität Regensburg, Germany

¹²INFN, Sezione di Torino, Italy

¹³Nicolaus Kopernicus Astronomical Center, Warsaw, Poland

¹⁴Bergische Universität Wuppertal, Germany

Contents

3	TESLA-N: Electron Scattering with Polarised Targets at TESLA	161
3.1	Introduction	165
3.2	Physics Prospects	167
3.2.1	Transversity Distributions	167
3.2.2	Helicity Distributions	171
3.2.3	Polarized Gluon Distribution	174
3.2.4	Higher Twist	176
3.2.5	Fragmentation Functions	177
3.2.6	Specific Deuteron Structure Functions	177
3.3	Layout of the Experiment	177
3.3.1	Polarized Target	177
3.3.2	Polarized Electron Beam	178
3.3.3	Overview of the Apparatus	180
3.3.4	Luminosity and Acceptance	182
3.3.5	Resolution in Kinematic Variables	185
3.3.6	Civil Engineering	186
3.4	Summary	186
	Bibliography	188

3.1 Introduction

Today there is widespread confidence that Quantum Chromodynamics (QCD) is the correct theory of strong interactions. On the level of unpolarized parton distribution functions the theory has been tested with considerable precision by many experiments. However, after 10 years of intense theoretical and experimental activities in studying the *polarized* nucleon, the angular momentum composition of the nucleon remains a territory with blank spots. High precision data in a large kinematic domain are required to fully explore the spin structure of QCD.

Measurements of polarized deep-inelastic scattering (DIS) were up to now mostly performed with longitudinally polarized nucleons. Hence, the majority of experimental information on the angular momentum composition of the nucleon is restricted to its longitudinal spin structure. This is characterized through the helicity distributions $\Delta q(x, Q^2)$ (also known as longitudinal quark spin distributions), where q denotes the quark flavor, the ‘Bjorken-variable’ x is the fraction of the nucleon momentum carried by the interacting parton and Q^2 is the virtuality of the exchanged photon. However, of equal importance for a complete understanding of the spin structure of the nucleon as seen in high-energy processes, are the hitherto unmeasured transversity distributions $\delta q(x, Q^2)$, which can only be measured with transversely polarized nucleons.

While a weighted sum of the helicity distributions $\Delta q(x, Q^2)$ is directly accessible in inclusive deep-inelastic scattering (DIS) as the longitudinal spin structure function $g_1(x, Q^2)$, the transversity distributions $\delta q(x, Q^2)$ do not appear in an inclusive structure function. They can, however, be measured in semi-inclusive DIS processes which implies a substantially higher experimental effort. In comparison, the perspectives of RHIC for a direct measurement of transversity are not good [1].

First results on transversity distributions can be expected from HERMES [2] and COMPASS [3] within 3-5 years from now, while a complete high precision mapping of their x - and Q^2 -dependence requires high statistics measurements that are beyond the scope of presently or soon running experiments.

An important reason for the interest in the transversity distributions and their first moments, the tensor charges, is the fact that these quantities are related to matrix elements of chirally odd operators in QCD [4]. All known low-energy probes of hadrons such as electromagnetic or weak currents are chirally even, so that low-energy experiments cannot provide any information about chirally odd matrix elements¹. Inclusive DIS at large Q^2 (both unpolarized and polarized) measures only chirally even operators, hence a whole class of operators so far remained unmeasured because of the lack of suitable ‘natural’ probes coupling to them. Hadrons are expected to react very differently to chirally odd probes as compared to chirally even ones; e.g. the coupling of the flavor non-singlet tensor charge to pions is completely different from that of the axial charge [5]. A measurement of the transversity distributions and tensor charges would for the first time provide an opportunity to access the ‘missing’ chirally odd operators. In this way it would greatly improve the understanding of the role of chiral symmetry

¹An exception is the so-called sigma term, whose effect on hadrons is, however, proportional to the small current quark masses.

in shaping the structure of the QCD ground state and of the low-mass hadrons.

The successful understanding and use of *unpolarized* distribution and fragmentation functions in various processes have given confidence that QCD can be used not only for the extension to polarized functions. Moreover, it is also applicable for contributions of higher orders in the coupling constant α_s or beyond leading order in an expansion in the inverse hard scale (Q for deep-inelastic leptonproduction), which is referred to as higher twist. Progress in these directions requires to develop new calculational techniques as well as novel methods to solve the evolution equations associated. These more involved aspects of QCD are just those that are perceived by many theorists to be the most interesting ones. It is widely accepted that QCD is rich enough as a theory to be able to generate the entire hadron and nuclear physics phenomenology. One crucial aspect, however, for most of the relevant physics, namely a complete and systematic control of all relevant higher-order and higher-twist contributions is still not in reach. Straightforward QCD perturbation theory often only converges for some limited kinematic configurations. This is in striking contrast to the fact that much of the available experimental data is easily interpreted by a combination of leading order perturbative calculations and some ‘intuitive’ power-correction terms. It suggests that for many signals a QCD-description could be pushed down to photon virtualities as low as $Q^2 = 1 \text{ GeV}^2$. High accuracy measurements in this domain will provide definitive tests for higher-order and higher-twist QCD calculations.

To the extent that the focus of hadron physics turns to higher energies and more exclusive reactions, a corresponding move is about to begin from the traditional, somewhat ‘model-oriented’ nuclear physics approach towards real QCD descriptions. Recent theoretical investigations encourage such efforts by strongly pushing the limits of previous QCD-techniques towards a much better description of semi-inclusive and exclusive reactions. This requires an extension of the classification of polarized twist-2 and twist-3 distribution and fragmentation functions plus a realistic phenomenology and more sophisticated hadron wave functions. A great potential to achieve an even deeper understanding of the nucleon structure may arise from a comprehensive, generalized analysis of many different processes based on the new tool of skewed parton distributions (SPDs).

The study of hadron structure has another important facet in that it would supply badly needed input for the interpretation of data from Tevatron and LHC. A better understanding of the interplay between soft and hard contributions in exclusive processes is relevant for the success of the B-factories at hadron colliders. Issues of great importance for the LHC include a better determination of the gluon distribution for the whole range of Bjorken- x as well as a better understanding of isolated photon production, which is an important background for $H \rightarrow \gamma + \gamma$.

Within the nuclear and particle physics communities there exists an increasing conviction in the necessity of a new facility to study polarized lepton-nucleon/nucleus scattering with very high luminosity and a high enough center-of-mass energy to cover a sufficient kinematic domain. This document outlines the TESLA-N project, which would use one arm of the TESLA linear collider at DESY for a polarized electron-nucleon fixed-target experiment. The current discussions about ELFE@DESY, ELFE@CERN,

eRHIC, EPIC, or a long-term high-energy option for CEBAF are all variations on the same subject. TESLA-N is a highly competitive and very cost-effective alternative option. Its distinguishing property is the unique combination of large center-of-mass energy and high luminosity.

3.2 Physics Prospects

The HERMES results that have emerged over the recent past are demonstrating the richness of polarized electron-nucleon physics. The higher energy and the much higher luminosity of TESLA-N are expected to again significantly enlarge the number and variety of observable effects as well as the precision with which they can be studied. Naturally, today a theoretical understanding is only available for a part of this potential. Hence, the following list of topics illustrates rather than exhausts the physics potential of TESLA-N.

Detailed projections for the statistical accuracy attainable in one of the TESLA-N key experiments, the precise measurement of the transversity distributions, are given in the following section. Projections for all other topics are included in the sections following below, whenever available. All given projections are based on an integrated luminosity of 100 fb^{-1} . This represents a conservative estimate for *one* year of data taking (cf. section 3.3.4).

3.2.1 Transversity Distributions

The nucleon as a spin 1/2 hadron is characterized by three independent flavor sets of (leading order) quark distributions. The distributions $q(x, Q^2)$ - or $f_1^q(x, Q^2)$ - describe the unpolarized nucleon. The transversity distributions $\delta q(x, Q^2)$ - also referred to as $h_1^q(x, Q^2)$ or sometimes as $\Delta_T q(x, Q^2)$ - as well as the helicity distributions $\Delta q(x, Q^2)$ - also referred to as $g_1^q(x, Q^2)$ - describe aspects of the internal spin structure of the nucleon. One important difference between the latter two lies in their different QCD evolution. In contrast to the helicity distributions, the transversity distributions decouple from gluons. The reason is, that the transversity distributions are chirally odd, involving correlations between left- and righthanded quarks. Since $\Delta q(x, Q^2)$ and $\delta q(x, Q^2)$ describe the quark polarization in longitudinally and transversely polarized nucleons, respectively, they are independent functions. However, in the most naive approximation using non-relativistic quarks $\delta q(x) \approx \Delta q(x)$ can be expected.

The first moments of the distribution functions give particular charges, which are matrix elements of local operators. For the unpolarized distributions the first moments of $q(x, Q^2) - \bar{q}(x, Q^2)$ give the flavor charges. For the helicity distributions the first moments of $\Delta q(x, Q^2) + \Delta \bar{q}(x, Q^2)$ give the axial charges $\Delta q(Q^2)$. The flavor sum of these axial charges, $\Delta \Sigma(Q^2)$, is the longitudinal quark spin fraction whose properties have given rise to all the commotion around the nucleon spin because of its anomalous evolution involving the polarized gluon distribution. The first moments of $\delta q(x, Q^2) - \delta \bar{q}(x, Q^2)$ are called tensor charges $\delta q(Q^2)$; their flavor sum is denoted

$\delta\Sigma(Q^2)$. Experimentally nothing is known about the tensor charges, in contrast to the flavor and axial charges. While for the axial charges the nonsinglet combinations can also be measured in low-energy experiments (weak decays), no such experiments are known for the tensor charges. The tensor charges $\delta q(Q^2)$ and their flavor sum $\delta\Sigma(Q^2)$ are valence objects and decouple from gluons and sea quarks. In this respect, the tensor charges are expected to be closer to the non-relativistic limit than the axial charges. This is supported by recent lattice QCD calculations [6, 7]. Reference [6] quotes values of $\Delta\Sigma = 0.18 \pm 0.10$ for the longitudinal quark spin fraction and $\delta\Sigma = 0.562 \pm 0.088$ for the quark tensor charge at $Q^2 = 2 \text{ GeV}^2$.

As mentioned previously, the transversity distributions $\delta q(x, Q^2)$ are not accessible in inclusive measurements, because they are chirally odd and only occur in combinations with other chirally odd objects. In semi-inclusive DIS of unpolarized leptons off transversely polarized nucleons several methods have been proposed to access $\delta q(x, Q^2)$ via specific single target-spin asymmetries:

1. An asymmetry that involves $\delta q(x, Q^2)$ in combination with the chirally odd polarized fragmentation function $H_1^{\perp(1)}(z)$ can be extracted from the azimuthal distribution of the produced single hadron [8, 9, 10, 11, 12]. This fragmentation function correlates the transverse spin of a quark with a preferred transverse direction for the production of the pion.
2. A measurement of the momenta of two leading pions gives access to an asymmetry in which $\delta q(x, Q^2)$ combines with a so-called interference fragmentation function [13, 14, 15]. Here the transverse spin of the quark is correlated with the relative transverse momentum between the pions.
3. The determination of transverse components of the spin vector of produced Λ particles allows the measurement of an asymmetry where $\delta q(x, Q^2)$ combines with a polarized fragmentation function $H_1(z)$ [16].
4. Vector-meson production provides other ways to probe $\delta q(x, Q^2)$ employing polarimetry and azimuthal asymmetries [17, 18]. For ρ -production, where the polarimetry involves a pion pair, it is part of the above two-pion production.

Option (1) offers the experimentally most direct access to $\delta q(x, Q^2)$. An appropriately weighted cross-section asymmetry can be expressed as a flavor-sum where each transversity distribution function $\delta q(x, Q^2)$ enters in combination with a hitherto unknown polarized fragmentation function $H_1^{\perp(1)q}(z)$ of the same flavor [10]:

$$A_T(x, Q^2, z) = P_T \cdot D_{nn} \cdot \frac{\sum_q e_q^2 \delta q(x, Q^2) H_1^{\perp(1)q}(z)}{\sum_q e_q^2 q(x, Q^2) D_1^q(z)} \quad (3.2.1)$$

Here D_{nn} is the transverse polarization transfer coefficient, P_T is the nucleon's transverse polarization, and $D_1^q(z)$ is the unpolarized quark fragmentation function that recently has attracted renewed interest (cf. section 3.2.5).

Measurements of different asymmetries in the production of positive and negative pions on proton and deuteron targets ($A_p^{\pi^+}$, $A_p^{\pi^-}$, $A_d^{\pi^+}$, $A_d^{\pi^-}$) allow the simultaneous reconstruction of the shapes of the unknown functions $\delta q(x, Q^2)$ and the ratio $H_1^{\perp(1)}(z)/D_1(z)$. This ratio is considered to be flavor independent in the context of this study. The relative normalization can be fixed through independent measurements of $H_1^{\perp(1)}(z)$, e.g. in e^+e^- experiments. Alternatively, an additional assumption can be used, where one of the possibilities is to relate $\delta q(x)$ to $\Delta q(x)$ at small values of Q^2 . The differences between both are smallest in the region of intermediate and large values of x , hence the normalization ambiguity can be resolved at $x_0 = 0.25$ by assuming [19]:

$$\delta u(x_0, Q_0^2) = \Delta u(x_0, Q_0^2) \quad (3.2.2)$$

Measurements of all possible asymmetries, $A_{p,d}^{\pi^+(\pi^-)}$, for $N_{(x,Q^2)}$ points in the (x, Q^2) -plane and for N_z points in z yield $4 \cdot N_{(x,Q^2)} \cdot N_z$ measurements. This must be compared to $4 \cdot N_{(x,Q^2)}$ unknown parameters, corresponding to the quark distributions $\delta u(x, Q^2)$, $\delta d(x, Q^2)$, $\delta \bar{u}(x, Q^2)$, $\delta \bar{d}(x, Q^2)$, and to N_z unknown values of $H_1^{\perp(1)}(z)/D_1(z)$. If kaon asymmetries are measured in addition, the distributions $\delta s(x, Q^2)$ and $\delta \bar{s}(x, Q^2)$ can be included as well. This defines an overconstrained set of coupled equations which can be solved using a standard minimization procedure.

For the determination of the projected statistical accuracies for future measurements of $\delta q(x, Q^2)$ at TESLA-N reasonable input is required for the unknown functions $\delta q(x, Q^2)$ and $H_1^{\perp(1)}(z)/D_1(z)$. The former ones were assumed to coincide with the GRSV LO parameterization [20] for $\Delta q(x, Q^2)$ at the initial scale of $Q^2 = 0.4 \text{ GeV}^2$ and evolved to higher values of Q^2 using the DGLAP equations for transversity distributions. The resulting distributions approximately obey the Soffer bound [21, 22]. All T-odd fragmentation functions are constrained by a sum rule [23] but otherwise hardly known. The ratio of fragmentation functions was modelled by adopting the approach of reference [10] and fitting the parameters to recent HERMES [24] and DELPHI [25] data. These results indicate that the fragmentation function $H_1^{\perp(1)}(z)$ may be quite sizeable. Hadron distributions in semi-inclusive production were obtained using the standard generators LEPTO [26] and JETSET [27].

The projected statistical accuracy for the measurement of the (x, Q^2) -dependence of the u_v -quark transversity distribution at TESLA-N is shown in figure 3.2.1. A broad range of $0.003 < x < 0.7$ can be accessed in conjunction with $1 < Q^2 < 100 \text{ GeV}^2$, with an impressive statistical accuracy over almost the full range. Because of u-quark dominance in pion electroproduction a somewhat lower accuracy is attained in the reconstruction of the other transversity distributions, δd_v , $\delta \bar{u}$, and $\delta \bar{d}$.

There is a technically different approach to determine the unknown quark distributions and fragmentation function ratios using parameterized transversity distributions. The starting point is a parameter-dependent ansatz for every $\delta q(x, Q_0^2)$, e.g.

$$\delta q(x, Q_0^2) = \eta_q \cdot x^{\alpha_q} (1-x)^{\beta_q} (1 + \gamma_q x + \rho_q \sqrt{x}) \quad (3.2.3)$$

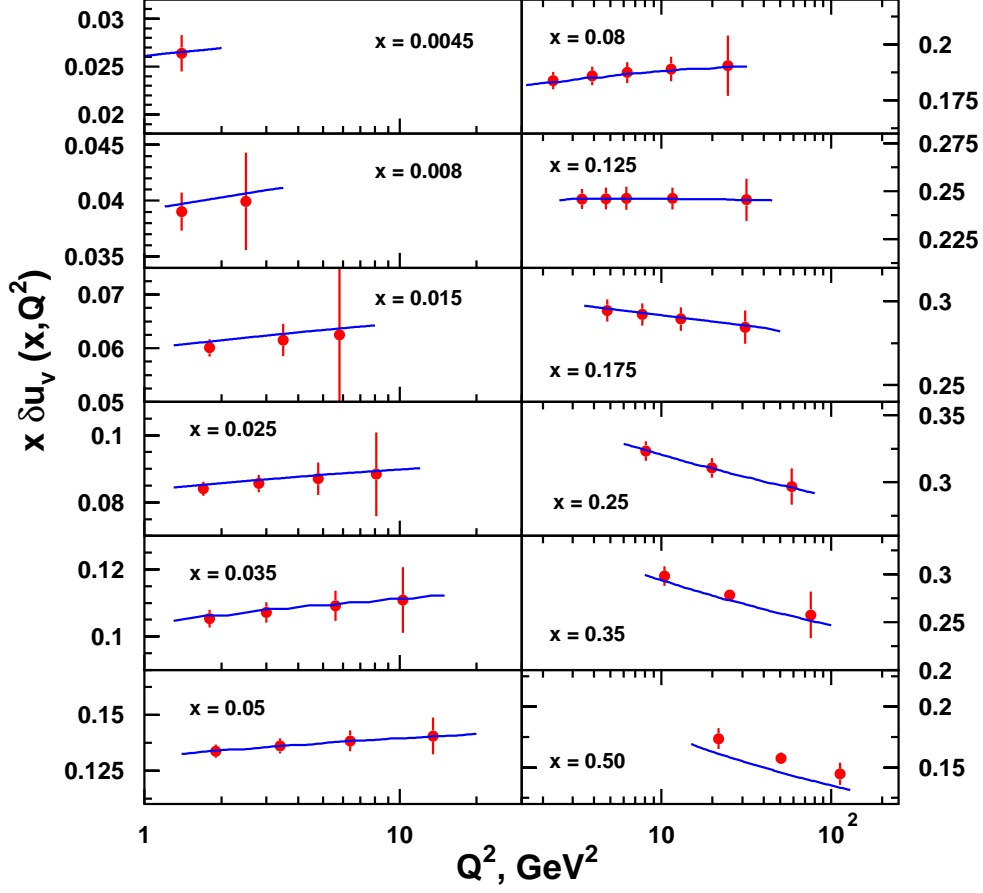


Figure 3.2.1: The valence u -quark transversity distribution as a function of x and Q^2 as it would be measured at TESLA-N, based on an integrated luminosity of 100 fb^{-1} . The curves show the LO Q^2 -evolution of the u_v -quark transversity distribution obtained with a fit to the simulated asymmetries.

at a reference scale Q_0^2 . Here η_q , α_q , β_q , γ_q , and ρ_q are free parameters. These free parameters and the unknown fragmentation function ratios $H_1^{\perp(1)}(z)/D_1(z)$ are fitted to the simulated values of the asymmetries, calculated through eq.(3.2.1). In this procedure the distribution functions are evolved in leading order to the necessary Q^2 -values using the above ansatz. The resulting functional dependence for $x \cdot \delta u_v(x, Q^2)$ is represented by the lines drawn in figure 3.2.1. In addition, the fit also provides a projection for the accuracy of the tensor charges of u - and d -quarks of 0.88 ± 0.01 and -0.32 ± 0.02 at the scale of 1 GeV^2 , respectively. Note that the absolute values of the tensor charges are defined to a large extent by the input distributions, although the values are rather close to those predicted by lattice QCD calculations. At the same time, the fit yields precise values for the ratio of polarized and unpolarized favored

quark fragmentation functions $H_1^{\perp(1)q}(z)/D_1^q(z)$. The projected accuracies, assuming flavor independence, are shown in figure 3.2.2.

Option (2) (cf. p. 168) focuses on the interference between the s - and p -wave of the two-pion system around the ρ mass. Via the interference effect the polarization information of the quark is contained in $\vec{k}_+ \times \vec{k}_- \cdot \vec{S}_\perp$, where \vec{k}_+ , \vec{k}_- , and \vec{S}_\perp are the three-momenta of π^+ , π^- , and the nucleon's transverse spin, respectively. The corresponding asymmetry depends on the chirally odd $s - p$ wave interference quark fragmentation function $\delta\hat{q}_I(z)$ which is unknown at present, although it can be measured in e^+e^- experiments as well. Theoretically, there is an upper bound for this function that allows the estimation of the maximum possible asymmetry at TESLA-N. The asymmetry is predicted to have different signs below and above the ρ -meson mass. To avoid averaging to zero, it must be considered separately in two regions of the two-pion mass, e.g. 0.51-0.74 GeV and 0.78-0.97 GeV. The corresponding expectations for the asymmetry are shown in figure 3.2.3.

At TESLA-N luminosity and kinematic range will be large enough to perform a full flavor separation of both the distribution and the fragmentation functions of the transversely polarized nucleon. This requires measurements of asymmetries in different final states, as well as Q^2 -values that are large enough for factorization to be effective. TESLA-N will meet these requirements.

3.2.2 Helicity Distributions

The luminosity and kinematic range available at TESLA-N will allow the determination of the longitudinal spin structure function $g_1(x, Q^2)$ through inclusive measurements with unprecedented accuracy. The structure function $g_1(x, Q^2)$ represents a particu-

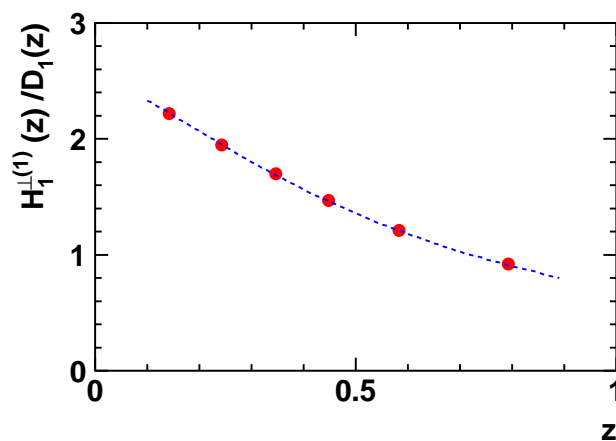


Figure 3.2.2: Projected accuracy of the ratio $H_1^{\perp(1)}(z)/D_1(z)$ of polarized and unpolarized fragmentation functions. The statistical errors are smaller than the point size.

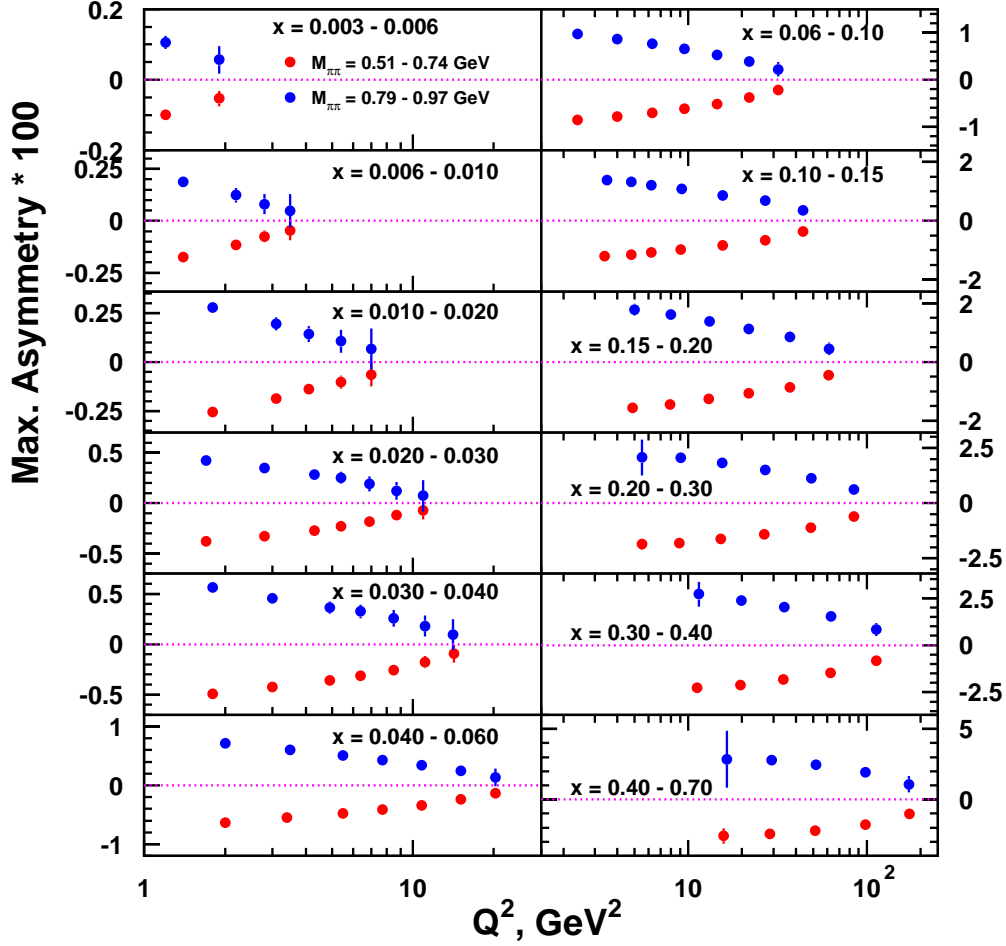


Figure 3.2.3: The maximum asymmetry for the two-pion system as a function of x and Q^2 as it would be measured at TESLA-N with an integrated luminosity of 100 fb^{-1} . Results are shown separately for both two-pion mass regions.

lar combination of the helicity distributions Δu , Δd and Δs and the corresponding antiquark distributions. The projection for $g_1^p(x, Q^2)$ is shown in figure 3.2.4. The anticipated precision in conjunction with the wide kinematic range will allow studies that so far have not been possible. Prominent examples are the determination of ΔG from NLO fits (cf. section 3.2.3), higher twist analyses (cf. section 3.2.4) and a precise determination of the strong coupling constant α_s through the Bjorken sum rule.

SMC [28] and HERMES [29] have provided relevant information on the longitudinally polarized u-quark and d-quark distribution functions. In addition, future HERMES data will allow to constrain $\Delta s(x, Q^2)$, $\Delta \bar{u}(x, Q^2)$ and $\Delta \bar{d}(x, Q^2)$, however, with limited precision. Semi-inclusive measurements with high precision can be provided at

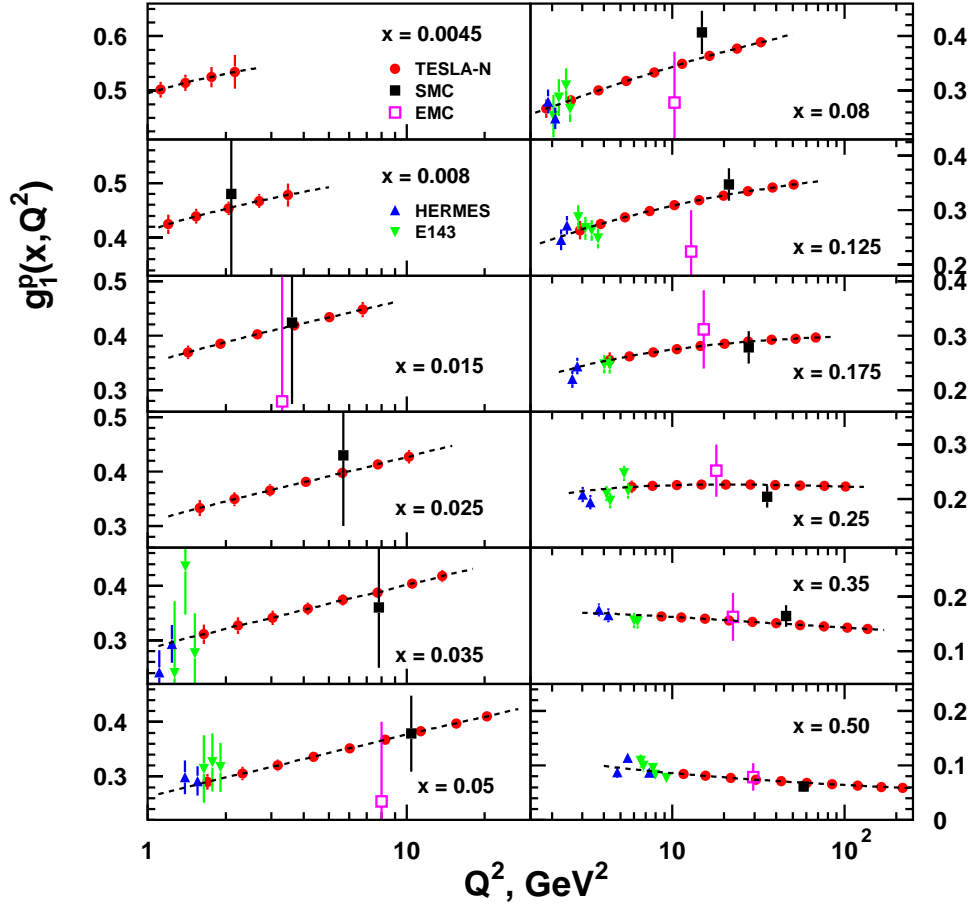


Figure 3.2.4: Projected statistical accuracy for a measurement of $g_1^p(x, Q^2)$ at TESLA-N, based on a luminosity of 100 fb^{-1} and a minimum detector acceptance of 5 mrad . Two EMC/SMC data points are outside of the shown vertical range.

TESLA-N, due to the increased luminosity and kinematic range.

For example, a precise measurement of $\Delta \bar{d}(x, Q^2) - \Delta \bar{u}(x, Q^2)$ will strongly influence the picture of the nucleon structure in general. This is the direct parallel to the unpolarized case, where the difference $\bar{d}(x, Q^2) - \bar{u}(x, Q^2)$ was measured to be large. An even larger effect is actually predicted for $\Delta \bar{d}(x, Q^2) - \Delta \bar{u}(x, Q^2)$ by e.g. the chiral quark-soliton model [30]. The same holds true for the polarized strange-quark distributions Δs and $\Delta \bar{s}$ which has been an unresolved central issue in the discussion of the nucleon spin structure for more than 10 years.

3.2.3 Polarized Gluon Distribution

The polarized gluon distribution $\Delta G(x, Q^2)$ of the nucleon is essentially unknown as of today. There is a variety of approaches to determine $\Delta G(x, Q^2)$; the most promising methods in polarized DIS are the analysis of pairs of high- p_\perp hadrons [31], and open charm production [32].

A first indication for the sign and approximate size of $\Delta G(x)$ has already been provided by HERMES through the analysis of quasi-photoproduced pairs of ‘high’- p_\perp hadrons [33]. However, the analysis has to rely on phenomenological event generators, which, due to the limited c.m. energy, are run at the limits of their validity range. The size of the resulting theoretical error is controversial, but it is generally not expected that HERMES can provide a precision measurement of $\Delta G(x)$ along these lines. In contrast, for the considerably higher energies of TESLA-N these problems should be tractable. The anticipated COMPASS results will provide very valuable information, but a high precision experiment like TESLA-N is eventually needed for a reliable result. At RHIC, the determination of $\Delta G(x)$ is also not without problems in view of the great theoretical uncertainties in direct photon and heavy quark pair production and accounting for the fact that the detectors PHENIX and STAR are optimized for heavy-ion physics. An independent determination in lepton-nucleon scattering is clearly needed to reach solid ground. Up to now, no projections exist for measurements of the Q^2 -dependence of the polarized gluon distribution.

The projected TESLA-N accuracy to measure $\Delta G(x)/G(x)$ is shown in figure 3.2.5, in comparison to projected accuracies for HERMES, COMPASS and RHIC. In comparison to COMPASS, TESLA-N will have at least 50 times more statistics (cf. section 3.3.4). Hence it will be the only envisaged polarized lepton-nucleon scattering experiment capable to determine the ratio $\Delta G(x)/G(x)$ over a wide range of x with an impressive statistical accuracy; systematic uncertainties have still to be studied (cf. caption). The overall x -range and the projected precision of the STAR measurement at RHIC are comparable to the TESLA-N projection. For completeness it has to be mentioned that high accuracy at large x can also be realized at JLAB, but their ‘theoretical’ systematic error can hardly be reduced below that at HERMES because of their low center-of-mass energy.

In addition to the direct methods described above, QCD NLO fits to the spin structure function $g_1(x, Q^2)$ are able to yield a parametric form of $\Delta G(x, Q^2)$. However, no QCD fit to the existing data has yet been able to deliver a statistically convincing determination of even the first moment $\Delta G(Q^2) = \int_0^1 dx \Delta G(x, Q^2)$. At present, this indirect determination of $\Delta G(x, Q^2)$ is problematic, because at lower energies the effects of the evolution due to $\Delta G(x, Q^2)$ cannot be cleanly separated from higher-twist effects. A precision measurement of $g_1(x, Q^2)$ at TESLA-N will dramatically enlarge the accuracy and the kinematic range, as can be concluded from figure 3.2.4. To obtain a projection for the first moment, a QCD NLO fit was performed in the $\overline{\text{MS}}$ scheme using all DIS data published until summer 2000, giving a result of 0.43 ± 0.21 (stat.), at the scale of $Q^2 = 1 \text{ GeV}^2$. The resulting structure function $g_1(x, Q^2)$, in its parametric form, was then evolved into the kinematical region of TESLA-N and then used as

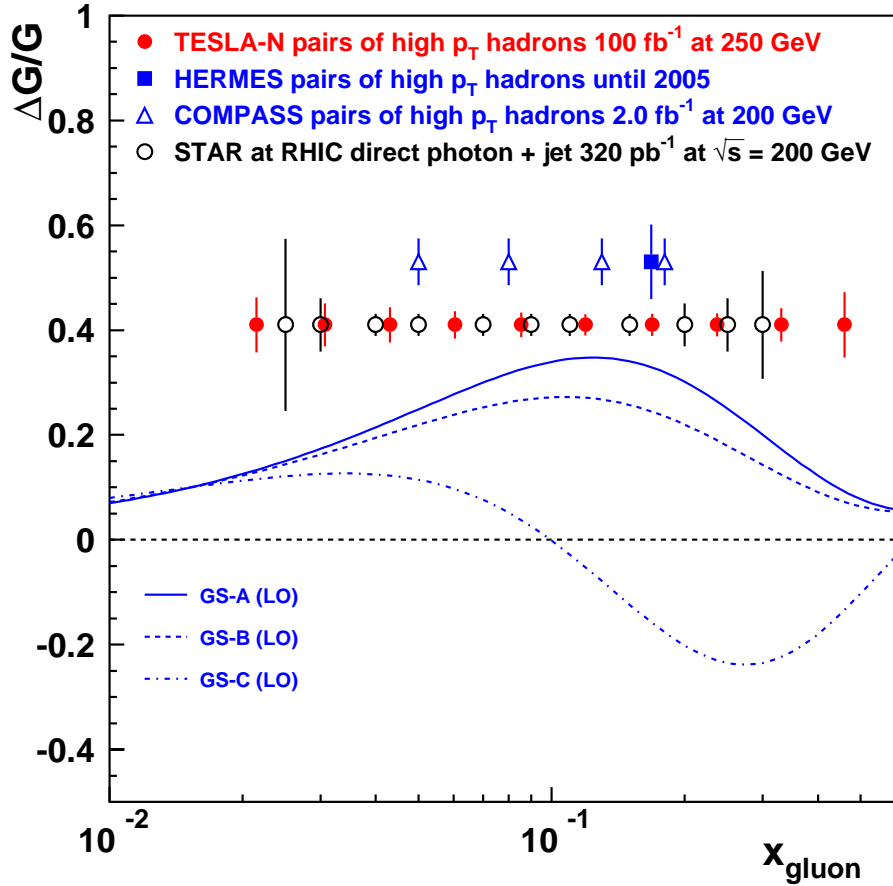


Figure 3.2.5: *Projected statistical accuracies for the measurement of $\Delta G(x)/G(x)$, based on an integrated luminosity of 100 fb^{-1} , in comparison to projections from RHIC [34], HERMES [35], and COMPASS [36]. A study of the systematic uncertainties due to the x_{gluon} reconstruction procedure and due to QCD background (right-most points) has not yet been completed. The phenomenological predictions [37] were calculated for $Q^2 = 10 \text{ GeV}^2$.*

additional input data for two new fits. Adding data that correspond to 100 fb^{-1} using a proton target improves the statistical accuracy down to ± 0.06 . An additional data set obtained with 100 fb^{-1} on a deuteron target yields a further improvement down to ± 0.04 . This additional deuteron data set considerably improves the statistical accuracy in the determination of the non-singlet quark distribution in the neutron, when comparing to existing data.

A comparison of this indirect determination of $\Delta G(x, Q^2)$ with the above described direct determinations will allow important consistency checks that in the end will lead to a reliable picture of how the gluons contribute to the nucleon spin.

Last, but not least, results for the *unpolarized* gluon distribution at large x are

of great importance to many searches for new physics and to the uncertainties in estimating conventional cross sections in the large- x region for background processes to the Higgs-search at LHC. Present fits to the unpolarized gluon distribution in the region $x > 0.15$ are still dominated by the old and partially inconsistent data of NA14/2, E691 and E687. The most suitable processes to determine the unpolarized gluon distribution at large x are, as in the polarized case, heavy-quark pair production and the production of pairs of high- p_{\perp} hadrons. These measurements will automatically also be available at TESLA-N.

3.2.4 Higher Twist

TESLA-N will be able to address a central issue of the present-day QCD discussions in inclusive and semi-inclusive physics, namely the role of higher twist. It is clear that the applicability of perturbative QCD will eventually come to an end for low photon virtualities due to the increase of higher-twist effects. They hence play a crucial role in relating conventional perturbative QCD results to the bulk of hadron phenomenology. Today it is difficult to predict at which scales higher-twist contributions become important in the small- x and large- x domain of the different observables since the relevant parameters controlling them are non-perturbative. Currently this is not even known for the well measured unpolarized structure function $F_2(x, Q^2)$. In addition, higher-order QCD corrections and higher-twist corrections cannot be dealt with independently (cf. e.g. [38, 39, 40, 41]). The knowledge of these corrections is also important for the presently available polarized data, which lie mostly in the Q^2 -domain of only a few GeV^2 . Obviously, a higher-twist analysis based on high precision data for $g_1(x, Q^2)$ could help to clarify the situation substantially. This would also be important for spin physics in general, because it would reduce in present-day fits the uncertainties due to neglected higher-twist contributions.

A precise measurement of the spin structure function $g_2(x, Q^2)$ remains a major challenge for future polarized DIS experiments with transverse target polarization. The measurements obtained so far [42] will be improved by TESLA-N, extending the measurements down to x -values of $5 \cdot 10^{-3}$. Besides its twist-2 contribution $g_2(x, Q^2)$ contains a twist-3 term the isolation of which is important. At lowest order in QCD twist-2 and twist-3 contributions to $g_1(x, Q^2)$ and $g_2(x, Q^2)$ are connected by integral relations [43, 44, 45, 46] which can be tested in this way. Moreover, if the Q^2 -dependence of the twist-3 contribution to $g_2(x, Q^2)$ can be isolated the validity of new QCD evolution equations, cf. e.g. [47], can be tested. Both issues provide new and important tests of QCD.

There are several more distribution and fragmentation functions for polarized electron-nucleon scattering. Mulders and collaborators have given a classification of all twist-2 and twist-3 functions [11, 12]. From a purist's point of view it can be argued that all of them are equally important, as they all test different features of nucleon structure and fragmentation dynamics. A more phenomenological point of view would be to concentrate on those that have an intuitive physics significance or probe specific QCD dynamics. Presently a lot of theoretical work is invested into the development of such

an intuition (cf. e.g. [48]).

3.2.5 Fragmentation Functions

A comprehensive study of fragmentation processes is of great value in itself. To make full use of the data collected by the B-factories and (partly) LHC will require a good understanding of many different fragmentation processes. The high quality DIS data generated by TESLA-N would allow the fine-tuning of the fragmentation codes used for this purpose. Contemporary semi-inclusive analyses usually assume knowledge of the fragmentation functions, as obtained from $e^+e^- \rightarrow hX$, and use these as a tool in studying the parton distribution functions. However, several new analyses of the e^+e^- data have appeared [51, 52, 53]. All agree very well with the data, yet their derived fragmentation functions differ significantly; in some regions of z by 40-100 %. As a result, it has become crucial to use semi-inclusive DIS data to measure parton distributions as well as fragmentation functions. There is no problem of principle; all that is required is a sufficiently large amount of high quality data [54]. While this is beyond present day experiments, TESLA-N should be able to stand up to the challenge. However, no specific projections have been worked out yet.

3.2.6 Specific Deuteron Structure Functions

In deep-inelastic scattering on a polarized spin 1 target new structure functions are involved that do not appear for a spin $\frac{1}{2}$ target. At leading twist the new functions are $b_{1(2)}(x, Q^2)$ [49] and $\Delta(x, Q^2)$ [50]. These hitherto completely unknown structure functions measure the extent to which the deuteron is not a trivial bound state of proton and neutron. $\Delta(x, Q^2)$ is especially interesting since it describes a flip of the photon helicity by two units. It probes the gluonic components of the deuteron wave function which cannot be identified with any contribution from the constituent nucleons or virtual pions.

The structure functions $b_{1(2)}(x)$ are accessible when the polarized electron beam is scattered off longitudinally polarized deuterons. The measurement of $\Delta(x, Q^2)$ requires an unpolarized electron beam and transversely polarized deuterons. In the latter case a characteristic azimuthal angular dependence of the cross section, $d\sigma \sim \cos 2\phi$, is predicted.

All these specific deuteron structure functions are expected to be of rather small size and thus a high luminosity polarized experiment as TESLA-N appears to be the ideal place to access information on this non-trivial parton composition of the deuteron.

3.3 Layout of the Experiment

3.3.1 Polarized Target

One of the main ingredients of the TESLA-N apparatus is the polarized target. To reach the required high luminosity with a small fraction (20 nA, cf. section 3.3.2) of

the total TESLA current (45 μA) a polarized solid state target of about 1 g/cm² areal density was chosen, similar in design to the one used at SLAC [55].

The polarized target will consist of a ⁴He evaporator cryostat, a 5 T Helmholtz-type magnet and a 140 GHz microwave system for permanent Dynamic Nuclear Polarization. The polarization is measured by Nuclear Magnetic Resonance. The maximum allowed heat load on the target is limited by the cooling power of the evaporator cryostat to about 1 W at a temperature of 1 K. The total heat load on the target due to the beam for a current of 20 nA has been calculated to be only about 50 mW [56]. Hence, there should be no basic problem with the cooling. Because 1 K is rather warm on the temperature scale of polarized targets, a strong magnetic field must be chosen to achieve reasonably high polarization values. The magnetic field is limited to 5 T, because the power of microwave sources with frequencies higher than 140 GHz is insufficient today. A symmetric Helmholtz design of the magnet combines excellent homogeneity with large opening angles for both, longitudinal and transverse polarization. The two main criteria for the choice of the target material are low dilution by unpolarized nucleons and resistance against radiation damage with respect to the intense TESLA beam. Therefore NH₃ ($P_T = 0.8$, $f = 0.176$) and ⁶LiD ($P_T = 0.3$, $f = 0.44$) presently appear as the best choices to study electron scattering off polarized protons or deuterons.

A large number of physics questions can be addressed in high luminosity running with different *unpolarized* nuclear targets. Targets with very high atomic numbers can be easily constructed forming appropriately thin foils. In this case electron beam currents may be possible that are considerably higher than 20 nA.

3.3.2 Polarized Electron Beam

The electrons for TESLA-N will be accelerated together with the positrons in the north arm of the TESLA main accelerator. This ‘opposite charge option’ was chosen to be able to realize a separation between the beam for the eN-experiment and the main beam by a static magnet system. This system would have a length of about 150 m and be located upstream of the separation for the two main interaction points (cf. figure 3.3.5). The beam energy initially will be 250 GeV; energies up to 500 GeV may be possible in a later phase of TESLA.

Both TESLA arms are planned to run with a 5 Hz macropulse repetition rate for e⁺e⁻-operation. Additional 5 Hz will be run along a limited fraction of the south arm to facilitate FEL operation. The corresponding time structure of the polarized electron beam is illustrated in figure 3.3.1. The 0.5 % north arm duty cycle in conjunction with the basic machine frequency of 1.3 GHz has most severe consequences for the proposed experiment. Using the same time structure as foreseen for the e⁺e⁻-experiment, i.e. one bunch of 20 ps length crossing the target every 337 ns, would result in as much as a few hundred quasi-real photo-production events within these 20 ps. This is an unacceptably high rate for an eN-experiment, because the scattered electron must be uniquely assigned to the hadrons produced in the same interaction. To minimize the number of multiple events per beam crossing while maximizing the luminosity, it is foreseen to fill every bucket of the bunch train (one every 0.77 ns), while limiting the

beam current to 20 nA. This corresponds to 20k electrons per bunch and to 6.2 million bunches per second crossing the TESLA-N target.

Although being beyond the scope of the present study, it should be noted that a few improvements for eN-operation appear to be feasible.

1. Also along (part of) the north arm a 10 Hz macropulse repetition rate could be used. This would double all performance figures for e⁻N-operation.
2. Two intermediate ejection points are technically feasible. For the FEL, i.e. in the south arm, there will be 2 ejection points (at about 25 and 50 GeV). By RF tuning a dynamic range of about 2 will be routinely available, such that de facto energies 12.5 to 25 GeV (at point 1) and 25 to 50 GeV (at point 2) can be 'dialed'. It is technically feasible to have two ejection points also in the north arm at e.g. 50 and 100 GeV. This would allow the selection of any energy between 25 and 100 GeV in addition to the full energy of 250 GeV.

Physics requirements suggest to study e⁺N-interactions as well. It is technically unproblematic to install an additional (low intensity) positron source besides the separate electron source that is already required for e⁻N operation. Since the 'eN-positrons' will need a kicker magnet to be separated from the 'collider-positrons', only the extra 5 macro pulses in the 10 Hz 'a la FEL' mode could be used, thus limiting the duty cycle to 0.5%. Presently no solution is known to obtain polarized positrons in such a

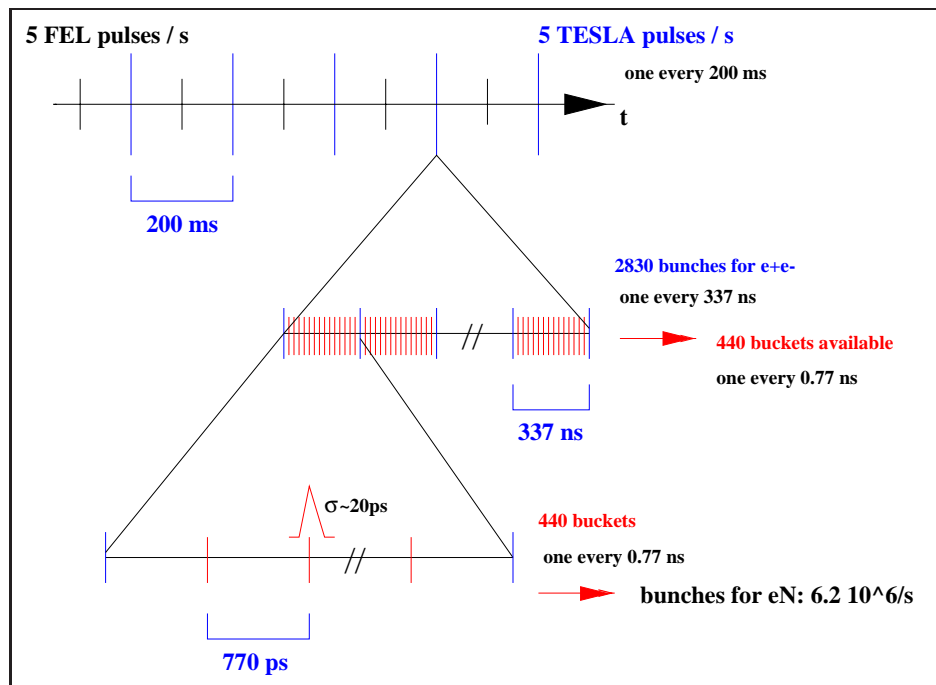


Figure 3.3.1: Time structure of the polarized electron beam in TESLA (south arm) fully exploiting the 1.3 GHz machine frequency.

configuration. The production of polarized positrons requires > 150 GeV electrons, as planned for TESLA e^+e^- operation. However, at present it appears not realistic to assume that this system could also deliver polarized positrons for eN.

An electron current of 20 nA constitutes only about 0.04% of the main beam current. Therefore the energy consumption for beam acceleration at TESLA-N can be considered to be almost negligible. This advantage implies the drawback that monitoring of the small electron beam cannot be done together with that of the high current beam in the main linac, but only before and after acceleration. This requires further studies.

3.3.3 Overview of the Apparatus

In a fixed-target electron-nucleon scattering experiment at 250 GeV, acceptable resolutions in particle momentum and scattering angle may only be achieved by using a multi-stage spectrometer. A schematic sketch of a possible TESLA-N apparatus is shown in figure 3.3.2. All three stages of the spectrometer will use large dipole magnets (SM1-3) for momentum analysis. As can be seen from the figure, the overall dimensions of the TESLA-N apparatus are comparable to those of COMPASS [3] because the kinematics of both experiments are similar.

Most hadrons are to be measured in Stage 1, while most of the scattered electrons and, in addition, a part of the leading hadrons will be detected in Stage 2. For both Stage 1 and 2 electron/hadron separation, hadron identification, and electron/photon separation will be very important and hence their design looks similar to the HERMES spectrometer [57]. Stage 3 is required to detect scattered electrons down to the lowest possible angles and will need adequate tracking capabilities combined with some electron/hadron separation.

While at COMPASS a thick target is traversed by incoming muons, the relatively thin solid state target planned for TESLA-N will be hit by electrons that cause a much higher rate of bremsstrahlung. Its rate amounts to about 20% of the incoming electron rate at a target thickness of 1 g/cm^3 . Due to the magnetic deflection, the resulting lower momentum electrons form a ‘sheet of flame’ on their way down the spectrometer. While the width of the sheet-of-flame itself is below 1 mm, its effective width corresponds to a possible wobbling area of the incoming electron beam that must be of the order of a few mm to match the target size. The electrons and the bremsstrahlung photons must not meet any material in their way to avoid background showers. The safest way to ensure this is to provide a vacuum chamber that contains not only the high energy beam electrons, but also the sheet-of-flame electrons and the radiated photons, as well as the synchrotron radiation produced in the three spectrometer magnets and the target magnet. Instead of only a vacuum pipe an extended vacuum vessel appears to be necessary. This vessel forms a narrow ‘slit’ whose height (in the bending plane) is increasing along the spectrometer, while its width can be as low as ± 2 cm.

The sheet-of-flame must be oriented towards a beam dump close to the experiment. To this end, the dipole fields in SM1-3 should be oriented horizontally and the above mentioned vacuum vessel extends vertically down from the beamline. As a further con-

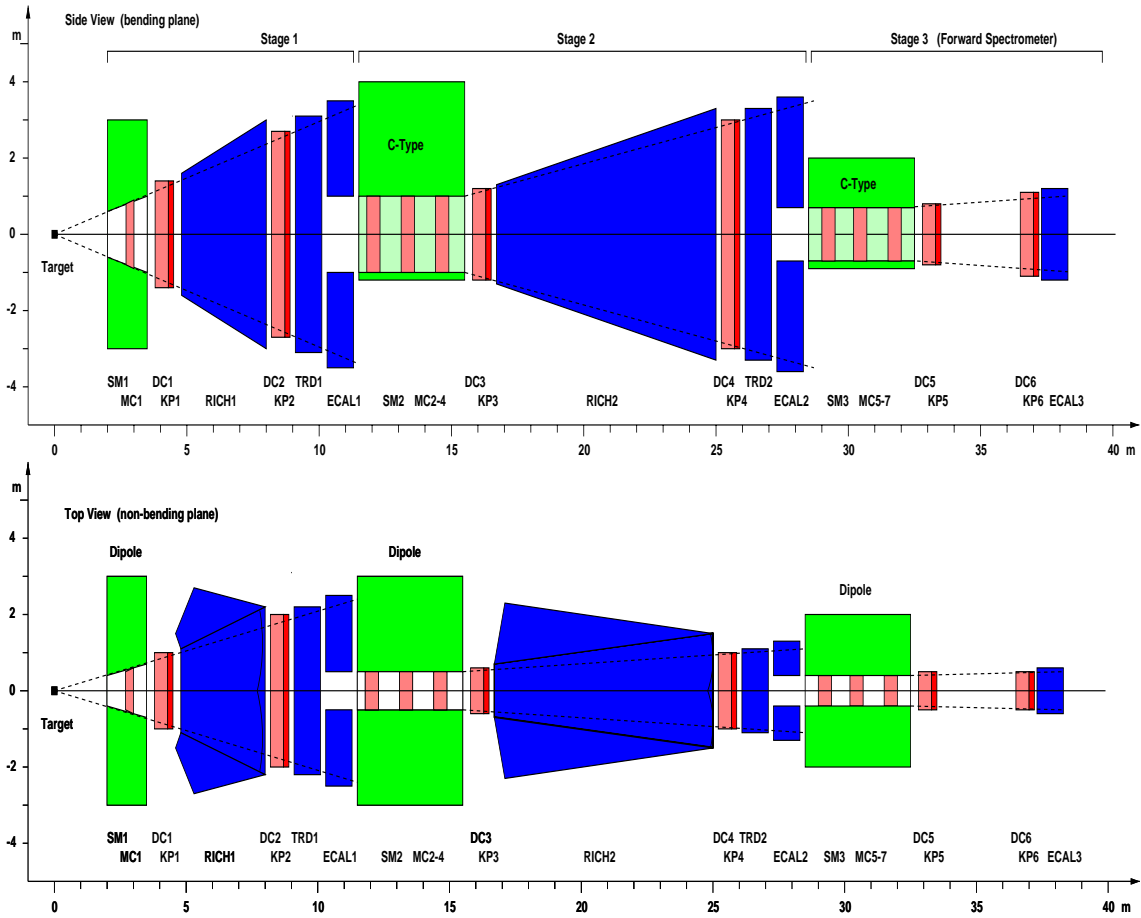


Figure 3.3.2: Schematic side view and top view of the envisaged TESLA-N apparatus. For an explanation of the acronyms see the text.

sequence, SM2 and SM3 will most likely be C-type magnets. The integrated magnetic fields will be 2 Tm for SM1 and 5 Tm each for SM2 and SM3.

The envisaged very high luminosity of the experiment leads to very high interaction rates, so that a few hundred charged tracks can be expected per ‘recorded event’. Here ‘recorded event’ stands for the pile-up of physics events over the typical integration time of the tracking detectors (cf. section 3.3.4). These conditions make it impossible for a single tracking device to have both the required very fast response and the necessary position resolution. Therefore it is planned to combine fast tracking detectors (e.g. scintillating fibres), so-called ‘key planes’ (KP1-6), with precise tracking detectors. These detectors could be drift chambers (DC1-6). Similar to COMPASS, where a 2 ns resolution was shown recently [58], the fast but less precise detectors will serve to ‘snapshot’ events on the bunch level which cannot be resolved by the slow but precise detectors (‘fast-slow tracking’).

The first section of SM1 will bend out the particles with momenta below a few hundred MeV. Hence a first slow and less precise position detector (‘magnet cham-

ber’, ‘MC1’) may possibly be already accommodated within the gap of SM1. Since Stage 1 of the spectrometer will analyse predominantly particles in the momentum range of 1 to some 10 GeV, where multiple scattering is still an issue, the thickness of all Stage 1 tracking detectors must be optimized against their precision and possibly a large low pressure container will be used. Choosing 150 ns as a representative integration time for the ‘slow’ detector, the cell size of all detectors must be small enough to deal with the expected high occupancies. The requirements for the Stage 2 detectors are expected to be less severe.

The electron-hadron separation in both Stage 1 and 2 will be provided by combinations of transition radiation detectors with electromagnetic calorimeters (TRD1/2, ECAL1/2), complemented by ring-imaging Cerenkov detectors for hadron identification (RICH1/2). For Stage 3 only an electromagnetic calorimeter (ECAL3) is foreseen. In addition, the gaps of SM2 and SM3 can be instrumented with suitable tracking detectors, e.g. proportional chambers (MC2-7), to minimize acceptance losses. Both ECAL1 and ECAL2 must not cover the entrance cone to the next spectrometer stage, while all other detectors in Stage 1 and 2 have to be designed with the central slit for the through-going flux of photons and high energy electrons, as discussed above.

Certain reaction channels greatly benefit from additional kinematic constraints that can be obtained by measuring ‘recoil’ particles. In the given kinematics, recoil particles leave the target under laboratory polar angles of a few tens of degrees. Their detection can hence be accomplished by a small-size barrel detector [56] surrounding the target and/or forward ‘wheels’ similar to those developed at HERMES [59]. The target holding field may even allow for some momentum analysis, while some particle identification may be possible through ionization signals.

3.3.4 Luminosity and Acceptance

An areal target density of 1 g/cm² of polarizable material that is hit by bunches carrying 20k electrons each, leads to a maximum possible luminosity of 12 mb⁻¹ per bunch. With the above explained 6.2 million bunches per second this corresponds to a luminosity of $7.5 \cdot 10^{34}$ cm⁻² s⁻¹, which represents the maximum value possible with the present TESLA design.

Table 3.3.1 shows the envisaged luminosity of TESLA-N in comparison to other current or planned electron scattering facilities. The first entry corresponds to the present TESLA design with a 5 Hz macropulse repetition rate in the north arm; the second entry applies if a (technically feasible) rate of 10 Hz is assumed (cf. section 3.3.2). When comparing luminosities of fixed-target experiments (upper panel) and collider experiments (lower panel), the degree of polarization and purity (= fraction of the polarized material) of the involved nucleon have to be taken into account. For example, when comparing a polarized NH₃-target and a circulating proton beam, the effective luminosity of the polarized fixed-target experiment is lower by a factor of about 25.

Adopting a conservative ansatz for efficiencies, namely a combined up-time of accelerator and experiment of 0.33 in conjunction with an efficiency of the experiment of 0.75, results in the conservative overall efficiency factor of 0.25. This factor leads

Experiment	c.m. Energy [GeV]	Luminosity [$\text{cm}^{-2} \text{s}^{-1}$]
TESLA-N	22	$7.5 \cdot 10^{34}$
TESLA-N (10 Hz)	22	$1.5 \cdot 10^{35}$
COMPASS	20	$5.0 \cdot 10^{32}$
SLAC (incl.)	$5 \div 10$	$5.0 \cdot 10^{34}$
HERMES (unpol.)	7.2	$4.0 \cdot 10^{33}$
HERMES (pol.)	7.2	$2.0 \cdot 10^{31}$
ELFE@CERN (unpol.)	7	$1.0 \cdot 10^{38}$
ELFE@CERN (pol.)	7	$5.0 \cdot 10^{35}$
HERA $\bar{e}p$	318	$1.0 \cdot 10^{31}$
HERA eA	150	$1.0 \cdot 10^{30}$
eRHIC	100	$2.0 \cdot 10^{32}$
EPIC	31	$1.0 \cdot 10^{33}$

Table 3.3.1: Comparison of luminosities and c.m. energies for current and planned electron scattering facilities

to maximum achievable integrated luminosities for TESLA-N of 1.6 fb^{-1} per effective day, 50 fb^{-1} per effective months, and 600 fb^{-1} per effective year. The term ‘effective’ was chosen here to characterize a running period during which both accelerator and experiment operate routinely including all usually occurring day-by-day problems.

At maximum luminosity every bunch (one every 0.77 ns) produces on average 0.2 quasi-real-photoproduction events with $\nu > 3 \text{ GeV}$. For an average multiplicity of about 3 detected charged hadron tracks per physics event this corresponds to about 100 hadron tracks in Stage 1 per recorded event. The typical integration time and thus the length of the recorded event is assumed to be 150 ns, corresponding to about 200 bunches. The additional rate from Möller electrons with an energy above 1.5 GeV amounts to about 1 per bunch, or about 200 electron tracks per recorded event. However, Möller electrons reaching the spectrometer can be uniquely distinguished from DIS electrons with $Q^2 > 1 \text{ GeV}^2$ by their kinematics. Only about one DIS event with $Q^2 > 1 \text{ GeV}^2$, $W^2 > 4 \text{ GeV}^2$ and polar angles above 5 mrad will be contained in one recorded event.

A crucial question for the analysis of DIS events is whether they can be cleanly identified or whether they are mixed with other events. For the above quoted 0.2 photoproduction events per bunch about 18% of all DIS events will be accompanied by a photoproduction event produced by the same bunch. Off-line cuts on the total deposited energy, the track multiplicity and the energy of the leading hadron have to be used to identify and remove these events. From preliminary considerations it is expected that in the end this multiple event fraction for DIS events can be safely reduced to a level of about 1% or less.

In certain areas more work has to be invested to solidify the assumptions made above:

i) It is presently assumed that a time resolution of 0.77 ns can be realized in the future for the fast tracking detectors at TESLA-N. As it was proven recently, today’s

technology already allows to reach 2 ns [58]. In a conservative approach a beam current lower by a factor of 3 would have to be assumed.

ii) The method to reduce the multiple event fraction in a DIS event from 18% to the envisaged 1% can only be developed on the basis of a careful Monte Carlo study. There is very little doubt that a factor of 3 can be realized easily. In a conservative approach a beam current lower by a factor of 6 would have to be assumed to arrive at the design value of 1%.

It is anticipated that adequate answers can be found for these questions. To leave a ‘safety margin’ until the above questions will have been answered, it was decided to assume for all physics projections a reduction of the beam current, i.e. consequently also of the luminosity, by a factor of 6. This decrease in beam current will relieve both point i) and ii). In the most conservative approach, where both i) and ii) are taken at their lower limits, the beam current and thus the luminosity for the physics projections needs not to be reduced further than the factor of 6, because another factor of 3 can be gained by running for three years instead of one. Altogether it thus appears to be a well-founded starting point that 100 fb^{-1} per effective year is the conservative integrated luminosity of TESLA-N. This number was taken to calculate all projected statistical uncertainties throughout this document. It appears worth noting that it is still a factor of 50 above the maximum achievable integrated luminosity of 2 fb^{-1} , presently planned for one effective year of COMPASS running with the same overall efficiency factor of 0.25.

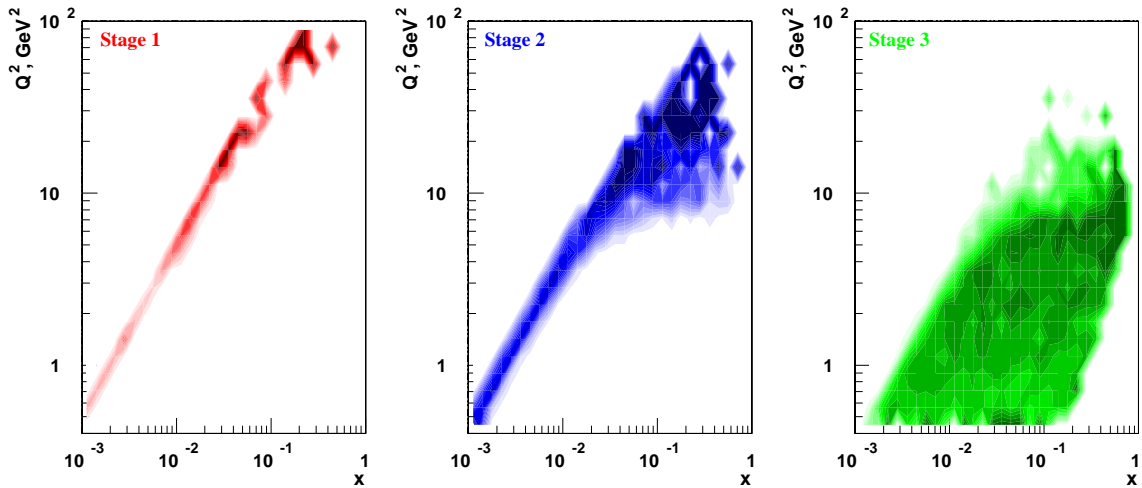


Figure 3.3.3: Acceptance of the TESLA-N spectrometer for the scattered electron.

The acceptance of the TESLA-N spectrometer for the scattered electron in the (x, Q^2) plane is shown in figure 3.3.3. Electrons with high Q^2 ($>10 \text{ GeV}^2$) are predominantly detected in Stage 2, while low- Q^2 electrons ($<10 \text{ GeV}^2$) are detected in Stage 3. Figure 3.3.4 shows the acceptance for leading hadrons as a function of $z = E_h/\nu$. More than 80% of all leading hadrons are detected in Stage 1 of the spectrometer while about 40% of them are detected both in Stage 1 and 2 (for $z > 0.15$). As a result,

these hadrons are detected with good momentum resolution independently of the vertex reconstruction. The opening of SM1 limits the acceptance to $\theta_x \leq 225$ mrad and $\theta_y \leq 280$. The lowest possible detection angle θ_{min} is about 5 mrad for momentum analysis within Stage 2 including the detection plane in front of SM 2. If Stage 3 is used including the detection plane in front of SM 3, θ_{min} can be reduced to values as low as 2-3 mrad. These approximate figures are based on a width of the vacuum vessel of ± 2 cm and a width of the DC frame next to it of 3 cm. For electrons, θ_{min} directly determines the lowest reachable Bjorken- x .

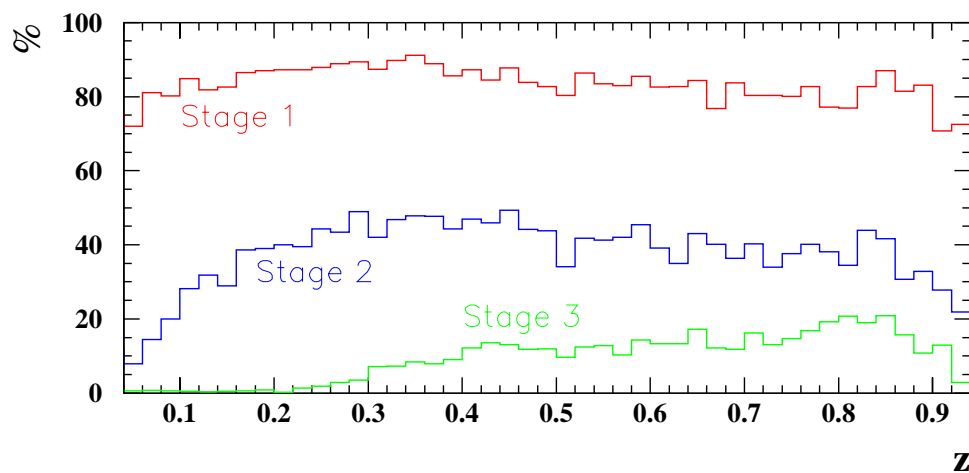


Figure 3.3.4: Acceptance of the TESLA-N spectrometer for the leading hadron.

3.3.5 Resolution in Kinematic Variables

Reliable values for the individual detector resolutions are not yet worked out. A momentum resolution on the level of 0.5 % appears to be a reasonable assumption. It can be achieved in spectrometer Stage 2 for tracks with momenta below 100 GeV, if a (realistic) position resolution of about 100 μm per space point is available. A similar momentum resolution for tracks crossing Stage 3 with momenta up to 200 GeV requires better position resolutions. For the angular resolution 0.3 mrad can be assumed as a preliminary value. The expected spread in the beam momentum (0.1%) is small enough to not affect the resolution in any of the kinematic variables. Possible beam energy losses prior to the interaction have not been studied yet.

The resolutions in the different kinematic variables are characterized by two different effects. On the one hand, the resolution in Q^2 is dominated by the resolution in the electron scattering angle. Only an angular resolution of the order of 0.3 mrad or better can lead to Q^2 -resolutions at the level of a few % at large x -values. None of the other spectrometer resolutions have such a strong impact on the Q^2 resolution. On the

other hand, the resolution in the variables ν , x and z is dominated by the momentum resolution of the spectrometer that, in turn, has little impact onto the Q^2 resolution.

Most of the non-leading and part of the leading hadrons will be detected in the Stage 1 of the spectrometer while the higher-momentum leading hadrons will be measured both in Stage 1 and Stage 2. A moderate *hadron* momentum resolution of the order of 1% would be acceptable, provided that the electron momentum resolution is good enough.

3.3.6 Civil Engineering

The basic layout for the proposed eN-experiment within the mostly fixed TESLA infrastructure is shown in figure 3.3.5. A separate electron gun system is required for

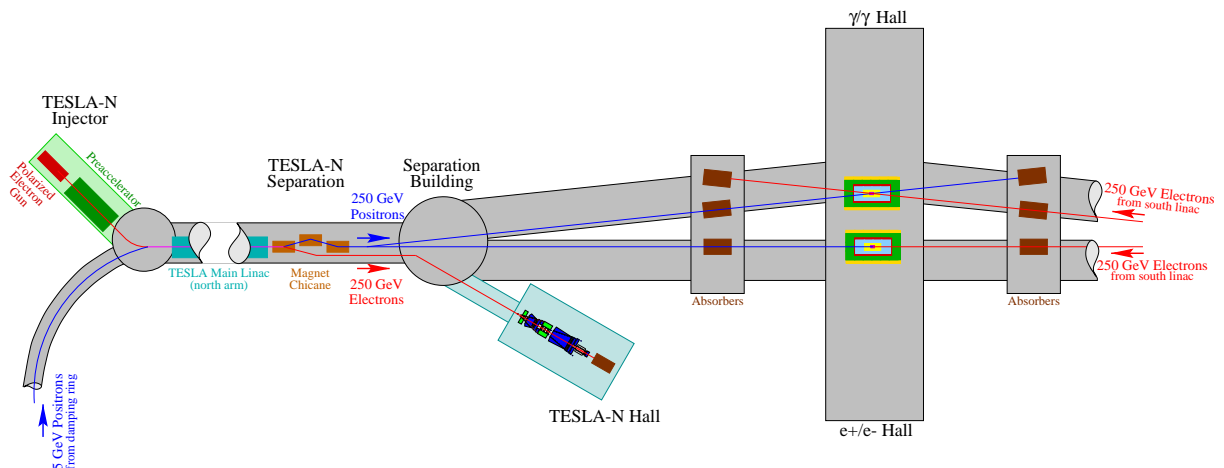


Figure 3.3.5: Schematic top view of the machine-related elements.

TESLA-N at the north end of the TESLA machine. It is envisaged to use a laser driven strained GaAs SLAC-type gun that must be made capable to deliver 20k highly polarized electrons per 0.77 ns. It must be followed by a separate preaccelerator whose end energy and type are under discussion. Present options are a TESLA-type accelerator or a normal-conducting MAMI-type microtron. A short extra tunnel is required from the separation building to the TESLA-N hall. The TESLA-N experimental hall would be placed as far north as the site permits to minimize construction costs. An extra beam absorber is required.

3.4 Summary

This document presents the prospects for a polarized deep-inelastic electron-nucleon scattering experiment at the TESLA facility at DESY. For the first time a complete mapping of the Q^2 - and x -dependence of both the helicity and the transversity dis-

tributions Δq and δq will become possible. Complemented by precise results on the polarized gluon distribution most of the components of the angular momentum structure of the nucleon will be determined with high precision. Hence, the measurements foreseen at TESLA-N will constitute one of the most comprehensive and precise investigations of hadronic properties and tests of QCD techniques in the polarized sector. These measurements will open an access to the hitherto unknown chirally odd operators in QCD and thus greatly improve the understanding of the role of chiral symmetry.

A possible layout for a fixed-target electron-nucleon scattering experiment TESLA-N is presented as well. A separate hall is foreseen north of the main e^+e^- -interaction point. First design considerations for a polarized target, a three-stage spectrometer and a recoil detector are discussed. It is concluded that the experiment is technically feasible, although many aspects of the design require further study.

The proposed deep-inelastic eN-experiment at TESLA constitutes a highly competitive and very cost-effective solution. It will be unique as it combines high luminosity with large center-of-mass energies, using highly polarized electron beams and targets. The possibilities of using unpolarized targets and of experiments with a real photon beam turn TESLA-N into a versatile next-generation facility at the intersection of particle and nuclear physics. Finally, this experiment would be the natural continuation of the HERA tradition at DESY in studying the structure of the nucleon with electromagnetic probes.

Bibliography

- [1] O. Martin, A. Schäfer, M. Stratmann, W. Vogelsang, *Phys.Rev.* **D60**, 117502 (1999)
- [2] HERMES Collaboration, Hermes internal note 00-003, DESY, 2000.
- [3] COMPASS Collaboration, CERN/SPSLC 96-14 (1996).
- [4] R. L. Jaffe, MIT-CTP-2685, hep-ph/9710465, Proc. of the workshop ‘Deep Inelastic Scattering off Polarized Targets: Theory meets Experiment’, DESY Zeuthen, 1997, ed. by J. Blümlein et al., p.167
- [5] P. V. Pobylitsa et al., Bochum University preprint RUB-TPII-15/00
- [6] S. Aoki, M. Doui, T. Hatsuda and Y. Kuramashi, *Phys. Rev.* **D56**, 433 (1997)
- [7] S. Capitani et al., *Nucl. Phys* **B79** (Proc.Suppl), 548 (1999)
- [8] J.C. Collins, *Nucl. Phys.* **B396**, 161 (1993)
- [9] J.C. Collins, S.F. Heppelmann, G.A. Ladinsky, *Nucl. Phys.* **B420**, 565 (1994)
- [10] A.M. Kotzinian, P.J. Mulders, *Phys. Lett.* **B406**, 373 (1997)
- [11] P.J. Mulders, R.D. Tangermann, *Nucl. Phys.* **B461**, 197 (1996)
- [12] D. Boer and P.J. Mulders, *Phys. Rev.* **D57**, 5780 (1998)
- [13] J. C. Collins and G. A. Ladinsky, hep-ph/9411444
- [14] R. L. Jaffe, X. Jin and J. Tang, *Phys. Rev. Lett.* **80** 1166 (1998)
- [15] A. Bianconi, S. Boffi, R. Jakob and M. Radici, *Phys. Rev.* **D62** 034008 (2000)
- [16] V. Barone, *Nucl.Phys.* **A666-667**, 282 (2000)
- [17] X. Ji, *Phys. Rev.* **D 49**, 114 (1994)
- [18] A. Bacchetta, P.J. Mulders, *Phys. Rev.* **D62**, 114004 (2000)
- [19] V.A. Korotkov, W.-D. Nowak, K.A. Oganessyan, *Eur. Phys. J. C*, in press, DESY 99-176, hep-ph/0002268.
- [20] M. Glück et al., *Phys. Rev.* **D53**, 4775 (1996)
- [21] J. Soffer, *Phys. Rev. Lett.* **74**, 1292 (1995)
- [22] O. Martin, A. Schäfer, M. Stratmann, W. Vogelsang, *Phys.Rev.* **D57**, 3084 (1998)
- [23] A. Schäfer and O. Teryaev, *Phys.Rev.* **D61**, 077903 (2000)
- [24] HERMES Coll., A. Airapetian et al., *Phys. Rev. Lett.* **84**, 9047 (2000)
- [25] A.V. Efremov, O.G. Smirnova, L.G. Tkachev, *Nucl. Phys. Proc. Suppl.* **74**, 49 (1999)
- [26] G. Ingelman, A. Edin, J. Rathsman, *CPC* **101**, 108 (1997)
- [27] T. Sjöstrand, *CPC* **82**, 74 (1994)

-
- [28] B. Adeva et al., *Phys. Lett.* **B420**, 180 (1998)
- [29] HERMES Coll., K. Ackerstaff et al., *Phys. Lett.* **B464**, 123 (1999)
- [30] K. Goeke, P.V. Pobylitsa, M.V. Polyakov, D. Urbano, *Nucl. Phys.* **A680**, 307 (2000)
- [31] A. Bravar, D. v.Harrach, A. Kotzinian, *Phys. Lett.* **B421**, 349 (1998)
- [32] M. Glück, E. Reya, W. Vogelsang, *Nucl. Phys.* **B351**, 579 (1991)
- [33] HERMES Coll., A. Airapetian et al., *Phys. Rev. Lett.* **84**, 2584 (2000)
- [34] L. Bland, Proc. of the workshop ‘Physics with a High Luminosity Polarized Electron Ion Collider’ (EPIC99), World Scientific, ed. by L. Bland et al., 255-274 (2000)
- [35] E. Aschenauer, W.D. Nowak, private communication
- [36] J. Nassalski, *Acta Phys. Pol.* **B29**, 1315 (1998)
- [37] T. Gehrmann, W.J. Stirling, *Phys. Rev.* **D53**, 6100 (1996)
- [38] U.K. Yang and A. Bodek, *Eur. Phys. J.* **C13**, 241 (2000)
- [39] A.L. Kataev et al., *Phys. Lett.* **B417**, 374 (1998)
- [40] A.L. Kataev, G. Parente, A.V. Sidorov, hep-ph/0001096
- [41] E. Stein, M. Maul, L. Mankiewicz, A. Schäfer, *Nucl. Phys.* **B536**, 318 (1998)
- [42] E155x Coll., P. Bosted et al., *Nucl. Phys.* **A663–664** 297 (2000)
- [43] S. Wandzura and F. Wilczek, *Phys. Lett.* **B72** 195 (1977)
- [44] A.V. Efremov, E. Leader, O.V. Teryaev, *Phys. Rev.* **D55** 4307 (1997)
- [45] J. Blümlein, A. Tkabladze, *Nucl. Phys.* **B553** 427 (1999)
- [46] J. Blümlein, A. Tkabladze, *Nucl. Phys. B Proc. Suppl.* **79** 541 (1999)
- [47] V.M. Braun, G.P. Korchemsky, and A.N. Manashov, *Phys. Lett.* **B476** 455 (2000)
- [48] M. Anselmino, F. Murgia, *Phys. Lett.* **B483**, 74 (2000)
- [49] R.L. Jaffe, A. Manohar, *Nucl. Phys.* **B321**, 343 (1989)
- [50] R.L. Jaffe, A. Manohar, *Phys. Lett.* **B223**, 218 (1989)
- [51] S. Kretzer, *Phys. Rev.* **D62**, 054001 (2000)
- [52] B.A. Kniehl, G. Kramer, B. Pötter, *Phys. Rev. Lett.* **85**, 5288 (2000)
- [53] L. Bourhis et. al., hep-ph/0009101
- [54] E. Christova, E. Leader, hep-ph/0007303
- [55] K. Abe et al., *Phys. Rev.* **D58**, 112003 (1998)
- [56] J.J.M. Steijger, G. v.d. Steenhoven, NIKHEF 2000-013 (2000)

- [57] K. Ackerstaff et al., *NIM A***417**, 230 (1998)
- [58] D. von Harrach, private communication
- [59] HERMES Collaboration, Hermes internal note 97-032, DESY (1997)

4 ELFE: The Electron Laboratory For Europe

M. Anselmino²¹, K. Balewski⁶, M. Battaglieri⁹, W. Bialowons⁶, N. Bianchi⁸, V. Braun¹⁸, R. Brinkmann⁶, P.H. Bruinsma⁶, N. D'Hose¹⁹, W. Decking⁶, M. Diehl⁶, K. Flöttmann¹⁹, P. Guichon¹⁹, M. Guidal¹⁶, D. von Harrach¹³, R. Jakob²⁴, F. Klein⁵, P. Kroll²⁴, J.M. Laget¹⁹, N. Meyners⁶, W.D. Möller^{1,15}, P. Mulders^{1,15}, E. Nappi², B. Pire¹⁷, H. Pirner¹¹, K. Rith⁷, H. Boer Rookhuizen¹⁸, J. Rümmler¹⁰, D. Ryckbosch¹⁰, E. De Sanctis⁸, A. Schäfer¹⁸, K. Sinram⁶, E. Steffens⁷, V. Vento²², R. Van de Vyver¹⁰, H. Weise¹⁴.

¹ Universiteit van Amsterdam, The Netherlands

² INFN, Sezione di Bari, Italy

³ Universität Bayreuth, 95440 Bayreuth, Germany

⁴ Ruhr-Universität Bochum, Germany

⁵ Rheinische Friedrich-Wilhelms-Universität Bonn, Germany

⁶ DESY, Hamburg and Zeuthen, Germany

⁷ Friedrich-Alexander-Universität Erlangen-Nürnberg, Germany

⁸ INFN Laboratori Nazionali di Frascati, Italy

⁹ INFN, Sezione di Genova, Italy

¹⁰ Universiteit Gent, Belgium

¹¹ Ruprecht-Karls-Universität Heidelberg, Germany

¹² Imperial College, London, UK

¹³ Johannes-Gutenberg-Universität Mainz, Germany

¹⁴ Ludwigs-Maximilians-Universität, München, Germany

¹⁵ NIKHEF, Amsterdam, The Netherlands

¹⁶ INP, Orsay, France

¹⁷ Ecole Polytechnique, Palaiseau, France

¹⁸ Universität Regensburg, Germany

¹⁹ DAPNIA-CEA, Saclay, France

²⁰ St. Petersburg State University, Russia

²¹ INFN, Sezione di Torino, Italy

²² Universidad de València, Spain

²³ Polish Academy of Sciences, Copernicus Astronomical Center, Warszawa, Poland

²⁴ Bergische Universität Wuppertal, Germany

Contents

4	ELFE: The Electron Laboratory for Europe	191
4.1	ELFE	195
4.2	The Physics Programme	195
4.3	Detector	200
4.4	The ELFE@DESY Project	203
	Bibliography	207

4.1 ELFE

ELFE –the acronym stands for Electron Laboratory For Europe– is planned to be a European center for fundamental research on the quark structure of matter. It is the European machine initiative proposed as the optimum experimental tool to probe the structure of the nucleons and nuclei by exclusive and semi-exclusive electron scattering. It will deliver an electron beam with: *i*) an energy in the 20–30 GeV range; *ii*) a large duty cycle; *iii*) a high intensity, guaranteeing a luminosity $\geq 10^{35}$ cm⁻²s⁻¹; *iv*) a good energy resolution, of the order of 10^{-3} ; *v*) a large longitudinal beam polarization, well above 60 %. The beam energy allows a virtuality Q^2 up to 20 GeV², or a momentum transfer t up to 20 GeV², to be reached at a reasonable scattering angle of the electron. The high luminosity and duty factor are needed to face the low probability of exclusive processes and to avoid a prohibitively large number of accidental events. The good energy resolution is mandatory to clearly identify exclusive channels. A highly longitudinally polarized beam allows the spin structure of the various amplitudes to be accessed. No other facilities, either planned or existing, provide such beam characteristics. In this energy range, their beam is either pulsed or the intensity is too low by more than two orders of magnitudes.

ELFE would not only make a new class of exclusive processes dubbed *Deeply Virtual Exclusive Scattering* (DVES) processes accessible, but would also allow one to pursue a rich program for inclusive and semi-inclusive experiments on nucleons and nuclei under ideal conditions. In particular high statistics experiments would allow a detailed decomposition of the (*transverse*) spin-flavour structure of parton distributions and fragmentation functions by utilizing the azimuthal dependencies of the cross sections of polarized semi-inclusive experiments.

Such a new experimental facility would attract a large fraction of the broad community of nuclear and particle physicists who are now investigating the structure of hadrons at high energy laboratories, like CERN, DESY and FNAL or lower energy facilities, like MAMI, GRAAL, ELSA and TJNAF. The consensus is that ELFE is the natural and necessary facility for the long term future of hadronic physics in Europe and that it will allow to understand the interplay between particle and nuclear physics. ELFE would be a large scale international facility, in the tradition of HERA, CERN and TJNAF.

This note is a short summary of comprehensive studies on the Physics Case and Detectors [1], as well as Machine Designs [2, 3, 4] which have been done over the past few years and completed during the last year of the XXth century. We refer the reader to these reports for a more detailed account.

4.2 The Physics Programme

The boundary between particle and nuclear physics remains a challenging scientific field representing one of the frontiers in contemporary nuclear physics. Quantum Chromodynamics has to come up with an explanation of e.g. confinement, the basic simplicity

of the constituent quark model and the pattern of chiral symmetry breaking including the role of the vacuum and its fluctuations. While certain input is expected to come from lattice calculations, experiment will remain the main guiding line for the development of a predictive theory.

The electromagnetic interaction provides one with a unique tool to address these issues. It is a well understood probe and it provides one with a formidable microscope, with a resolution that can be varied from the size of the largest nuclei down to distances much smaller than the size of a single proton.

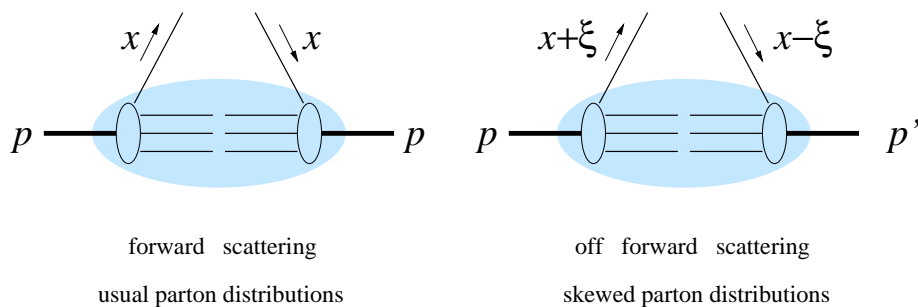


Figure 4.2.1: *The relation between SPDs and usual distribution functions*

The detailed investigation of exclusive processes induced by energetic electrons on hadrons, which is the main mission of ELFE, will allow us to measure properties of the hadronic wave functions which were hitherto inaccessible. The orbital angular momentum of quarks in a hadron or the spin structure of unstable particles are examples for the potential of this approach. A recent theoretical breakthrough, namely the description of DVES by means of so called *skewed parton distributions* (SPDs) [5, 6, 7], makes it possible to achieve this goal in a theoretically controlled manner. SPDs are a generalization of the well-known parton distributions and interpolate between parton densities and form factors. While the usual parton distributions are related to hadronic forward matrix elements, SPDs are related to the off-forward matrix elements. As depicted in Fig. 4.2.1, a parton is emitted with a certain fraction $x + \xi$ of the momentum $(p + p')/2$ of the nucleon and reabsorbed with a different fraction $x - \xi$. Factorisation theorems have been derived that put the description of DVES on a firm theoretical ground [8]. Radiative corrections were calculated up to next-to-leading order [9], twist-3 corrections were studied in detail [10], and the relationship to hadronic wave functions was exploited [11]. In sum, the theoretical level of understanding of SPDs approaches that of the usual distribution functions. This will allow one to study new universal hadron properties with *controllable accuracy*.

As illustrated in Fig. 4.2.2, SPDs describe a variety of different reactions. In the forward limit, i.e. when the proton momenta p and p' become equal, one recovers the usual parton distributions, which thus provide boundary conditions for the SPDs. Via sum rules, i.e. equations fulfilled by integrals over the momentum fraction x , they are also connected to elastic nucleon form factors like F_1 and F_2 (Pauli and Dirac form

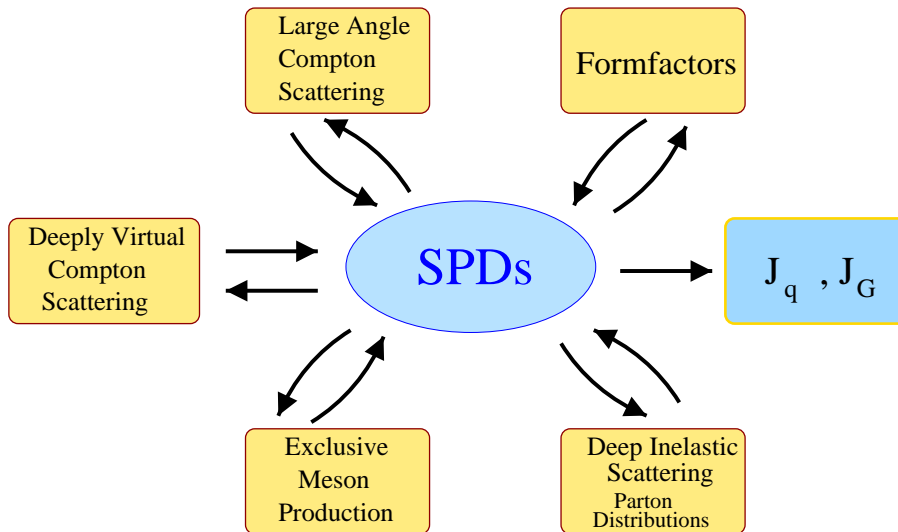


Figure 4.2.2: *Skewed Parton Distributions provide one with a unifying description of many reaction channels, which may lead to the determination of the total angular momentum of quarks, J_q , and gluons, J_G .*

factors). Thus they relate the two types of quantities which so far have been the prime sources of our knowledge of hadron structure: parton distributions, which tell us about the longitudinal momentum structure of a fast-moving nucleon, and form factors, which contain information on its transverse structure, such as its charge radius.

In inclusive reactions, when only the scattered electron is detected and the hadronic final state remains unobserved, the interaction of the hit parton with the hadronic remnants can effectively be neglected. The theoretical description can therefore avoid the complicated question of the final state interaction and reduces the information to one-parton densities.

In elastic scattering processes described by form factors, the struck quark must recombine with the spectators to form the original hadron. This process favours rare configurations where there are no sea quarks and gluons altogether. These special states are simpler than the hadron wave functions as a whole, and a theoretical description again becomes possible.

The physics aspects probed in the two cases are very different and the DVES processes fill the gap between these extremes. In that sense, SPDs interpolate between parton densities and form factors. They involve rich nonperturbative dynamics and give rise to a variety of novel sum rules. For example, the distribution of angular momentum among nucleon constituents can only be accessed through SPDs. Models of SPDs are available and allow one to estimate the experimental accuracy which will be obtainable by ELFE. Lattice-QCD allows one to calculate some leading moments of SPDs and will in the near future further constrain these models.

In addition to the situation shown in Fig. 4.2.1, where a parton is extracted from the nucleon with a certain momentum fraction $x + \xi$ and returned with a different one $x - \xi$, SPDs also have a region in x where a quark-antiquark or a gluon pair is emitted

from the initial proton, changing its momentum from p to p' , see [12, 13, 14]. This illustrates again how SPDs combine information from different processes. As in the case of form factors, SPDs can also describe the transition between different hadrons, allowing one to probe the overlap of their respective wave functions. This opens the way to study baryons not available as beam particles. Prominent examples of transition SPDs appear for the reactions $ep \rightarrow e\Delta^+ \gamma$ and $ep \rightarrow en \pi^+$.

Various constraints based on fundamental symmetries give helpful guidance for the modeling of SPDs. On the other hand the dynamics they contain is extremely diverse. This diversity is reflected in the notable conceptual differences between current models, ranging from constituent quarks and the bag models to studies based on chiral solitons and the instanton vacuum of QCD [11], [15]-[19]. Experimental data on SPDs will elucidate the relationship between these models. The great advantage of SPDs is, generally speaking, that their large information content allows one to connect different observables and to determine quantities of physical interest which cannot be extracted directly from individual observables. The most prominent of these quantities is the total angular momentum of quarks, J_q and of gluons, J_G . For instance, J_q can be expressed as an integral

$$\frac{1}{2} \left[\int_{-1}^1 dx x [H_q(x, \xi, \Delta^2) + E_q(x, \xi, \Delta^2)] \right]_{\Delta^2 \rightarrow 0} = J_q$$

of the quark SPDs $H_q(x, \xi, \Delta^2)$ and $E_q(x, \xi, \Delta^2)$, defined by

$$\begin{aligned} \int \frac{d\lambda}{2\pi} e^{i\lambda x} \langle p' | \bar{\psi}(-\lambda n/2) \gamma^\mu \psi(\lambda n/2) | p \rangle &= H_q(x, \xi, \Delta^2) \bar{U}(p') \gamma^\mu U(p) \\ &+ E_q(x, \xi, \Delta^2) \bar{U}(p') \frac{i}{2M_N} \sigma^{\mu\nu} \Delta_\nu U(p) \end{aligned} \quad (4.2.1)$$

Here $\psi, \bar{\psi}$ are quark fields at the space-time points $\pm\lambda n/2$, n is a 4-vector defined such that $n \cdot (p + p')/2 = 1$ and $n^2 = 0$, and $\Delta_\nu = p'_\nu - p_\nu$ is the momentum transferred to the proton.

Up to now only the spin content of the nucleon originating from quark and gluon spins could be studied. Combining such results with the knowledge of J_q and J_G would determine also the orbital angular momentum contributions and thus provide an essential part for the complete experimental determination of the nucleon spin structure.

Detailed measurements of DVES processes represent the core of the physics programme at ELFE. The interest in DVES, underscored by the rapid theoretical development, originates from the fact that these processes bridge a gap between two different regimes in which the QCD description of hadronic reactions has been successful in the past. In both cases the electromagnetic probe transfers a large momentum via a highly virtual photon to a single parton inside a hadron. This programme includes [1] the study and determination of:

- Deeply Virtual Compton Scattering (DVCS) cross sections;

- Deeply Virtual Meson Production (DVMP) cross sections;
- Meson form factors;
- Exclusive reaction cross sections at large angles.

Current experiments like HERMES, H1 and ZEUS at DESY or planned experiments at CERN and TJNAF are exploring their capacity to address these new observables. The few pioneering results seem to confirm the expectations about their size and symmetries [20]. However, since these experiments either lack luminosity or energy resolution or they fall short in their kinematical range, a quantitative controlled analysis is not possible.

The proposed experimental facility ELFE will overcome these limitations. It has a luminosity of $10^{35} - 10^{38} \text{ cm}^{-2}\text{s}^{-1}$ (depending on the detector set-up) and a beam energy of more than 25 GeV. Its energy resolution of about 0.1%, required by the smallness of the pion mass, allows one to separate individual exclusive channels including the most interesting one – deeply virtual Compton scattering. It can access the range of $x > 0.02$ and reach a “partonic” resolution of $Q^2 \approx 10 \text{ GeV}^2$ at $x \approx 0.2$. A much higher energy would increase the kinematical range in the direction of smaller x at the expense of energy resolution. A lower energy would reduce the lever arm in Q^2 in the important region of x around 0.1 to 0.2 to unacceptably low values which would not allow one to verify scaling.

In addition, ELFE obviously will contribute significantly also to refine our understanding of other fields.

In the past twenty years experiments at CERN, FNAL, DESY and SLAC have tried to determine and refine parton distributions through the study of hard inclusive processes. The theoretical foundations are solid and the calculations are mostly under control. The obtained information is vital for the use of hadrons as quark-gluon beams at the high energy particle physics frontier. This program is advanced but still incomplete since it lacks detail about distributions of (transverse) spin, flavour and gluons. A new generation of semi-exclusive (where the undetected final state is partially constrained) and semi-inclusive (where the undetected final state is unknown) experiments, aiming to decipher the complete spin, flavour and transverse-momentum structure of nucleons and hadrons, will fill these gaps of our knowledge. More specifically, the physics programme at ELFE will involve [1]:

- The precise determination of inclusive parton distribution at medium to large x ;
- The flavour and valence-sea decomposition of parton distributions;
- The access to the transverse (spin and momentum) degrees of freedom;
- The access to the spin properties of distribution and fragmentation functions.

Finally, the use of the nucleus as a “femto-detector” will allow one to determine the space time structure of elementary processes, providing further constraints on the interplay between hard and soft mechanisms at large momentum transfer. Examples are [1]:

- Propagation and interaction of compact rare configurations of hadrons (Colour Transparency);
- Quark propagation and hadronization;
- Rare multi-quark configurations in nuclei;
- Charm production near threshold.

In summary, ELFE would indeed be a unique facility, well suited for the study of the structure of hadrons and the dynamics of confinement by means of

- the determination of new parton distributions and quark distribution amplitudes through the measurement of exclusive and semi-exclusive reactions at high momentum transfer;
- an accurate determination of hadron structure functions (parton distribution functions, quark–gluon correlations and parton fragmentation functions) especially at large and medium-large x in inclusive and semi-inclusive measurements;
- the study of hadron propagation in nuclei, which will select compact hadron configurations, and the study of hadronization, which can be tuned to take place either inside or outside a nuclear target.

4.3 Detector

The measurement of exclusive processes in deeply inelastic electron scattering puts rather high requirements on the beam and detector quality. The smallness of the exclusive cross sections demands high luminosities of more than about $L = 10^{35} \text{ cm}^{-2} \text{ s}^{-1}$ and a high duty factor to avoid pile up with intense backgrounds. A limit is set by the production of hadrons from the absorption of quasi-real photons by the target nucleons. The detector must be fast enough to assign an observed signal unambiguously to a single scattering event. This does not mean that all parts of the detector must have a time resolution in the 100 ps range. A coarse grained coverage with fast detectors however will be necessary to assign an event time to signals from slower detectors. The acceptance for the coincident observation of the electron and at least (n-1) final state particles from the hadronic system has to be much larger than 10% to assure efficient running. In fact a large forward dipole spectrometer, as it is used by HERMES [21] and recent muon scattering experiments, can achieve efficiencies close to 100% for some simple cases like exclusive charged meson (π, K) production. This is due to the predominance of small transverse momenta of the produced hadrons relative to the virtual photon direction. At beam energies around 30 GeV a horizontal acceptance of $\Theta \approx 3Q/E = 25^\circ$ appears sufficient to cover the kinematical region up to momentum transfers of $Q^2 = 25 \text{ GeV}^2$. Although focusing spectrometers would offer a momentum resolution of better than $\delta p/p \approx 10^{-4}$ for charged particles, their small acceptance would be adequate in a few cases only (see for instance Ref. [22]). For a large

acceptance spectrometer on the other hand it is a very challenging task to obtain a momentum resolution of about $\delta p/p \approx 10^{-3}$. This resolution would be necessary to assure the exclusivity of an event by the reconstruction of missing masses. The smallness of the pion mass as compared to the beam energy sets this scale. It is very important that the energy spread of the beam does not exceed 10^{-3} since this would then degrade the missing mass resolution. The limiting accuracy of the measurement of momenta of charged particles in a forward dipole is set by the amount of multiple scattering between the particles origin and its final detection after having traversed some magnetic field. In principle the two extreme positions can be measured or experimentally defined to any accuracy. For the determination of the particle momentum at least one intermediate measurement is necessary. This unavoidably introduces multiple scattering. The combined requirement of high spatial resolution together with fast response and low mass appears presently to be met best with a scintillating fiber detector. A procedure for operating such a detector in vacuum has been worked out. Together with a 5 Tm dipole a momentum measurement with 10^{-3} resolution is achievable.

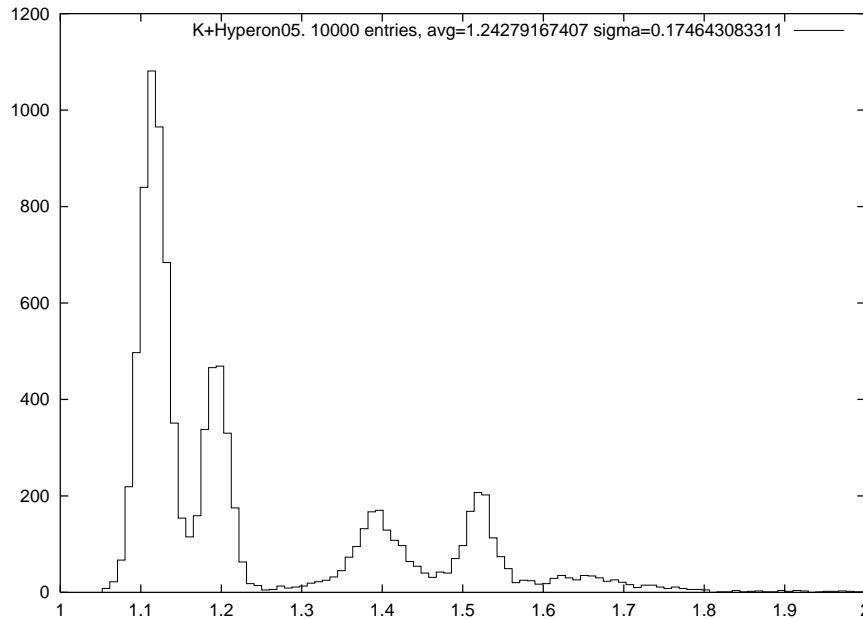


Figure 4.3.1: *Missing mass spectrum for exclusive K^+ production at $x=0.2$, $Q^2=4 \text{ GeV}^2$ simulated for the apparatus shown in figure 4.3.2. With the assumed energy width of the 25 GeV electron beam of $\sigma_E/E = 5 \cdot 10^{-4}$ the missing mass resolution is $\sigma_M = 16 \text{ MeV}$. A beam energy width of $\sigma_E/E = 10^{-3}$ degrades the mass resolution to 21 MeV. The relative cross sections for the different hyperon states were taken from recent CEBAF data at 4 GeV beam energy. The natural widths are taken from the Particle Data Group compilation.*

Figure 4.3.1 shows a simulated missing mass spectrum for the K^+ electroproduction at 25 GeV beam energy with the proposed forward detector. The simulation assumes

the presence of a performant particle identification system. A large dual radiator RICH is part of the proposed detector. With the use of a thin target and a well defined beam diameter the origin of the particle track can be sufficiently constrained in order not to worsen the mass resolution. For extended targets and particles originating from secondary vertices an additional vertex detector can be introduced which then determines the origin of a particle track before entering the spectrometer. It turns out that the loss of angular resolution of the primary track by multiple scattering in the target or the vertex detector is not as severe as a loss of resolution in the absolute momentum. For the exclusive measurement of deeply virtual Compton scattering a forward spectrometer alone can not provide the desired separation from events where the target is excited. A fine grained calorimeter as foreseen for the ELFE detector can detect the photon with good angular resolution and an energy resolution of about $\delta p/p \approx 3 \cdot 10^{-2}/\sqrt{p[GeV]}$. While the spatial resolution will help to detect π^0 and thus provide means for background subtraction, the energy resolution is insufficient for the separation of inelastic channels via a missing mass determination. The obvious solution is the detection of the recoiling proton. A minimum momentum of typically 100-200 MeV/c is necessary for its detection. This momentum is directly related to the minimum transverse momentum of the real photon relative to the virtual photon accessible to measurement. The addition of a recoil detector with a very low momentum threshold is another necessary feature of the proposed spectrometer. The massive production of Moeller electrons in the forward and backward direction sets limits to the detector acceptance. While at forward angles these electrons can be removed by cutting out a “Moeller-parabola” from the acceptance, causing only mild losses of good events, at backward angles an axial field will curl up the abundant low momentum electrons. The biggest cross sections will occur for purely radiative events. By not instrumenting the median plane of the forward dipole spectrometer the radiative photons as well as the electrons can leave the detector without further interaction. The exclusive production of unstable mesons decaying in or close to the target, like $\eta, \eta', \rho, \omega, \phi$ and K_s^0 , poses an acceptance problem to the spectrometer. The lower momentum charged mesons from their decays can not pass the spectrometer. Instrumenting the inner side faces of the dipole recovers these particles with sufficient resolution. The recoil detector will also serve to detect decay mesons at larger angles ($\Theta > 25^\circ$).

Figure 4.3.2 shows a view of the proposed detector system including the recoil detector. The cost of such a detector will be of the order of 25-50 MEUR.

A particular difficult problem is represented by exclusive measurements with polarized proton or deuterium targets. Target materials which can maintain a high degree of polarization at beam currents of 100 nA have been used at SLAC. Useful targets are typically one cm thick and require a field of 5 T for continuous polarization build up and methods to distribute the heat load over a larger volume. It appears feasible to integrate such targets into the spectrometer without compromising acceptance and resolution too much.

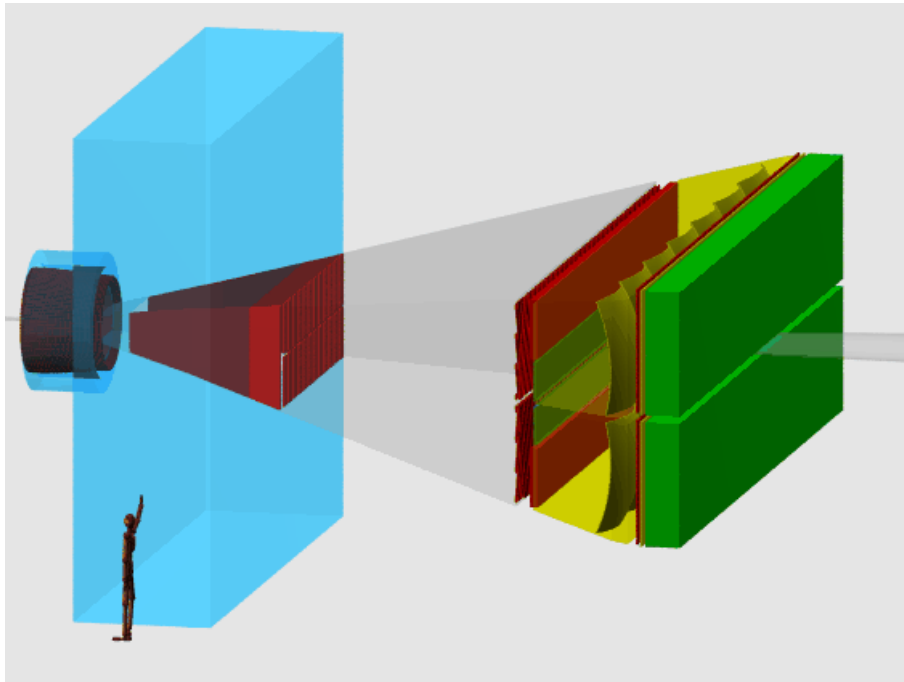


Figure 4.3.2: View of the ELFE spectrometer. The beam enters from the left. The total length is about 10 m. It consists of a dipole magnet (blue) equipped with three fibre trackers (red), a particle identification section with a RICH (yellow), a TRD, an hodoscope/TOF (red) and a calorimeter (green). The cylinder in front of the dipole is the recoil detector.

4.4 The ELFE@DESY Project

A proposal of incorporating ELFE into an extended TESLA project (ELFE@DESY) was presented in 1995 [2]. It consists in using only a fraction of the TESLA linac (a 27 GeV linac) together with the HERA electron ring as a pulse stretcher. The proposal is based on the fact that the superconducting linac, that is operated at low duty-cycle (about 0.4%) for e^+e^- collider mode, is available for other tasks during the time between collider pulses. A fraction of the beam pulses produced by TESLA could be injected into the HERA ring until the ring is filled. Then, the principle of ELFE@DESY is the following:

- Short pulses are produced at low frequency (10 Hz) by TESLA and accumulated in the HERA ring until they fill the ring.
- The stored beam is then slowly extracted from the ring over the time period between the accelerator pulses by switching on nonlinear lenses in the ring that induce a controlled beam instability (resonant growing of particle oscillation amplitudes).
- When the ring is empty, new pulses from the linac are stored and the extraction process start again.

In 1996 a group of accelerator physicists from Bonn, DESY, Frascati, Grenoble, NIKHEF and Saclay has explored the possibility of combining TESLA and HERA to produce a beam for the ELFE physics program. The group has concentrated the efforts on the following problems:

- Modification of the HERA e-ring lattice for the needs of slow extraction.
- Beam extraction: analysis of possible extraction methods, simulation of the extraction process, definition of the extraction channel.
- Beam injection: optics and hardware.
- New RF system in HERA and multi-bunch instabilities.
- Time structure of the injected beam, compensation of beam-loading in the injection linac.

Solutions have been found for all these problems. For the repetition rate to fill HERA a compromise must be chosen between a high peak current in the ring and the stronger requirements for the linac RF-system to accommodate more frequent pulses. A repetition rate of 10 Hz has been assumed for the ELFE mode, twice the TESLA design value. Since the same linac section is also used to generate the drive beam for the Free-Electron Laser facility at a rate of 5 Hz, this means that the part of the TESLA linac used as the injector for the stretcher ring will be pulsed at a rate of 20 Hz, which seems feasible with moderate modifications of the pulsed RF-power sources. For an extracted beam intensity of $30 \mu\text{A}$, the current stored in the HERA ring is 150 mA, which appears possible both from the point of view of RF-system requirements and instabilities in the stretcher ring. The design linac beam pulse length of $800 \mu\text{s}$ is matched by using a multiturn injection scheme in the ring. The bunch-train consists of 38 batches of 220 bunches, spaced by the HERA revolution time ($T_{rev} = 21.1 \mu\text{s}$) plus 50 ns to account for the kicker gap (see Figure 4.4.1). The bunch spacing is chosen as three times the linac bucket spacing, consistent with a 433 MHz RF-system in the ring.

For using HERA in stretcher-mode all the elements for e-p collisions have to be removed, sextupoles have to be inserted into the lattice at suitable positions with respect to the extraction septum, optical functions have to be properly defined because of their influence on extraction parameters and the horizontal tune must be close to a third-order resonance. The achievable performances of the extracted beam have been calculated assuming that the effects of machine imperfections could be corrected. The results of the feasibility study are reported in the ref. [3]: they demonstrate that it is possible to extract electrons from HERA used as a stretcher ring and produce a high luminosity quasi continuous beam suitable for exclusive experiments. A possible scheme of the linac arrangement with respect to the HERA ring is illustrated in Figure 4.4.2. The TESLA source is not far from the HERA ring, one end of the roughly 32 km long linear collider is close to the experimental West Hall, with the linac being exactly tangential to the HERA West straight section. Then, the injector linac for ELFE

experiments with high luminosities, in the range $10^{35} \text{ cm}^{-2}\text{s}^{-1}$ (with large acceptance detectors) to $10^{38} \text{ cm}^{-2}\text{s}^{-1}$ (with well shielded magnetic spectrometers). The large duty factor will enable coincident experiments which are excluded otherwise.

Table 4.4.1: *Expected performances of ELFE@DESY.*

Energy range	15-27 GeV
Maximum current	30 μA
Duty-factor	88 %
Bunch spacing (433.33 MHz)	2.3 ns
Horizontal emittance (90% of the particles)	4 mm μrad at 15 GeV 12 mm μrad at 25 GeV
Energy spread (FWHM)	1.2 10^{-3} at 15 GeV 2.2 10^{-3} at 25 GeV

Bibliography

- [1] M. Anselmino et al., NuPECC Report (*in press*);
http://www-dapnia.cea.fr/Sphn/Elfe/Report/ELFE_phys.pdf
- [2] R. Brinkmann, DESY Internal Report DESY-TESLA-95-14.
- [3] R. Brinkmann et al., Nucl. Phys. A622 (1997) 187c.
- [4] K. Aulenbacher et al., CERN Report 99-10, December 1999.
- [5] X. Ji, J. Phys. G 24 (1998) 1181;
Phys. Rev. Lett. 78 (1997) 610.
- [6] A. Radyushkin, Phys. Lett. B 380 (1996) 417.
- [7] M. Vanderhaeghen, P. Guichon and M. Guidal, Phys. Rev. D60 (1999) 094017.
- [8] J.C. Collins, L. Frankfurt and M. Strikman, Phys. Rev. D56 (1997) 2982;
J.C. Collins and A. Freund, Phys. Rev. D59 (1999) 074009.
- [9] A.V. Belitsky, D. Müller, L. Niedermeier, A. Schäfer, Phys. Lett. B474 (2000) 163;
Nucl. Phys. B546 (1999) 279.
- [10] A.V. Radyushkin and C. Weiss, hep-ph/0010296;
N. Kivel, M.V. Polyakov, A. Schäfer, and O.V. Teryaev, hep-ph/0007315.
- [11] M. Diehl, T. Feldmann, R. Jakob and P. Kroll, Eur. Phys. J. C8 (1999) 409.
- [12] L. Mankiewicz, G. Piller and A. Radyushkin, Eur. Phys. J. C10 (1999) 307.
- [13] L. L. Frankfurt, P. V. Pobylitsa, M. V. Polyakov and M. Strikman, Phys. Rev. D60 (1999) 014010.
- [14] M. V. Polyakov and C. Weiss, Phys. Rev. D60 (1999) 114017.
- [15] X. Ji and W. Melnitchouk, Phys. Rev. D56 (1997) 5511.
- [16] L. Mankiewicz, G. Piller and T. Weigl, Eur. Phys. J. C5 (1998) 119.
- [17] I.V. Musatov and A.V. Radyushkin, Phys. Rev. D61 (2000) 074027.
- [18] M.V. Polyakov and C. Weiss, Phys. Rev. D60 (1999) 114017.
- [19] M. Penttinen, M.V. Polyakov and K. Goeke, hep-ph/9909489.
- [20] M. Amarian for the HERMES Coll., Proc. of SPIN 2000, XIV Int. Spin Physics Symposium. Oct. 18-21, 2000, Osaka, Japan.
- [21] HERMES Coll., K. Ackerstaff et al., Nucl. Instr. and Meth. A417 (1998) 230.
- [22] O. Bing et al., Conference Proceedings of the Italian Physical Society, 44 (1992) 475.